Probing Molecule-Surface Interactions through Thermal Desorption Rates

Dissertation
for the award of the degree
"Doctor rerum naturalium"
of the Georg-August University Göttingen

within the doctoral program
"Benchmark Experiments for Numerical Quantum Chemistry"
of the Georg-August University School of Science (GAUSS)

submitted by
Dmitriy Borodin
from Moscow

Göttingen, 2021

Thesis Committee

Prof. Dr. Alec M. Wodtke
Institute of Physical Chemistry

Prof. Dr. Dirk Schwarzer
Max-Planck-Institute for Biophysical Chemistry

Prof. Dr. Hua Guo
Department of Chemistry and Chemical Biology,
University of New Mexico

Member of the Examination Board

Reviewer: Prof. Dr. Alec M. Wodtke
Institute of Physical Chemistry

Second Reviewer: Prof. Dr. Dirk Schwarzer
Max-Planck-Institute for Biophysical Chemistry

Further Members of the Examination Board

Prof. Dr. Theofanis N. Kitsopoulos
Department of Chemistry, University of Crete

Prof. Dr. Jürgen Troe
Institute of Physical Chemistry

Prof. Dr. Konrad Koszinowski
Institute of Organic and Biomolecular Chemistry

Prof. Dr. Jörg Behler
Institute of Physical Chemistry

Date of the oral examination: 14.12.2021

Acknowledgements

First, I would like to thank Alec M. Wodtke and Theofanis N. Kitsopoulos for allowing me to work in their group for my doctoral studies. Thank you for teaching me how science works and for the freedom you gave me to pursuits my own ideas. I enjoyed many hours of discussions and paper writing with you. Thank you for the opportunity to learn from you.

Next, I would like to thank the Beamer-II-Team. Thank you Michael Schwarzer and Jan Fingerhut for your valuable help, all the "special" discussions and just the fun time in the lab and office. Thank you Nils Hertl for the interesting discussions, the calculations and your valuable corrections of my thesis. I would also like to thank Stefan Hörandl and Florian Nitz for their great work during their bachelor theses. All the work presented here was a team effort.

Furthermore, I would like to thank the world-class scientists with whom I had the pleasure to work. Especially, I would like to thank: Dan J. Auerbach, Dirk Schwarzer, Alexander Kandratsenka, G. Barratt Park, Kai Golibrzuch and Georgios Skoulatakis. Thank you for sharing your experience and clever ideas with me. I would also like to thank Oihana Galparsoro and Hua Guo for providing very important theoretical calculations and their discussions. Thank you Igor Rahinov for the nice discussions, for teaching me your organization philosophy and the fun paper writing. Thank you for the possibility to learn from all of you.

In addition, I would like to thank Prof. Dr. Jürgen Troe, Prof. Dr. Jörg Behler and Prof. Dr. Konrad Koszinowski for agreeing to review this work.

Finally, I would also like to thank my family and friends for their constant support during my studies in every possible way. Thank you Valentina for being my bright star on the horizon. This work would not have been possible without your love and support.

Abstract

The accurate description of chemical reaction rates at surfaces is essential for the understanding of heterogeneous catalysis. As industrial catalysts are in general complex, fundamental understanding on how they work requires input from theory, typically using density functional and transition state theory. These methods are the state-of-the-art tools to acquire elementary rate constants, which serve as building blocks of kinetic mechanisms. The resulting mechanisms allow us to evaluate the catalyst's activity and selectivity for a particular chemical transformation. Unfortunately, the established theoretical methods for prediction of rate constants lack validation from detailed experiments of which there are few. In the present cumulative thesis, experimental techniques and analysis procedures were developed, allowing to test the established methods for rate constant prediction based on accurate measurements of thermal desorption rates. Kinetic experiments on single crystal surfaces were made possible by the velocity resolved kinetics approach under ultra-high vacuum conditions. I exploited the far-transition-state concept, based on which the molecule's binding energy to and entropy at the surface are directly obtained from thermal desorption rate constants. The binding energies are valuable benchmarks to evaluate the accuracy of the electronic-structure theory. The entropies serve as a critical test to models employed for the description of adsorbate's partition function, essential for the description of thermodynamic and kinetic properties of surface chemistry. In addition, adsorbate entropies serve as a valuable probe for molecule-surface interactions. In this work I present experimental and kinetic modeling studies on four molecule-surface systems—H_2/Pt(111,332), NO/Pd(111,332), CO/Au(111,332) and NH_3/Pt(111,332)—which allowed me to make the following conclusions: 1) Thermal desorption rates are a sensitive probe for molecule-surface interactions and can provide information beyond binding energies only. Detailed modeling of adsorbate entropy allows the quantification of diffusion barriers and vibrational relaxation times based on thermal desorption rates. 2) Established models for adsorbate partition functions lack accuracy as they ignore quantum effects and rely on the assumption of decoupled degrees of freedom. Strategies to account for these effects are presented. 3) The desorption rate from surfaces with atomic steps can be dominated by entropic effects, despite the molecule's higher energetic stabilization at steps. These effects will likely be important for surface reactions as well. 4) Elementary parameters obtained from experiments at single crystal surfaces and models developed to explain these experiments have enough transferability to understand aspects of heterogeneous catalysis at industrially relevant conditions and at real catalytic materials. This work provides a perspective that reaction kinetics at surfaces can be a more exact science.

Associated Publications

"Measuring Transient Reaction Rates from Nonstationary Catalysts"

D. Borodin, K. Golibrzuch, M. Schwarzer, J. Fingerhut, G. Skoulatakis, D. Schwarzer, T. Seelemann, T. Kitsopoulos, A. M. Wodtke, *ACS Catalysis* **2020**, *10*, 14056–14066, DOI 10.1021/acscatal.0c03773, Ref. [1], Sec. 2.1

"Quantum influence on H atom recombination on Pt"

D. Borodin, N. Hertl, G. B. Park, J. Fingerhut, M. Schwarzer, Y. Wang, F. Nitz, G. Skoulatakis, A. Kandratsenka, D. J. Auerbach, D. Schwarzer, H. Guo, T. N. Kitsopoulos, A. M. Wodtke, **2021**, *(submitted)*, Ref. [2], Sec. 3.1

"NO Binding Energies to and Diffusion Barrier on Pd Obtained with Velocity-Resolved Kinetics"

D. Borodin, I. Rahinov, J. Fingerhut, M. Schwarzer, S. Horandl, G. Skoulatakis, D. Schwarzer, T. N. Kitsopoulos, A. M. Wodtke, *Journal of Physical Chemistry C* **2021**, *125*, 11773–11781, DOI 10.1021/acs.jpcc.1c02965, Ref. [3], Sec. 4.1

"Following the microscopic pathway to adsorption through chemisorption and physisorption wells"

D. Borodin, I. Rahinov, P. R. Shirhatti, M. Huang, A. Kandratsenka, D. J. Auerbach, T. L. Zhong, H. Guo, D. Schwarzer, T. N. Kitsopoulos, A. M. Wodtke, *Science* **2020**, *369*, 1461–1465, DOI 10.1126/science.abc9581, Ref. [4], Sec. 4.2

"Kinetics of NH3 Desorption and Diffusion on Pt: Implications for the Ostwald Process"

D. Borodin, I. Rahinov, O. Galparsoro, J. Fingerhut, M. Schwarzer, K. Golibrzuch, G. Skoulatakis, D. J. Auerbach, A. Kandratsenka, D. Schwarzer, T. N. Kitsopoulos, A. M. Wodtke, *Journal of the American Chemical Society* **2021**, *143*, 18305–18316, DOI 10.1021/jacs.1c09269, Ref. [5], Sec. 4.3

Contents

Introduction

Catalysts are substances and materials that enforce chemical transformations, which in their absence would not be able to occur. There are three general criteria based on which a catalyst is chosen for the desired application: activity, selectivity and practicability[6–8]. First of all, a catalyst should be active enough to convert the reactants to the desired product. Second, by doing so, it should selectively favor only the formation of the desired products and, ideally, prevent side reactions to take place. Finally, the catalyst should not only be able to perform well in the laboratory, but also have the potential to be used on large scale. Heterogeneous catalysis takes a special role in this context. Here, the reactants and products are in different states of matter than the catalyst. Usually, solid catalysts are used. This is a desired condition, because additional procedures where the catalyst is separated from the reaction product are not required. Heterogeneous catalysis finds broad applicability, for example in large scale production of various chemicals, in exhaust gas purification or in electrochemistry[6, 8].

The practicability of heterogeneous catalysis does not take away the need to evaluate a catalytic material regarding its activity and selectivity for the desired chemical transformation. Unfortunately, most of the catalysis research still follows the "cook-and-look" procedures. Clearly, the desire for a systematic framework allowing rational design of new and better performing catalyst is high. To understand what the expectations of a good catalyst are one has to realize what a catalyst actually does. In the end of 19th century Wilhelm Ostwald, has provided the precise definition of catalytic action that we know today: Catalysts accelerate the rates of chemical reactions but do not affect their equilibrium outcome. This definition reflects the fact that the "natural language" of catalysis is chemical reaction kinetics. Understanding the kinetics allows us to understand catalysis.

Realizing the importance of reaction rates leads to the question on how they can be quantified. The net product formation rate is build upon the underlying rates of participating elementary processes. Elementary processes are microscopic, reactive and nonreactive, events between atoms and molecules, which are, from the kinetics point of view, not further reducible. Such processes provide the building blocks for reaction mechanisms. Hence, we have to know which elementary processes have to be considered in heterogeneous catalysis. The research effort in surface science over the past decades has provided this knowledge[6, 9, 10]. The following processes can be involved: Reactants, typically from the gas phase, hit the surface and may adsorb to it. Subsequently, they can either desorb without prior reaction or diffuse to the active sites on the catalytic surface where they can either decompose or react with other adsorbates. Finally, the reaction product desorbs from the catalyst. These processes form the basis of the Langmuir-Hinshelwood[6] reaction mechanism which is the most common mechanism in surface reaction kinetics.

Every elementary process can be linked to a temperature dependent rate constant, which determines how fast the respective process occurs. Knowing these parameters

allows to quantitatively evaluate a catalyst upon its activity and selectivity to form the product of interest. Consider, for example, a catalyst that selectively decomposes a molecule. Once adsorbed, the probability for the molecule to be decomposed is reflected by its competition between desorption and diffusion with subsequent bond breaking at the active site. The selectivity for the desired decomposition product is reflected by the competition between the individual rates of the decomposition and the undesired reactions with other adsorbates[7].

In principle, each of the elementary processes can dominate the overall product formation sequence and be rate limiting, but this is not known *a priori*. Thus, it is important to reliably predict all elementary step rate constants to characterize the catalyst-reactant system. Unfortunately, so far this is the main obstacle in catalysis research.

Theoretical prediction of surface reaction rates is based on Transition State Theory (TST) and Density Functional Theory (DFT). Electronic structure characterization of the reactants and the transition states (TSs) are done on idealized model catalysts like an atomically-flat Pt(111) or an atomically-stepped Pt(211) surfaces. Besides the uncertainties of DFT, the determination of elementary rate constants ignores TS recrossing corrections and involves simplifying descriptions of adsorbate's and TS's entropy. Unfortunately, these *ab initio* rate constants, with all their simplifications, are rarely compared directly to accurate experimental elementary rate constants—simply because such benchmark data are rarely available[11]. Comparisons between predicted and experimental rates are often restricted to stationary product formation rates and are indirect. The modeling of reaction rates requires a characterization of all elementary rate constants in a multi-step kinetic mechanism. Based on this mechanism reaction rates are simulated at experimental conditions[12, 13]. Even if good agreement between experiment and model is accomplished, one cannot exclude error compensation for the individual rate constants. There is a strong desire to test experimental and theoretical rate constants directly, to evaluate the applicability of simplifications in the *ab initio* predicted rates.

The aim of this work is to provide accurate experimental elementary rate constants that serve as benchmarks for testing the simplifications employed in the modeling of elementary rates for surface processes. The determination of accurate rate constants made it necessary to improve the existing experimental methods and the development of detailed analysis procedures to simulate kinetic experiments with molecular beams. In this work, I have focused on molecular and recombinative thermal desorption rates as they provide a sensitive probe for the entropy of adsorbates that are strongly related to the molecule-surface interactions. Based on the detailed comparison between experiment and theory, I was able to test the existing adsorbate entropy models and improve them. Through use of accurate entropy models, thermal desorption rates could be analyzed in much higher detail than before and thus provided a broad range of energetic parameters related to the interaction of molecules with catalytic surfaces.

This cumulative thesis is organized as follows: In the first chapter I will review established (Sec. 1.1) and improved experimental methods (Sec. 1.2) for the study of surface reaction kinetics. Also theoretical methods for the prediction of reaction rates will be explained in detail (Sec. 1.3). The first chapter will be concluded by formulating a research strategy that I have employed in this work (Sec. 1.4). The second chapter provides our published paper on the study of kinetics on nonstationary catalysts with high-repetition-rate detection (Sec. 2.1). The third chapter provides our submitted manuscript in which we test the simplifying approximations used for prediction of rate

constants on the example of hydrogen atom recombination at Pt surfaces (Sec. 3.1). The fourth chapter contains three published papers dealing with molecular desorption in NO/Pd (Sec. 4.1), CO/Au (Sec. 4.2) and NH_3/Pt (Sec. 4.3) systems. In the fifth chapter I provide a unifying discussion on the results obtained in this work and give some recommendation for future effort (Sec. 5). In the end I will summarize the main conclusions of this work (Sec. 6).

Chapter 1

Basics of Surface Reaction Kinetics

1.1 Established Experimental Methods

The experimental methods allowing us to measure elementary processes at catalytic surfaces are often conducted under ultrahigh vacuum (UHV) conditions. UHV provides a well controlled environment, since the catalyst remains clean over a long period of time and only those molecules participate in the reaction which are selectively introduced into the vacuum chamber. Here, catalytic materials are either prepared *in situ* or cleaned prior to the experiments. This general strategy is known as the surface science approach to heterogeneous catalysis research[14].

When the kinetics of surface reactions is studied, the knowledge of reaction and adsorption enthalpies can be instructive. These quantities can be used for the construction of kinetic mechanisms and, by the use of Sabatier's principle, they can provide a qualitative idea of the material's ability to enable the desired chemical transformation[15, 16].

Adsorption enthalpies can be determined from measurements of adsorption isotherms. The equillibrium coverage of the adsorbate is determined as a function of the molecules pressure above the sample. The isosteric heats of adsorption, i.e. constant coverage conditions, along with adsorbate entropies can be obtained from a Clausius-Clapeyron-type analysis. Usually the coverage is inspected by the changes of the sample's work-function[17, 18], Helium and Ion scattering methods[19, 20] or surface vibrational spectroscopy[21].

An alternative method is Temperature Programmed Desorption (TPD) which is widely used to determine binding energies. At low temperatures, the surface is dosed with molecules. The dosing temperature is chosen in such a way that the adsorbates residence time is long compared to the duration of the experiment—typically several minutes. After dosing, the surface temperature is increased using a linear heating rate, while the adsorbates desorption rate is monitored with a mass spectrometer. From the analysis of the desorption rate as a function of surface temperature the desorption barriers can be derived. Often in TPD literature binding energy and desorption barrier are used interchangeably, but this is only true if the adsorption process has no barrier. This assumption fails for chemisorption of H_2 at some metal surfaces[22, 23]. The main difficulty of TPD data analysis is that time and temperature are coupled in the experiment making analysis methods rely on simplifying assumptions. Some of this methods involve desorption prefactor guessing for the estimation of desorption barriers, others estimate them based on rising edges close to the baseline or the variation of heating rates and most of them rely on coverage independent desorption barriers[24, 25]. Most accurate results are obtained when the TPD experiment is numerically simulated or

the full shape of the TPD peak is deconvoluted[26], but this is rarely done.

Unfortunately, when adsorption is no longer reversible then adsorption isotherms and TPD spectra cannot be directly used for the determination of adsorption enthalpy. Reversible adsorption holds for example for molecular adsorption and desorption of CO. When the adsorbing molecule, like NO, decomposes and its fragments desorb in form of N_2 and O_2, then this method is no longer applicable.

For irreversible adsorption Single Crystal Adsorption Calorimetry (SCAC) has proven itself to be a very powerful tool[27, 28]. The heat release upon adsorption and reaction on a thin crystal is measured directly using a pyroelectric detector[29], which is the most accurate method today. Following the heat release as a function of time allows heat release upon adsorption and reaction to be distinguished[30]. SCAC can be seen as the state-of-the-art technique for measuring enthalpies of surface reactions.

Despite the fact that UHV provides a controlled environment, elementary rate constants for surface processes, which are relevant for heterogeneous catalysis, can only be directly measured in exceptional cases. This difficulty arise from the fact that chemical reactions involve multiple parallel reaction pathways which are not always known. In exceptional cases, like for hopping rates, where Scanning Tunneling Miscroscopy (STM) is used to track individual molecules position as a function of time, it is possible to measure the rate of individual elementary processes[31, 32].

Usually, the rate constants are parametrized based on a mean-field kinetic mechanism, including multiple processes and various intermediates, which are designed to analyze experimental observation of a kinetics experiment. Support for mechanism development can be provided from surface spectroscopy methods which are able to identify reaction intermediates at low surface temperatures by their vibrational or photoelectron spectrum. Less frequently, these methods are also employed to measure the rates of surface processes[7, 33, 34], likely due to their low sensitivity and limited time resolution[7, 35]. Certainly, the quality of experimentally derived rate constants depends on the range of experimental conditions considered in kinetics experiments and the detailed nature of the employed mechanism. The existing methods to obtain kinetics information for surface reactions can be roughly divided into two groups: stationary and transient.

Stationary methods are very simple and require rarely more than the standard UHV equipment. These methods analyze the stationary gas phase composition during a catalytic reaction, with different external conditions employed. These external conditions are the static partial pressures of the reactants, which are leaked into the chamber, or the surface temperature. Varying the reactants pressure allows to determine the kinetic order of the product formation process, which is typically tracked with a mass spectrometer. Variations of surface temperature provides apparent activation energies of the product formation rate. Stationary methods are helpful to screen materials for the ability to catalyze the product formation[36]. Furthermore, such methods can be highly error-prone and require a careful background subtraction, which is emerging from the intrinsic reactivity of the UHV chamber—hot filaments can also be catalytically active—which leads to product formation even in the absence of the catalyst that is supposed to be investigated. However, the main issue of static methods is that they are weakly sensitive to the detailed mechanistic aspects of a reaction. This leads to high uncertainties in the derived rate coefficients which in turn should be regarded as qualitative at best[36].

Transient methods for studying surface reactions, especially when combined with molecular beams, have been found to be much better at providing mechanistic and

kinetic insights compared to stationary methods[37]. The main idea of transient kinetics methods is that a short pulse, for example a pulse of molecules or a sudden temperature-jump[38], introduces a perturbation to a system at a stationary-state or equilibrium. The relaxation of the perturbed system back to its initial state is followed on a longer timescale than the perturbation time. Tools to track this evolution can be mass spectrometers or time resolved spectroscopy[7, 37]. The initializing pulses are modulated at a given frequency but are typically chosen in such a way that the investigated system can return to the initial state between the perturbations. Such methods have been established before the first kinetics experiments at surfaces[39, 40] and are today know as pump-probe methods.

The aim of transient methods in surface kinetics is to determine the rate of product formation as a function of reaction time—the kinetic trace[11, 41]. Below I will describe in detail a method that came very close to obtain this information. The Modulated (molecular) Beam Relaxation Spectrometry (MBRS) was a widely applied method to study surface reaction kinetics and can be regarded as the ancestor of Velocity-Resolved-Kinetics (VRK), the current state-of-the-art method for investigating surface kinetics. By going into some more detail of how MBRS was typically used and how it works, I want to highlight the general problems of past molecular beam methods and the improvements of VRK.

In Figure 1.1 the setup and the key experimental observables of a MBRS are shown[42]. A molecular beam of reactants, modulated at an angular frequency ω, hits the surface which is held at isothermal conditions. A second reactant can be introduced as a background gas or by a continuous molecular beam. When surface reactions occur, the modulated function of the first reactant beam gets modified by reactive (and non-reactive) processes at the surface. Surface reactions modify the reactants modulation function and the products are formed at an altered modulation. This product modulation function in time-domain is the product waveform. Its change with respect to the reactant modulation allows to obtain kinetics information. In contrast to stationary methods, the general product formation mechanism (Langmuir-Hinshelwood or Eley-Rideal) can be clarified easily by considering the change of the MBRS product waveform as a response to temperature variation[43]. The scattered gas pulse composition and the temporal response of product waveform is recorded with a mass spectrometer. Besides the residence and reaction time τ, associated with the surface processes which are of interest in the experiment, the time delay between reactant ejection and product detection includes also the reactant-to-surface flight time t_1 and the product-to-detector time of flight t_2. The temporal response does not directly reflect the modification specific to the kinetics of surface processes $T(t)$, but is convoluted over the reactant surface dosing function $I(t)$ and the velocity distribution of the scattered molecules $G(t)$. For accurate information about the kinetics, one has to either make proper corrections or work under conditions where these parasitic effects are negligible[37, 42].

While today it is routine to measure the product density ion-signal as a function of time, during the active time of MBRS experiments, roughly from the late 1960s to the late 1980s, digital acquisition of the product waveforms in the time domain were rarely done, mostly because appropriate electronics were not available[44, 45]. The vast majority of MBRS studies made use of phase-sensitive detection with the help of a lock-in amplifier[43, 45–51]. The modulation signal of the molecular beam was used as a reference for determining the phase-lag φ and the amplitude ε of the fundamental mode, i.e. first Fourier component of the product waveform in the frequency domain. The surface kinetics information is contained in the transfer function $\tilde{T}(\omega)$ (also called

the reaction product vector) and gives the relationship on how the amplitude and the phase depend on the modulation frequency. This function is used for mechanism identification and rate constant quantification—see Refs. [37, 47].

For demonstration, the introduced functions and parameters are shown for the rate equations describing a simple molecular adsorption-desorption system. The rate equation describing the evolution of the adsorbate's coverage θ over time can be written as

$$\frac{\mathrm{d}\theta}{\mathrm{d}t} = S_0\, I(t) - k_\mathrm{d}\, \theta. \qquad (1.1)$$

Hereby $I(t)$ is the time dependent reactant flux, S_0 is the sticking probability of the impinging molecules and k_d is the thermal desorption rate constant. The time domain desorption flux $P(t)$ is given by

$$P(t) = k_\mathrm{d}\, \theta. \qquad (1.2)$$

Since the experimental data are obtained with a lock-in amplification technique, the probed quantity is assumed to be the product signal in frequency domain $\tilde{P}(\omega)$. Based on Eq. 1.1 alone, $P(t)$ reflects the convolution of $I(t)$ with the concentration-time profile of the adsorbate $T(t)$. In frequency domain, $\tilde{P}(\omega)$ reflects the product of the Fourier transforms of $I(t)$ and $T(t)$ and we can define the transfer function $\tilde{T}(\omega)$ to be:

$$\tilde{T}(\omega) = \frac{\tilde{P}(\omega)}{\tilde{I}(\omega)}. \qquad (1.3)$$

Notice that this Equation ignores the spread introduced by the product's time-of-flight distribution. After Fourier transforming the rate Eqs. 1.1 and 1.2 and some algebraic rearrangement (see Refs. [37, 47, 52] for details), the product vector can be written as

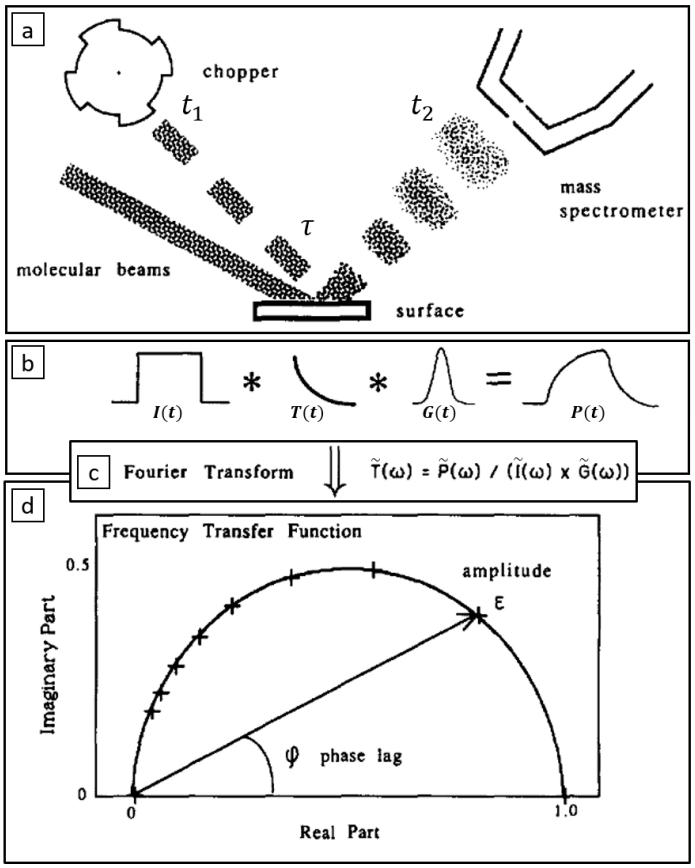

Figure 1.1: **(a)**: A simplified Modulated Beam Relaxation Spectrometry (MBRS) setup is shown. Two molecular beams participate in the experiment. The first reactant is supplied by a continuous molecular beam to the catalytic surface, while a second reactant is introduced by a modulated beam. A mass spectrometer detects the formed product density in time or, more widely applied, in frequency domain. The product's arrival at the detector is delayed with respect to the modulation signal, by the reactant-to-surface flight time t_1, the actual reaction time τ and the product-to-detector flight time t_2. **(b)**: The time-domain product waveform $P(t)$ is a convolution of the molecular beam pulse shape $I(t)$, the surface reaction kinetics $T(t)$ and the product's velocity distribution $G(t)$. **(c)**: Schematic relationship between the time-domain product waveform and the product vector $\tilde{T}(\omega)$ obtained from phase sensitive lock-in amplification. The tilde on top denotes the Fourier transforms of the corresponding time-domain function. **(d)**: Polar-plot of experimentally derived adsorption-desorption kinetics data (amplitude and phase lag of the product vector) from a MBRS experiment. Adapted and reprinted with permission from Ref. [42].

$$\tilde{T}(\omega) = \varepsilon(\omega)\, \exp\left(-i\varphi(\omega)\right), \tag{1.4}$$

with the amplitude

$$\varepsilon(\omega) = \frac{S_0}{\sqrt{1 + \left(\frac{\omega}{k_\mathrm{d}}\right)^2}} \tag{1.5}$$

and the phase-lag

$$\varphi(\omega) = \arctan\left(\frac{\omega}{k_\mathrm{d}}\right). \tag{1.6}$$

The product vector is typically represented as a polar plot, which shape is characteristic for the underlying mechanism. For a simple first-order process the product vector is shown in Fig. 1.1(d).

This procedure is representative for how the analysis of MBRS data was conventionally done. However, there are three implicit critical assumptions within this procedure:

1. Eq. 1.2 reflects the desorption flux, but the ionizer of the mass spectrometer is a density detector. One assumes that the velocity correction to density leads to negligible modification of the product waveforms.

2. Eq. 1.3 assumes that the measured signal at the mass spectrometer is merely given by the convolution of the reactant dosing function and the kinetic response at the surface, but the convolution over the time-of-arrival distribution $G(t)$ (i.e. velocity spread) of desorbing molecules is ignored.

3. The time axis of Eq. 1.1 to 1.2 is implicitly assumed to be reflected by the reaction or residence time at the surface τ but the signal at the detector is shifted by the reactant and product time of flights t_1 and t_2, see Fig. 1.1(a). For typical apparatus geometries and molecular beam velocities this contribution will be on the order of $\sim$400 µs and will influence the measured phase-lag of the product waveform and can lead to erroneous conclusions about the magnitude of the rate constant.

Correction schemes were suggested, but were typically more like rule-of-thumb scaling relations[44, 45]. However, kinetic experiments using MBRS bypassed those conditions where corrections of flight times and velocity spreads are needed. Based on the flight times and associated velocity spreads, residence and reaction times above $\sim$1 ms are expected to be artifact free. If these conditions are fulfilled, the desorption rate constant can be in principle quantified from the phase-lag of a single measurement. However, in practice the phase lag is measured for various beam modulation frequencies, which allows to determine k_d from a linearization of Eq. 1.6. This is needed, since the accuracy of the phase lag measurement depends on the ratio of the these two quantities and since k_d is not known *a priori*, ω has to be "tested" over a broad enough range[37, 52]. Only when a broad range of modulation frequencies is employed and residence times below 1 ms are not taken into account, accurate Arrhenius rate parameter could be extracted from MBRS experiments. In general, when comparing to rates derived from a MBRS experiment, it is better to do so based on the absolute magnitude of measured rate constants in the temperature range of the experiment, instead of the values derived from reported Arrhenius parameters.

The determination of the phase-lag and the amplitude of the first Fourier component of the product waveform fully characterizes a kinetic mechanism that is based on a network of first- and pseudo-first order (linear) rate equations. This is also a precondition that a transfer function can be formulated[52]. However, if non-linear, i.e. second order processes, are involved, the product waveform cannot be reconstructed from the fundamental harmonic only[44, 46]. As a consequence, the kinetic information of the reaction process will be lost. This problem was attempted to be solved experimentally by trying to avoid truly second-order processes through stationary dosing conditions[42] and the detection of higher harmonics[37, 46]. Also slightly dubious pseudo-first order analysis methods for truly second-order processes were sugested[42, 53]. The acquisition of full product waveforms in time domain, that emerged routinely in the mid of the 1980s[42, 54–56], has taken away the disadvantage of lock-in amplification techniques, which allowed only partial reconstruction of the product signal. Despite this advantage, the determination of second-order rate constants, in contrast to first-order processes, requires the absolute adsorbing molecular beam flux, but accurate calibration was rarely possible, due to geometric restrictions of MBRS setups[44]. This is partially the reason why second-order rate constants, e.g. for hydrogen atom recombination, are reported as pseudo-first order rate constants in earlier MBRS work[49, 56].

A more recent kinetic method in combination with molecular beam dosing is Time Resolved IR Absorption Spectroscopy (TR-IRAS)[7, 35]. The procedure is very similar to MBRS, but after molecule pulse adsorption the concentration of reactants and intermediates at the catalyst is followed in time yielding the kinetic trace. Problems associated with detection of product flux and time of arrival are avoided this way. However, since IRAS is rather insensitive, except for special cases such as CO and NO, which have a high transition dipole moment, the time resolution of the experiment is larger than 100 ms. More common are timescales of 1 s and above. Unfortunately, this low time resolution makes this method inherently restricted to low surface temperatures where solvation and clustering[11, 57–59] of reactants and intermediates tend to dominate the reaction mechanisms. Still, the idea behind this method is very appealing, as intermediate concentration-time profiles can be measured, which contain delicate information for surface kinetics.

In this section I have reviewed some of the relevant techniques that are used to study the kinetics of surface processes. Special emphasis has been placed on reviewing the MBRS technique which has been the most useful method to study kinetics of surface reactions until recently. Despite its advantages, it dealt with major difficulties that remained for long time unresolved. A lot of the described issues can be solved with the VRK approach which I will describe in the next section.

1.2 Velocity Resolved Kinetics (VRK): Improvements and remaining Difficulties

A major limitation of Modulated Beam Relaxation Spectrometry (MBRS) is that the reaction rate is either not obtained directly or only with limited time resolution. In addition, the electron impact ionizer of a mass spectrometer probes number density, instead of the required desorption flux. The main difficulty is that velocity distributions cannot be disentangled from the kinetics. In the standard MBRS setups, where the detector is positioned in the scattering plane, independent measurements of velocity distributions could only be made at temperatures where surface kinetics were

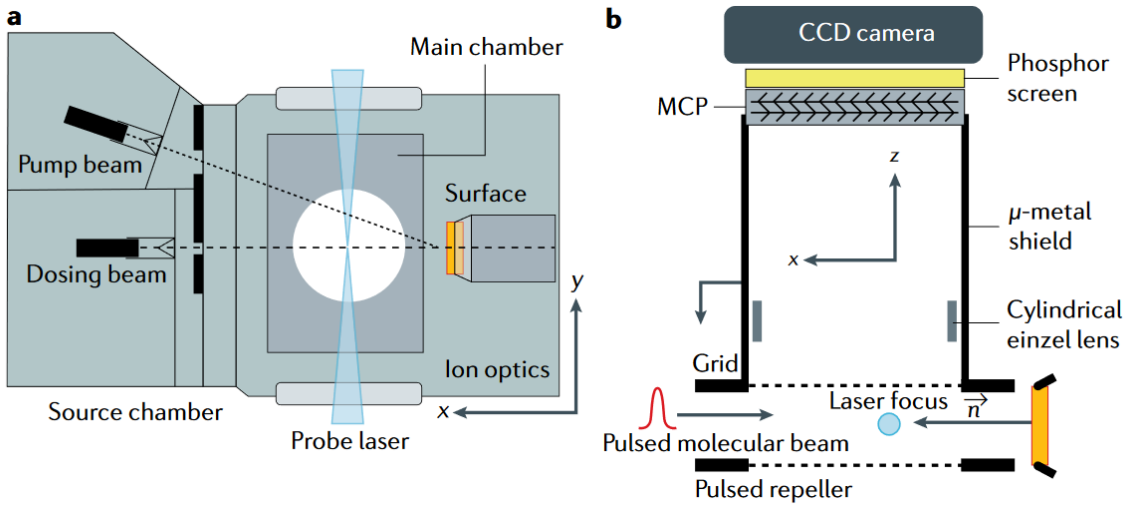

Figure 1.2: **(a)**: Top-view on the "Beamer-II" apparatus used in this work. Two pulsed molecular beams cross the reactants at the surface, located in an Ultra High Vacuum (UHV) chamber. In a pump-probe scheme, one of the nozzle pulses is scanned with respect to the ionizing laser pulse, by which the transient product formation rates are obtained. The open white circle indicates the region from which ions can be projected on the imaging detector. Within this region the product angular distribution and beam's dosing function can be characterized. **(b)**: Side-view on the ion imaging detector. Ions formed by a laser pulse are projected to the imaging detector by a pulsed homogeneous electric field between the repeller and the grid electrode. The pulsed imaging detector consists of a MCP detector (Z- or Chevron-stacked), a Phosphor screen (P43 or P47) and a CCD camera. A cylindrical einzel lens provides the possibility to conduct Velocity Map Imaging[62, 63] experiments. Using a delay between the ion extraction and detection allows to separate different species by their time of flight. Reprinted with permission from Ref. [11].

fast compared to the time of arrival[54, 55]. This precludes density-to-flux conversion and product waveform deconvolution. Thus, the main requirement for a better experiment is the ability to measure the surface kinetics independently from the velocity distribution of the desorbing products within the same measurement.

The first successful attempt was the CO desorption study from Pt(111) by Golibrzuch *et al.*, where a clever two-laser double resonance experiment was employed[60]. The residence time of CO molecules at the surface, provided from a short molecular beam pulse, is scanned by the delay between the nozzle and a UV laser, positioned close to the surface. This laser excites CO into its lowest triplet state and since this state has a long lifetime another UV laser can be used, positioned at some distance from the first laser, to selectively ionize the molecules in this state. Scanning the delay between the two lasers allows an independent determination of the velocity distribution and thus an independent velocity and residence time measurement. Despite the elegance of this work, the potential of which was realized in the community[61], the employed double resonance scheme is not universally applicable to other molecules. In addition, the experiments are challenging due to two independent delays that have to be scanned, which is very time consuming. A more general method is thus required.

The Velocity-Resolved-Kinetics (VRK) method solves this problem, essentially, through the use of ion imaging[64]. The VRK technique was developed around 2017 in Göttingen for the study of surface reactions[65, 66]. The original implementation of VRK in the "Beamer-II" apparatus, which was used during this work, is sketched in Fig. 1.2. A detailed description of the apparatus can be found in Refs. [66, 67]. Some

of the successful elements from MBRS are kept like multiple molecular beams for reactant dosing, which are crossed at the surface, and UHV conditions under which the experiment is conducted. In contrast to the previously used methods, we use pulsed supersonic beams which provide high instantaneous beam flux and pulses as narrow as 10 µs which dictates the time resolution of the experiment. Unlike previous ion imaging applications in surface science[68, 69], our detector is positioned parallel to the scattering plane, spanned by the surface normal and the the incoming beam vectors. This configuration is the key to success as it allows the in-plane velocities of desorbing molecules to be measured independently from the rates of surface processes.

The desorbing molecules are ionized by a focused laser. Depending on the experiment we use resonance enhanced and non-resonant multiphoton ionization using a dye-ns or a Ti:saphire-fs laser, respectively. The ionization takes place between two parallel flat meshes, where a homogeneous electric field along z-axis (orthogonal to the scattering plane) is applied. This allows the ions to be projected onto the area sensitive ion imaging detector, while conserving their in-plane (xy) velocities. The laser focus (width < 100 µm) is positioned 20 mm from the surface, naturally discriminating velocity components in z-direction by laser slicing[70]. Different species can be distinguished by their time-of-flight to the detector. In the experiment, this time is selected *via* the delay between the pulsed ion extraction and the pulsed ion detection at the front MCP of the imaging detector. This time is also required to convert the ion's positional distribution, with respect to the laser focus, into velocity distributions. This information is necessary to convert the density signal of the spatial ion images to flux, reflecting the desorption rate—see Refs. [1, 11, 41, 66, 67] for more details.

Similar to a standard pump-probe experiment, the time evolution of the reaction rate is obtained by scanning the delay between the molecular beam pulse (pump), which initiates the reaction, and the laser pulse, which ionizes the products (probe). As in MBRS experiment the beam-laser-delay axis includes parasitic contributions from reactant and product flight times. Since we measure the velocities of the incident beam and the desorbing products in the experiment, it is straightforward to correct for these parasitic contributions and to assign each flux image to a time, which is only associated with the surface kinetics—the reaction time. This procedure yields the kinetic trace.

Inherently, MBRS is an indirect method especially when combined with lock-in detection. Just consider why an accurate determination of first-order rate constants requires a change of molecular beams modulation frequency. The modulation does not influence or alter any of the kinetic parameters of the system, which is to be determined, but merely makes the product waveform "more visible" to phase-sensitive detection. Also the interpretation of phase-lag data and their analysis were subject of major confusion even by the leading groups in that field[71, 72]. The data emerging from VRK are very direct and only a short chain of analysis procedures is required to compare predictions of a kinetic model to the experiment. With a long chain of data analysis or data extraction procedures it is less likely that minor mechanistic contributions can be identified and clarified. Besides that, the ability to determine the reaction dynamics while monitoring the reaction rate provides complimentary information that can be used for mechanism identification.

The special advantage of VRK was successfully used to disentangle the site-specific reaction mechanism of CO oxidation on Pt[66]. In this work we found that CO_2 is formed *via* two reaction channels with different dynamics. One of these channels had a hyperthermal kinetic energy distribution and a narrow angular distribution peaking at the surface normal. The other channel had a thermal kinetic energy distribution with

broad angular distribution. Both channels had a different rate of formation. Through a detailed investigation of CO oxidation kinetics at Pt surfaces, with different density of atomic steps, we showed that the hyperthermal channel was formed at (111) terraces and the thermal channel by reaction at steps. A kinetic mechanism was developed which is able to quantitatively explain the observations and allows the determination of the elementary rate constant for CO oxidation at Pt(111) terraces—see Sec. 1.3.3 and Refs. [66, 67] for details.

Despite the clear advantages which VRK has over the established methods it has to be clarified that it is not (yet) the universal-remedy for all problems in surface reaction kinetics. Below I will outline some of the problems which we faced at the start of the present work.

One issue comes along with the molecule densities that can be provided to the surface. Typically the molecule dose per pulse is limited to 1 % of a Monolayer (ML, $1\,\mathrm{ML} \approx 1.5 \times 10^{15}\,\mathrm{cm}^{-2}$) restricting all pump-probe type methods for surface reactions to low coverage. Usually this limitation arises as a compromise between high pumping speed (big chambers required), differential pumping (multiple pumping stages between source and UHV chamber) and the requirement of a short beam-to-surface distance (to prevent divergence of beam density)[44, 45]. On the one hand, this allows to probe the molecule-surface interaction more selectively but on the other hand makes it difficult to estimate the adsorbate-adsorbate interactions which will be important at high coverages that are typical for industrial catalysis.

A related problem has to do with the practical limitation of the reaction probabilities that can be studied with molecular beam methods. In contrast to a reactor, in a VRK experiment molecules adsorbing at the surface have only one chance to react. If they desorb without prior reaction, they cannot interact with the surface again. Depending on the exact experimental configuration (e.g. efficiency of detection, molecular beam pulse strength) reaction probabilities around 10^{-5} set the lower limit of what can be investigated in VRK. This limit emerges from two contributions: a) fractional sampling of the angular distribution of desorbing products—dictated by the geometry of the laser focus and its distance to the surface ($\approx 20\,\mathrm{mm}$)—and b) the finite sampling width of the laser detection of the kinetic trace in time, emerging from the spatial width ($< 100\,\mu\mathrm{m}$) of the laser focus. Each contribution reduces the probability to detect a product molecule from a beam of reactants by $\approx 10^{-4}$. With a reaction probability of 10^{-5}, a reactant sticking and product detection probability of unity and with a total number of 10^{13} molecules per pulse we are left with only one detected particle per laser shot. This estimate ignores the dilution of product signal in time, which would decrease this number even further. Unfortunately, most real world heterogeneous catalysis reactions have much lower reaction probabilities than 10^{-5} and thus cannot be studied. Certainly low counting rates can be compensated by higher repetition rate of the experiment—100 Hz can be easily used—but a more fundamental reason lies in the inherently low duty cycle of the pump-probe method (see Sec. 2.1).

In conventional VRK, i.e. with a pump-probe detection scheme, the kinetic traces are acquired by fixing a beam-laser delay and averaging an ion image for multiple pump-probe cycles. The procedure is repeated for various beam-laser delays. From each molecular beam pulse, which initiates a kinetic trace, the pump-probe scheme detects only a small fraction at a fixed time. A detection scheme which allows sampling of a single-pulse kinetic trace at various reaction times, would allow to follow the kinetics of processes with very low reaction probabilities (see Sec. 2.1).

Besides the efficiency argument, the pump-probe detection scheme has another

problem. It is often observed that catalysts change their structure and/or composition during their use. In some cases catalysts are losing their ability to catalyze the reaction and in other cases they can become more efficient. However, this can be a sequential process, too. The loss of catalytic ability can also happen to a surface science model catalyst that is studied with VRK. Often these changes are observed indirectly through drift of experimental rates at constant external conditions. Such changes can be also found due to accumulation of of carbon coverage after a sequence of experiments, because a minor reaction pathway exists that causes formation of carbon atoms, while the major pathway is investigated with transient kinetics methods. As a consequence, each molecular beam pulse initiates a process at a different initial condition. For a pump-probe experiment it is a strict requirement that the investigated system returns to its initial state after each pump-probe cycle. Depending on the underlying processes this can substantially affect the conclusions drawn from a pump-probe method, since these changes might not be noticed during the experiments. Consequently, interpretations of kinetic data can lead to wrong conclusions on the underlying mechanism. A method that allows kinetic traces, initiated by each subsequent pulse, to be measured in real-time would make investigation of nonstationary phenomena possible (see Sec. 2.1).

Another limitation is that the measured quantity in VRK experiments is relative flux vs reaction time. Our analysis procedures rely on the shape of the kinetic trace and its amplitude changes at different conditions. While this is good enough for first order processes, it is insufficient for second order processes. For a second-order process, like recombination of hydrogen atoms, either the absolute flux or the initial concentration of hydrogen atoms has to be known[44, 57]. It is a common routine to estimate the incident beam flux based on the pressure raise in the UHV chamber. With estimations of the chambers pumping speed, beams projection diameter and a sticking coefficient it is possible to determine the initial concentration[73, 74]. Due to the applied assumptions this estimation is a rough estimate only. If high accuracy is desired, this method is insufficient. A more accurate method allows to scan the spatial extend of the molecular beam, e.g. via laser ionization, and can be absolutely calibrated by a static gas at known density. This allows the characterization of exact spatial distribution of the initial concentrations directly (see Sec. 3.1).

Another challenge in surface kinetics is to measure concentrations of reaction intermediates on the surface. The most important information—the holy grail—in kinetic studies are intermediate concentration-time-profiles. These set critical benchmarks for the development of a reliable kinetic mechanism. Unfortunately, with the current VRK implementation we are not able to obtain this information. Measuring the desorption rate of the reactants surviving at the surface, we are sensitive to reaction and desorption pathways in the beginning of a reaction sequence. Furthermore, by following the rate of product formation we are sensitive to the rate determining step along the product formation sequence. Since it is unlikely for intermediates to thermally desorb from the surface no knowledge is obtained. As already mentioned, surface spectroscopy could in principle be used, but is rather insensitive to allow short time resolution. A more promising option, which is currently under development for VRK, is the use of laser induced desorption of reaction intermediates. Here the idea is to use one laser, delayed with respect to the molecular beam pulse, to induce a rapid temperature jump which causes the desorption of intermediates. A second ionization laser scans the desorbed product distribution, which is mapped onto an imaging detector. The integral of the product distribution reflects the relative concentration of the intermediate at a

given reaction time. Possibly this experiments will be able to provide new important information for VRK experiments soon.

The last point is less a problem of VRK but rather a general difficulty in the study of active-site specific reaction rates. In the case of CO oxidation on Pt the formed CO_2 fortuitously experienced non-equilibrium desorption dynamics, which helped to understand the active site specific reaction mechanism[66]. Unfortunately, fingerprints from reaction dynamics are rather exceptional and—if present—almost always specific to H_2, N_2, CO_2 or N_2O, because they tend to have a weak interaction with the catalyst and desorb from the surface before accommodation[75]. Furthermore, reactants might not be restricted or diffusion limited for the exchange between the active sites. Only if this is the case, differences in the transient reaction rate are expected between the active sites. This is a simple consequence of independent or slowly exchanging concentration pools. However, if reactants reach a pre-equilibrium between the active sites, i.e. fast exchange between steps and terraces, the corresponding reaction/desorption rate will be characteristic of a mixture of both active-sites. This means, that even in the simple case of desorption, e.g. from a (111) surface, the observation of a single exponential decay does not exclude contribution from minor defect sites at which the molecule might tend to bind stronger. It is a good practice to consider complimentary experiments at surfaces with varying amount of step. In any case, it appears a valuable question how much information can be derived from surface kinetics if the dynamics is restricted in providing support. One might even question whether this is feasible at all.

In this section I have introduced the state-of-the-art method for studying kinetics of surface processes—Velocity Resolved Kinetics—which was also used for the major part of this work. I tried to highlight the improvements over past techniques and point out some remaining problems. By the end of this thesis I will show how some of the problems could be solved, while others should be addressed in the future. Although it is important to have accurate measurements of the rates of surface processes, it is as important to be able to accurately model them. Only if agreement between theory and experiment is achieved, one can be sure of having understood the underlying system well. Some of the key modeling aspects are discussed in the next section.

1.3 Kinetic Modeling of Surface Reactions

1.3.1 Approximations in Microkinetic Modeling

The description of industrial heterogeneous catalysis requires modeling on different length scales[76, 77]. First, we need to account for the microscopic scale which characterizes the molecule-catalyst interaction. Then, we include description of the mesoscopic scale which accounts for the reactant interplay, responsible for the reaction rate. Finally, catalytic reactors are described at the macroscopic scale which accounts for mass and heat transport. In this section I will focus on the discussion of the microscopic and the mesoscopic scale in more detail.

At the microscopic scale the molecule-catalyst interaction is obtained from electronic structure theory, where Density Functional Theory (DFT) at the level of Generalized Gradient Approximation (GGA) can be considered as the standard method. This involves calculation of binding and reaction energies such as the associated thermodynamic state functions required for the determination of rate constants. The determination of accurate rate constant is part of the next sections—here we consider these properties as known. In some cases it is possible to use a fraction of the micro-

scopic scale information to get an idea about the activity of a catalyst. For example binding energies are found to be useful descriptors for screening catalysts, as they tend to correlate to catalytic activity[16, 78–80]. In heterogeneous catalysis research we know this as Sabatier's principle[15], but the simple physical basis for this is the correlation of reaction barriers with the corresponding reaction energies[81].

The described screening procedures assume implicitly that there is one rate determining step, i.e. an elementary process with a high activation barrier, which is closely associated with the screened binding energy. One of the most prominent examples is the N_2 dissociation, which is the rate limiting step in Haber-Bosch chemistry. Here, the barrier for N_2 dissociation has a linear dependence with N_2 chemisorption energy[79, 80], which qualifies it to be a representative quantity for the catalysts ability to split the N_2 bond. Unfortunately, often enough the rate determining steps are not known *a priori* and one microscopic property is unable to represent the full catalytic process. In such cases the Degree of Rate Control[82, 83], a method which allows identification of rate determining steps, can be used. However, this requires the simulation of the underlying reaction rates, with all elementary steps included, which reflects the interplay of different elementary steps at given external conditions like temperature or pressure.

The first task is always to identify all the relevant elementary steps and quantify their rate constants. Unfortunately, there exists no straightforward scheme that describes how reactants are combined or which processes can occur and therefore a lot of educated guessing is applied to identify the relevant elementary steps. Clearly, if an important pathway is missed the selectivity and activity of a catalyst will not be predicted correctly. Possibly, automated mechanism generators for heterogeneous catalysis[84], similar as known from combustion chemistry research[85], can bring some systematics into these procedures. Despite that, once a set of elementary processes is considered complete for the desired purpose, there are two general procedures which can be used to construct (and solve) the underlying rate equations—mean-field kinetics and kinetic Monte Carlo (kMC).

Usually, mean-field rate equations, as they are used for gas phase reactions, are used for kinetic simulations on catalysts. Unfortunately, this implicitly assumes that reactants are homogeneously mixed, or differently stated, it assumes that reactants encounter each other on a much shorter timescale than the reaction occurs. As used, mean-field models are intrinsically unable to deal with the concept of space. This makes them in general inappropriate to describe reactants active site exchange[76, 77]. It is still an open dispute whether the mean field approximation for surface reactions is reasonable or not. Theoretical calculations on one hand claim that diffusion barriers are universally low, supporting the use of mean-field models[86, 87]. Experiments on the other hand find evidence for the breakdown of mean-field models[88] and also evidence for their applicability even under conditions where the surface is fully saturated[31]. When a surface reaction is diffusion limited there is no chance for accurate description within this framework and other methods are required.

A more general way of solving rate equations provides kMC simulations which accurately accounts for adsorbates spatial distribution on a catalyst. The rate equations are solved stochastically using random numbers that are generated based on the underlying rate constants. Event occurrences like hopping, reaction or desorption are followed over time, providing the rates of surface processes. In kMC only reactants that are placed close to each other on a lattice, which represents the catalyst, are able to react. The advantage of kMC is best demonstrated on the example of CO oxidation at Pt, under low temperature conditions, where it is known that the reaction takes place at oxygen

island perimeters[89]. This means that from all oxygen atoms at the surface only a small fraction is reactive and contributes to the reaction rate. This situation could not be accurately described with mean-field equations as they only deal with average surface concentrations without the knowledge of their spatial distribution. Furthermore, kMC simulations account for reactant hopping and are capable of describing diffusion limited reaction rates. In general, kMC procedure should be preferred over the conventional mean-field rate equations as it provides a more general framework. However, especially when event occurrences are on a very different timescale it is possible that kMC simulations become inefficient and some combination of mean-field equations and kMC procedures becomes the optimal choice[90].

While the materials used in industrial heterogeneous catalysis are highly complex, the rates of reactions are simulated at idealized surfaces. Various materials such as Zeolites or Metal-Oxides were successfully modeled and the associated reaction rates investigated[12, 91]. Of special interest are also metallic catalysts like Pt and Pd, which are often approximated by ideal single-crystal facets like (111), (110) or (211)[92–97]. More recently metallic nano-particles got some attention as well[94, 98]. The effect of reaction promoters, bulk-oxides and catalytic poisons, certainly relevant for real catalysis, are often not considered. The idealized single-crystal surfaces are predominantly studied in surface science under UHV conditions. Unfortunately, microkinetic modeling studies are rarely compared to kinetic experiments so that their approximations remain unvalidated. Clearly, if approximations for such simple systems are inappropriate or wrong, there is no perspective for rational design of heterogeneous catalysis for real materials[99]. How well is electronic structure theory suited for prediction of binding and reaction energies? How accurate are the rate constants modeled? How universal is the mean-field kinetics approach for heterogeneous catalysis? How well is the interplay of different active sites, present at the model catalyst, taken into account? All these questions are still insufficiently answered in our field.

1.3.2 Transition State Theory (TST)

The calculation of thermal reaction rate constants requires the knowledge of the underlying relationship between interatomic distances and potential energy—the Potential Energy Surface (PES). When this quantity is known or can be obtained, it is in principle possible to conduct molecular dynamics simulations to determine the rate of a chemical processes. Hereby, trajectories evolving from the reactant state are followed over time and from the number of occurrences of the process of interest it is straightforward to determine its rate. Unfortunately, this approach is impractical, because chemical reactions are rare events in molecular dynamics simulations. This is due to the fact that the trajectory of atoms on a PES sample the configuration space in a Boltzmann weighted manner. Those regions which lie high in energy, such as the barrier, will only scarcely be sampled and therefore either a lot of trajectories have to be started parallel or a long run-time is required. Both options are computationally demanding, though, especially if one does not have a model PES[77]. A desired approach, excludes the need of simulating non-reactive atomic motion, while still providing the rate of chemical processes with high accuracy. This is what is provided by Transition State Theory (TST)[100].

With TST it is possible to calculate thermal reaction rates. Here a dividing surface is introduced, which separates the reactant and the product state at the PES. Through use of equilibrium statistical mechanics one evaluates the fraction of reactants that

occupies the phase space volume element of the dividing surface. With this knowledge the one-way flux through the dividing surface towards the product site is evaluated and is assumed to reflect the reaction rate[101, 102]. The associated rate constant is quantified by the simple formula

$$k_{\mathrm{TST}}(T) = \frac{k_{\mathrm{B}}T}{h}\frac{Q^{\ddagger}}{Q}\exp\left(-\frac{E_0}{k_{\mathrm{B}}T}\right), \tag{1.7}$$

with E_0 being the energy barrier associated with the position of the dividing plane and with $Q^{\ddagger}$ and Q reflecting the partition functions of the transition state and the reactants, respectively. This formulation is based on classical mechanics but quantum corrections are introduced as tunneling correction to the barrier height and quantum partition functions. The use of Eq. 1.7 requires that reactants are equilibrated in the canonical ensemble or, put differently, the depletion of the reactant states, capable for reaction, is slower than their replenishment by thermalization processes. A well known consequence for the inaplicability of this assumptions is the fall-off region observed for unimolecular reaction in the gas phase[103]. The frequently appearing pre-equillibrium assumption[52] between the transition state and the reactants is not an additional requirement but follows from the two fundamental assumptions of TST—the thermalization requirement and the "no-return" approximation[101, 102].

The TST rate constant, assuming that the barrier and the partition functions are known exactly, will always provide the upper limit to the real rate constant. This is a consequence of the fundamental assumption that reactant trajectories crossing the dividing surface will also form the product. While it is often assumed that the dividing plane is placed at the transition state, i.e. the saddlepoint along the minimum energy pathway, it is not a strict requirement. TST does not restrict the choice of the dividing surface. Usually, the dividing surface is chosen in such a way so that the lowest TST rate constant is obtained, which is expected to be closest to the experimental rates. The saddle point provides a low rate constant due to the high potential energy barrier. Through optimization of the dividing plane along the reaction path it is possible to minimize the rate constant even further, and thus to improve the TST prediction[104]. Essentially, one searches for the free energy barrier.

In exceptional cases TST rate constant can underestimate the actual reaction rate, for example when the reaction proceeds by crossing multiple transition states but the flux through only one of them is characterized. Especially for surface reactions this can be important as the catalyst provides a variety of binding sites where transition states can be stabilized[105].

TST provides a way to estimate the rate of rare events based on statistical considerations only. Theoretically, the (less practical) global molecular dynamics simulations are still more accurate. A way to improve the statistical rate prediction is to couple it with local dynamical correction schemes which enter in form of the so-called recrossing coefficient κ. The exact thermal rate constant is then

$$k(T) = \kappa\, k_{\mathrm{TST}}(T). \tag{1.8}$$

The most efficient way to obtain the exact thermal rate is to chose a dividing surface which results in the lowest possible TST rate and initialize, based on appropriate initial conditions and distribution functions, molecular dynamics trajectories. The inspection of this trajectories allows to determine κ and correct the TST rate[106]. The choice of the dividing plane is merely to obtain accurate results with lowest number of trajectories.

The same procedure can in principle be done for any dividing surface and would provide exactly the same thermal rate[101, 104].

The inaccuracy of TST for the prediction of thermal rates for surface processes can be manifold. Likely the assumption of reactant thermalization is satisfied when molecules are in contact with a catalyst. To demonstrate this one could assume that the catalyst and the molecule have a number of collisions that is close to the Debye frequency of the catalyst. A metal catalyst like Pt or Pd has frequencies on the order of $\approx 10^2\,\mathrm{cm}^{-1}$ and thus one collision per $\approx 10^2$ fs. Even if the reaction proceeds on the subns timescale enough collisions would ensure energy redistribution. While the same could be assumed for reactions in liquid phase, it is known that rate constants strongly deviate from the TST expectations due to reactant-solvent friction at the transition state[107, 108] affecting the passage of reactants through the transition state. While somewhat similar friction effects could be expected to be present at metals, especially due to the presence of electron-hole pairs, little effort is invested from theory to understand such effects on systems relevant to heterogeneous catalysis[10]. Evaluating the importance of such effects is made further difficult as accurate experiments, for comparison with theoretical models, are simply absent.

Another important source of errors for modeling reactions at surfaces can be the accuracy of the underlying electronic structure theory, but this should not be confused with a failure of TST. PES inaccuracies are not related to accuracy of a method aiming to determine thermal rates based on this input. The reaction barrier will be affected by the accuracy of DFT and is known to depend on the underlying exchange-correlation functional[109]. Besides that, uncertainties are introduced by simplifying assumptions on the partition functions. Consider when a molecule at the surface has a low rotational barrier but its partition function is treated as harmonic oscillator. Clearly, this approximation will be unable to describe the density of states over a broad temperature range. Such descriptions are wrong, not because of errors of the underlying electronic structure theory but because of the simplifying assumptions made to approximate the phase space. Although such errors can be avoided or better approximations can be used[92] this is rarely done. Interestingly, in some cases the disagreement between theory and experiment can be tracked back to exactly these problems—see the next section.

1.3.3 Models for Adsorbate Entropies

The TST rate constant can be subdivided into two contributions. The first one is the energy barrier and the other one is the pre-exponential factor, which carries the information of the entropy difference between the transition and reactant state. Calculating the prefactor of a thermal process requires an accurate evaluation of the underlying partition function for the reactant and the transition state. Unfortunately, reactions at surfaces are multidimensional problems, for which we would ideally like to have an accurate multidimensional PES, but this remains out of reach. Thus, different models are used to approximate the underlying phase space based on different portions of the full PES. I will explain several models that are used to acquire the adsorbate partition function, which are subsequently used in the computation of thermal rate constants. Accurate rate constants allow us to evaluate the rate of CO oxidation at an idealized Pt(111) surface and thus are mandatory. I will review these models by discussing their assumptions and limitations. Furthermore, I will critically compare the TST rate constant predictions, using different partition function models, based on previously obtained experimental results.

Commonly, adsorbate entropy models assume a static catalytic surface[92, 110–113]. This reduces the dimension of the problem to $3N$ where N is the number of atoms within the molecule. A major contribution to the entropy of an adsorbate is its translational entropy, which is associated with in-plane motion of an adsorbed particle at the surface. Describing this contribution accurately is essential for the acquisition of an accurate rate constant. Below I introduce some of the main models that are approximating translational entropy of adsorbates—see also Fig. 1.3.

The most widely applied method for the estimation of partition functions is the Harmonic Approximation (HA)[8]. The adsorbates partition function is evaluated based on the harmonic frequencies of the adsorbate that is placed at its most stable binding site at the surface. Based on the derived harmonic frequencies the partition function is evaluated by the product of harmonic oscillator partition functions. Certainly, this approach can be rather accurate for some degrees of freedom, like for stiff bonds inside a molecule, or in general for low temperatures. Unfortunately, this approximation cannot be made *a priori* for the translational entropy. For example, a CO molecule at Pt(111) has a rather low diffusion barrier of $\sim 0.1\,\mathrm{eV}$ and will tend to exchange binding sites even at moderate temperatures. Effectively it will tend to explore the PES outside of the energy minimum, making a partition function model that is restricted to this minimum inappropriate.

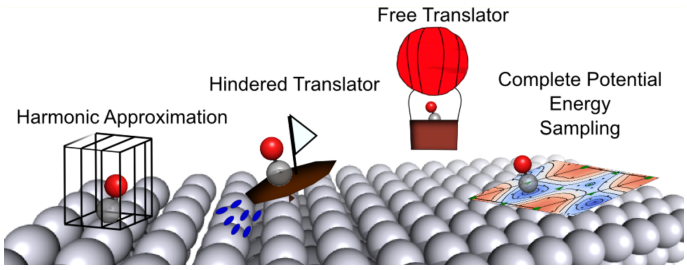

Figure 1.3: A Schematic representation of different approaches for the description of the translational entropy of a CO molecule on the Pt(111) surface: Harmonic Approximation (HA), Hindered Translation (HT), Free Translator (FT) and Complete Potential Energy Sampling (CPES). Reprinted with permission from Ref. [92].

A physically reasonable partition function is able to predict entropies of adsorbates that are equal to the HA at low temperatures, but in addition at high temperatures they predict the entropies of a free translator (FT) or, equivalently, free 2D ideal gas. When temperatures are much higher than the the diffusion barriers the particle will tend to occupy regions around and at the barriers instead of staying localized in the minimum. The Hindered Translator (HT) model[113] is doing exactly that. Essentially, this model is an adaption of the hindered rotor model that was used to explain the temperature dependence of the heat capacity associated with the torsional mode in Ethane[114, 115]. It assumes a simple periodic potential which is imitating the binding sites and diffusion barriers separating them on the surface. It is parametrized based on the frequencies and/or diffusion barriers of the adsorbate obtained from DFT calculations. Unfortunately, this model is unable to describe multiple binding sites within a unit cell of the surface lattice.

For example CO on Pt(111) can bind to hollow, bridge and top sites with similar strength. Within an elementary cell of Pt(111) it thus has six local minima with different stability, which is not possible to describe with HT model accurately. To account for such situations one should conduct DFT calculations for CO positioned (and relaxed) at different coordinates on the lattice. With this information it is possible to determine the classical partition function of an arbitrary potential in two dimensions. Often, this approach is referred to as Complete Potential Energy Sampling (CPES)[92]. In my opinion, this expression is misleading, because the full-dimensional configuration

Table 1.1: Calculated preexponential factors for rate constants of three elementary step processes involving CO* and O* at Pt(111) at 400 K[92]. Different adsorbate entropy models were employed: Harmonic Approximation (HA), Hindered Translation (HT), Free Translator (FT) and Complete Potential Energy Sampling (CPES).

process → method ↓	CO* desorption $\log_{10}(A_{\mathrm{d}}^{\mathrm{CO}} \,/\, \mathrm{s}^{-1})$	CO* + O* reaction $\log_{10}(A_{\mathrm{r}} \,/\, \mathrm{cm}^2\,\mathrm{s}^{-1})$	O* recombination $\log_{10}(A_{\mathrm{rec}}^{\mathrm{O}} \,/\, \mathrm{cm}^2\,\mathrm{s}^{-1})$
HA	15.5	−2.5	0.75
CPES	14.6	−4.7	−0.07
HT	14.4	−5.4	−0.64
FT	14.1	−6.9	−3.1

space is not sampled. Instead, the sampling is conducted only for a restricted number of degrees of freedom and thus "complete" has to be understood with regard to the reduced dimensionality. Despite the high accuracy of CPES it remains a classical partition function and is unable to yield accurate low temperature limits. However, for most applications (except of hydrogen atoms) the inaccuracy appears only at very low temperatures which are less important for heterogeneous catalysis modeling.

The information output from CPES is certainly the highest but it also requires the largest input of DFT data. On the other hand, HA is the least accurate but also requires the least amount of information about the PES. The HT model is a compromise between accuracy and effort. In the worst case, it is as accurate as HA and at best it is as accurate as CPES approach. The HT model's disadvantage is its simple model potential. However, unlike the CPES and HA approach, it captures both the low and high temperature limit correctly. This advantage makes it a rather reliable translational entropy estimate over a broad range of temperatures. The impact of the different translational entropy approximations for the pre-exponential factor for CO desorption, oxidation and O-atom recombination at Pt(111) are shown in Table 1.1.

The translational entropy is a major contribution to the partition function and is of special interest, but this does not exclude the need to accurately account for the residual $3N - 2$ degrees of freedom. The residual degrees of freedom are typically described within the HA. Therefore the harmonic frequencies of the adsorbate at its most stable binding site on the surface are used. Especially for chemisorbed molecules this can be a rather good approximation, as the interaction with the surface is typically strong. When molecules are weakly adsorbed this requires to account for hindered rotation or consider anharmonicity of soft vibrational modes[91, 116]. Independent of the model to estimate the associated density of states, the description is based on the assumption of separable degrees of freedom. A simple example may help clarifying the problem. Consider CO at Pt(111) and ignore for the moment all other degrees of freedom except of its stretch frequency and its in-plane coordinates. From metal-carboxyl complexes is well known that CO stretch frequency depends on the coordination number of metal atoms. The same situation is present at Pt(111) when CO is bound to different binding sites like fcc-hollow or on-top site. Due to the approximation of decoupled modes, one assumes that the corresponding energy contributions are additive and thus the partition functions are multiplied. Clearly, for the CO stretch frequency, which is on the order of $2000\,\mathrm{cm}^{-1}$, this is of no relevance and does not alter the underlying phase space at any relevant temperature range. This shall merely serve as an example to demonstrate the problem of normal mode approximation, which may not be accurate for softer modes that are strongly associated with the molecule's position on the surface.

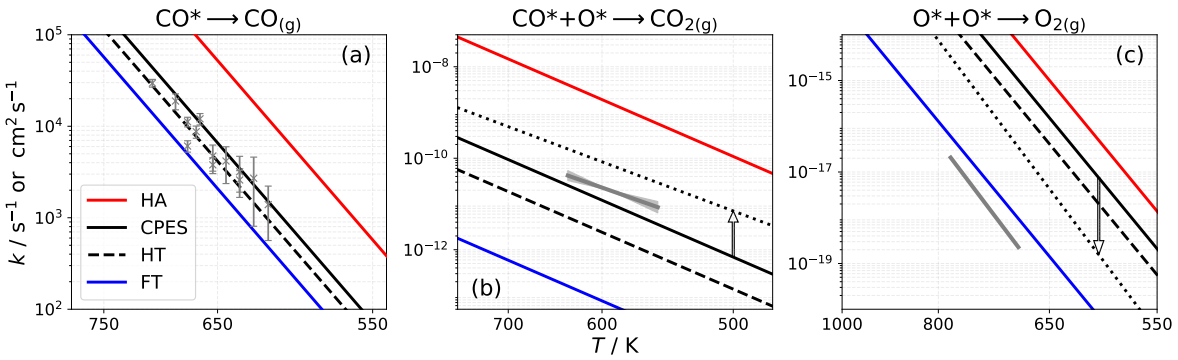

Figure 1.4: Comparison of three *ab initio* predicted rate constants[92], using different entropy models, with experimental results[60, 66, 118] for **(a)** CO desoprtion, **(b)** CO oxidation by O-atoms and **(c)** O-atom recombination at Pt(111). The rate ronstant in (a) has units of s^{-1}, while for (b) and (c) it has $cm^2\,s^{-1}$.

A comparison of *ab initio* rate constants using different translational entropy approaches with experiments is provided in Fig. 1.4. The CO desorption rate constant from Pt(111) was reported in Ref. [60], where the authors have successfully disentangled the terrace and defect site contributions in their experiments, which makes them suitable for comparison. In Fig. 1.4(a) these experimental results are compared to rate constant calculations from Jørgensen and Grönbeck[92]. The HA and FT model set the upper and lower bound to the rate constant, respectively. See Table 1.1. The rate constant determined with the HT model and CPES approach are both agreeing very well with the experiment.

While the comparison can just be considered very good, a drop of bitterness remains. The CO binding energy used in Fig. 1.4(a) is 1.39 eV, while the independent experimental determination provided 1.47 ± 0.04 eV. Besides that, the most stable binding site of CO on Pt(111) is known experimentally to be the on-top site while DFT calculations suggest the fcc-hollow site. This is a famous problem of exchange-correlation functionals at the GGA level[117]. Furthermore, the *ab initio* rate constants are modeled based on TST, without the use of recrossing corrections. Clearly, compensation of errors in this situations cannot be excluded.

Unfortunately, the experimental rate constants for CO desorption are not accurate enough to decide if the HT or CPES is the more accurate approach. The high uncertainty of previous work was mostly related to the difficult analysis of desorption data from Pt(111) where terrace and step contribution were present. If additional experiments at stepped Pt surfaces would have been investigated, a more accurate analysis would have been possible, too. This idea should be kept in mind.

In Fig. 1.4(b) a similar comparison can be made for the oxidation of CO by atomic oxygen. The experimental rate constants were derived based on a comprehensive mechanism from VRK experimental data at two different Pt surfaces[66]. As before the HA and FT model represent the upper an lower limit for the model rate constant. It should be noticed that, since CO oxidation is a second-order reaction, the choice of the adsorbate entropy model has a higher impact on the reaction rate constant. As before the CPES and HT model show the best agreement with the experiment. However, both models predict the rate constant to be too low compared to the experiment, which is not expected from TST rate constant. It is certainly possible that multiple transition states are present which have not been identified. In addition, one has to realize that the transition state is characterized with the HA. If anharmonic corrections

would be considered, which leads to an increased prefactor, one could expect a better agreement between theory and experiment. It is also possible that the DFT calculated reaction barrier is not correct. Errors up to 0.2 eV are typical for DFT at the GGA level[109, 119, 120]. In addition to the CPES rate constant with a DFT barrier of 0.74 eV (black solid line), I also included a CPES based rate constant with a reduced barrier of 0.64 eV depicted as black dotted line in Fig. 1.4(b). I do it only for this entropy approach, as it should be considered most accurate in this case. It becomes clear that the mismatch can be traced back to errors that are typical from electronic structure theory. If the experimental activation energy—0.6 ± 0.1 eV—would have a lower uncertainty one could consider (including proper corrections) to include the experimental reaction barrier into the TST rate expression. This would allow to make further conclusions about possible re-crossing corrections—see also Ref. [11]. Unfortunately, with the present uncertainty, this would be speculation.

The point of recrossing corrections can be made much better on the basis of oxygen atom recombination at Pt(111), depicted in Fig. 1.4(c). For this comparison I use the experimental values derived from TPD[118] measurements. Previous work has accurately accounted for coverage dependent rate parameters and it should be less sensitive to the presence of steps. This is due to the high coverages present in TPD experiments. Unlike for CO desorption and oxidation the experimental rate constants are not within the limits provided by HA and FT model. The CPES and HT predicted rate constants are three orders magnitude too high. As before, one could assume that the mismatch is due to a DFT binding energy error and increase the DFT-based barrier by 0.2 eV for the best model. The corresponding CPES rate constant would then be given by the black dotted line in Fig. 1.4(c)—still two orders of magnitude mismatch with experiment.

Certainly, to bridge this gap, one should consider recrossing corrections. The dividing plane for the O* recombination rate constant was defined far away from the surface, such that the O_2 molecule in gas phase represents the transition state. As a consequence of detailed balance, in this particular situation, the recrossing coefficient is given by the thermal sticking coefficient of the molecule[121–123]. For O_2 at Pt(111) it is known to be on the order of a few percent[118], which would result in a large modification of the *ab initio* rate constant and come very close to the experimental values.

Another important feature to realize is that the present rate constants do not include any information about the electronic partition functions. These are important contribution to thermal reactions in gas phase[102]. The electronic partition function typically only reflects the degeneracy of the electronic ground state. The O_2 molecule, which is used here as the transition state, has a triplet ground state and an O atom, in the gas phase, has (ignoring the spin-orbit interaction) a ninefold degeneracy. For a gas phase reaction, ignoring the electronic partition function would lead to a rate constant that is factor of ~ 27 too high. Certainly one would need to consider that some of the electronic states of O* would be lifted in energy through the interaction with Pt. In any case, the electronic partition functions are commonly ignored for surface reactions, which is rather unsatisfying.

It is interesting to realize that while in CO desorption the best models are close to the FT model, in O* recombinative desorption better agreement with the HA is observed. This comparison reflects the nature of the adsorbate-surface interactions. While CO has a diffusion barrier smaller than 0.1 eV, oxygen has one that is larger than 0.5 eV. This leads to the fact that the density of states of CO* are more comparable

to those of a free translator while the density of states of O* are better reflected by a strongly localized adsorbate. This comparison indicates that it is feasible, with accurate experimental rates, to gain insights into the adsorbate-surface interactions.

1.4 Strategy for Probing Molecule-Surface Interactions by Thermal Desorption

In the previous section I showed that the rates of surface processes requires accurate modeling of the underlying PES, reflecting the adsorbate interactions with the catalyst. It is reasonable to assume that when thermal rate constants are obtained with high accuracy from an experiment, then it is possible to critically test different adsorbate entropy models which are derived based on information from the PES. However, one has to be careful exploiting this concept because adsorbate entropies are not probed directly by thermal rates or rate constants. Experiments have to be analyzed within the framework of exact thermal rates (Eq. 1.8), including recrossing corrections and entropies of the transition state. Below, I want to discuss the key points to take into account when this ideas are to be used.

First of all, it should be clarified which process offers the potential to probe a molecule's density of states as direct as possible. Certainly, reactions like CO*+O* can be used, but they have the problem that the probed quantity is not specific to the reactants only, but rather to the entropic difference between the reactants and the transition state. Assuming that a clever separation between the transition state and reactants contributions can be made, there remains the problem that two different reactants are participating in the reaction. This leads to the fact that the entropic contribution is the sum of both adsorbates and is not specific to the individual molecule. Much better suited for this purpose are molecular desorption, e.g. CO desorption from Pt(111), or recombinative desorption of the same adsorbate, like O* recombination.

The next question is how accurate the different processes can be measured. Often reactions like CO*+O* are derived based on kinetic mechanisms with various elementary processes included. These have either elementary rate constants included based on complimentary measurements—for example CO* desorption and O* recombination—or rate constants which are fitted to an experimental observable. Fitting a kinetic mechanism with multiple processes requires that the input parameters have low uncertainties and the correlations of parameters are suppressed through a broad range of experimental conditions. Ideally different complimentary experiments contribute to the fitting procedure with an accurate data analysis. The basis for any useful outcome sets a comprehensive and physically reasonable kinetic mechanism. Clearly, the shorter the chain of required analysis procedures and the less reactions participate in the system the higher the accuracy of derived rate constants.

Based on the desire to keep the system under study simple, molecular desorption appears to be the ideal choice. Analysis of first-order processes for the most part, requires only the knowledge of the relative desorption flux. No absolute flux calibration is required. On the other hand, second-order processes are much more sensitive to the adsorbate entropy and thus are more useful for a critical test of the underlying partition function models. Unfortunately, determining second order rate constants requires knowledge of absolute adsorbing reactant flux, which is experimentally challenging. When considering the accuracy of experimental determination and the sensitivity upon the property to be studied, both processes are equally well suited for

probing the adsorbate entropies. Since the nominally flat single crystal surfaces have minor contribution of defects, which can influence the kinetics of thermal desorption, complimentary studies at highly stepped surfaces should always be made. This at the same time allows to probe adsorbate entropy effects on stepped surfaces, which are of interest to real catalysts, too.

As I have explained in Sec. 1.2, Velocity Resolved Kinetics provides the possibility to follow the rate of chemical processes through an independent measurement of their dynamics. In the context of probing molecule-surface interactions through rates of thermal desorption this is a huge advantage, as this provides the possibility to derive sticking coefficients from the speed distributions using detailed balance arguments. Especially, for barrierless adsorption this method is very powerful, as absolute sticking coefficient can be determined, with some reasonable assumptions. When sticking coefficients are known, we may use the flexibility of TST to define the dividing plane far away from the surface such that the transition state becomes the gas phase molecule (reduced by one translational degree of freedom). This has two advantages: 1) We can calculate the transition state partition function based on accurately known molecule parameters in gas phase and 2) the thermal sticking coefficient serves as the recrossing correction to the TST rate. This definition of the dividing surface allows us to shift the remaining unknown information from the pre-exponential factor of a rate constant, to the partition function of the adsorbates and thus provide its accurate determination. I will refer to this as the far-transition-state approach to thermal desorption rates.

An additional advantage of VRK is that we can make use of rather high temporal resolution ($\approx 10\,\mu s$) to probe surface processes also at high temperatures. This is advantageous because the relative importance of the pre-exponential factor to the rate constant increases for higher temperatures. In addition, a high temporal resolution allows us to sample a big temperature region and thus provide more accurate rate parameters.

Finally, the determination of the prefactor, which includes information about the adsorbate entropy, will go hand-in-hand with a determined binding energy of the molecules. With our definition of the transition state the obtained property is truly a binding energy and not a desorption barrier. The advantage of modeling the adsorbate entropy allows simultaneously to derive real binding energies, instead of temperature dependent Arrhenius activation energies. While DFT is often reliable for relative energies of adsorbates on the surface, the predicted binding energies are strongly functional dependent[109]. Experimental binding energies might be instructive for choosing an appropriate functional for the desired application or at least estimating the expected uncertainties of the calculated properties. Despite the general tendency that relative energies of adsorbates on metal surfaces are accurate[124], there are some exceptions like CO/Pt(111)[117], which have to be treated with care. The real challenge will be the development of a correct adsorbate entropy model, which is not only easy to implement, but also reliable for the description of relevant adsorbate-surface interaction energies.

A combination of precise experiments, their accurate analysis and detailed modeling of adsorbate entropy are the key recipes for the success of this work.

Chapter 2

Velocity-Resolved Kinetics for Nonstationary Catalysts

2.1 *"Measuring Transient Reaction Rates from Nonstationary Catalysts"*

Author contributions: TS provided the high-repetition rate camera. The experimental setup was done by KG, TK and DB. The experiments were conducted by KG and DB. KG and DB analyzed the data. The reaction-diffusion kinetic model was developed by DB. MS and DB made complementary experiments to proof the model. The paper was written by AMW and DB. All authors contributed to the discussion of the results. All authors contributed to the revision of the manuscript.

ACS Catalysis

pubs.acs.org/acscatalysis

Research Article

Measuring Transient Reaction Rates from Nonstationary Catalysts

Dmitriy Borodin, Kai Golibrzuch, Michael Schwarzer, Jan Fingerhut, Georgios Skoulatakis, Dirk Schwarzer, Thomas Seelemann, Theofanis Kitsopoulos,* and Alec M. Wodtke*

Cite This: ACS Catal. 2020, 10, 14056−14066

Read Online

ACCESS | Metrics & More | Article Recommendations | Supporting Information

ABSTRACT: Up to now, methods for measuring rates of reactions on catalysts required long measurement times involving signal averaging over many experiments. This imposed a requirement that the catalyst return to its original state at the end of each experiment—a complete reversibility requirement. For real catalysts, fulfilling the reversibility requirement is often impossible—catalysts under reaction conditions may change their chemical composition and structure as they become activated or while they are being poisoned through use. It is therefore desirable to develop high-speed methods where transient rates can be quickly measured while catalysts are changing. In this work, we present velocity-resolved kinetics using high-repetition-rate pulsed laser ionization and high-speed ion imaging detection. The reaction is initiated by a single molecular beam pulse incident at the surface, and the product formation rate is observed by a sequence of pulses produced by a high-repetition-rate laser. Ion imaging provides the desorbing product flux (reaction rate) as a function of reaction time for each laser pulse. We demonstrate the principle of this approach by rate measurements on two simple reactions: CO desorption from and CO oxidation on the 332 facet of Pd. This approach overcomes the time-consuming scanning of the delay between CO and laser pulses needed in past experiments and delivers a data acquisition rate that is 10−1000 times higher. We are able to record kinetic traces of CO_2 formation while a CO beam titrates oxygen atoms from an O-saturated surface. This approach also allows measurements of reaction rates under diffusion-controlled conditions.

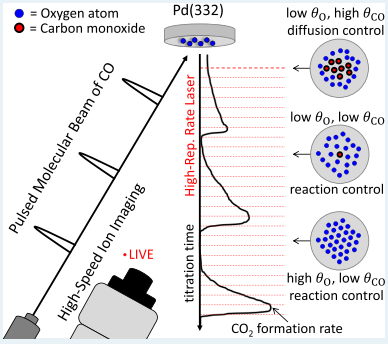

KEYWORDS: *high-speed imaging, velocity-resolved kinetics, CO oxidation, molecular beams, heterogeneous catalysis*

1. INTRODUCTION

Methods to measure the kinetics of surface reactions are fundamental to improving our understanding of heterogeneous catalysis. Traditionally, temperature-programmed reaction, molecular beam relaxation spectrometry, and phase-lag detection have been available to experimentalists.[1−4] Recently, the kinetic trace was obtained using velocity-resolved methods[5] based on ion imaging.[6−8] This is essentially a pump−probe technique where a molecular beam pump−pulse initiates the reaction and pulsed laser ionization probes the desorbing products. Varying the delay between the two pulses provides the time base of the reaction kinetics. The ionized products are recorded with ion imaging providing product velocity information with every detection pulse. This allows measured product densities to be converted to product flux, which is by definition the reaction rate for a surface reaction. Furthermore, flight times irrelevant to the reaction time can be subtracted from the experimental time axis.[9] Like all pump−probe measurements, during the time that the delay between pump and probe is being scanned, the catalyst under study must not change—furthermore, it must return to its original state between each pump−probe experiment. However, catalysts are often dynamic. Catalyst composition can change dramatically under reactive conditions[10]—living catalyst[11−13]—and catalytic use can lead to poisoning.[14] Hence, we need methods that can rapidly obtain kinetic information, providing real-time rates on a measurement time scale that is faster than the speed with which the catalyst is changing.

In this work, we demonstrate velocity-resolved kinetics with high-repetition-rate detection. The reaction starts when a pulse of molecules arrives at the surface, and ion images are recorded for each pulse of a high-repetition-rate laser that ionizes desorbing products. The ion images preserve the velocity information from which the rate of reaction is derived. The inverse repetition rate of the laser sets the temporal resolution. We demonstrate a duty cycle that is 1−3 orders of magnitude higher than previous methods,[5] allowing measurements on a changing catalyst. The present experiments use a 1 kHz Ti:sapphire laser—future experiments with Yb-fiber lasers operating at 10^{2-3} kHz provide a perspective for improvement.

Received: August 29, 2020
Revised: November 6, 2020
Published: November 17, 2020

ACS Catalysis pubs.acs.org/acscatalysis Research Article

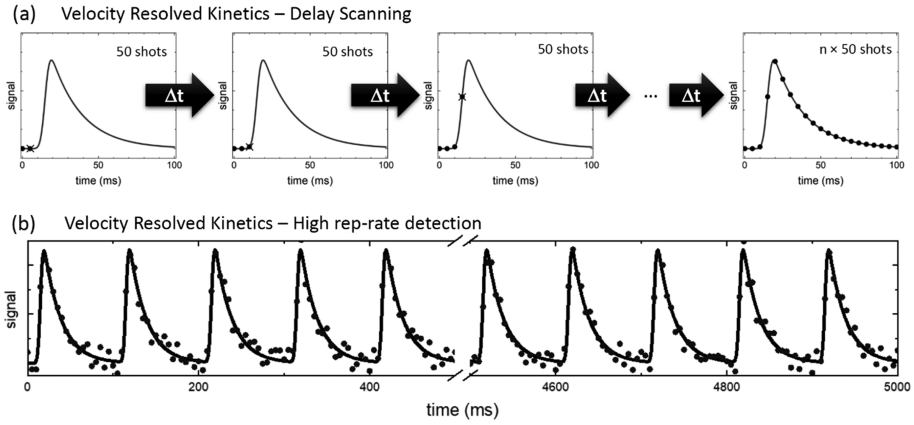

Figure 1. Comparison of delay scanning versus high-rep-rate detection employed in velocity-resolved kinetics measurements. (a) Delay scanning involves the acquisition of many (e.g., 50) images at each time delay between the initiating molecular beam pulse and the laser ionization pulse. Points in the kinetic trace recorded by scanning the delay between a molecular beam pulse that initiates the reaction and a laser ionization pulse that detects the products. The catalytic system must be stable throughout the course of the delay scanning procedure. (b) High-rep-rate detection with high-speed imaging records many points in the kinetic trace for each molecular beam pulse. Here, the molecular beam initiates the reaction every 0.1 s and points in the kinetic trace are recorded by each pulse of a 1 kHz detection laser. The duty cycle of this method can be much higher than delay scanning. Furthermore, the kinetics can be recorded while the catalyst is changing.

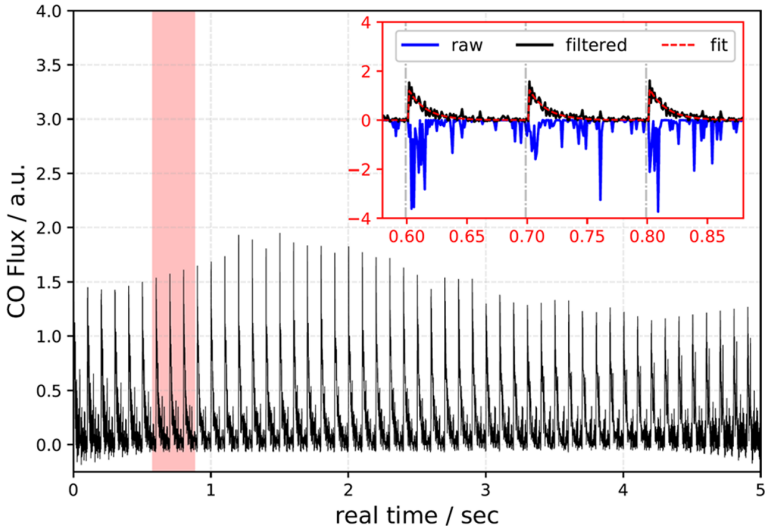

Figure 2. CO trapping/desorption from Pd(332) as a proof of principle for high-rep-rate detection. The CO pulsed beam runs at 10 Hz, while the detection laser runs at 1 kHz. The Pd crystal was held at 593 K. Inset: Raw data (blue line) is treated by the Savitzky−Golay filter (see text) to yield the filtered data (black line). The gray dash-dotted line indicates the time at which the CO pulse initiates the reaction. The dashed red line is a periodic first-order decay convoluted with the temporal profile of the CO beam and is used to extract the desorption rate constant.

2. EXPERIMENT

We previously described the apparatus in detail elsewhere.[6−8] Briefly, we produce two molecular beams in two vacuum chambers, each equipped with piezo-electrically actuated pulsed valves. The valves' repetition rates are variable up to 500 Hz. The pulse durations can be as low as 30 μs. Each beam passes through two differential pumping chambers, before entering an ultrahigh vacuum (UHV) chamber with a base pressure of 2×10^{-10} mbar, where they intersect with one another and collide with a Pd(332) surface. One beam collides at normal incidence dosing the sample with oxygen. The second beam, incident at 30° to the normal, initiates the reaction with a pulse of CO. The CO beam can either be used alone to study CO trapping/desorption or with an oxidized surface to initiate CO_2 formation. A single crystal of Pd cut and polished to expose the (332) surface is mounted on a 5-axis manipulator and can be heated to 1150 K using electron bombardment. The instrument is equipped with an Ar^+ sputtering source for cleaning the surface as well as an Auger electron spectrometer to check its cleanliness.

A homogeneous electric field oriented parallel to the surface is formed by two parallel flat meshes (repeller and extractor), between which both molecular beams pass. After ionization of the reaction products by a nonresonant multiphoton process, using an ultrashort Ti:sapphire laser (Coherent Astrella, 800 nm, 35 fs, 0.5 mJ, 1 kHz) focused with a 150 mm plano-convex lens, a 3 kV pulse applied to the repeller of the ion imaging system directs the ions to the imaging detector. This maps the products' density and in-plane velocity vectors, which is used

https://dx.doi.org/10.1021/acscatal.0c03773
ACS Catal. 2020, 10, 14056−14066

to create a flux image. A region of the flux image is then integrated to provide the rate of reaction at a specific time. We record ion images with a 56 mm Chevron MCP detector coupled to a P43 phosphor screen, whose phosphorescence detected by a high-frame-rate CMOS camera (Vision Research Phantom VEO 710). We took advantage of commercial data acquisition software (DaVis LaVision GmbH) and a software-controlled timing unit (PTUX, LaVision GmbH). The timing unit is triggered both at 10 Hz—synchronized with the pulsed nozzle—and at 1 kHz—synchronized with the laser. Several thousand images are recorded over several seconds and stored on the camera's internal memory, only to be transferred later to a computer's hard disk.

Figure 1 shows a comparison to methods requiring the delay between pulsed molecular beam and laser, t_{BL}, to be scanned. In that case (Figure 1a), an ion image is measured for a fixed value t_{BL} and an ion image is accumulated over many (typically 50) molecular beam pulses. t_{BL} is then incremented and the process is repeated. Here, one ion image is recorded for every molecular beam pulse, whose repetition rate is typically 10–100 Hz. Using high-repetition-rate detection, the ion image is recorded every millisecond. Each pulse of the laser (points in Figure 1b) corresponds to a point in the temporal evolution of the reaction. The P43 phosphor screen decays over $\tau_{90\rightarrow10\%}$ = 1.3 ms, while the time between laser pulses is only 1 ms. Hence, after downloading the image sequence to the computer, we subtracted from each image the "afterglow background" remaining from the previous image.

3. RESULTS AND DISCUSSION

3.1. Proof of Principle: Application to CO Desorption from Pd(332). As a proof of principle, we performed measurements on CO trapping/desorption from Pd(332) between 583 and 623 K. Here, a clean Pd(332) crystal is exposed to a pulsed molecular beam of pure CO operating at 10 Hz. The surface temperature is controlled so that a 1 kHz detection rate is sufficiently rapid to follow the desorption kinetics, while also ensuring that all CO molecules desorb between molecular beam pulses. Following refs 6, 7, we extract the kinetic trace by integrating flux images between 300 and 900 m/s and ±4° from the surface normal. This captures most of the desorbing molecules, while suppressing signal from directly scattered (higher velocity) and background (lower velocity) CO.

Figure 2 shows data from a typical 5 s experiment, requiring 1% the measurement time needed for delay scanning. Fifty kinetic traces result, one from each of 50 CO molecular beam pulses. The inset shows three kinetic traces in detail. We filter the raw data (blue) with a periodic Savitzky–Golay filter[15] applied by first sorting the data according to t_{BL} (the delay between CO beam pulse and ionizing laser pulse) and then employing a moving linear fit to a single data point and 10 of its neighboring data points—all with the same t_{BL}. The value of the fitted line then replaces the data point, and the process is repeated on the next data point. This leads to the filtered output (black). The CO desorption rate constant, k_d, is determined by fitting each pulsed decay with a function that convolves the incident CO beam's temporal profile with an exponential decay—red dashed line in the inset of Figure 2.[5] In this way, we derive 50 independent values of k_d, from which we obtain an average value and a standard deviation.

Figure 3 shows k_d values for CO on Pd(332) and Pd(111) using several different methods. The rate constants obtained

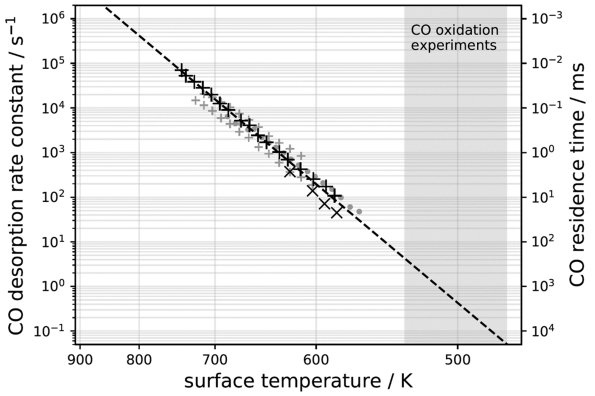

Figure 3. Desorption rate constants of CO from Pd(332) and Pd(111) vs surface temperature. × indicates values obtained from high-rep-rate detection; + indicates results from delay scanning gray plus used delay scanning with Pd(111),[7] and gray circle solid indicates results on Pd(111) from modulated molecular beam spectrometry.[16] The black dashed line is an Arrhenius fit ($A = 10^{15.6 \pm 0.3}$ s^{-1} and E_a = 1.58 ± 0.02 eV) to all desorption rate constants on Pd(332). The gray shaded region indicates the temperature range at which CO oxidation measurements in this work are conducted—see Section 3.3. Uncertainties in the rate constants determined from delay scanning and high-rep-rate detection are smaller than the symbols.

from the data of Figure 2 (×) are in good agreement with other methods. We note that the observed desorption rates depend little on the presence of atomic steps that are found in high concentration on the Pd(332) surface.[7,16] Clearly, steps do not significantly stabilize CO on Pd, a conclusion that is consistent with reported isosteric heats of adsorption.[17] An Arrhenius fit to k_d values using Pd(332) results yields E_a = 1.58 ± 0.02 eV and $A = 10^{15.6\pm0.3}$ s^{-1}.

3.2. Duty Cycle Analysis. We consider now the quantitative duty cycle improvements possible with high-rep-rate detection, within the specific context of desorption rates near zero coverage. We first define a characteristic desorption time, τ, which is the inverse of the desorption rate constant, $\tau = k_d^{-1}$. This imposes an upper limit of the molecular beam's repetition rate (f_{MB}^{max}) and therefore a minimum repeat time, $t_{min} = 1/f_{MB}^{max}$, needed to maintain the low-coverage condition. While there is some ambiguity involved, we set $t_{min} = 5\tau$, the time at which a first-order decay has reached 0.7% of its initial value. Data obtained within t_{min} are most important to the fitting—we label this data "relevant".

The number of relevant data obtained from each molecular beam pulse used in the high-rep-rate approach, n_{HRR}, is given by

$$n_{HRR} = t_{min} \times f_L \quad (1)$$

where f_L is the detection laser repetition rate and data acquisition rate, $\dot{n}_{HRR}$, is given by

$$\dot{n}_{HRR} = t_{min} \times f_L \times f_{MB} \quad (2)$$

where f_{MB} is the repetition rate of the pulsed molecular beam.

The number of relevant data per molecular beam pulse in a conventional delay scanning experiments, n_{DS}, is 1, and the data acquisition rate is then

$$\dot{n}_{DS} = f_{MB} \quad (3)$$

https://dx.doi.org/10.1021/acscatal.0c03773
ACS Catal. 2020, 10, 14056–14066

Taking the ratio of these two data acquisition rates, we find that the theoretical improvement in duty cycle is given by

$$\frac{\dot{n}_{\mathrm{HRR}}^{\max}}{\dot{n}_{\mathrm{DS}}^{\max}} = t_{\min} \times f_{\mathrm{L}} = f_{\mathrm{L}} / f_{\mathrm{MB}}^{\max} \tag{4}$$

The data acquisition rate using the delay scanning approach is limited by $t_{\min}^{-1}$ and, of course, technical limitations to the rep-rate of pulse beams (in our experience, ~500 Hz), whereas f_{L} is the only limiting factor to the data acquisition rate for the high-rep-rate method. We emphasize that f_{L} can be improved dramatically. This work used a Ti:sapphire laser, f_{L} = 1 kHz; newly available Yb-fiber lasers achieve repetition rates of 10^2–10^3kHz, while still providing pulse energies and peak intensities sufficient for nonresonant multiphoton ionization.

The analysis so far neglects the number of ions produced in each experiment, which is equally important as the rate of data acquisition. All velocity-resolved kinetics signals are proportional to the rate of product formation.[6] Hence, in the desorption experiments presented above, the number of ions detected per laser pulse is proportional to $1/\tau$. The dependence on τ reflects the temporal dilution seen for slow reactions. Each molecular beam pulse deposits the same number of CO molecules on the surface; so, the observed density is diluted greatly over time for slow reactions and less so for fast reactions. Taking this into account, we may define the "count acquisition rate" (CAR).

$$\mathrm{CAR} \equiv \frac{\dot{n}}{\tau} = \dot{n} \times k_{\mathrm{d}} \tag{5}$$

$$\mathrm{CAR}_{\mathrm{DS}} \equiv \frac{f_{\mathrm{MB}}}{\tau} \tag{6}$$

$$\mathrm{CAR}_{\mathrm{HRR}} \equiv \frac{5\tau \times f_{\mathrm{L}} \times f_{\mathrm{MB}}}{\tau} = 5 \times f_{\mathrm{MB}} \times f_{\mathrm{L}} \tag{7}$$

This quantity determines the signal-to-noise ratio (S/N) of the data obtained in any experiment. These equations point out that experiments using delay scans exhibit a stronger decrease of S/N than high-rep-rate measurements, as τ increases. This, of course, mirrors the implications of eq 4. This also means that comparing different data acquisition methods should be done as a function of τ.

Figure 4 shows calculated values of CAR vs τ for a few different experimental configurations. Here, we only consider τ values larger than the shortest molecular beam pulse, which defines the kinetic resolution (black vertical line). To ensure that the CAR results only from relevant data, the molecular beam repetition rate should be matched to $t_{\min} = 5\tau = 1/f_{\mathrm{MB}}$. This is true for either delay scanning or high-rep-rate detection. This gives rise to CAR plots for optimized delay scanning (blue dashed line) and optimized 1 kHz detection (blue solid line) in Figure 4. The red solid line shows CAR when using optimized 100 kHz detection. We also show in Figure 4 the CAR vs. τ for unoptimized experiments. Specifically, we show the CAR plot for a delay scan experiment with a fixed 20 Hz molecular beam (green dashed line) as well as a 1 kHz detection experiment with a 10 Hz rep-rate molecular beam (magenta solid line).

The range of rates that can be measured with a high S/N is much larger for high-rep-rate detection than for delay scanning. Note that for the optimized experiments, CAR is decreasing with τ; thus, long lifetimes are harder to measure with high S/N than are short lifetimes. However, for delay scanning, the CAR is proportional to τ^{-2} while for high-rep-rate experiments, it is proportional to τ^{-1}. This is reflected in Figure 4 through the slope of CAR vs τ for delay scan measurements, which is steeper than that of high-rep-rate experiments. Furthermore, increasing f_{L} further increases CAR. This shows that the high-rep-rate method becomes extremely attractive for measuring slow rates. From our experience, the feasibility limit in an optimized delay scanning experiment is reached for $\tau \sim 10$–40 ms. Delay scanning measurements under these conditions take on the order of 1 h. The same limit is reached in a 1 kHz measurement when $\tau \sim 5$ s, which can be extended to 500 s with 100 kHz detection. This shows that the high-rep-rate detection approach can be applied to measure τ^{-1} values over ~7 orders of magnitude, whereas delay scanning is limited to at most 3 orders of magnitude. High-rep-rate detection thus enables measurements over a wider temperature range, providing more accurate Arrhenius parameters and greater sensitivity to non-Arrhenius behavior.

We also compare experimentally observed CARs obtained from our actual CO desorption experiments. The vertical gray dash-dotted line of Figure 4 (marked with τ@593 K) represents the temperature at which the CO desorption experiments presented in Figure 2 were carried out. Here, delay scanning required 20 min to obtain ~250 relevant data,

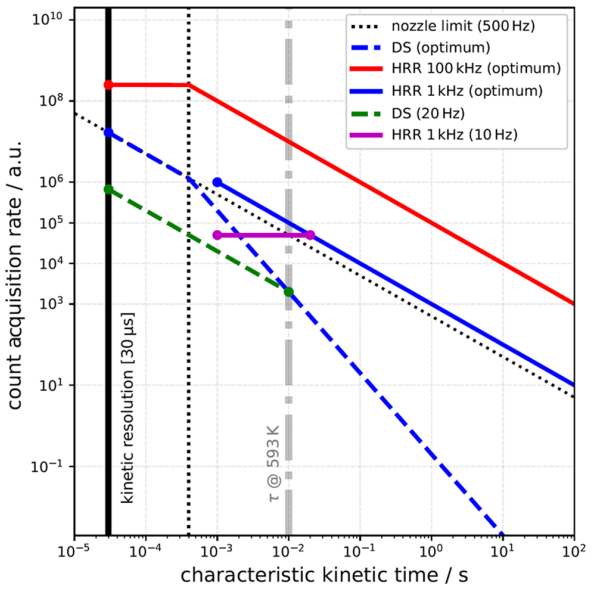

Figure 4. Theoretical count acquisition rates (CAR) vs characteristic kinetic time, τ, for a variety of experimental configurations. Optimized delay scanning (DS, blue dashed line) and 1 kHz high-rep-rate detection (HRR, blue solid line) as well as an optimized high-rep-rate detection with 100 kHz detection (red solid line) experiment are shown—here, only relevant data (see text) is obtained. Experimental configurations presented in this paper are also shown for delay scanning (green dashed line, CO nozzle at 20 Hz) and 1 kHz detection with CO beam operating at 10 Hz (magenta solid line). The gray dash-dotted line indicates the value of τ relevant to our experiments on CO trapping/desorption, where we measured the improvement to the CAR. The temporal resolution for a transient kinetics experiment is limited by the duration of the molecular beam pulse (black solid line). The minimum time between molecular beam pulses is limited by pumping speed and maximum pulsed valve frequency of 500 Hz (black dotted line).

https://dx.doi.org/10.1021/acscatal.0c03773
ACS Catal. 2020, 10, 14056−14066

while 1 kHz detection provided ~70 relevant data in 10 s. The derived rate constants were of similar accuracy for both methods. Normalizing to the number of relevant data points obtained, we find that CAR increased by a factor of ~30 for 1 kHz detection compared to delay scanning. Seen at the τ-value at 593 K, the theoretical CAR plots (magenta line) and (green dashed line) show a theoretical enhancement factor that is close to the observed enhancement.

3.3. Real-Time Titration Experiment for CO Oxidation at Pd(332). The velocity-resolved kinetics experiment carried out with delay scanning provides time-resolved information by recording a signal arising from two pulses with a variable delay. Such experiments require that the system under study does not change between each pulse pair; however, this requirement is often not fulfilled in surface chemistry. For example, catalysts can become poisoned with use by buildup of carbon[14] or other trace impurities. Furthermore, the composition of the surface can change under reactive conditions.[10] This also has an important implication for molecular beam experiments. For example, if we begin with the Pd(332) crystal used above for CO desorption, clean it, and start dosing with the CO and O_2 pulses, the concentration of adsorbed oxygen, [O*], will change with time in a way that is determined by the competitive kinetics of O_2 dissociation and adsorption, CO adsorption, reaction, and desorption. Thus, [O*] is a complex function of the two beam fluxes and the rates of each elementary process.

This has been shown in detail for CO oxidation on Pt(111) using delay scanning,[6] where a steady-state oxygen concentration, $[O^*]_{SS}$, is established over a period of few seconds. Velocity-resolved kinetics exploit such steady-state conditions to investigate the reaction rate's dependence on oxygen coverage. Specifically, CO and O_2 pulsed beams run asynchronously at a controlled repetition rate ratio (RRR) to fix $[O^*]_{SS}$. Each new value of RRR gives a new value of $[O^*]_{SS}$ that is determined by a titration. The titration involves first saturating the Pt(111) surface with oxygen by running the O_2 beam for several minutes. This is known to produce an O* coverage of $[O^*]_{sat}$ = 0.25 Monolayer (ML). We then turn off the O_2 beam and run many CO molecular beam pulses while monitoring the CO_2 formation rate at a specific time within the kinetic trace, t_{BL}, the beam laser delay time. The CO_2 formation rate at the chosen t_{BL} changes as more CO pulses react at the surface, eventually going to zero when all of the O* is removed from the surface. However, from the titration measurement at a single t_{BL} it is not possible to determine the oxygen coverage. This is because the transient rate of CO_2 formation becomes slower as O* is removed from the surface. By choosing only one specific t_{BL} we miss the change of the kinetic trace as a function of titration time. To account for the change of the kinetic trace during the titration, measurements are repeated for various t_{BL}, and the titration curves are integrated over t_{BL}. The integral of such titration curves is proportional to the total oxygen coverage on the surface. We compare the integral from oxygen saturated surfaces with those obtained from a steady-state oxygen covered surface to determine the fraction of the total oxygen coverage that remains under steady-state conditions. Clearly, this procedure is not optimal; ideally, one would like to know the kinetic trace at each point in the titration. While this is tremendously tedious and time-consuming to perform with delay scanning, it is easily achieved with high-rep-rate detection.

Figure 5 shows such a measurement carried out on Pd(332) at T_S = 503 K. Here, we first saturated the surface with oxygen

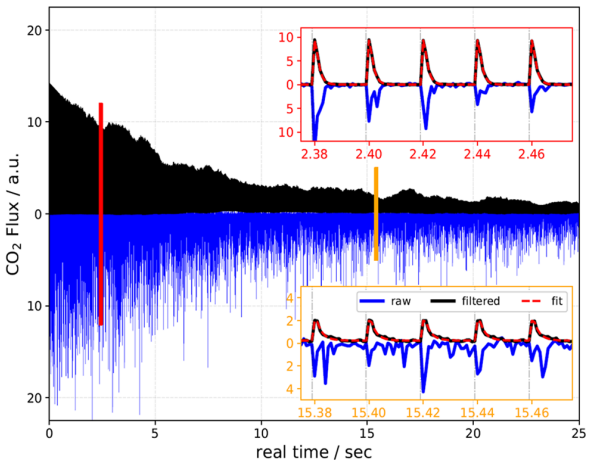

Figure 5. High-rep-rate detection of velocity-resolved kinetics for a nonstationary catalyst. The kinetics of CO oxidation on Pd(332) are recorded starting with saturated oxygen coverage. Adsorbed oxygen is removed during the experiment, and the kinetics change accordingly. The surface temperature was 503 K, and the CO beam operated at 50 Hz. The CO beam cleans up a preoxidized surface that had been exposed to 300 ± 80 ML of O_2. The raw data are shown as blue lines, the Savitzky−Golay filtered data are shown as black lines. Kinetic fits (first-order decay convoluted with incident beam shape) are shown as red dashed lines in the insets. The insets are indicated by colored bars and borders. The gray dash-dotted line in the insets indicates the reaction time at which the reaction is initiated by the pulsed CO beam.

by dosing with a 500 Hz O_2 molecular beam pulse for 5 min (total exposure, 300 ± 80 ML). The flux of the O_2 molecular beam operating at 500 Hz is $1.0 \pm 0.3 \frac{ML}{s}$ with $\approx 2 \times 10^{-3} \frac{ML}{pulse}$ The high-rep-rate raw data (blue lines) results from a CO pulsed beam operating at 50 Hz. The CO molecular beam operating at 50 Hz provides a flux of $(6 \pm 2) \times 10^{-2}$ ML/s with $\approx 1 \times 10^{-3} \frac{ML}{pulse}$ With each CO titrant pulse, a certain amount of oxygen is removed from the surface so that each kinetic trace probes a different O-atom surface coverage. Using a 51-point periodic Savitzky−Golay filter, as described above, we filtered the raw data (blue lines of Figure 5) to yield the filtered data (black lines of Figure 5). The insets in Figure 5 show representative kinetic traces at early and late times in the titration. We find that the signal amplitude decreases and the rate slows with increasing titration time, reflecting the consumption of oxygen with each subsequent CO pulse. The filtered data can be represented by a first-order decay for the entire 30 s titration time and for temperatures between 473 and 533 K.

3.4. Reaction Rate Analysis at High Oxygen Coverages. This approach provides new information about the nature of the kinetics and improves the performance of the velocity-resolved kinetics methods. One advantage is the ability to obtain rates of reactions at saturated oxygen coverage, where the absolute oxygen coverage is unambiguously defined. To demonstrate this, we apply a simple model previously suggested by Engel and Ertl to describe CO oxidation kinetics on Pd.[18] The model incorporates four processes

https://dx.doi.org/10.1021/acscatal.0c03773
ACS Catal. 2020, 10, 14056−14066

$$F_t(O_{2,g}) \xrightarrow{S_{O_2}} 2\ O^* \quad (8)$$

$$F_t(CO_g) \xrightarrow{S_{CO}} CO^* \quad (9)$$

$$CO^* \xrightarrow{k_d} CO_g + * \quad (10)$$

$$CO^* + O^* \xrightarrow{k_r} CO_{2,g} + 2^* \quad (11)$$

where X* indicates an adsorbed species X to the surface, * indicates a free adsorption site, and F_t is the time-dependent flux provided by the molecular beams to the surface. S_X is the sticking coefficient of the species X. Under conditions of excess oxygen, the effective first-order rate constant, k_{eff}, is given by

$$k_{eff} = k_r[O^*] + k_d \quad (12)$$

and the CO_2 formation rate is given by

$$\frac{d[CO_{2,g}]}{dt} = k_r[O^*][CO^*] \quad (13)$$

We take advantage of the fact that the velocity-resolved kinetics signal is directly proportional to the rate of $CO_{2,g}$ formation and that during the first few CO pulses arriving at the surface, we probe a well-defined oxygen coverage $[O^*]_{sat}$ = 0.292 ML.[6] We present examples of such kinetic traces in Figure 6, averaged over the first 20 CO pulses for three values of T_S. We fit each trace to obtain a first-order time constant ($\tau_{eff} = k_{eff}^{-1}$). Since k_d is known—in fact, under these conditions, desorption is not competitive and $k_{eff} = k_r[O^*]_{sat}$; see the blue shaded area of Figure 3—and coverage $[O^*] \equiv [O^*]_{sat}$, we can easily determine k_r at all three values of T_S. The derived effective reaction rate constants ($k_r[O^*]_{sat}$) are shown in Figure 7 as an Arrhenius plot. Note that in Figure 6 for T_S = 533 K, the temporal resolution is insufficient to provide a reliable fit. This problem could be solved by repetitive measurements of this type at a variety of delays of the CO molecular beam pulse—interleaved in 0.1 ms steps. One could also use a higher repetition rate laser. Alternatively, k_r can be obtained simply from the amplitude of the kinetic trace, shown as arrows in Figure 6, which is proportional to the initial rate of product formation. This allows the rate constants at all three temperatures to be placed on the same scale using the Arrhenius law. In Figure 7, the values derived from initial rates (×) are placed on an absolute scale in comparison to the rate constants obtained by exponential fitting at the lower two temperatures (o). The best-fit Arrhenius parameters for the reaction rate constant k_r are E_a = 0.76 ± 0.02 eV and $A = 10^{11.0 \pm 0.4}$ s^{-1} ML^{-1}. These results are consistent with independently obtained results using delay scanning.

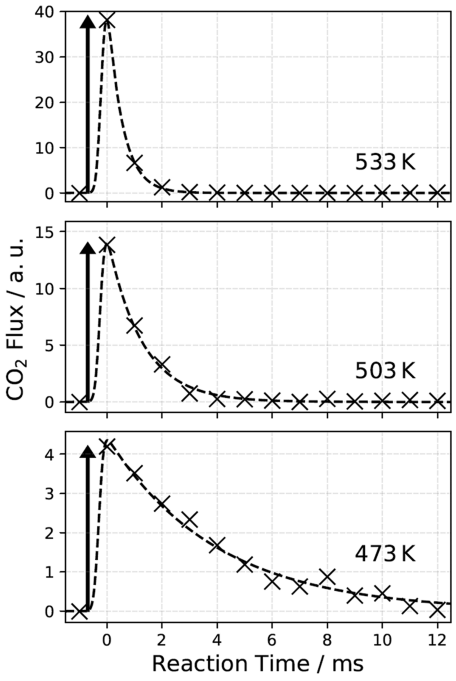

Figure 6. CO oxidation kinetics at saturated oxygen coverage. Kinetic traces (crosses) obtained by averaging over the first 20 pulses in experiments like those of Figure 5. The dashed lines are fits to a first-order decay (convoluted over the incident beam). The arrows indicate the relative initial rates in the three experiments.

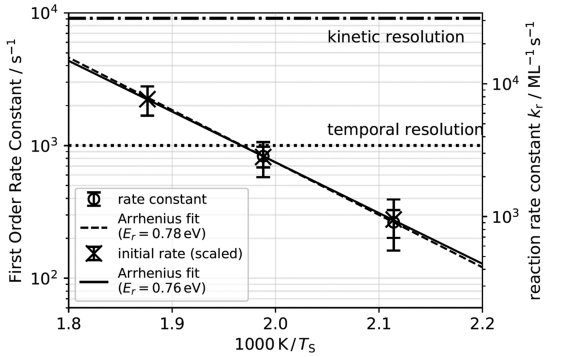

Figure 7. Temperature dependence of CO oxidation rate constants at saturated oxygen coverage. The first-order rate constants for CO_2 formation determined from the data of Figure 6. The circles are the rate constants determined from the shape of the single-pulse kinetic trace, and the crosses are initial rates determined from their amplitude. The initial rates are scaled to match the first-order rate constants at low temperatures. The dotted line is the limit above which the rate constants cannot be derived from the shape of the kinetic trace. The dash-dotted line is the kinetic resolution (in this experiment, around 110 μs) above which no kinetic information can be derived from transient kinetics. The full and dashed curves are Arrhenius fits to the initial rate and the first-order rate constant, respectively.

3.5. Diffusion-Limited Surface Reaction Rates. In the course of studying the behavior of high-rep-rate detection, we made what were, at first, surprising observations. We found that near the end of titrations when the rate of CO_2 formation had nearly vanished, oxygen coverage remained on the surface in regions outside the crossing region of the two molecular beams. By translating the crystal in a direction perpendicular to the surface normal, we could observe a sudden increase of the CO_2 production rate. These observations indicated that a successful modeling of these experiments would require characterizing both the spatial and temporal evolution of the reactant coverages.

In this section, we describe such modeling showing that titration experiments often produce conditions where CO diffusion affects the rates of reactions.

https://dx.doi.org/10.1021/acscatal.0c03773
ACS Catal. 2020, 10, 14056−14066

We first imagine dividing the reacting surface into j spatial elements. The concentrations of CO* and O* in spatial element j, defined as $[O^*]_j$ and $[CO^*]_j$, are given by reactive terms

$$\left(\frac{d[CO^*]}{dt}\right)_j^{rct} = S_{CO,j}F_{t,j}(CO_g) - k_d[CO^*]_j - k_r[O^*]_j [CO^*]_j \quad (14)$$

$$\left(\frac{d[O^*]}{dt}\right)_j^{rct} = 2\,S_{O_2,j}F_{t,j}(O_{2,g}) - k_r[O^*]_j[CO^*]_j \quad (15)$$

and diffusive terms

$$\left(\frac{d[CO^*]}{dt}\right)_j^{dif} = D_{CO,j}\Delta[CO^*]_j \quad (16)$$

$$\left(\frac{d[O^*]}{dt}\right)_j^{dif} = D_{O,j}\Delta[O^*]_j \quad (17)$$

The total rate is the sum of reactive (eqs 14 and 15) and diffusive (eqs 16 and 17) contributions. In eqs 16 and 17, D_n and $\Delta[n^*]_j$ are the species-specific and concentration-independent diffusion coefficients and Laplacian of the concentration, respectively, used in application of Fick's second law of diffusion, and $F_{t,j}$ is the time-dependent incoming flux to the spatial element j, produced by the molecular beams.

The dosing function $F_{t,j}$ is described with a periodic function (in time) that reassembles the spatial, $g(r_j)$, and temporal, $f(t)$, shapes of our molecular beams. Specifically, we modeled it with

$$f(t) = \cos^{2n}(\pi RR\,(t - t_0)) \quad (18)$$

where RR is the repetition rate of the nozzle, t_0 is the reference timing, and n is an integer chosen to best represent the temporal shape of the beam. Using ion imaging, we experimentally determined the spatial intensity profile of each molecular beam, from which we deduced their radial profiles. Both molecular beams have a nominal projected diameter of 2 mm. For $F_{t,j}$, we use a flattop Gaussian that resembles the experimentally determined radial profile, $g(r_j)$, of the beam, which is given by

$$g(r_j) = \exp\left(-\left[\frac{r_j^2}{2\sigma^2}\right]^m\right) \quad (19)$$

where m and σ are the parameters representing the shape of the experimental beam profile. The combined and normalized dosing function is then given by

$$F_{t,j} = \frac{g(r_j)f(t)}{N} \quad (20)$$

where N is the normalization to define the observed molecular beam flux.

We made sure that both molecular beams overlap on the surface and checked this by ensuring that oxygen coverage remained symmetrically distributed around the molecular beams crossing point at the end of the titration measurement. Hence, we conclude that our experiments approximately preserve radial symmetry, which allows us to solve the diffusion equations, eqs 16 and 17, in polar coordinates. The diffusion formalism is derived in the Supporting Information (SI). The rate equations including diffusion and reaction are solved numerically using LSODA from the Fortran ODEPACK library.[19] The concentrations of CO* and O* in each spatial element j are propagated in time.

To simulate measurements like those of Figure 5, we initiate the model calculations with adsorbed oxygen produced by many pulses of the O_2 beam. This requires an initial O* spatial profile (black line in Figure 8) that is much broader than the nominal O_2 beam profile (thick gray line in Figure 8), as O* coverage quickly saturates near the center of the beam, and after that, only the wings of the O_2 beam add additional O*. We simulated the spatial evolution of concentrations within a radial extent of 3 mm and with each spatial element, j, being 5 μm in size. The corresponding total CO_2 formation rate is given by summing the rate of each spatial element j and weighting it by the respective area A_j, in the following manner

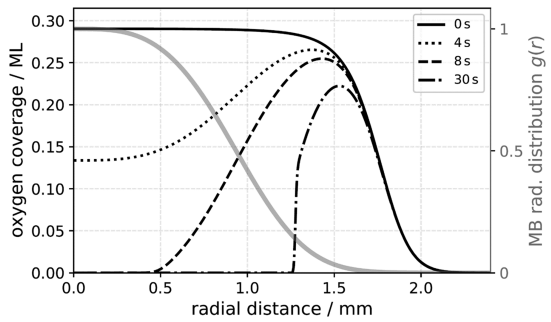

Figure 8. Spatial distributions of adsorbed oxygen atoms during a CO oxidation titration. The distributions are assumed cylindrically symmetrical about the CO beam axis. The radial distance from the CO beam center line is shown on the x-axis. The solid black line indicates the initial oxygen coverage distribution produced by long exposure with a molecular beam of O_2. The radial distribution of the CO beam (gray thick line) peaks near 0 and preferentially removes O atoms there. As time progresses, a "doughnut hole" reaction develops, where the CO is concentrated along the CO beam center line and adsorbed oxygen atoms form a ring around the CO beam. In later stages of titration, the reaction forms a front where the CO and O concentrations overlap. Diffusion of CO from the center of the doughnut hole to the oxygen ring also influences the reaction rate.

$$\frac{d[CO_2]_t}{dt} = k_r \sum_{j=0}^{j_{max}} [O^*]_{t,j}[CO^*]_{t,j}A_j \quad (21)$$

where the area of the jth spatial element is given by

$$A_j = \pi(2j + 1)l_0^2 \quad (22)$$

The simulation accounts for the influence of reactions 8−11 as well as CO diffusion. The reaction rate constants were determined previously (see Sections 3.1 and 3.3). Oxygen desorption is unimportant at these surface temperatures.[20,21] Oxygen diffusion is found to be unimportant under our conditions.[22] We estimated the diffusion coefficient for CO using an activation energy of 0.12 eV from ref 23, and the fitted prefactor for CO diffusion needed to obtain agreement with our measurements. The optimized prefactor was $10^{-3.7\pm0.3}$ cm^2 s^{-1}. The CO diffusion rates we obtain in this way are

https://dx.doi.org/10.1021/acscatal.0c03773
ACS Catal. 2020, 10, 14056−14066

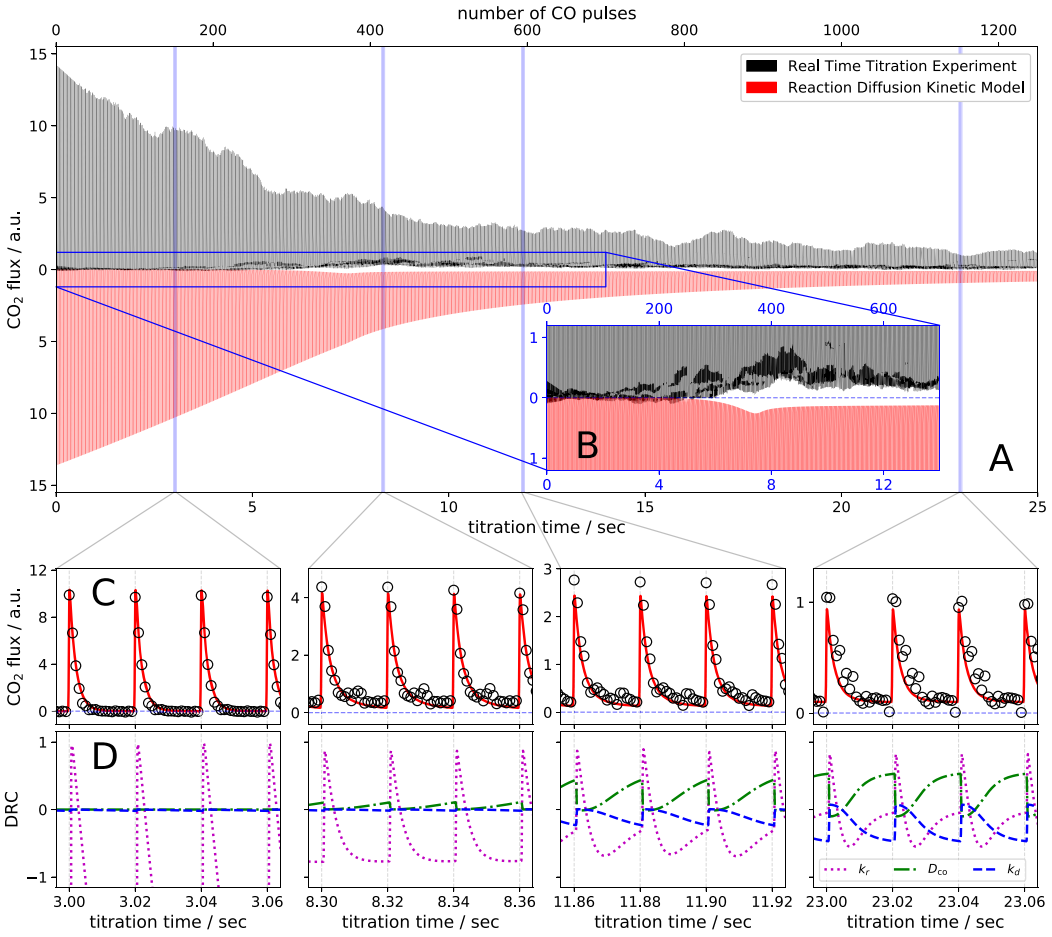

Figure 9. Comparison of the model of real-time titration (red solid lines) with measurements (black solid lines and open circles). The onset of the diffusion-controlled regime is indicated in (B), where a continuous CO_2 production rate forms. (C) Results at 3.0, 8.3, 11.9, and 23.0 s after the start of the titration. The degree of rate control (DRC) is shown in (D) for three elementary processes: CO oxidation reaction (magenta dotted line), CO desorption (blue dashed line), and CO diffusion (green dash-dotted line). The DRC for O diffusion is for all conditions at least 2 orders of magnitude smaller and is therefore not shown. See text. Experimental conditions are as stated in Figure 5.

consistent with previous measurements on Pd(111)—see the SI.

We derived the absolute incident beam fluxes from measurements of the steady-state pressures of CO and O_2 in the UHV chamber combined with a knowledge of the chamber pumping speed. The model results were insensitive to the O_2 flux, but highly sensitive to the assumed CO flux. We found best agreement with experiment when using a CO flux ~30% smaller than that derived from our experimental estimate.

We used a second-order Langmuir expression for the coverage-dependent sticking coefficient of O_2,

$$S_{O_2}([O^*]) = S_{O_2,0}\left(1 - \frac{[O^*]}{[O^*]_{max}}\right)^2 \quad (23)$$

with $S_{O_2,0} = 0.4$.[16] Best agreement with the experiment is achieved when an oxygen coverage-independent sticking coefficient of 0.6 ± 0.1 is used for CO. We assume that the sticking probability of CO decreases linearly with CO coverage.

Figure 9A shows a comparison of this model to the titration experiment of Figure 5. Note that the amplitude quickly decays over the first 300−400 CO beam pulses, thereafter decaying more slowly, a behavior that is captured in the kinetic model. The transition between the fast and slow decay regions is accompanied by an increase of the baseline (shown in magnification in Figure 9B). This indicates a continuous production of CO_2. The experimentally observed increase of the baseline is also present in the model. Looking in more detail (Figure 9C), we find that the single-pulse transient rate is decreasing with increasing titration time; furthermore, the transient rates are well reproduced by the kinetic model as is the continuous production of CO_2 seen in the later stages of the titration.

The qualitative behavior can be understood by recalling that the amplitude of the titration curve reflects the initial rate of CO_2 production, which is directly proportional to the oxygen coverage. With increasing titration time, the initial rate decreases, indicating that the oxygen coverage is dropping. As a consequence of the reduced reaction rate at a lower oxygen coverage, the lifetime of CO molecules on the surface increases, while the rate of CO adsorption remains constant. Since CO's desorption rate is slow at these temperatures, CO begins to build up from one molecular beam pulse to the next;

https://dx.doi.org/10.1021/acscatal.0c03773
ACS Catal. 2020, 10, 14056−14066

this leads to quasi-continuous CO_2 formation and to baseline increase at later times in the titration.

We also performed a sensitivity analysis of the fit to the titration kinetics. The degree of rate control[24] exhibited by the kinetic parameter, k_i, is given by a sensitivity coefficient, $X_{i,t}$

$$X_{i,t} = \frac{k_i}{R_t}\left(\frac{dR_t}{dk_i}\right)_{k_{j\neq i}} \quad (24)$$

where R_t is the CO_2 formation rate. A high absolute value of $X_{i,t}$ indicates the importance of the process to the reaction rate. A positive (negative) value of $X_{i,t}$ means that an increase of the rate parameter produces an increase (decrease) of the CO_2 formation rate. In Figure 9D, we plot $X_{i,t}$ for reaction (purple, dotted), CO desorption (blue, dashed), and CO diffusion (green, dash-dotted).

The reaction between CO* and O* dominates the rate of product formation up to a titration time of about 7 s; thereafter, CO desorption and diffusion become increasingly important. Between 12 and 24 s, where the three processes are of similar importance, their influence appears at different points in the kinetic trace. Consider the kinetic traces found at ~23 s. Here, the beginning of the kinetic trace is dominated by the influence of the reaction, whereas diffusion and desorption influence later times in the trace. Note that desorption decreases while diffusion increases the rate of CO_2 production. This can be understood by realizing that at later stages of the titration, O* has been depleted near the center of the CO beam. Each new CO pulse produces a higher CO* concentration in the doughnut hole of O* concentration (see Figure 8). These are the conditions where the quasi-continuous CO_2 formation rate (i.e., the CO_2 being produced prior to the next pulse) can appear as it is due to a diffusion-controlled reaction between CO* and O*.

Figure 8 shows the model's predictions of the oxygen's spatial distribution at various times during the titration. As explained above, the initial oxygen coverage distribution (black solid line) on the surface is broader than the CO or O_2 beam's spatial profiles (gray solid line) used to dose the surface. At the early stages of titration (4 s—dotted black line), CO flux is highest near the beam center line where O* removal proceeds most rapidly. At 8 s (dashed black line), oxygen is removed near the center of the CO beam. In the central region of the spatial distribution, where O* has now been depleted, CO's lifetime increases and begins building up from pulse to pulse. Hence, a spatially inhomogeneous "doughnut" reaction is produced with high CO coverage near the center of the beam and high O-coverage near the wings of the beam (see the SI). The quasi-continuous CO_2 formation is produced at the intersection of the CO*- and O*-rich regions, forming a reaction front. The product formation rate at the reaction front depends not only on the reaction rate constant but also on the CO diffusion coefficient. While the stationary CO_2 formation is from a diffusion-controlled reaction, the transient rate induced by a CO pulse at late titration times is due to direct population of oxygen-rich regions from the outer flanks of the CO beam and is only slightly influenced by the mobility of the reactants.

With our validated kinetic model, we can also estimate the associated reaction front speed (see the SI), which is a characteristic property that can be measured for spatiotemporal pattern formation. In Figure 10, the reaction front speed at 503 K is shown as a function of titration time. Prior to 6 s after the beginning of the titration, no reaction front is formed.

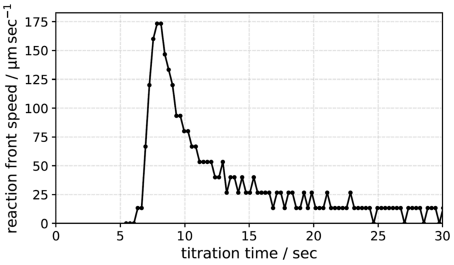

Figure 10. Model's prediction of the reaction front speed as a function of titration time at a surface temperature of 503 K.

However, from 6 to 8 s titration time, a reaction front forms and its speed accelerated to 175 μm/s. With increasing titration time, the front speed decreases, reaching speeds of around 10 μm/s at titration times longer than 15 s. We emphasize that the derived values of front speed are similar to those obtained in previous work for CO oxidation on Pt(110), which ranged from 1 to 100 μm/s.[25,26] The fact that we derive front speeds nearly a factor of 2 higher than that work probably results from faster thermal diffusion for CO on Pd compared to Pt.[23,27]

It is important to highlight that we have modeled the real-time titration experiment without coverage-dependent rate constants. Since we achieve good correspondence with the experiment, we claim that the rate constants have weak dependence on oxygen coverage in CO oxidation on Pd(332). However, this is in contradiction to the findings that were previously made on Pd(111) by Engel and Ertl.[18] We also find that our reaction rate constant is about 4−8 times higher than those reported from Pd(111). We think that steps lead to a higher reaction rate, consistent with previous observations on Pd[28] and Pt.[6] The reason why we have not taken reaction at steps and terraces explicitly into account is that we have not needed it for good match with the experiment. This is probably due to a rather fast exchange of CO and O atoms between terraces and steps, which leads to an effective reaction rate composed of both reactions at steps and terraces. We plan to investigate the details of the kinetic mechanism of CO oxidation at steps and terraces of Pd further in future.

4. CONCLUSIONS

This work shows how high-repetition-rate lasers and ion imaging detection can be used to obtain the kinetic traces of catalytic processes from a single molecular beam pulse, overcoming the need for delay scans that are typical for pump−probe methods. The new approach provides an increased duty cycle, resulting in rates of acquisition for kinetic data that are 10−1000 times faster than conventional delay scanning methods. The new method can measure rates over 5−7 orders of magnitude, dramatically better than when using delay scanning. The method is particularly attractive for measuring slow processes where temporal dilution would make delay scanning impossible.

This new approach can also be used to study catalytic reaction rates under conditions where the catalyst composition is changing under reactive conditions. We demonstrated this with a real-time titration experiment, where the transient CO_2 production rates were obtained at many points in a CO oxidation titration experiment. Specifically, we showed that the transient rate of CO_2 formation could be measured from each subsequent CO pulse, where each pulse probes a different O-

https://dx.doi.org/10.1021/acscatal.0c03773
ACS Catal. 2020, 10, 14056−14066

atom coverage on the surface. From accurate modeling of the titration experiment, we are able to derive various rate constants relevant to CO oxidation on Pd(332). Of particular novelty, we easily found conditions where the CO oxidation was diffusion-controlled. The constants obtained in this work for CO oxidation reaction, CO desorption, and CO diffusion, respectively, are summarized here

$$\frac{k_r(T)}{\mathrm{ML}^{-1}\,\mathrm{s}^{-1}} = 10^{11.0\pm0.4}\exp\left(-\frac{0.76\pm0.02\ \mathrm{eV}}{k_B T}\right)$$

$$\frac{k_d(T)}{\mathrm{s}^{-1}} = 10^{15.6\pm0.3}\exp\left(-\frac{1.58\pm0.02\ \mathrm{eV}}{k_B T}\right)$$

$$\frac{D_{CO}(T)}{\mathrm{cm}^2\,\mathrm{s}^{-1}} = 10^{-3.7\pm0.3}\exp\left(-\frac{0.12\ \mathrm{eV}}{k_B T}\right)$$

Our results are also consistent with an oxygen-coverage-independent sticking coefficient of CO of 0.6 ± 0.1. The desorption and diffusion rate constants of CO agree well with the parameters determined earlier from Pd(111), indicating that CO has no energetic preference for steps and that they are not influencing its mobility on the surface. The reaction rate constant is found to be approximately a factor 4−8 higher than previous reports for Pd(111), indicating that steps are more reactive for CO oxidation on Pd than terraces.

While in this work we were limited to a detection rep-rate of 1 kHz due to the fact that we used a Ti:sapphire laser, we plan to extend our capabilities to a detection rate of 100 kHz and study reaction rates at changing catalyst conditions in more detail using a Yb-Fiber laser. We think that this method offers the possibility to accurately study catalytic reaction rates and kinetic mechanisms at the intersection between the well-defined conditions that are desirable for surface science and the more dynamic conditions relevant to industrial catalysis.

■ ASSOCIATED CONTENT

Supporting Information

The Supporting Information is available free of charge at https://pubs.acs.org/doi/10.1021/acscatal.0c03773.

Diffusion equations for simulation of titrations, comparison of CO diffusion rates to previous reports, and details on the determination of reaction front speeds (PDF)

■ AUTHOR INFORMATION

Corresponding Authors

Theofanis Kitsopoulos − *Institute for Physical Chemistry, Georg-August University of Goettingen, 37077 Goettingen, Germany; Department of Dynamics at Surfaces, Max Planck Institute for Biophysical Chemistry, 37077 Goettingen, Germany; Department of Chemistry, University of Crete, 70013 Heraklion, Greece; Institute of Electronic Structure and Laser FORTH, 70013 Heraklion, Greece;* orcid.org/0000-0001-6228-1002; Email: theo.kitsopoulos@mpibpc.mpg.de

Alec M. Wodtke − *Institute for Physical Chemistry and International Center for Advanced Studies of Energy Conversion, Georg-August University of Goettingen, 37077 Goettingen, Germany; Department of Dynamics at Surfaces, Max Planck Institute for Biophysical Chemistry, 37077 Goettingen, Germany;* orcid.org/0000-0002-6509-2183; Email: alec.wodtke@mpibpc.mpg.de

Authors

Dmitriy Borodin − *Institute for Physical Chemistry, Georg-August University of Goettingen, 37077 Goettingen, Germany; Department of Dynamics at Surfaces, Max Planck Institute for Biophysical Chemistry, 37077 Goettingen, Germany*

Kai Golibrzuch − *Department of Dynamics at Surfaces, Max Planck Institute for Biophysical Chemistry, 37077 Goettingen, Germany*

Michael Schwarzer − *Institute for Physical Chemistry, Georg-August University of Goettingen, 37077 Goettingen, Germany*

Jan Fingerhut − *Institute for Physical Chemistry, Georg-August University of Goettingen, 37077 Goettingen, Germany*

Georgios Skoulatakis − *Department of Dynamics at Surfaces, Max Planck Institute for Biophysical Chemistry, 37077 Goettingen, Germany*

Dirk Schwarzer − *Department of Dynamics at Surfaces, Max Planck Institute for Biophysical Chemistry, 37077 Goettingen, Germany;* orcid.org/0000-0003-3838-2211

Thomas Seelemann − *LaVision GmbH, 37081 Goettingen, Germany*

Complete contact information is available at: https://pubs.acs.org/10.1021/acscatal.0c03773

Funding

D.B. thanks the BENCh graduate school, funded by the DFG (389479699/ GRK2455). T.K. and A.M.W. acknowledge the European Research Council (ERC) under the European Union's Horizon 2020 research and innovation program under grant agreements 833404 and 742422, respectively.

Notes

The authors declare no competing financial interest.

■ REFERENCES

(1) Schwarz, J. A.; Madix, R. J. Modulated beam relaxation spectrometry. *Surf. Sci.* **1974**, *46*, 317−341.

(2) Gland, J. L.; Kollin, E. B. Carbon monoxide oxidation on the Pt(111) surface: Temperature programmed reaction of coadsorbed atomic oxygen and carbon monoxide. *J. Chem. Phys.* **1983**, *78*, 963−974.

(3) Brown, L. S.; Sibener, S. J. A molecular beam scattering investigation of the oxidation of CO on Rh(111). I. Kinetics and mechanism. *J. Chem. Phys.* **1988**, *89*, 1163−1169.

(4) Zaera, F. Use of molecular beams for kinetic measurements of chemical reactions on solid surfaces. *Surf. Sci. Rep.* **2017**, *72*, 59−104.

(5) Golibrzuch, K.; Shirhatti, P. R.; Geweke, J.; Werdecker, J.; Kandratsenka, A.; Auerbach, D. J.; Wodtke, A. M.; Bartels, C. CO desorption from a catalytic surface: elucidation of the role of steps by velocity-selected residence time measurements. *J. Am. Chem. Soc.* **2015**, *137*, 1465−1475.

(6) Neugebohren, J.; Borodin, D.; Hahn, H. W.; Altschaffel, J.; Kandratsenka, A.; Auerbach, D. J.; Campbell, C. T.; Schwarzer, D.; Harding, D. J.; Wodtke, A. M.; Kitsopoulos, T. N. Velocity-resolved kinetics of site-specific carbon monoxide oxidation on platinum surfaces. *Nature* **2018**, *558*, 280−283.

(7) Harding, D. J.; Neugebohren, J.; Hahn, H.; Auerbach, D. J.; Kitsopoulos, T. N.; Wodtke, A. M. Ion and velocity map imaging for surface dynamics and kinetics. *J. Chem. Phys.* **2017**, *147*, No. 013939.

(8) Harding, D. J.; Neugebohren, J.; Auerbach, D. J.; Kitsopoulos, T. N.; Wodtke, A. M. Using Ion Imaging to Measure Velocity Distributions in Surface Scattering Experiments. *J. Phys. Chem. A* **2015**, *119*, 12255−12262.

(9) Park, G. B.; Kitsopoulos, T. N.; Borodin, D.; Golibrzuch, K.; Neugebohren, J.; Auerbach, D. J.; Campbell, C. T.; Wodtke, A. M. The kinetics of elementary thermal reactions in heterogeneous catalysis. *Nat. Rev. Chem.* **2019**, *3*, 723−732.
(10) Kondratenko, E. V.; Ovsitser, O.; Radnik, J.; Schneider, M.; Kraehnert, R.; Dingerdissen, U. Influence of reaction conditions on catalyst composition and selective/non-selective reaction pathways of the ODP reaction over V2O3, VO2 and V2O5 with O2 and N2O. *Appl. Catal., A* **2007**, *319*, 98−110.
(11) Reuter, K.; Scheffler, M. Composition, structure, and stability ofRuO2(110)as a function of oxygen pressure. *Phys. Rev. B* **2001**, *65*, No. 1038.
(12) Reuter, K.; Scheffler, M. First-principles atomistic thermodynamics for oxidation catalysis: surface phase diagrams and catalytically interesting regions. *Phys. Rev. Lett.* **2003**, *90*, No. 046103.
(13) Reuter, K.; Scheffler, M. Composition and structure of theRuO2(110)surface in anO2and CO environment: Implications for the catalytic formation ofCO2. *Phys. Rev. B* **2003**, *68*, No. 368.
(14) Beebe, T. P.; Goodman, D. W.; Kay, B. D.; Yates, J. T. Kinetics of the activated dissociative adsorption of methane on the low index planes of nickel single crystal surfaces. *J. Chem. Phys.* **1987**, *87*, 2305−2315.
(15) Savitzky, A.; Golay, M. J. E. Smoothing and Differentiation of Data by Simplified Least Squares Procedures. *Anal. Chem.* **1964**, *36*, 1627−1639.
(16) Engel, T. A molecular beam investigation of He, CO, and O2 scattering from Pd(111). *J. Chem. Phys.* **1978**, *69*, No. 373.
(17) Conrad, H.; Ertl, G.; Koch, J.; Latta, E. E. Adsorption of CO on Pd single crystal surfaces. *Surf. Sci.* **1974**, *43*, 462−480.
(18) Engel, T.; Ertl, G. A molecular beam investigation of the catalytic oxidation of CO on Pd(111). *J. Chem. Phys.* **1978**, *69*, 1267−1281.
(19) Petzold, L. Automatic Selection of Methods for Solving Stiff and Nonstiff Systems of Ordinary Differential Equations. *SIAM J. Sci. Stat. Comput.* **1983**, *4*, 136−148.
(20) Banse, B. A.; Koel, B. E. Interaction of oxygen with Pd(111): High effective O2 pressure conditions by using nitrogen dioxide. *Surf. Sci.* **1990**, *232*, 275−285.
(21) Guo, X.; Hoffman, A.; Yates, J. T. Adsorption kinetics and isotopic equilibration of oxygen adsorbed on the Pd(111) surface. *J. Chem. Phys.* **1989**, *90*, 5787−5792.
(22) Rose, M. K.; Borg, A.; Dunphy, J. C.; Mitsui, T.; Ogletree, D. F.; Salmeron, M. Chemisorption of atomic oxygen on Pd(111) studied by STM. *Surf. Sci.* **2004**, *561*, 69−78.
(23) Mitsui, T.; Rose, M. K.; Fomin, E.; Ogletree, D. F.; Salmeron, M. Diffusion and pair interactions of CO molecules on Pd(111). *Phys. Rev. Lett.* **2005**, *94*, No. 036101.
(24) Campbell, C. T. The Degree of Rate Control: A Powerful Tool for Catalysis Research. *ACS Catal.* **2017**, *7*, 2770−2779.
(25) Jakubith, S.; Rotermund, H. H.; Engel, W.; von Oertzen, A.; Ertl, G. Spatiotemporal concentration patterns in a surface reaction: Propagating and standing waves, rotating spirals, and turbulence. *Phys. Rev. Lett.* **1990**, *65*, 3013−3016.
(26) Rotermund, H. H.; Jakubith, S.; von Oertzen, A.; Ertl, G. Solitons in a surface reaction. *Phys. Rev. Lett.* **1991**, *66*, 3083−3086.
(27) Reutt-Robey, J. E.; Doren, D. J.; Chabal, Y. J.; Christman, S. B. CO diffusion on Pt(111) with time-resolved infrared-pulsed molecular beam methods: Critical tests and analysis. *J. Chem. Phys.* **1990**, *93*, 9113−9129.
(28) Blomberg, S.; Zetterberg, J.; Zhou, J.; Merte, L. R.; Gustafson, J.; Shipilin, M.; Trinchero, A.; Miccio, L. A.; Magaña, A.; Ilyn, M.; Schiller, F.; Ortega, J. E.; Bertram, F.; Grönbeck, H.; Lundgren, E. Strain Dependent Light-off Temperature in Catalysis Revealed by Planar Laser-Induced Fluorescence. *ACS Catal.* **2016**, *7*, 110−114.

https://dx.doi.org/10.1021/acscatal.0c03773
ACS Catal. 2020, 10, 14056−14066

Supporting Information

Measuring transient reaction rates from non-stationary catalysts

Dmitriy Borodin[1,2], Kai Golibrzuch[2], Michael Schwarzer[1], Jan Fingerhut[1], Georgios Skoulatakis[2], Dirk Schwarzer[2], Thomas Seelemann[3], Theofanis Kitsopoulos[1,2,4,5]* and Alec M. Wodtke[1,2,6]**

[1]Institute for Physical Chemistry, Georg-August University of Goettingen, Tammannstraße 6, 37077 Goettingen, Germany.

[2]Department of Dynamics at Surfaces, Max Planck Institute for Biophysical Chemistry, Am Fassberg 11, 37077 Goettingen, Germany.

[3]LaVision GmbH, Anna-Vandenhoeck-Ring 19, 37081 Goettingen, Germany.

[4]Department of Chemistry, University of Crete, 70013 Heraklion, Greece

[5]Institute of Electronic Structure and Laser – FORTH, 70013 Heraklion, Greece

[6]International Center for Advanced Studies of Energy Conversion, Georg-August University of Goettingen, Tammannstraße 6, 37077 Goettingen, Germany.

Email: *theo.kitsopoulos@mpibpc.mpg.de, **alec.wodtke@mpibpc.mpg.de

Treatment of Diffusion

We use Fick's second law to account for CO diffusion which becomes important at later times in titration experiments. Assuming circular symmetry, Fick's law describes diffusion through a ring r_j with eq S1, written in polar coordinates.

$$\dot{n}_j = D_n\left(\left.\frac{\partial^2 n}{\partial r^2}\right|_{r=r_j} + \left.\frac{1}{r_j}\frac{\partial n}{\partial r}\right|_{r=r_j}\right) \tag{S1}$$

In our application, the center of circular symmetry is crossing point of the center lines of the two molecular beams on the Pd surface. The coordinate system is sketched in figure S1. The CO beam axis is rotated by only 30° from the symmetry axis introducing a slightly elliptical CO spatial profile; but this is a small effect that we approximate as circular. We simulate the diffusion on the surface in a uniform sized radial grid, with l_0 being the radial width of each grid element and r_j being the radial distance from center of circular symmetry (coordinate system origin) to the spatial element j.

$$r_j = \left(j + \frac{1}{2}\right)l_0 \tag{S2}$$

Here, j is an integer from 0, 1, …, $j_{\max}$.

Using finite differences, eq S1 can be expressed as:

$$\dot{n}_j = D_n\left(\frac{n_{j+1} + n_{j-1} - 2n_j}{l_0^2} + \frac{1}{r_j}\frac{n_{j+1} - n_{j-1}}{l_0}\right). \tag{S3}$$

The result from eq S3 is identical to a formulation that can be found in reference 1, treating diffusion in a single component systems; however, we require a treatment of a two-component system. This is necessary because of site blocking effects that make the diffusion of two components dependent on one another. See figure S2.

Fick's law can be recast using the finite difference method into a circularly symmetric grid-hopping formalism (eq S4, comparable to reference 2):

$$\dot{n}_j = k_{\mathrm{H},j+1}n_{j+1} + k_{\mathrm{H},j-1}n_{j-1} - k_{\mathrm{H},j}n_j - k_{\mathrm{H},j}n_j \tag{S4}$$

where $k_{\mathrm{H},j}$ is the hopping rate constant of n associated with the spatial element j.

We also need to consider that the perimeter of each grid element in polar coordinates increases with increasing radial distance—for example, the rate of hopping from j to $j+1$ will be favored over that from

j to $j-1$ as the diffusion circumference is larger for the former. The resulting grid hopping rate constants are simply related to the diffusion coefficients:

$$k_{\mathrm{H},j+1} = \frac{D_n}{l_0^2}\left(1 + \frac{1}{2(j+0.5)}\right), \tag{S5}$$

$$k_{\mathrm{H},j} = \frac{D_n}{l_0^2}, \tag{S6}$$

$$k_{\mathrm{H},j-1} = \frac{D_n}{l_0^2}\left(1 - \frac{1}{2(j+0.5)}\right). \tag{S7}$$

The hopping transition rate for spatial element j (eq S4) consists of 4 contributions: transitions from $j-1$ and $j+1$ to j and trasnitions from j to $j-1$ and $j+1$. The advantage formulating the diffusion problem in this way is that the diffusion of multiple species can be easily coupled to one another. This is done by introducing an occupation factor, γ, to each contribution of eq S4 reflecting the binding site occupation of the spatial element to which the transition is described (e.g. to the term $k_{\mathrm{H},j-1}n_{j-1}$ the occupation of j is relevant). The modified form of eq S4 yields:

$$\dot{n}_j = k_{\mathrm{H},j+1}n_{j+1}\gamma_j^{(n)} + k_{\mathrm{H},j-1}n_{j-1}\gamma_j^{(n)} - k_{\mathrm{H},j}n_j\gamma_{j+1}^{(n)} - k_{\mathrm{H},j}n_j\gamma_{j-1}^{(n)}, \tag{S8}$$

where $\gamma_j^{(n)}$ is the occupation factor for the species *n*. We define $\gamma_j^{(n)}$ in the following way:

$$\gamma_j^{(n)} = \left(1 - \frac{m_j}{m_j^{\max}}\right), \tag{S9}$$

where m_j is the concentration of species *m* in spatial element j and $m_j^{\max}$ its concentration at maximum coverage. This approach means that the diffusive transport of species *n* is hindered by coverages of species *m*. This is justified for CO and O on Pd, because both species are most stably bound at the same 3-fold site.

The rate formulation at the origin and outer edge of the coordinate system, i.e. at $j = 0$ and $j = j_{\max}$, is given by eq's. S10 and S11.

$$\dot{n}_0 = 4k_{H,0}n_1\gamma_0^{(n)} - 4k_{H,0}n_0\gamma_1^{(n)} \tag{S10}$$

$$\dot{n}_{j_{\max}}^{\mathrm{closed}} = k_{H,j_{\max}-1}n_{j_{\max}-1}\gamma_{j_{\max}}^{(n)} - k_{H,j_{\max}}n_{j_{\max}}\gamma_{j_{\max}-1}^{(n)} \tag{S11}$$

At $j_{\max}$ (eq S11) the system may be closed—diffusion beyond this point is not possible—ensuring mass conservation as the system evolves. Alternatively, the system may be open—molecules can diffuse beyond $j_{\max}$ but cannot return back, which yields eq S12:

$$\dot{n}_{j_{\max}}^{\text{open}} = k_{H,j_{\max}-1} n_{j_{\max}-1} \gamma_{j_{\max}}^{(n)} - k_{H,j_{\max}} n_{j_{\max}} - k_{H,j_{\max}} n_{j_{\max}} \gamma_{j_{\max}-1}^{(n)}. \quad \text{(S12)}$$

We used the open termination condition in our analysis, but tested the closed termination. We found no differences because the simulated cell size was big enough.

Comparison of CO diffusion rates

In figure S3 we compare the fitted CO diffusion coefficient from this work to previous reports of CO diffusion rates on Pd(111). In previous work STM (Scanning Tunneling Microscopy) was used to measure the site-to-site hopping rate [3], whereas PEEM and LID [4-5] (Photo Electron Emission Microscopy and Laser induced desorption) provide a measure of macroscopic diffusion. Using our derived set of Arrhenius parameters, we reproduce previously reported diffusion constants well. This supports the idea that atomic steps of Pd(332) have no influence on the diffusive mobility of CO. This is consistent with our observations from desorption rate measurements that show no energetic preference for CO at steps of Pd(332). Although previous studies suggested that step influenced diffusion may be important for this system [4], we find no evidence for this. It is possible that use of a too tightly limited temperature range and/or approximations on the dimensionality of the diffusion problem lead to erroneous conclusions.

Estimation of the reaction front speed

In figure S4, we show the radial concentration profiles of CO* and O* at several late titration times. The rather steep decrease of both concentration profiles indicates a diffusion-controlled regime. The quasi-stationary CO_2 production is confined near the reaction front. In the titration experiment, the oxygen coverage steadily decays, while the CO coverage builds up. The reaction moves out from the center toward the outer flanks where the CO coverage steadily removes O*. An established characteristic for diffusion-controlled reactions is the reaction front propagation speed. We use plots like those shown in figure S4 to estimate the reaction front speed that is shown in figure 10 of the main text.

Figures

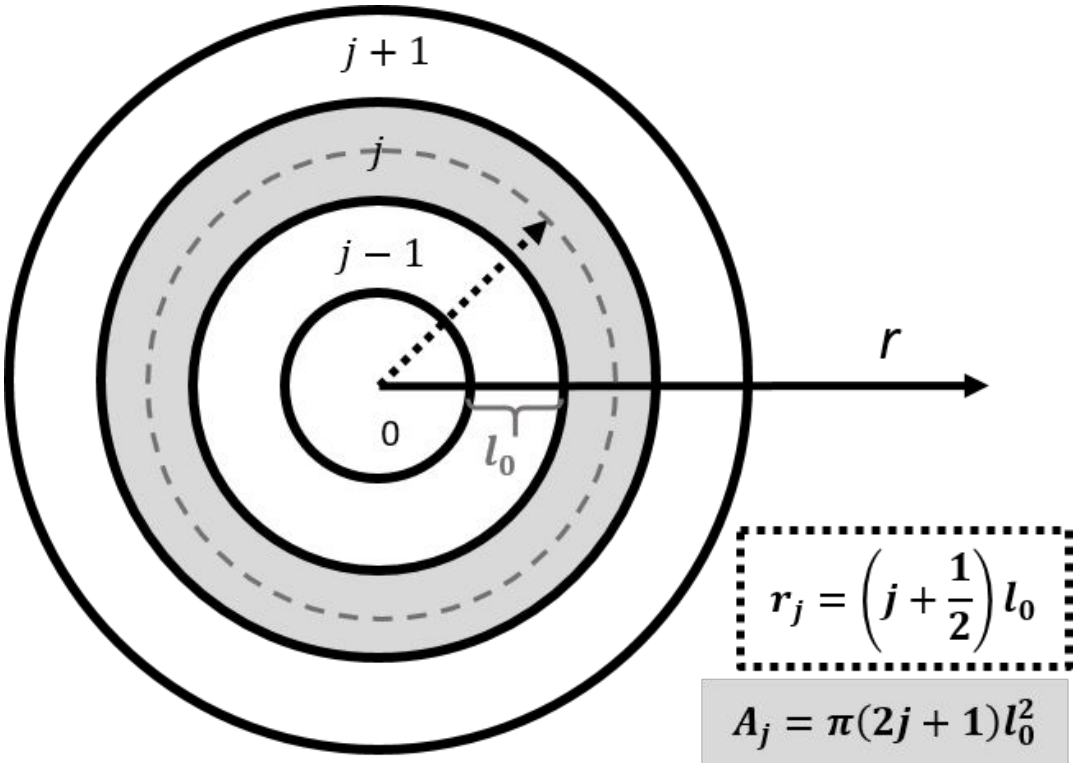

Figure S1: The coordinate system used for diffusion reaction modelling with key definitions.

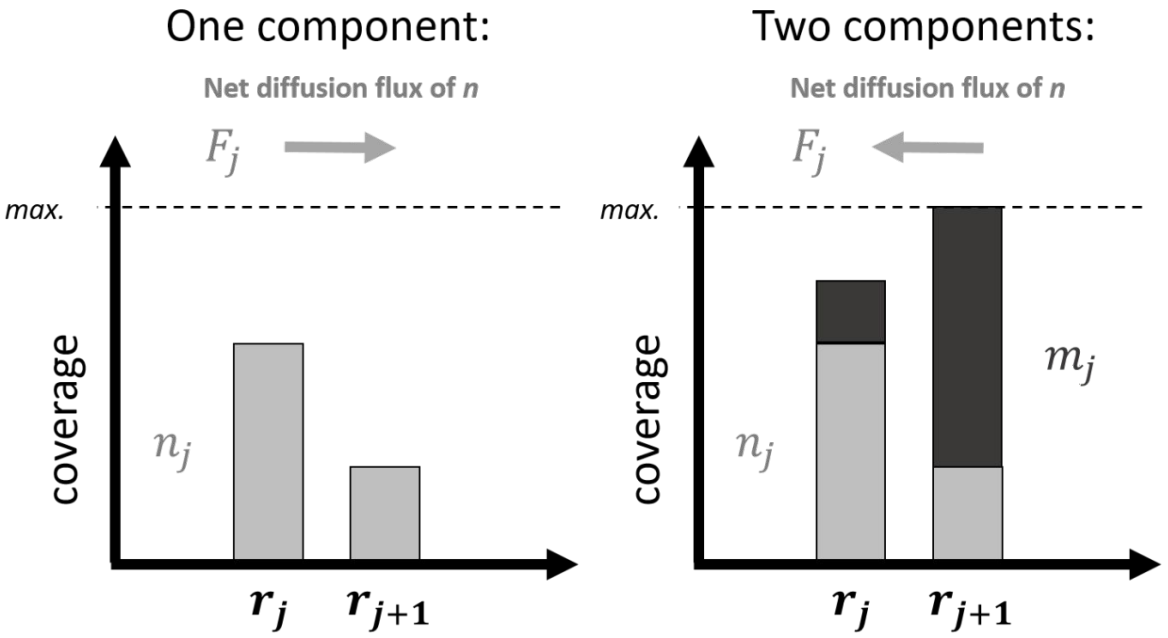

Figure S2: Illustration of the direction of the net diffusion flux of component *n* in a one-component system (left) and in a two-component system (right). In the one-component system the flux goes in the direction of steepest concentration gradient as expected from Fick's equations. However, when a second component *m* is present, this eventually leads to site blocking for component *n*. For situations as sketched on the right, only if the site blocking term $\gamma^{(n)}$ is introduced, which couples the concentrations of *n* and *m*, the right direction of the net diffusive flux is obtained for *n*.

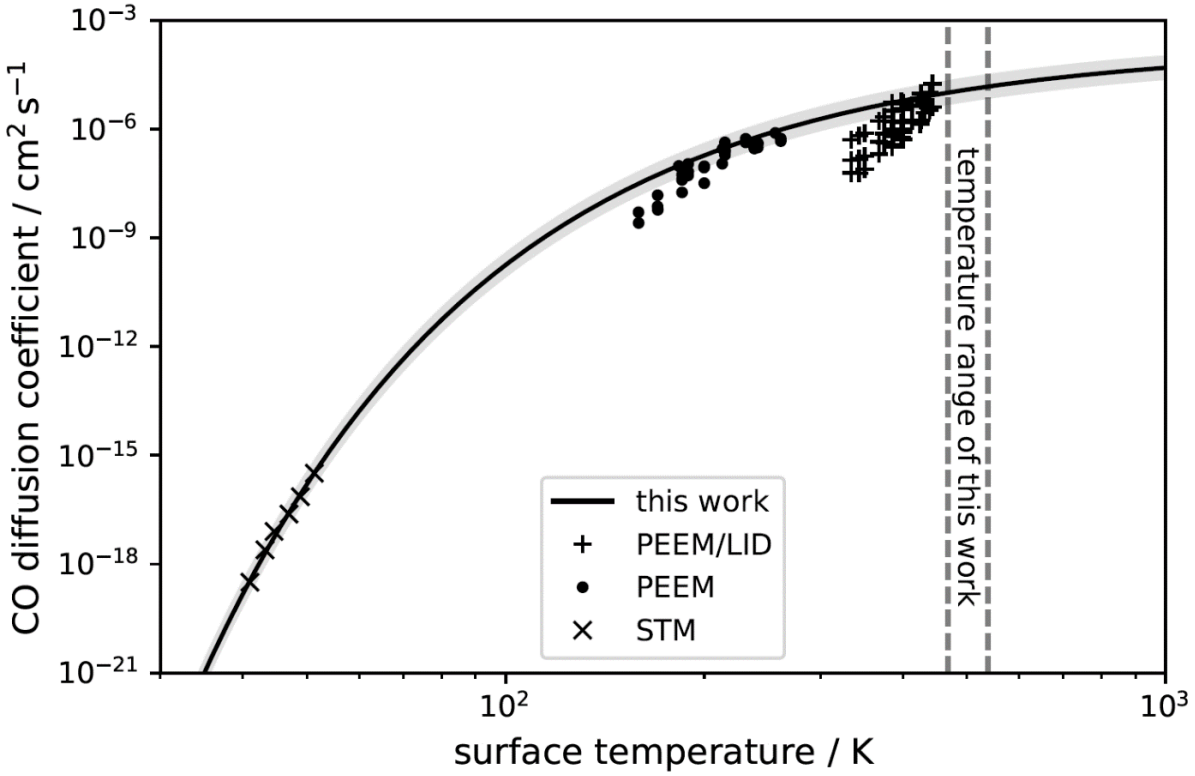

Figure S3: Thermal CO diffusion coefficients are shown for various studies (crosses[3], circles[4] and pluses[5]) on Pd(111) as a function of surface temperature. The methods by which the diffusion rates are determined are indicated in the legend. The results of this work are shown as solid black lines with grey shaded region indicating the estimated error range. The dashed vertical lines in the plot indicate the temperature range of this work.

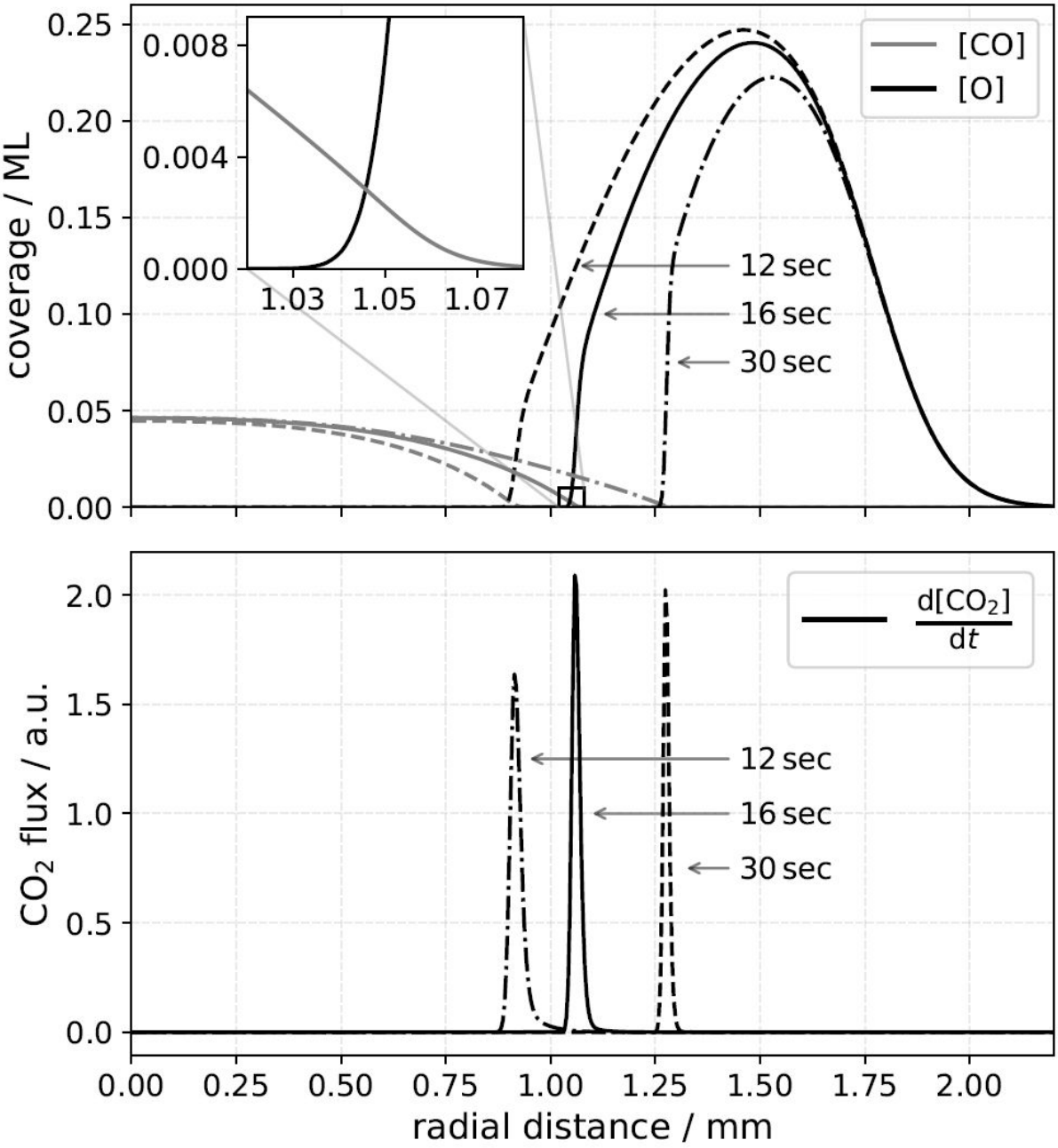

Figure S4: Top: CO* and O* coverage profiles at late titration times at 503 K are shown. The inset of the top plot shows the intersection of the concentration profiles. Bottom: The stationary CO_2 formation rate as a function of the radial distance associated with the coverage profiles from the above plot. From the temporal evolution of the peak maximum the reaction front speed is estimated.

References

1. Crank, J., *The Mathematics of Diffusion*. Clarendon Press: Oxford, 1975; Vol. 2.

2. Serri, J. A.; Tully, J. C.; Cardillo, M. J., The influence of steps on the desorption kinetics of NO from Pt(111). *The Journal of Chemical Physics* **1983,** *79* (3), 1530-1540.

3. Mitsui, T.; Rose, M. K.; Fomin, E.; Ogletree, D. F.; Salmeron, M., Diffusion and pair interactions of CO molecules on Pd(111). *Phys Rev Lett* **2005,** *94* (3), 036101.

4. Šnábl, M.; Borusík, O.; Cháb, V.; Ondřejček, M.; Stenzel, W.; Conrad, H.; Bradshaw, A. M., Surface diffusion of CO molecules on Pd{111} studied with photoelectron emission microscopy. *Surf Sci* **1997,** *385* (2-3), L1016-L1022.

5. von Oertzen, A.; Rotermund, H. H.; Nettesheim, S., Investigation of diffusion of CO absorbed on Pd(111) by a combined PEEM/LITD technique. *Chem Phys Lett* **1992,** *199* (1-2), 131-137.

Chapter 3

A Critical Test of Transition State Theory for a Surface Reaction

3.1 *"Quantum Influence on H Atom Recombination on Pt"*

Author contributions: The kinetic experiments were conducted by DB. Most DFT calculations were conducted by NH. Initial calculations were conducted by YW, JZ and HG. Laser based calibration of molecular beam flux was developed by BGP, DJA and DB. Mathematical formalism for the analysis of molecular beam flux was developed by MS, FN and DB. The data was analyzed by DB. Modelling of TST rate constants was done by DB based on the DFT calculations of NH. The paper was written by AMW and DB. All authors contributed to the discussion of the results. All authors contributed to the revision of the manuscript.

Parts of this chapter have been submitted to a peer-review journal (Ref. [2] in this thesis). The text and the figures were modified to meet the journal's policy on submitted articles.

Quantum influence on hydrogen atom recombination on Pt

Dmitriy Borodin, Nils Hertl , G. Barratt Park, Jan Fingerhut, Michael Schwarzer, Yingqi Wang, Junxiang Zuo, Florian Nitz , Georgios Skoulatakis, Alexander Kandratsenka, Daniel J. Auerbach, Dirk Schwarzer, Hua Guo, Theofanis N. Kitsopoulos and Alec M. Wodtke

ABSTRACT

Transition state theory (TST) is the leading tool for the prediction of elementary chemical reaction rates. Unfortunately for reactions at metal surfaces, which are crucially important to heterogeneous catalysis, there are few tests of its accuracy against elementary rate constants from experiments. Here, we report accurate experimental rate constants for hydrogen atom recombination on Pt(111) and (332) and a model of exact thermal rates, based on the equilibrium assumption of TST, which reproduces experimental results with no adjustable parameters over a broad temperature range. The model accounts for transition state re-crossing and uses an adsorbate entropy for H atoms which is fully derived from quantum mechanics. A classical calculation of hydrogen atoms translational entropy parallel to the surface introduces large errors even at temperatures as high as 1000 K. Neglecting the electron spin of hydrogen atoms, i.e. electronic partition function, introduces a large temperature-independent error. The importance of entropy is also reflected by the fact that recombinative desorption is faster on the highly stepped Pt(332) surface compared to the nearly step-free Pt(111) surface, despite H atom's binding preference at steps. Our modeled adsorbate entropies for Pt(111) and (332) are in good agreement with measurements made for Pt nano-particles and help to explain how adsorbate entropy depends on the nano-particle size. This study demonstrates the high accuracy of TST, but only when the quantum mechanical effects are correctly included.

The rates of thermal reactions at metal surfaces determine the effectiveness of many heterogeneous catalysts [1-3]. Thus, experimental rate constants for elementary reactions at surfaces are needed [4-7]. Unfortunately, the measurements are challenging and only few rate constants are accurately known. Consequently, modelling of heterogeneous catalyst's activity and selectivity relies heavily on theory, which uses Density Functional Theory (DFT) in combination with Transition State Theory (TST) [8-11]. Sadly, theoretically predicted rate constants have rarely been compared to accurate experiments and thus their accuracy remains unknown. The lack of high quality benchmarks is one problem, while uncertainties about TST and limitations of DFT are another.

To show how TST can fail, we review its principles and how it is commonly used in practice. Modern TST formulations prescribes a dividing surface, referred to as the transition state (TS), through which molecules must pass to form the products. The thermal rate constant is calculated as the classical equilibrium one-way flux through the TS in the direction of the product [12-14]. TST provides an upper limit to the rate, since the equilibrium flux includes trajectories that can re-cross the TS and not lead to products. If re-crossing corrections are neglected, which is routinely the case, the choice of TS may strongly affect the calculated rate. However, accurate rate constants can be obtained from any choice of the TS as long as the corresponding dynamical correction is included [12, 13]. Most common formulations of TST are based on classical mechanics[15] and quantum mechanical corrections are included by an *ad hoc* replacement of classical partition functions by quantum expressions, typically based on simple model systems—*e.g.,* harmonic oscillators or hindered translators and rotors[16, 17]. One then computes the physical parameters of the quantum models with DFT for the system of interest [16, 18]. Although well understood from studies of gas-phase reactions[15], effects due to electron spin, i.e. electronic partition functions, are generally omitted when TST is applied to reactions at metal surfaces.

We see that TST's predicted rates may deviate from experiments for several reasons including: 1) failure of the equilibrium approximation, 2) neglect of or incorrect accounting for the quantum mechanics and 3) errors associated with dynamical TS re-crossing. To understand deviations between experiment and theory, one must be able to disentangle these effects.

Recombination of hydrogen atoms at platinum is a crucial step in practical applications like electrochemical hydrogen evolution reactions[19]. It is also—on single-crystal surfaces—the simplest possible reaction well suited for testing theoretical models of reaction rates. DFT at the level of the generalized gradient approximation (GGA) can accurately characterize the H/Pt potential

energy surface (PES) within the static surface approximation. Relative energies of H-atoms at different positions on the Pt surface are more accurate than absolute energies and depend only weakly on the choice of the exchange-correlation functional [20, 21]. We can then use the PES to obtain H atom's adsorbate partition functions using classical or quantum approaches—essential ingredients of TST rate constants.

In this paper, we present an accurate model to TST rate constant calculations, hereafter referred to as quantum potential energy sampling (QPES). The QPES approach uses a quantum partition function for H and D atom adsorbates, computed by directly counting vibrational eigenstates at the static surface. This requires only solving the two-dimensional in-plane Schrödinger equation of an anharmonic PES from DFT. The states associated with the H-Pt stretching coordinate are included as harmonic oscillators using a vibrationally adiabatic approximation. This use of a quantum partition function, together with accounting for the electronic partition function, i.e. the H's electron spin, allows us to describe accurately the quantum entropy of hydrogen atoms adsorbed to Pt surfaces (H*), which is also related to the pre-exponential factor in the TST rate constant. These rate constant predictions are then compared to experiment. We find that TST agrees extremely well with experiments over a wide temperature range, but more importantly, unless the influence of quantum entropy is included, large errors arise.

A problem of our approach would be if we would rely on DFT-GGA to characterize the TS. Our results would strongly depend on the choice of the exchange-correlation functional [22, 23]. In fact, it is not even clarified whether or not dissociative adsorption of H_2 at Pt(111) passes over an activation barrier [22-24]. Uncertainties in DFT-derived reaction barriers and TS-structures would prevent a meaningful comparison to the experimental rate constants. In our QPES-TST approach we solved this problem by positioning the dividing plane far from the Pt surface. This effectively makes the TS a gas-phase molecule, reduced by one translational degree of freedom. This has three advantages. First, the partition function of a gas-phase H_2 molecule can be easily computed from experimental parameters. Second, the re-crossing correction is identical to the thermal sticking probability [25]. These sticking probabilities are accurately known from previous experiments [26-29]. Third, the experimentally determined adsorption energy [30, 31] can be used instead of a DFT-based energy for recombinative desorption.

In order to test QPES-TST, we required kinetic data that are far more accurate than that previously available. Therefore, we carried out velocity-resolved kinetics [6, 7, 32] measurements in

the temperature range of 550 to 950 K, which provided accurate rate constants for three isotopic recombination reactions: $2H^* \rightarrow H_2$, $H^* + D^* \rightarrow HD$ and $2D^* \rightarrow D_2$ on Pt(111) and Pt(332). In the velocity resolved kinetics approach—see Sec. S1a of the Supporting Information (SI)—the Pt(111) or (332) single crystal facets are exposed to a pulsed molecular beam with a known mixture of H_2 and D_2. With spatial ion imaging, we were able to characterize the absolute flux and the spatial profile of the incident molecular beam. With this information and the sticking coefficients for H_2 and D_2 [26, 28, 29], we determine the initial absolute atomic surface concentration $[H^*]_0$ and $[D^*]_0$ needed for the determination of second-order rate constants from experimental rates[33]. See the SI, Sec. S2 and S3 for more details.

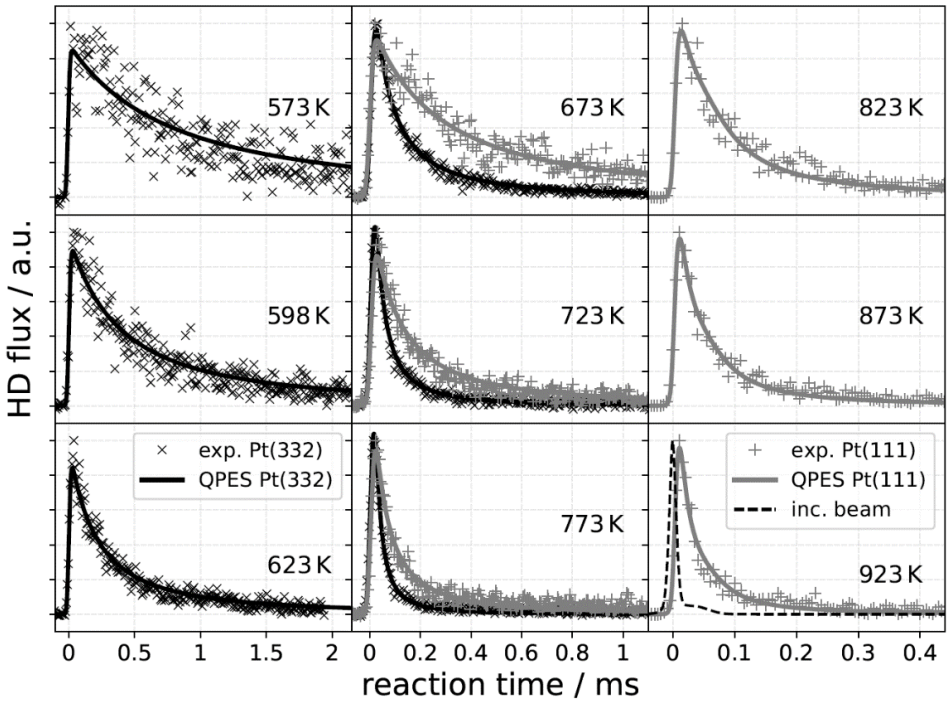

Figure 1: Measured and theoretically predicted HD formation rates. Measured HD formation rates are shown as grey + for Pt(111) and as black × for Pt(332). The predictions of the QPES-TST model are shown as grey and black solid lines for Pt(111) and Pt(332), respectively. The rates are simulated with a H_2 binding energy of 0.75 eV for Pt(111) and 0.93 eV for Pt(332), which are derived from reported isosteric heats of adsorption [30, 31]—see Sec. S4 of the SI. Isotopic specificity in the recombination rate constants arises from mass-dependent differences in partition functions and the zero-point-energy (ZPE) of the reactants and the TS, all of which is accounted for by the QPES-TST model. The black dashed line displays the incident molecular beam pulse, reflecting the temporal resolution of the experiment.

Fig. 1 shows the experimentally obtained HD formation rates for reaction on Pt(111) (+) and Pt(332) (×), reflecting the coupled kinetics of three isotopic recombination reactions. The black and grey curves in Fig. 1 show the QPES-TST rates of HD formation (S4 and S5 in the SI). The

simulation of the HD formation rates accounted for isotope specific rate constants (Section S5c and Fig. S9 in the SI) as well as the spatial density distribution of the molecular beam pulse, a problem that remained unsolved in earlier molecular beam studies [34]—see SI Section S6. The QPES-TST based kinetic isotope effect is small e.g., the relative rate constants at 800 K for H_2:HD:D_2 formation are 1.0:1.9:1.0. This was found to be consistent with further experiments we carried out that probed the relative yields of H_2, HD and D_2 after thermal recombination—see Section S7 and Fig. S10 of the SI.

The agreement between QPES-TST and experiment is in good agreement for both Pt(111) and (332) without any adjustable parameters in the model. We find—consistent with previous work [20]—that the choice of the DFT functional does not alter the resulting QPES partition function significantly—see also Section S1b of the SI. We observe a clear effect of steps—the HD formation rates were systematically ~4× higher on Pt(332) compared to the same reaction on Pt(111). The transient rate of the 2nd order reactions is proportional to the product of atom surface density and rate constant. As a result, the faster rates on Pt(332) are due to both the ~2× higher sticking coefficient as well as the ~2× larger reaction rate constant on Pt(111).

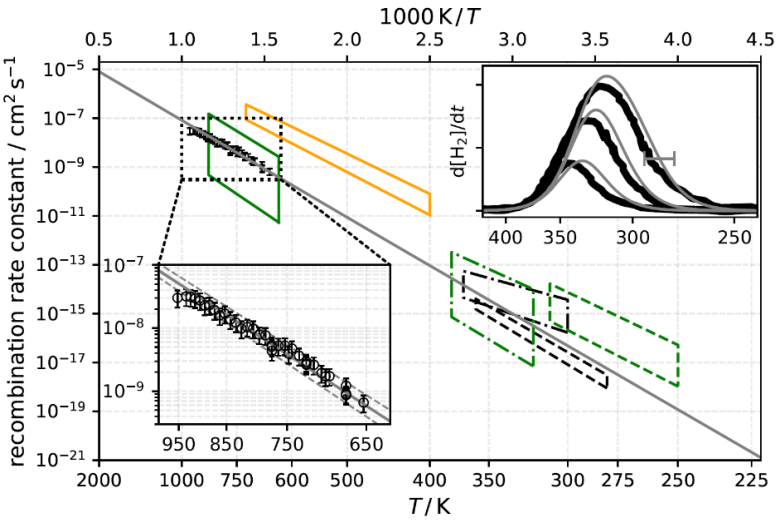

Figure 2: Rate constants for H atom recombination on Pt(111). Results of velocity resolved kinetics experiments with 2σ-error bars (o) are compared to the predictions of the QPES-TST model (grey solid line). Lower-left inset is an expanded view. Upper-right inset compares simulated temperature programmed desorption (TPD) spectra based on the QPES-TST (grey lines) with three TPD spectra (bold black lines, Ref. [35]), using initial H* coverages of 0.1, 0.2 and 0.3 ML. The horizontal error bar on one of the modeled TPD spectra reflects the uncertainty of the H_2 chemisorption energy, as does the region between the two dashed lines in the lower left inset. Note that the QPES-TST model of hydrogen atom recombination has no adjustable parameters. Solid trapezoids show the range of results from modulated molecular beam relaxation spectrometry (MBRS) experiments for: D* recombination (——) [36] and for H*+D* recombination (——) [37]. Other trapezoids are from TPD: H* recombination (— - —) [38] and (- - -) [31] and D* recombination (— - —) [39] and (- - -) [40].

Fig. 2 shows the QPES TST model's predictions for H* recombination at Pt(111) over a wider temperature range (solid grey line) along with comparisons to the present results (open circles) and the range of results from previous experiments (trapezoids). The colors of the trapezoids in Fig. 2 reflects experiments using different isotopes. The isotope effect found in the present work is substantially smaller than the uncertainties of the prior work—see Fig. S9 of the SI. The predictions of the QPES-TST model are consistent with the rate constants obtained from modulated molecular beam relaxation (MBRS) from Ref. [36], but are strongly different from those of Ref. [37]. The rate constants derived from temperature programmed desorption (TPD) at low temperatures are in reasonable agreement with the predictions of QPES-TST. The derivation of rate constants from TPD data often involve crude approximations like ignoring the coverage dependence of rate parameters or making simplified estimations of prefactors. For a better comparison to TPD data, we simulated TPD spectra with the QPES-TST model directly and included the previously reported coverage dependence of the binding energy based on isosteric heats of adsorption [30, 31]—see Fig. S8 of the SI. This procedure yielded the grey curves in the inset of Fig. 2, which is in good agreement with TPD data (black bold lines, Ref. [35]) up to an H-atom coverage of 0.3 ML. The comparisons shown in Fig. 2 demonstrates that the QPES-TST model is reliable for predicting H* recombination rates on Pt(111) at least between 250 and 950 K and up to 0.3 ML coverage.

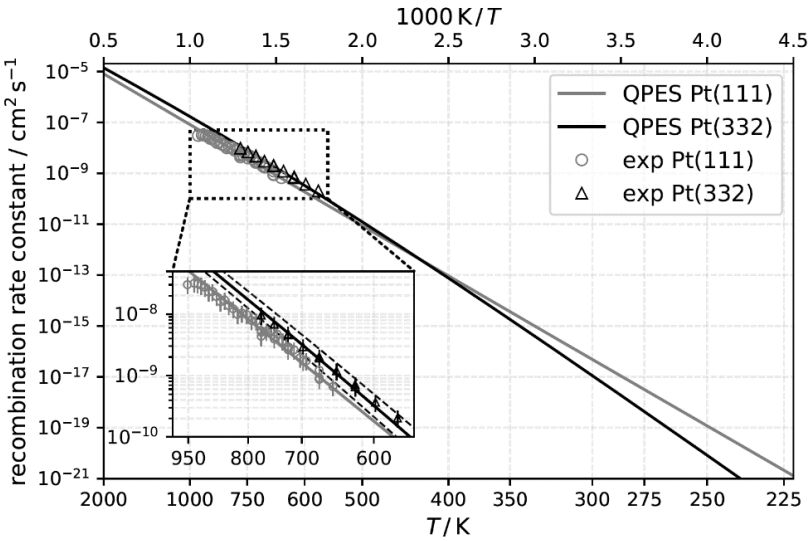

Figure 3: Rate constants for H atom recombination on Pt(332). Rate constants derived from velocity resolved kinetics for hydrogen atom recombination on Pt(111) and on Pt(332) are compared to their QPES-TST model predictions. The 2σ error bars arise from uncertainties in the flux calibration. The uncertainty of the Pt(332) model (2σ, region between the black dashed lines) is due to uncertainty in the H_2 binding energy to Pt(332). The QPES-TST model has no adjustable parameters. The solid black line used a binding energy of 0.93 ± 0.03 eV on Pt(332). The difference in H_2 binding energy between steps and terraces is 0.18 eV and is in agreement with previous experiments [30] and our DFT calculations (~0.18 eV, see SI Section S1b and S4).

Fig. 3 shows the influence of steps on H atom recombination, comparing the experimental results obtained with velocity resolved kinetics to QPES-TST. Desorption from (332) is clearly faster than from (111) at the temperatures of the velocity resolved kinetics experiments. This is surprising since often adsorbates bind more strongly at steps and an increased binding energy often reduces desorption rates [41, 42].

Indeed, there is strong evidence to conclude that H atom's binding energy to B-type steps $E_S^{H^*}$ is larger than its binding energy at terraces $E_T^{H^*}$: in particular our DFT calculations as well as previous ion scattering experiments [30] agree on $\Delta E_{ST} = 0.18$ eV $(= 2E_S^{H^*} - 2E_T^{H^*})$—see SI Section S4 for an in-depth discussion. Consistent with ΔE_{ST} and a binding energy at terraces of 0.75 ± 0.03 eV, the black line in Fig. 3 was obtained by setting the binding energy of H_2 at Pt(332) to 0.93 ± 0.03 eV which yields excellent agreement with the results of velocity resolved kinetics data.

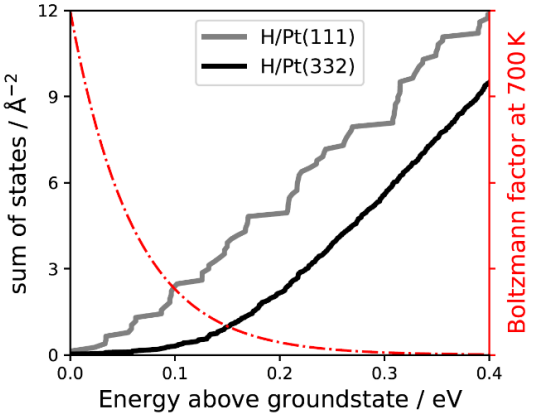

Figure 4: H-atoms sum of states at Pt(111) and Pt(332). H-atom sum of states (per unit area) on Pt(111) (grey line) and Pt(332) (black line). The first H/Pt(332) eigenstate that is located on terraces is at ~92 meV. At the same temperature there are fewer populated eigenstates for H/Pt(332) than H/Pt(111) leading to a lower adsorbate entropy on the stepped surface. The red line indicates the Boltzmann factor—$\exp(-E/k_BT)$—at 700 K.

Despite H atom's stronger binding energy at steps, the associated reduction of entropy leads to recombinative desorption from (332) that is faster than that from (111). Increased binding energy often reduces desorption rates [41, 42], but the energetic preference for steps can also reduce adsorbate's entropy, leading to faster thermal desorption [43, 44]. We can directly evaluate the quantum entropy for H atoms adsorbed on Pt(111) and (332) using QPES—it is substantially smaller on (332) between 600 and 800 K. Quantification of the sum of states and inspection of the probability densities of the thermally populated eigenstates show that at these temperatures H atoms

tend to remain localized at step sites on (332). As a consequence the entropy of an adsorbed H atom is reduced and leads to an increased desorption rate—see Fig. 4.

The importance of a correct adsorbate entropy description has been realized in studies of the equilibrium coverage of H* on catalytic Pt nano-particles [20], whose major facet is identified to be (111). Fig. 5(a) shows experimentally obtained entropies from that work along with classical and quantum entropies obtained using the classical complete potential energy sampling (CPES)[17] and QPES method from this work. See SI Section S9 for details. Although CPES samples the full anharmonicity of the PES, it fails to accurately predict H adsorbate entropy. This has erroneously led to a suggestion that H adsorbate entropy on Pt nano-particles are best described by a free 2D ideal gas model [20]. This study has neglected the entropic contribution of the electronic partition function. In Fig. 5(a) we show that the QPES entropy of H* on Pt(111) is in good agreement with the measured entropies, suggesting that the agreement between the classical ideal gas entropy and experiment was accidental. In addition, the QPES entropy for adsorbed H atoms is lower on Pt(332) than Pt(111). This reflects the measured entropies' dependence on nano-particle size. Larger nano-particles have a larger fraction of (111) facets [20] and smaller ones a larger fraction of step sites. This comparison suggests that relative step density may explain at least part of the dependence of the measured entropies on nano-particle size.

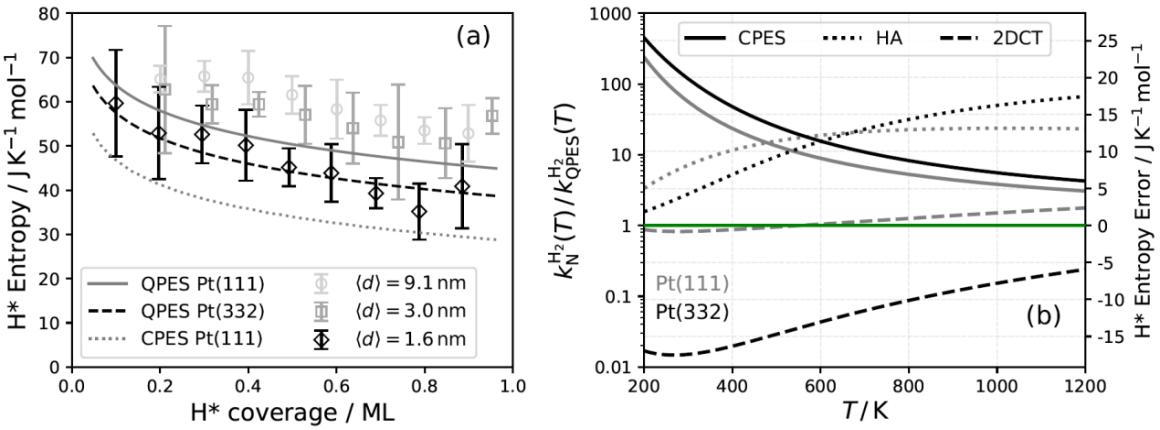

Figure 5: Quantum influence on H-atom adsorbate entropy. (a) Experimentally obtained entropies at 598 K for Pt nano-particles of various sizes from Ref. [20] (symbols with error bars) are compared to quantum entropies from QPES and classical entropies (ignoring spin) from CPES[20] for Pt (111) and (332). The comparison suggests the H* entropy for nano-particles is strongly influenced by the density of steps. (b) H* Entropy Errors ($S^{H^*}_{QPES} - S^{H^*}_{N}$) arising from common approximations to the adsorbate's partition functions are shown as ratios of different recombination rate constant models to the QPES-TST rate constant for H*+H* on Pt(111) and (332). The green horizontal line indicates agreement with the experimentally validated rate constant and adsorbate entropy. The subscript N reflects the employed method for the rate constant estimation that is shown in the legend. The grey and black line indicate modeled rate constants at Pt(111) and Pt(332), respectively. Neglect of electronic partition function in the QPES TST model (not shown) results in temperature independent error of ~5.8 kJ mol^{-1}.

We can elucidate these points further by using the QPES-TST model to evaluate errors introduced by established approximations [17] to describe translational entropy of H* on Pt—see Fig. 5(b). Here, temperature dependent rate constants obtained with three approximate methods are divided by the QPES-TST rate constants. In this comparison, the harmonic approximation (HA), CPES [17] and QPES methods are compared using the same PES. The two dimensional classical collision theory model (2DCT) is based on the classical 2D ideal gas entropy for H* and requires no PES.

Using the harmonic approximation at high temperatures leads to drastically overestimated rate constants (underestimated adsorbate entropy) as this approximation cannot describe H atom delocalization present on the underlying PES, which is highly anharmonic. The classical CPES method also fails, especially at low temperatures where it drastically underestimates the adsorbate entropy. Remarkably, even at 1000 K the rate predicted using an accurate classical entropy is 5× too high.

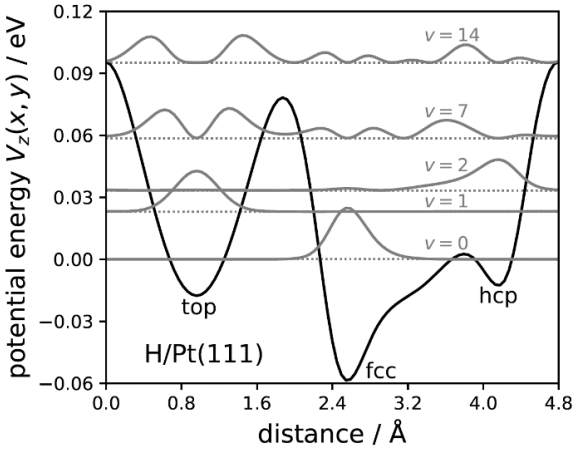

Figure 6: H-atoms eigenstates at Pt(111). A 1D cut through the H/Pt(111) interaction potential with selected probability density distributions is shown. The black line reflects the H-atom interaction potential $V_z^H(x,y)$. The grey dotted lines indicate the eigenstates with the corresponding probability density distribution shown as grey solid line. The zero-point energy correction has a predominant influence on the description of hydrogen atom entropy, while classical description fails in reproducing the experiment.

This error in CPES arises because it does not properly account for the 2D in-plane zero-point energy (ZPE), which is crucial for a correct description of H-atom entropy on metal surfaces—see Fig. 6. The height of the classical diffusion barrier (60 meV) can be seen as an indicator to which degree the adsorbate is a free translator. The 2D in-plane ZPE of H* on Pt(111) is 58 meV and cannot be neglected if accurate entropy is desired—see Fig. 6. In fact, the error introduced to the translational entropy when neglecting ZPE accounts for nearly all of the deviation between CPES

and QPES. This discussion highlights the fact that while ZPE is often taken correctly into account in determining binding energies and reaction barriers, its contribution to adsorbate entropy cannot be ignored either.

We also noted that the 2D collision theory model agreed well with the QPES rate constants for Pt(111) but failed badly for Pt(332). This apparently resulted from an accidental error cancellation for Pt(111) that did not arise for (332). Clearly, 2D collision theory does not reflect the right physics of hydrogen atom recombination.

Other quantum effects on the reaction should be also noted, in particular tunneling and spin. Tunneling through the adsorption barrier (an energetic effect) was not observed in sticking coefficient determination and is considered unimportant[28, 29]. Tunneling through diffusion barriers (an entropic effect) can be seen in Fig. 6 as a delocalization of the wave function. We think that this contribution is minor and that the contribution of accurate accounting of in-plane ZPE is the crucial point. The QPES partition function included H atom's electron spin in counting the states of the adsorbate. This was essential to yield agreement with experimental rate constants of a second order reaction as this contribution is squared in the TST rate constant expression. While including spin is straightforward, it is often neglected, perhaps with the idea that only the local spin in the region of the H atoms matters. This is a misconception. H_2 dissociation on Pt leads to two unpaired spins in the system, which become decoupled from one another, regardless of the local spin density at the Pt-H bonds. Hence, there is a two-fold degeneracy of spin states for each H atom, which for two H atoms represent four spin states which are all degenerate. These states are conserved in the molecule forming the electronic singlet ground state ($^1\Sigma_g^+$) and the first excited triplet state ($^3\Sigma_u^+$), which does not contribute to the electronic partition function of H_2. The neglect of spin degeneracy increases the rate constant by a factor of 4, independent of temperature.

The work presented here shows several key points relevant to the theoretical prediction of reaction rates in catalytic reactions. First, the equilibrium assumption of TST is accurate for the hydrogen atom recombination reaction and, while it has not been tested fully for other reactions, this conclusion is likely to be general. The equilibrium assumption is valid in gas-phase reactions at high pressures, a topic that has been thoroughly investigated [45]. The high density of atoms in surface chemistry suggests that surface chemistry may resemble the high pressure limit of gas phase TST. Second, it becomes clear that large quantum effects contribute to H atom adsorbate entropy at temperatures even as high as 1000 K—classical methods should be avoided if accuracy

is required. This is likely to apply to adsorbed H atoms on all surfaces. Third, DFT-GGA is sufficiently accurate to provide first principles quantum entropy for H atoms adsorbed on many metals. This becomes evident as the main contribution to the total H* entropy is the in-plane translational entropy. Finally, it appears that models based on H atom interactions with simple single crystal surfaces—e.g. Pt(111) or (332)—accurately describe H atom adsorbate entropy on Pt nano-particles, showing that a fundamental understanding of properties of real world catalysts can be obtained from accurate experiments from surface science.

11

REFERENCES

[1] C. Stegelmann, A. Andreasen, C.T. Campbell, Degree of rate control: how much the energies of intermediates and transition states control rates, J Am Chem Soc, 131 (2009) 8077-8082.

[2] G.B. Park, T.N. Kitsopoulos, D. Borodin, K. Golibrzuch, J. Neugebohren, D.J. Auerbach, C.T. Campbell, A.M. Wodtke, The kinetics of elementary thermal reactions in heterogeneous catalysis, Nature Reviews Chemistry, 3 (2019) 723-732.

[3] M. Salciccioli, M. Stamatakis, S. Caratzoulas, D.G. Vlachos, A review of multiscale modeling of metal-catalyzed reactions: Mechanism development for complexity and emergent behavior, Chemical Engineering Science, 66 (2011) 4319-4355.

[4] J.A. Schwarz, R.J. Madix, Modulated beam relaxation spectrometry, Surf. Sci., 46 (1974) 317-341.

[5] M.P. D'Evelyn, R.J. Madix, Reactive scattering from solid surfaces, Surface Science Reports, 3 (1983) 413-495.

[6] D. Borodin, K. Golibrzuch, M. Schwarzer, J. Fingerhut, G. Skoulatakis, D. Schwarzer, T. Seelemann, T. Kitsopoulos, A.M. Wodtke, Measuring Transient Reaction Rates from Nonstationary Catalysts, ACS Catalysis, 10 (2020) 14056-14066.

[7] J. Neugebohren, D. Borodin, H.W. Hahn, J. Altschaffel, A. Kandratsenka, D.J. Auerbach, C.T. Campbell, D. Schwarzer, D.J. Harding, A.M. Wodtke, T.N. Kitsopoulos, Velocity-resolved kinetics of site-specific carbon monoxide oxidation on platinum surfaces, Nature, 558 (2018) 280-283.

[8] H. Eyring, The theory of absolute reaction rates, Transactions of the Faraday Society, 34 (1938) 0041-0048.

[9] M. Jørgensen, H. Grönbeck, First-Principles Microkinetic Modeling of Methane Oxidation over Pd(100) and Pd(111), ACS Catalysis, 6 (2016) 6730-6738.

[10] K. Reuter, M. Scheffler, First-principles kinetic Monte Carlo simulations for heterogeneous catalysis: Application to the CO oxidation atRuO2(110), Physical Review B, 73 (2006).

[11] S. Bhandari, S. Rangarajan, M. Mavrikakis, Combining Computational Modeling with Reaction Kinetics Experiments for Elucidating the In Situ Nature of the Active Site in Catalysis, Acc Chem Res, 53 (2020) 1893-1904.

[12] J.L. Bao, D.G. Truhlar, Variational transition state theory: theoretical framework and recent developments, Chem. Soc. Rev., 46 (2017) 7548-7596.

[13] S.C. Tucker, D.G. Truhlar, Dynamical Formulation of Transition State Theory: Variational Transition States and Semiclassical Tunneling, in: New Theoretical Concepts for Understanding Organic Reactions Springer Netherlands, 1989, pp. 291-346.

[14] J.C. Keck, Variational Theory of Reaction Rates, in: I. Prigogine (Ed.) Advances in Chemical Physics, John Wiley and Sons, London, 1967, pp. pp. 85.

[15] D.G. Truhlar, B.C. Garrett, S.J. Klippenstein, Current status of transition-state theory, J Phys Chem-Us, 100 (1996) 12771-12800.

[16] L.H. Sprowl, C.T. Campbell, L. Arnadottir, Hindered Translator and Hindered Rotor Models for Adsorbates: Partition Functions and Entropies, Journal of Physical Chemistry C, 120 (2016) 9719-9731.

[17] M. Jørgensen, H. Grönbeck, Adsorbate Entropies with Complete Potential Energy Sampling in Microkinetic Modeling, The Journal of Physical Chemistry C, 121 (2017) 7199-7207.

[18] C.T. Campbell, L.H. Sprowl, L. Arnadottir, Equilibrium Constants and Rate Constants for Adsorbates: Two-Dimensional (2D) Ideal Gas, 2D Ideal Lattice Gas, and Ideal Hindered Translator Models, Journal of Physical Chemistry C, 120 (2016) 10283-10297.

[19] A. Godula-Jopek, Hydrogen Production by Electrolysis, Wiley-VCH, 2015.

[20] M. García-Diéguez, D.D. Hibbitts, E. Iglesia, Hydrogen Chemisorption Isotherms on Platinum Particles at Catalytic Temperatures: Langmuir and Two-Dimensional Gas Models Revisited, The Journal of Physical Chemistry C, 123 (2019) 8447-8462.

[21] G. Kallen, G. Wahnstrom, Quantum treatment of H adsorbed on a Pt(111) surface, Physical Review B, 65 (2002).

[22] E.W.F. Smeets, G.J. Kroes, Designing new SRP density functionals including non-local vdW-DF2 correlation for H-2 + Cu(111) and their transferability to H-2 + Ag(111), Au(111) and Pt(111), Physical Chemistry Chemical Physics, 23 (2021) 7875-7901.

[23] E. Nour Ghassemi, M. Wijzenbroek, M.F. Somers, G.-J. Kroes, Chemically accurate simulation of dissociative chemisorption of D2 on Pt(1 1 1), Chemical Physics Letters, 683 (2017) 329-335.

[24] P. Kraus, I. Frank, On the dynamics of H-2 adsorption on the Pt(111) surface, Int J Quantum Chem, 117 (2017).

[25] J.C. Tully, The Dynamics of Adsorption and Desorption, Surf. Sci., 299 (1994) 667-677.

[26] R. van Lent, S.V. Auras, K. Cao, A.J. Walsh, M.A. Gleeson, L.B.F. Juurlink, Site-specific reactivity of molecules with surface defects-the case of H2 dissociation on Pt, Science, 363 (2019) 155-157.

[27] K. Cao, R. van Lent, A.W. Kleyn, L.B.F. Juurlink, A molecular beam study of D2 dissociation on Pt(111): Testing SRP-DFT calculations, Chemical Physics Letters, 706 (2018) 680-683.

[28] I.M.N. Groot, A.W. Kleyn, L.B.F. Juurlink, Separating Catalytic Activity at Edges and Terraces on Platinum: Hydrogen Dissociation, Journal of Physical Chemistry C, 117 (2013) 9266-9274.

[29] A.C. Luntz, J.K. Brown, M.D. Williams, Molecular beam studies of H2 and D2 dissociative chemisorption on Pt(111), J Chem Phys, 93 (1990) 5240-5246.

[30] B.J.J. Koeleman, S.T. de Zwart, A.L. Boers, B. Poelsema, L.K. Verhey, Adsorption study of hydrogen on a stepped Pt(997) surface using low energy recoil scattering, Nuclear Instruments and Methods in Physics Research, 218 (1983) 225-229.

[31] B. Poelsema, K. Lenz, G. Comsa, The dissociative adsorption of hydrogen on defect-'free' Pt(111), J Phys Condens Matter, 22 (2010) 304006.

[32] D.J. Harding, J. Neugebohren, H. Hahn, D.J. Auerbach, T.N. Kitsopoulos, A.M. Wodtke, Ion and velocity map imaging for surface dynamics and kinetics, Journal of Chemical Physics, 147 (2017).

[33] D. Borodin, M. Schwarzer, H.W. Hahn, J. Fingerhut, Y.Q. Wang, D.J. Auerbach, H. Guo, J. Schroeder, T.N. Kitsopoulos, A.M. Wodtke, The puzzle of rapid hydrogen oxidation on Pt(111), Mol Phys, (2021).

[34] D.R. Olander, Heterogeneous chemical kinetics by modulated molecular beam mass spectrometry, Journal of Colloid and Interface Science, 58 (1977) 169-183.

[35] S.K. Jo, Weakly-bound hydrogen on defected Pt(111), Surf. Sci., 635 (2015) 99-107.

[36] G.E. Gdowski, J.A. Fair, R.J. Madix, Reactive scattering of small molecules from platinum crystal surfaces: D2CO, CH3OH, HCOOH, and the nonanomalous kinetics of hydrogen atom recombination, Surf. Sci., 127 (1983) 541-554.

[37] M. Salmerón, R.J. Gale, G.A. Somorjai, A modulated molecular beam study of the mechanism of the H2–D2 exchange reaction on Pt(111) and Pt(332) crystal surfaces, J Chem Phys, 70 (1979) 2807-2818.

[38] K. Christmann, G. Ertl, T. Pignet, Adsorption of hydrogen on a Pt(111) surface, Surf. Sci., 54 (1976) 365-392.

[39] P. Samson, A. Nesbitt, B.E. Koel, A. Hodgson, Deuterium dissociation on ordered Sn/Pt(111) surface alloys, J Chem Phys, 109 (1998) 3255-3264.

[40] M.J. van der Niet, A. den Dunnen, L.B. Juurlink, M.T. Koper, The influence of step geometry on the desorption characteristics of O_2, D_2, and H_2O from stepped Pt surfaces, J Chem Phys, 132 (2010) 174705.

[41] J.A. Serri, J.C. Tully, M.J. Cardillo, The influence of steps on the desorption kinetics of NO from Pt(111), J Chem Phys, 79 (1983) 1530-1540.

[42] K. Golibrzuch, P.R. Shirhatti, J. Geweke, J. Werdecker, A. Kandratsenka, D.J. Auerbach, A.M. Wodtke, C. Bartels, CO desorption from a catalytic surface: elucidation of the role of steps by velocity-selected residence time measurements, J Am Chem Soc, 137 (2015) 1465-1475.

[43] D.E. Starr, C.T. Campbell, Large entropy difference between terrace and step sites on surfaces, J Am Chem Soc, 130 (2008) 7321-7327.

[44] D. Borodin, I. Rahinov, J. Fingerhut, M. Schwarzer, S. Horandl, G. Skoulatakis, D. Schwarzer, T.N. Kitsopoulos, A.M. Wodtke, NO Binding Energies to and Diffusion Barrier on Pd Obtained with Velocity-Resolved Kinetics, Journal of Physical Chemistry C, 125 (2021) 11773-11781.

[45] K.A. Holbrook, M.J. Pilling, S.H. Robertson, Unimolecular Reactions, 2nd ed., John Wiley & Sons, New York, 1996.

Supporting Information
for
Quantum influence on H atom recombination on Pt

Dmitriy Borodin, Nils Hertl, G. Barratt Park, Jan Fingerhut, Michael Schwarzer, Yingqi Wang, Junxiang Zuo, Florian Nitz, Georgios Skoulatakis, Alexander Kandratsenka, Daniel J. Auerbach, Dirk Schwarzer, Hua Guo, Theofanis N. Kitsopoulos and Alec M. Wodtke

S1. METHODS AND MATERIALS

a. Experimental Methods

The velocity resolved kinetics setup has been described previously [1-3]. For this study, a supersonic molecular beam with a mixture of D_2 in H_2 was produced with a piezo-electrically driven pulsed nozzle. The beam passed two differentially pumped stages and entered the surface-scattering chamber—base pressure 2×10^{-10} mbar—before striking Pt(111) or Pt(332) (MaTeck GmbH) at an incidence angle $30°$ from the surface normal. The molecular pulse had a full width at half maximum of 15 μs.

We used two target crystals, a Pt(111) single crystal and a dual facet Pt sample cut with a (111) and a (332) facet [4] as shown in Fig. S1. The facets of the dual facet sample are sufficiently spaced to ensure that reactions at different surface cuts do not interact due to exposure from molecular beam or diffusion. The step density of the Pt(111) crystals is 0.4 ± 0.2 %, determined using atomic force microscopy, and the step density of the (111) facet of the dual facet crystal was estimated to 0.15 ± 0.05 %, based on the surface cut angle accuracy. For all experiments the Pt(332) surface was aligned such that the step propagation axis is parallel to the scattering plane. Before kinetics measurements were performed, the target was prepared by sputtering with Ar^+ (3 keV) for 15 min and subsequent annealing at 1300 K for 20 min and its cleanliness was checked with Auger electron spectroscopy.

The molecular hydrogen isotopologues were ionized 20 mm from the surface, using either 2+1 resonance enhanced multiphoton ionization (REMPI) *via* the $E, F^1\sum_g^+$ state[5] or with non-resonant multiphoton ionization using an ultrashort pulse of the Ti:Sapphire laser (800 nm, 35 fs, 0.3 W at 1 kHz). A pulsed homogeneous electric field, formed between two parallel flat wire meshes, projected the ions onto an imaging detector (MCPs and Phosphor screen) and the image was recorded with a CCD camera. Recombined HD product formed at Pt(111) was detected with REMPI and, unless otherwise stated, we probed the $J = 3$, $v = 0$ state. Pulses of light (~2.5 mJ) with wavelengths between 201 and 209 nm were generated by frequency tripling the output of a pulsed dye laser running on a mixture of Rh B and Rh 101 in ethanol. We used non-resonant multi-photon-ionization (MPI) for isotopic branching measurements and for kinetic measurements at the dual facet Pt sample. The incident beam flux and the radial beam profile were characterized with non-resonant MPI—see Section S2 of the SI.

Each pixel in the ion image contains information about the product density—the pixel intensity—and velocity—the pixel position in the image. We used this information to determine the flux of the desorbing molecules. Previously this was done by integrating a narrow rectangular stripe of the image reflecting molecules with nearly identical velocities [3, 6] and correcting for the corresponding time of flights. For this work, we used an improved procedure determining the traces from several stripes and averaging them, thereby improving the signal-to-noise ratio.

b. Computational Methods

DFT Calculations

The potential energy surface (PES) for an H atom on Pt(111) or Pt(332) was computed with the *Vienna Ab-initio Simulation Package* (VASP, Version 5.3.5)[7-10]. Electronic exchange and correlation were incorporated at the generalized gradient approximation (GGA) level by making

use of the RPBE functional[11]. The valance electrons were expanded with plane wave basis functions with the energy cutoff set to 400 eV and electron-core interactions were described with the projector augmented wave approach[12]. A single point calculation was considered to be converged when the energy difference between two optimization steps was smaller than 0.01 meV and a structure optimization was stopped when forces < 0.01 eV/Å were reached. A smearing scheme of Methfessel-Paxton[13] of 1st order was employed and the thermal broadening was set to 0.1 eV. The Brillouin zone was sampled with a $4 \times 4 \times 1$ k-point mesh using the method of Monkhorst and Pack[14].

The Pt(111) surface was modelled as a four layered slab with a $p(3 \times 3)$ super cell, with the top three layers relaxed and the bottom layer kept fixed. The Pt(332) surface was modelled as a slab with a $p(4 \times 5)$ supercell and four layers. The electronic energies of the H/Pt(111) PES were acquired by calculating a 20×20 equidistant energy grid along the basis vectors that span the (1×1) surface cell. For H/Pt(332) PES we spanned a 5×28 equidistant grid along the irreducible part of the Pt(332) surface. We permitted relaxation only of the H-atom's degree of freedom perpendicular to the surface plane (along the z-axis) and the structure optimization was stopped when forces < 0.01 eV/Å were reached. The corresponding z-axis position is $z_{\min}$ and the procedure yielded $V(x, y, z_{\min})$. The optimized geometry served as a starting point for the calculation of harmonic H(D)-Pt stretch frequency, which was determined from the dynamic matrix using a finite difference method with four displacements along the z-axis. We added ZPE associated with the H(D)-Pt harmonic stretch frequency to $V(x, y, z_{\min})$, giving us the isotope specific 2D H(D)/Pt-interaction potential $V_z^{\mathrm{H(D)}}(x, y)$, corrected for z-axis ZPE. See, for example, Fig. S2.

Solving the 2D Schrödinger Equation

We solved the nuclear Schrödinger Equation (SE) on an adiabatically separated two-dimensional PES to determine the quantum partition function for the in-plane motion of the H atom. The SE for a coordinate system at a skew angle γ is given by:

$$-\frac{\hbar^2}{2m\sin^2(\gamma)}\left(\frac{\partial^2}{\partial x^2} - 2\cos(\gamma)\frac{\partial}{\partial x}\frac{\partial}{\partial y} + \frac{\partial^2}{\partial y^2}\right)\psi(x,y) + V_z^{\mathrm{H(D)}}(x,y)\psi(x,y) = E^{\mathrm{H(D)}}\psi(x,y) \qquad \text{(S1)}$$

For the Pt(111) (Pt(332)) surface we used $\gamma = 60°(90°)$. To find the wave function and the corresponding eigenenergies, E, we made use of the finite difference method to express the derivatives and curvatures of the wave function and then transformed the corresponding set of equations into an eigenvalue problem. The eigenvalue problem was solved using the LAPACK Fortran package wrapped in *scipy.linalg.eigh* method in Python – similar as used in Ref. [15]. This yielded the wave functions and eigenenergies. The procedure is closely related to the one used by Cooney *et al.,[16]* but we adapted it to work for two-dimensional problems. In addition, to account for periodicity of the lattice, we also introduced periodic boundary conditions to the Hamiltonian.

We solved the SE for the energy eigenvalues by using a 80×80 (60×282) grid for the Pt(111) (Pt(332)) unit cell. We found, by testing grids with fewer points, that the eigen-energies have converged within 0.1% up to an energy of 1 eV above the ground state (for H and D) and we used this as the cut-off for the quantum mechanical partition functions.

We did not use plane wave functions, strictly required for periodic problems, but we tested the convergence of the partition functions by increasing the number of unit cells, e.g., 1×1, 4×4, 7×7 for Pt(111), considered for determining the eigenstates. We found that the area normalized adsorbate partition function, used for determining the rate constants, were converged already for solutions in a single unit cell and accurate within 0.05 % at temperatures above 100 K. Despite the approximations we used, our results are consistent with the work of Källén and Wahnström [17].

We used also the PES, generated with the PBE exchange-correlation functional in an earlier study [18], to test the functional sensitivity on the partition function. We find an average deviation for the H and D partition functions ~17% between 100 and 2000 K, confirming a small dependence on the functional in describing adsorbate entropies. This conclusion is consistent with previous reports [19].

S4

S2. CALIBRATION OF THE ABSOLUTE MOLECULAR BEAM FLUX

The determination of the absolute flux of the molecular beam is critical to the success of this study. Since it is not commonly performed, we request the patience of the reader as we explain in detail why and how this was done.

a. Why is the absolute flux needed

Quantifying 2nd order reaction rate constants with molecular beam methods has proven to be challenging [20], since either the absolute product flux or the absolute initial concentration of reactants is required [21]. Consider the analytic solution to the 2nd order rate equation for $H_{2(g)}$ formation from two adsorbed H atoms

$$\frac{\mathrm{d}\left[\mathrm{H}_{2(\mathrm{g})}\right]_t}{\mathrm{d}t} = \frac{k_\mathrm{r}\,[\mathrm{H}^*]_0{}^2}{(1+2\,k_\mathrm{r}\,[\mathrm{H}^*]_0 t)^2}. \tag{S2}$$

Here, $[\mathrm{H}^*]_0$ is the initial concentration of adsorbed H atoms and k_r is the recombination rate constant. Note that $\mathrm{d}\left[\mathrm{H}_{2(\mathrm{g})}\right]_t/\mathrm{d}t$ is the time dependent absolute product flux which is proportional to the kinetic trace F_t^{VRK} obtained from velocity resolved kinetics experiment. While calibrating for absolute product flux is in principle possible, we found it more practical to pursue an alternative. To demonstrate the idea of our approach we linearize the relative H_2 product flux, obtained from the experiment, by taking the inverse square root of it:

$$\frac{1}{\sqrt{F_t^{\mathrm{VRK}}}} \propto 1 + 2k_\mathrm{r}[\mathrm{H}^*]_0 t, \tag{S3}$$

The slope of this linearized function is $2k_\mathrm{r}[\mathrm{H}^*]_0$ showing that to obtain k_r we require the initial reactant concentration $[\mathrm{H}^*]_0$. For practical use we multiply Eq. S2 by $\alpha/\left(k_\mathrm{r}\,[\mathrm{H}^*]_0{}^2\right)$, with α as an arbitrary scaling factor, which results in F_t^{VRK} obtained from the experiment:

$$F_t^{\mathrm{VRK}} = \frac{\alpha}{(1+2\,k_\mathrm{r}\,[\mathrm{H}^*]_0 t)^2}. \tag{S4}$$

With an independent measure of initial reactant concentration $[\mathrm{H}^*]_0$, we can fit α (amplitude parameter) and k_r (shape parameter) to the kinetic trace F_t^{VRK}. $[\mathrm{H}^*]_0$ is obtained by measuring the absolute molecular beam flux and combining it with known sticking probabilities[22-25], as explained below.

b. How is the absolute flux obtained

To determine absolute beam fluxes, we followed a strategy similar to that employed in Ref. [26], where the authors calibrated the density signal in ion images using a static background gas, whose pressure was monitored by a calibrated ion gauge. This was used to obtaining the density of the molecular beam. While simple in principle, it is crucial to account for the differing spatial factors present when laser-ionizing background gas and pulsed molecular beams.

We start by defining a Cartesian coordinate system where the x-axis is parallel to the surface normal, the y-axis is along the laser propagation axis and the z-axis is parallel to the normal direction of the ion image.

The number of ionized molecules, N_{ion}, results from their ionization efficiency function, $E(x,y,z)$, which is related to the spatial intensity distribution of the laser light and the molecule's density distribution function, $D(x,y,z)$, which is different for background gas compared to a molecular beam sample

$$N_{\mathrm{ion}} = \iiint D(x,y,z)\, E(x,y,z)\, \mathrm{d}x\mathrm{d}y\mathrm{d}z. \tag{S5}$$

The integration proceeds over the full volume of the ion Newton sphere. Assuming that the above spatial distributions is separable, i.e. $D(x,y,z) = \delta_x(x)\delta_y(y)\delta_z(z)$ and $E(x,y,z) = \varepsilon_x(x)\varepsilon_y(y)\varepsilon_z(z)$, Eq. S5 is simplified to:

$$N_{\mathrm{ion}} = \int \delta_x(x)\, \varepsilon_x(x)\mathrm{d}x \int \delta_y(y)\, \varepsilon_y(y)\mathrm{d}y \int \delta_z(z)\, \varepsilon_z(z)\mathrm{d}z. \tag{S6}$$

Here, small Greek letters indicate 1D distributions for density δ and ionization efficiency ε.

The measured xy-dependent ion image signal intensity, $S_{\mathrm{II}}(x,y)$, is proportional to:

$$S_{\mathrm{II}}(x,y) \propto \Big(\delta_x(x)\, \varepsilon_x(x)\delta_y(y)\, \varepsilon_y(y) \otimes s(x,y) \Big) \int \delta_z(z)\, \varepsilon_z(z)\mathrm{d}z, \tag{S7}$$

where integration over z results due to the long time-gate applied to the microchannel plate (MCP) that allows detection of all ions created in the ionization volume. The function $s(x,y)$ describes the changes of the formed ion cloud during its flight towards the MCP detector, without altering its integral value, by a convolution (indicated by $\otimes$). It is important to realize that $s(x,y)$ is different for the background gas sample $s^{\mathrm{BG}}(x,y)$ compared to the molecular beam sample $s^{\mathrm{MB}}(x,y)$. By comparing Eq. S6 and S7, we see that N_{ion} is proportional to the x- and y-integrated signal of the ion image

$$N_{\mathrm{ion}} \propto \int \int S_{\mathrm{II}}(x,y)\mathrm{d}x\mathrm{d}y, \tag{S8}$$

The ionization efficiency function, E, depends on the shape of the laser focus, specifically its spatial intensity distribution, and the laser power. However, we do not require absolute values of ionization efficiency; it is sufficient that it remains constant and the same for both the calibration measurement (using static background gas) and the molecular beam density measurement. Both the laser power and the position of the laser focus must remain unchanged. In practice, we position the laser focus to hit the center of the molecular beam in time and space, which we define as $(x,y,z) = (0,0,0)$. As we will show below, the only required contribution to E is $\varepsilon_y(y)$ which we are able to derive from $S_{\mathrm{II}}(x,y)$ in the calibration measurement from static background gas.

To calibrate each species, we leaked H_2 and D_2, individually into the scattering chamber and recorded the pressure reading from a calibrated ion gauge. For the calibration of the ion imaging detector we used species-specific pressures between 2×10^{-7} and 1×10^{-6} mbar. This procedure avoided problems that can occur using an MCP detector when the pressure in the chamber is too high, while providing enough sample to allow us to accumulate signal with the reduced laser power that is required to prevent space charge during density measurement of the

molecular beam. We ensure that neither the MCP detector nor the CCD camera was saturated in the calibration process.

We verified that there are negligible pressure gradients between the ion gauge and the detection position through a simulation of the spatial profile of the static gas pressure in our apparatus during admission of gas from the leak value and active pumping of the chamber[27]. The molecular density in a static gas is uniform, allowing the following approximation to describe the number of ionized molecules:

$$N_{\mathrm{ion}}^{\mathrm{BG}} = D^{\mathrm{BG}} \int \varepsilon_x(x)\mathrm{d}x \int \varepsilon_y(y)\mathrm{d}y \int \varepsilon_z(z)\mathrm{d}z. \tag{S9}$$

Here D^{BG} is the background gas density obtained from the calibrated ion gauge pressure with help of the ideal gas law.

Fig. S3 shows an ion image from the calibrated pressure of H_2 background gas $S_{\mathrm{II}}^{\mathrm{BG}}(x,y)$. One dimensional projections of the ion image $h_x^{\mathrm{BG}}(x)$ and $h_y^{\mathrm{BG}}(y)$ are also shown and defined as follows.

$$h_x^{\mathrm{BG}}(x) = \int S_{\mathrm{II}}^{\mathrm{BG}}(x,y)\mathrm{d}y, \tag{S10}$$

$$h_y^{\mathrm{BG}}(y) = \int S_{\mathrm{II}}^{\mathrm{BG}}(x,y)\mathrm{d}x. \tag{S11}$$

The shape of ion image is given by the spatial dependence of the ionization efficiencies $\varepsilon_x(x)\varepsilon_y(y)$ together with the background gas's Maxwell-Boltzmann velocities, which modifies the shape of the packet of laser ionized molecules as it travels to the detector. The spreading function $s^{\mathrm{BG}}(x,y)$ is given by:

$$s^{\mathrm{BG}}(x,y) = N \exp\left(-\frac{m(x-x_0)^2}{2k_{\mathrm{B}}Tt_{\mathrm{TOF}}^2}\right)\exp\left(-\frac{m(y-y_0)^2}{2k_{\mathrm{B}}Tt_{\mathrm{TOF}}^2}\right) \equiv N\, s_x^{\mathrm{BG}}(x)s_y^{\mathrm{BG}}(y) \tag{S12}$$

where N is a normalization factor and m is the molecule mass. Notice that we convert the velocity distribution to a spatial distribution using the ion's time of flight to the MCP detector t_{TOF}. Furthermore, we note that $s^{\mathrm{BG}}(x,y)$ is separable.

We next examine the measured $h_x^{\mathrm{BG}}(x)$, which we find can be well represented by $s_x^{\mathrm{BG}}(x)$ if T is set to 295 K—see blue line of Fig. S3. From this we confirm that $\varepsilon_x(x)$ possesses a negligible width (< 100 μm). We also note that the size of the individual ion events appearing on the ion camera (FWHM≈ 0.2 mm) can be neglected in this analysis. We next obtain $\varepsilon_y(y)$, which we approximate by a flattop Gaussian, by fitting the convolution $\varepsilon_y(y) \otimes s_y^{\mathrm{BG}}(y)$ to $h_y^{\mathrm{BG}}(y)$–see Fig. S3. The resulting $\varepsilon_y(y)$ is shown in Fig. S4.

In Fig. S5 we show the ion image for H_2 obtained at the maximum of the molecular beam's density profile found by adjusting the delay between the laser and molecular beam pulses, t_{BLD}. The molecular beam propagation axis is indicated by the dashed white line in the image, and is incident 30° with respect to the surface normal. Since the molecular beam passes through a skimmer and an orifice, we assume that velocities perpendicular to molecular beams propagation axis are negligible and thus spatial broadening of the ion image $s^{\mathrm{MB}}(x,y)$ can be neglected. The ion signal of the molecular beam is displaced from the image center, defined at the position of the laser focus,

due to translation of the molecular beam towards the surface. The mean speed of the molecular beam at each t_{BLD} is determined from the center position of the flat-top Gaussian fits—$x_0(t_{\mathrm{BLD}})$ and $y_0(t_{\mathrm{BLD}})$—to the histograms $h_x^{\mathrm{MB}}(x)$ and $h_y^{\mathrm{MB}}(y)$ (see Fig. S5) by:

$$\langle v\rangle_{\mathrm{MB}}(t_{\mathrm{BLD}}) = \sqrt{\left(\frac{x_0(t_{\mathrm{BLD}})}{t_{\mathrm{TOF}}}\right)^2 + \left(\frac{y_0(t_{\mathrm{BLD}})}{t_{\mathrm{TOF}}}\right)^2}. \tag{S13}$$

We notice hereby that $h_y^{\mathrm{MB}}(y)$ does not *a priori* represent the y-axis slice through the cross-section of the molecular beam. This is because non-resonant multiphoton ionization is most efficient at the waist of the laser focus, i.e. at $y = 0$, falling off rapidly in all directions away from this position. The observed $h_y^{\mathrm{MB}}(y)$ thus reflects $\delta_y^{\mathrm{MB}}(y)\ \varepsilon_y(y)$, where $\delta_y^{\mathrm{MB}}(y)$ represents its density profile that we aim to determine. We determine the shape of $\delta_y^{\mathrm{MB}}(y)$ from a measurement similar to that depicted in Fig. S5, where we accumulate the ion image while the position of the laser focus is translated slowly from -5 to $+5$ mm along the y-axis with constant speed. We make sure that no ions are observed at -5 and $+5$ mm. The translation of the laser focus, while accumulating the ion image, makes the ionization efficiency homogeneous along y, allowing us to map-out $\delta_y^{\mathrm{MB}}(y)$ of the molecular beam directly (see Fig. S4).

The number of ionized molecules from the molecular beam is given by:

$$N_{\mathrm{ion}}^{\mathrm{MB}} = \int \delta_x^{\mathrm{MB}}(x)\ \varepsilon_x(x)\mathrm{d}x \int \delta_y^{\mathrm{MB}}(y)\ \varepsilon_y(y)\mathrm{d}y \int \delta_z^{\mathrm{MB}}(z)\ \varepsilon_z(z)\mathrm{d}z. \tag{S14}$$

Next, we determine the absolute number of molecules in the beam using the results from Fig. S3 and S5. Consider the ratio of the ionized molecules in the beam and in the background gas:

$$\begin{aligned}\frac{N_{\mathrm{ion}}^{\mathrm{MB}}}{N_{\mathrm{ion}}^{\mathrm{BG}}} &= \frac{\int \delta_x^{\mathrm{MB}}(x)\ \varepsilon_x(x)\mathrm{d}x \int \delta_y^{\mathrm{MB}}(y)\ \varepsilon_y(y)\mathrm{d}y \int \delta_z^{\mathrm{MB}}(z)\ \varepsilon_z(z)\mathrm{d}z}{D^{\mathrm{BG}} \int\ \varepsilon_x(x)\mathrm{d}x \int \varepsilon_y(y)\mathrm{d}y \int\ \varepsilon_z(z)\mathrm{d}z} \\ &\equiv \frac{\iint S_{\mathrm{II}}^{\mathrm{MB}}(x,y)\mathrm{d}x\mathrm{d}y}{\iint S_{\mathrm{II}}^{\mathrm{BG}}(x,y)\mathrm{d}x\mathrm{d}y}.\end{aligned} \tag{S15}$$

Due to the tight laser focus, the integrals over x and z can be simplified, which results in:

$$\frac{N_{\mathrm{ion}}^{\mathrm{MB}}}{N_{\mathrm{ion}}^{\mathrm{BG}}} = \frac{\delta_x^{\mathrm{MB}}(0)\ \varepsilon_x(0)\ \Delta x}{\varepsilon_x(0)\ \Delta x}\ \frac{\delta_z^{\mathrm{MB}}(0)\ \varepsilon_z(0)\ \Delta z}{\varepsilon_z(0)\ \Delta z}\ \frac{\int \delta_y^{\mathrm{MB}}(y)\ \varepsilon_y(y)\mathrm{d}y}{D^{\mathrm{BG}} \int \varepsilon_y(y)\mathrm{d}y}, \tag{S16}$$

or after cancelation and removing $\delta_y^{\mathrm{MB}}(0)$ from the integral over y, we obtain:

$$\frac{N_{\mathrm{ion}}^{\mathrm{MB}}}{N_{\mathrm{ion}}^{\mathrm{BG}}} = \frac{\delta_x^{\mathrm{MB}}(0)\ \delta_y^{\mathrm{MB}}(0)\delta_z^{\mathrm{MB}}(0) \int \frac{\delta_y^{\mathrm{MB}}(y)}{\delta_y^{\mathrm{MB}}(0)}\ \varepsilon_y(y)\mathrm{d}y}{D^{\mathrm{BG}} \int \varepsilon_y(y)\mathrm{d}y}, \tag{S17}$$

We note that $\delta_x^{\mathrm{MB}}(0)\ \delta_y^{\mathrm{MB}}(0)\delta_z^{\mathrm{MB}}(0) = D^{\mathrm{MB}}(0,0,0)$, which is the peak molecular beam density—the target of this analysis. We re-arrange Eq. S17, replacing D^{BG} by the density expression from the ideal gas law, to obtain an expression for $D^{\mathrm{MB}}(0,0,0)$

$$D^{\mathrm{MB}}(0,0,0) = \frac{p}{k_{\mathrm{B}}T} \frac{\int \varepsilon_y(y)\mathrm{d}y}{\int \frac{\delta_y^{\mathrm{MB}}(y)}{\delta_y^{\mathrm{MB}}(0)}\, \varepsilon_y(y)\mathrm{d}y} \frac{\iint S_{\mathrm{II}}^{\mathrm{MB}}(x,y)\mathrm{d}x\mathrm{d}y}{\iint S_{\mathrm{II}}^{\mathrm{BG}}(x,y)\mathrm{d}x\mathrm{d}y}. \tag{S18}$$

All contributions on the right hand side of this equation are derived from experiment. We notice that the x-axis can be equivalently converted to the t-axis (beam-laser delay) for convenience. The flux is given by multiplying the density by the speed of the beam. The adsorbing flux of H_2 (and D_2) must also be multiplied by the sticking coefficient $S(E)$ at the kinetic energy, E, of the particle at t. The instantaneous adsorbing flux at $(y,z) = (0,0)$ is then given by:

$$F^{\mathrm{MB}}(t,0,0) = S\left(\frac{m\langle v\rangle_{\mathrm{MB}}^2(t)}{2}\right) \langle v\rangle_{\mathrm{MB}}(t)\, D^{\mathrm{MB}}(0,0,0)\, \tilde{\delta}_t^{\mathrm{MB}}(t), \tag{S19}$$

where $\tilde{\delta}_t^{\mathrm{MB}}(t)$ is the peak normalized density profile vs. beam-laser delay time. Approximating the projection of the molecular beam at the yz-plane to be radially symmetric, we can express the total number of adsorbing molecules as:

$$N_{\mathrm{ads}}^{\mathrm{MB}} = 2\pi D^{\mathrm{MB}}(0,0,0) \int S\left(\frac{m\langle v\rangle_{\mathrm{MB}}^2(t)}{2}\right) \langle v\rangle_{\mathrm{MB}}(t)\ \tilde{\delta}_t^{\mathrm{MB}}(t)\mathrm{d}t \int_0^\infty r\tilde{\delta}_r^{\mathrm{MB}}(r)\ \mathrm{d}r \tag{S20}$$

Where $\tilde{\delta}_r^{\mathrm{MB}}(r)$ is the peak-normalized radial distribution function of molecular beam density, which we determine from $\delta_y^{\mathrm{MB}}(y)$.

We note that the laser crosses the molecular beam at 60°—strictly speaking this prevents the approximation of radial symmetry. More specifically $\delta_y^{\mathrm{MB}}(y)$ overestimates the width of the radial projection (perpendicular to beam propagation axis) by 15.5%. We compensate this artificially introduced error, by assuming radial symmetry and scaling down the width of measured $\delta_y^{\mathrm{MB}}(y)$ by 7.5%. This allows us to ensure determination of the correct number of particles in the beam, while making a simplifying approximation regarding its shape.

We show illustrative examples of the molecular beam flux projected onto the yz plane and compare it with the approximated shape of the molecular beam in the present analysis – see Fig. S4. The results of the calibration procedure are shown in Fig. S6.

S3. DETERMINATION OF INCIDENT BEAM STICKING COEFFICIENT

We use the sticking coefficient of molecular hydrogen measured from Luntz *et al.[25]* (and confirmed by many others[23, 28]) for Pt(111) and Juurlink and coworkers [22, 24] for stepped Pt surfaces. We fitted the sticking coefficients from Luntz *et al.* to an error-function as used in Ref. [29] and as shown in Fig. S7. We use normal energy scaling to account for the incidence angle dependence of the sticking coefficient, consistent with previous measurements at 30° incidence angle, required to estimate the sticking from our incident molecular beam.

Measurements of absolute sticking coefficients on Pt(332) do not exist, however Juurlink and coworkers measured the sticking coefficients at Pt(557), which have the same step density as Pt(332) with a different step type. To correct for step type, we use previous measurements of the effect of the step type on the sticking coefficients on curved Pt(111) single crystals[22] as a function of step density. We use the relative differences of sticking coefficients obtained at A- and B-type steps (see Fig. 2f of Ref. [22]) to scale the sticking coefficients from Pt(557) accordingly (Ref. [24]). This yields the black squares of Fig. S7. In order to use the sticking probabilities to determine TS re-crossing, we require a reasonable model function fit to the two squares of Fig. 7 that represent sticking at Pt(332). Juurlink and coworkers developed a $S(E)$ sticking coefficient model for H_2 at Pt accurately reproducing the step-density dependence of the crystal. In agreement with theoretical work[30, 31], they introduced three contributions to $S(E)$: indirect nonactivated at steps ($A\exp(-\alpha E)$), direct nonactivated at steps (B) and direct activated at terraces ($C\,E$). The additive contribution of the three functions yields the following formula:

$$S(E) = A\exp(-\alpha E) + B + C\,E \qquad \text{(S21)}$$

with A, B, C and α as fitting coefficients. We use this model to refit the Pt(557) data (from Fig. 8 of Ref. [24]), which provides a set of four fitting parameters. It was recently found that the same model applies also to sticking coefficients for Pt surfaces with B-type steps[32]. The parameter C reflects the sticking efficiency at the terrace and A reflects the probability of trapping into the molecular binding well of H_2 located at the steps. Both parameters are sensitive to the geometry at the surface i.e. step density. The parameter α is sensitive to the well depth of the molecular binding state of H_2 at steps, while B reflects the efficiency of H_2 to react by direct impact with the step. Both parameters depend on the nature of the active sites present at steps. We assume that the parameters C and A are the same for Pt(557) and Pt(332) because the step density of the two crystals is equal. Since the reactivity of the A- and B-type steps is different we fit parameter α and B to the Pt(332) sticking coefficients and obtain the black line of Fig. S7.

As we have done for Pt(111), we also assume normal energy scaling here to obtain the sticking probability of our beam. Our estimated sticking coefficient at 30° incidence angle on Pt(332) is consistent with observations made earlier on other stepped surface[33] and is shown as black dashed line in Fig. S7. There is no isotope effect found for sticking coefficient of molecular hydrogen on Pt(111) and stepped Pt surfaces[24, 25].

We combine the incident molecular beam sticking probabilities with the results of our absolute flux determinations to arrive at initial H and D atom concentrations on the Pt surfaces.

S4. DETERMINATION OF THE H_2 BINDING ENERGY AT PT(111) AND PT(332) IN THE ZERO COVERAGE LIMIT

The isosteric heats of H_2 adsorption at Pt(111) were previously measured with Ar^+-ion Low Energy Recoil Scattering[34] and Thermal Energy Helium Scattering[35]. These techniques are most sensitive to majority sites on the Pt(111) surface and can thus be seen as a selective probe for terrace binding energies, despite the presence of defects. This is the reason why we restrict ourselves to these reports.

For the use in our TST rate model we require the isosteric heats of adsorption at 0 K. The average energy, $\langle E \rangle(T)$, reflects the sum of microstate energies weighted by their population probabilities at a particular temperature. This property can be derived from the partition function, Q, to be:

$$\langle E \rangle(T) = k_\mathrm{B} T^2 \frac{\partial \ln(Q)}{\partial T} \tag{S22}$$

To obtain the isosteric heat of H_2 adsorption at 0 K we apply the following formula:

$$H_\theta(0\ K) = H_\theta\left(T_\mathrm{exp}\right) - k_\mathrm{B} T_\mathrm{exp} - \langle E \rangle_{\mathrm{H_{2(g)}}}\left(T_\mathrm{exp}\right) + 2\langle E \rangle_{\mathrm{H^*}}\left(T_\mathrm{exp}\right) \equiv E_0^{\mathrm{HH}} \tag{S23}$$

where T_exp is the temperature at which the heat of adsorption is measured and $H_\theta(0\ K)$ is identical to the H_2 binding energy (E_0^{HH}) that is used for TST modelling. The $k_\mathrm{B}T$ accounts for H_2's enthalpy to inner energy conversion. The partition functions for H_2 and H* are introduced in the next section. The results of Ar^+-ion and He scattering works from Pt(111) are corrected by the temperature dependent terms from Eq. S23, are shown as dots and crosses of Fig. S8. To obtain the coverage dependence of the adsorption energies we use the following function:

$$H_\theta(0\ K) = A\left(\mathrm{erfc}\left(\frac{\theta - \theta_0}{\sigma}\right) + 1\right) + B \tag{S24}$$

with erfc as the complementary error function and A, B, σ and θ_0 as fitting parameters to determine the zero-coverage binding energy of H_2 at Pt(111) ($H_0(0\ K)$)—see grey line of Fig. S8. The extracted value—0.75 ± 0.03 eV—is corrected by the ZPE yielding D_e and used for estimation of the HD and D_2 binding energy in the modeling of the rate constant.

The binding energy of H_2 at Pt(332) has not been measured previously. However the binding energy difference between B-type steps—present at Pt(332)—and (111) terraces was found to be 0.18 eV from low energy ion scattering experiments[34]. This is consistent with the DFT predicted binding energy difference for H* between steps and terraces on Pt(332). We determine it by solving the nuclear Schrödinger Equation for H* at Pt(332) and inspecting the probability distribution of H*. The ground state is located at the steps and the first eigenstate that is localized at the terrace site is 0.092 eV higher (corresponds to 0.184 eV per molecule). Note that this procedure already includes the ZPE correction. DFT calculations and experiments are consistent, such that we use a binding energy of 0.93 ± 0.03 eV for H_2 at Pt(332) for the TST rate constant.

S5. MODELING OF THE RECOMBINATION RATE CONSTANTS

The rate constants for H* and D* recombination on Pt(111) are described within the framework of exact thermal rates using Transition State Theory (TST). The general formula is given by:

$$k_{\mathrm{XY}}(T) = \kappa(T) \times k_{\mathrm{TST}}(T)$$
$$= \langle S \rangle(T) \times \frac{k_{\mathrm{B}}T}{h} \frac{Q^{\neq}_{\mathrm{XY}}}{Q^{\mathrm{X}}Q^{\mathrm{Y}}} \frac{A_{\mathrm{X}}A_{\mathrm{Y}}}{A^{\neq}_{\mathrm{XY}}} \exp\left(-\frac{E_0^{\mathrm{XY}}}{k_{\mathrm{B}}T}\right). \quad \text{(S25)}$$

Here, X and Y can be H or D. $\kappa(T)$ is the re-crossing correction. Notice that for 2nd order rate constants the partition functions are divided by the corresponding reference area from which they are derived. This means that e.g., if the SE is solved for the Pt(111) unit cell, the corresponding partition function is divided by the area of the unit cell. This is required so that k_{XY} will be expressed in the correct units. $\langle S \rangle(T)$ is the thermally averaged sticking coefficient, which corrects for TS re-crossing—see main text. It was earlier found to be isotopologue independent[24, 25]. The classical TST expression involves partition functions for the TS, $Q^{\neq}_{\mathrm{XY}}$, and reactants, $Q^{\mathrm{X}}Q^{\mathrm{Y}}$, as well as an exponential energy term with the energy of the TS, E_0^{XY} [36, 37]. We note that for our choice of TS, E_0^{XY} is the Zero-Point-Energy (ZPE) corrected hydrogen chemisorption energy. We next explain how each piece of this formula is implemented.

a) Modeling the TS partition function and ZPE correction for E_0^{XY}

We have chosen the TS for hydrogen recombination to be gas-phase molecular hydrogen at infinite separation from the surface. With this choice the TS partition function is given by:

$$Q^{\neq}_{\mathrm{AB}} = q^{\neq}_{\mathrm{tr}} q^{\neq}_{\mathrm{rot}} q^{\neq}_{\mathrm{vib}}. \quad \text{(S26)}$$

Here $q^{\neq}_{\mathrm{tr}}$ is the translational partition function for an ideal 2D-gas given by:

$$q^{\neq}_{\mathrm{tr}} = \frac{2\pi m k_{\mathrm{B}}T}{h^2} A \ . \quad \text{(S27)}$$

With T as the temperature, A as the reference area and m as the mass of the hydrogen molecule or its isotopologue. The "missing translational degree of freedom" is along the reaction coordinate and does not appear in the partition functions. The rotational partition function is given by:

$$q^{\neq}_{\mathrm{rot}} = \frac{k_B T}{\sigma_{\mathrm{XY}} B_{\mathrm{XY}}}. \quad \text{(S28)}$$

With B as the rotational constant and σ_{XY} as the symmetry number of the hydrogen isotopologue XY. This partition function is accurate above 300 K, with a maximum deviation of 10%, for all temperatures relevant for the kinetics studies. To account for the temperature dependence of the isosteric heats of adsorption (150-300 K) for H_2 we use its explicit rotational partition function, given by:

$$q^{\mathrm{expl}}_{\mathrm{rot}} = \frac{1}{4}\left(\sum_{J\,\mathrm{even}} (2J+1) \exp\left(-\frac{B_{\mathrm{HH}} J(J+1)}{k_B T}\right) + 3 \sum_{J\,\mathrm{odd}} (2J+1) \exp\left(-\frac{B_{\mathrm{HH}} J(J+1)}{k_B T}\right)\right). \quad \text{(S29)}$$

The vibrational partition function is given by the harmonic oscillator partition function:

$$q^{\neq}_{\mathrm{vib}} = \frac{1}{1 - \exp\left(-\frac{h\nu_{\mathrm{XY}}}{k_{\mathrm{B}}T}\right)}. \tag{S30}$$

With ν_{XY} as the stretch frequency of the XY hydrogen isotopologue. We also account for the ZPE correction in the TST rate expression following:

$$E_0^{\mathrm{XY}} = D_e - \mathrm{ZPE}_{\mathrm{X}^*} - \mathrm{ZPE}_{\mathrm{Y}^*} + \mathrm{ZPE}_{\mathrm{XY}}. \tag{S31}$$

Here D_e is the classical isotope independent binding energy, $\mathrm{ZPE}_{\mathrm{XY}}$ is the ZPE of the hydrogen isotopologue in the gas phase and depends on its vibrational frequency. The $\mathrm{ZPE}_{\mathrm{X}^*}$ and $\mathrm{ZPE}_{\mathrm{Y}^*}$ are the ZPE corrections for the two adsorbed H-atoms. It includes contributions from the z-stretch frequency of the atom at the most stable binding site and the ground state of the in-plane (xy) energy levels derived from the Schrödinger equation.

b) Transition State (TS) re-crossing correction

The sticking coefficients of H_2 on Pt(111) are experimentally well known and thus we use them directly to account for re-crossing in the desorption rate. The sticking coefficients for Pt(332) are estimated based on previous experiments and the model of Juurlink and coworkers (see Section S3). Despite the measurement of the relative desorption flux along the surface normal we are sensitive to the lifetime of H* and D* on the surface, which is determined by recombinative desorption at all angles. Thus, the re-crossing correction has to be equal to the angle and thermal energy weighted sticking coefficient. To obtain this we follow the procedure described in Ref. [38] which is only recapitulated here for completeness.

We assume normal energy scaling, $E_\perp = E\cos^2(\theta)$, and use the experimental sticking coefficients obtained at normal incidence, $S(E_\perp, 0°)$ (grey and black solid line of Fig. S7, left panel for Pt(111) and Pt(332), respectively), to determine the thermal sticking coefficient $\langle S\rangle(T)$ from:

$$\langle S\rangle(T) = \frac{\int_0^{\frac{\pi}{2}}\int_0^{\infty} S(E_\perp, 0°)\, F\left(\frac{E_\perp}{\cos^2(\theta)}, T\right) \mathrm{d}E_\perp \sin(\theta)\, \mathrm{d}\theta}{\int_0^{\frac{\pi}{2}}\int_0^{\infty} F\left(\frac{E_\perp}{\cos^2(\theta)}, T\right) \mathrm{d}E_\perp \sin(\theta)\, \mathrm{d}\theta}. \tag{S32}$$

Here $E_\perp$ is the normal kinetic energy and $F(E,T)$ is the thermal Maxwell-Boltzmann distribution of flux. The corresponding thermal sticking coefficients are shown in Fig. S7, right panel.

We note that we assume cylindrical symmetry in the analysis, which is a good approximation for Pt(111). For Pt(332) the sticking coefficient has been observed to be anisotropic with the polar angle φ [39]. We think that our approximation remains accurate (within ~15%) as i) the anisotropies are restricted to a narrow azimuthal angle range θ and ii) the anisotropies will likely cancel out from the integration over all angles—see Fig. 1 of Ref. [39].

We note in passing that neglect of TS re-crossing introduces an error of factor of ~3 on Pt(332) and factor of 4-10 on Pt(111). However, we also note that this error is specific to our choice of the TS.

c) Modeling the H*(D*) partition function at Pt(111) and Pt(332)

We have employed three different approaches to model the partition function for adsorbed hydrogen atoms. In the Harmonic Approximation (HA), atoms are described using the vibrational partition function of an immobilized adsorbate. This approach assumes that the atom X is fixed to its binding site for which the partition function is given by:

$$Q^{\mathrm{X}}_{\mathrm{HA}} = q^{\mathrm{X}}_{\mathrm{vib},x} q^{\mathrm{X}}_{\mathrm{vib},y} q^{\mathrm{X}}_{\mathrm{vib},z}, \tag{S33}$$

where $q^{\mathrm{X}}_{\mathrm{vib},i}$ is the partition function of the harmonic oscillator for three frequencies derived from the most stable binding site of the atom X. This approach works best at low temperatures where adsorbates tend to be localized.

In the second approach often referred to as Complete Potential Energy Surface Sampling (CPES)[40, 41], we obtain the classical partition function from the configuration integral

$$q^{\mathrm{X}}_{\mathrm{CPES},xy} = \frac{2\pi m_{\mathrm{X}} k_{\mathrm{B}} T}{h^2} A \int_0^1 \int_0^1 \exp\left(-\frac{V_z^{\mathrm{X}}(x,y)}{k_B T}\right) \mathrm{d}x\mathrm{d}y \tag{S34}$$

employing a two dimensional in-plane PES $V_z^{\mathrm{X}}(x,y)$ that we obtain from DFT. Note that $V_z^{\mathrm{X}}(x,y)$ is corrected to account for the ZPE associated with the X-Pt stretch vibration. Note that, as defined, the configuration integral is unit-less. CPES is considered to work well at high temperatures where the adsorbate is able to explore the whole surface. For the total CPES partition function we include the stretching vibration partition function, $q^{\mathrm{X}}_{\mathrm{vib},z}$, at the most stable binding site to account for hydrogens atom motion along the z-axis. The total CPES partition function is then given as:

$$Q^{\mathrm{X}}_{\mathrm{CPES}} = q^{\mathrm{X}}_{\mathrm{CPES},xy}\, q^{\mathrm{X}}_{\mathrm{vib},z} \tag{S35}$$

In the third approach called Quantum Potential Energy Sampling, QPES, we employ $V_z^{\mathrm{X}}(x,y)$ to solve the nuclear Schrödinger Equation (SE) for H*(D*) on either Pt(111) or Pt(332), see Eq. S1. We solve the SE to obtain the eigenenergies, from which we construct the in-plane partition function. The detailed procedure to solve the SE is explained in Section S1b. Since the stretching frequencies of H*(D*) are high, we solve the Schrödinger Equation in 2D, restricted to the surface plane, by making use of the vibrationally adiabatic approximation. In this way, we obtain the in-plane partition function by explicit summation over the eigenstates, with the energy E_i, as:

$$q^{\mathrm{X}}_{\mathrm{QPES},xy} = \sum_{i}^{E_i \leq 1\ \mathrm{eV}} \exp\left(-\frac{E_i - E_0}{k_B T}\right). \tag{S36}$$

We utilize the partition function for stretch vibrations as for the HA and CPES approach and obtain the total quantum mechanical partition function as follows:

$$Q^{\mathrm{X}}_{\mathrm{QPES}} = q^{\mathrm{X}}_{\mathrm{QPES},xy}\, q^{\mathrm{X}}_{\mathrm{vib},z} \tag{S37}$$

We also include the electronic partition function for H atoms at Pt to account for their electron spin states.

$$Q^{\mathrm{X}}_{\mathrm{el}} = 2 \tag{S38}$$

We note that the spin degeneracy, which has often been ignored in past applications of TST to surface reactions, must be included to account for the full state count of adsorbed H atoms. It appears that there may be some confusion in the community about this point, perhaps due to the fact that TST applications in many gas phase reactions are carried out assuming a transition state that conserves spin with the reactant and product. However, for example the calculation of the equilibrium constant for the dissociation of H_2 in gas phase to form two H atoms ignoring the spin degeneracy of the atoms would result in erroneous results. It should be clear that dissociation of H_2 to form two uncoupled H atoms on a metal surface is not different.

The TST recombination rate constant with quantum corrections thus becomes:

$$k_{\mathrm{XY}}^{\mathrm{QPES}}(T) = \langle S \rangle(T) \times \frac{k_{\mathrm{B}}T}{h} \frac{Q_{\mathrm{XY}}^{\neq}}{Q_{\mathrm{QPES}}^{\mathrm{X}} Q_{\mathrm{el}}^{\mathrm{X}} Q_{\mathrm{QPES}}^{\mathrm{Y}} Q_{\mathrm{el}}^{\mathrm{Y}}} \frac{A_X A_Y}{A_{\mathrm{XY}}^{\neq}} \exp\left(-\frac{E_0^{\mathrm{XY}}}{k_{\mathrm{B}}T}\right) \qquad \text{(S39)}$$

where A indicates the reference area in which the corresponding in-plane partition function is defined. The recombination rates (Fig. 1) and the corresponding recombination rate constants (Fig. 2 and Fig. 3) using this expression are shown in the main text. We emphasize that this approach converges in the limit of low temperatures to the HA-TST approach and in the limit of high temperatures to results of the CPES-TST approach, exactly as expected – see Fig. 5(b) of the main text.

d) Modeling the recombination rate with 2D collision theory (2DCT)

Earlier work found that recombination rate constants for hydrogen on metals are close to values expected from 2DCT[42]. Here we also test this simplistic model, where rate expression is determined by:

$$k_{\mathrm{XY}}^{\mathrm{2DCT}}(T) = \langle S \rangle(T) \frac{r_{\mathrm{XY}}}{\sigma_{\mathrm{XY}}} \sqrt{\frac{2\pi k_{\mathrm{B}}T}{\mu_{\mathrm{XY}}}} \exp\left(-\frac{E_0^{\mathrm{XY}}}{k_{\mathrm{B}}T}\right) \qquad \text{(S40)}$$

where μ_{XY} is the reduced mass of colliding particles X and Y, σ_{XY} is the symmetry number of the product hydrogen molecule—correcting for the double counting of collisions—and r_{XY} its equilibrium distance—0.74 Å. Since the 2DCT can be derived from the TST rate expression—using the simplifying assumptions of free translating particles and 1D rotation of the TS—we also include the re-crossing correction, $\langle S \rangle(T)$, for a fair comparison with the other TST rate constant models. See Fig. 5(b) in the main text.

S6. SIMULATION OF KINETIC TRACES AND ISOTOPIC BRANCHING FRACTIONS

Fig. S6 shows the radial profile of time integrated dose of H_2 delivered by each molecular beam pulse—the inset shows the pulsed beam's temporal distribution. These quantities are taken explicitly into account in the modeling of the observed kinetic trace, in the form of time and space dependent dosing functions, $f(t,r)$. We solve the rate equations below in a grid of 300 radially symmetric regions within radial distance of up to 3 mm from the center of the dosing pulse.

$$\frac{\mathrm{d}[\mathrm{H}^*]_{t,r}}{\mathrm{d}t} = D_{\mathrm{H}^*}\Delta_r[\mathrm{H}^*]_{t,r} + 2\langle S\rangle f_{\mathrm{H}_2}(t,r) - 2k_{\mathrm{HH}}[\mathrm{H}^*]_{t,r}^2 - k_{\mathrm{HD}}[\mathrm{H}^*]_{t,r}[\mathrm{D}^*]_{t,r} \quad \text{(S41)}$$

$$\frac{\mathrm{d}[\mathrm{D}^*]_{t,r}}{\mathrm{d}t} = D_{\mathrm{D}^*}\Delta_r[\mathrm{D}^*]_{t,r} + 2\langle S\rangle f_{\mathrm{D}_2}(t,r) - 2k_{\mathrm{DD}}[\mathrm{D}^*]_{t,r}^2 - k_{\mathrm{HD}}[\mathrm{H}^*]_{t,r}[\mathrm{D}^*]_{t,r} \quad \text{(S42)}$$

$$\frac{\mathrm{d}[\mathrm{H}_2]_{t,r}}{\mathrm{d}t} = k_{\mathrm{HH}}[\mathrm{H}^*]_{t,r}^2 \quad \text{(S43)}$$

$$\frac{\mathrm{d}[\mathrm{D}_2]_{t,r}}{\mathrm{d}t} = k_{\mathrm{DD}}[\mathrm{D}^*]_{t,r}^2 \quad \text{(S44)}$$

$$\frac{\mathrm{d}[\mathrm{HD}]_{t,r}}{\mathrm{d}t} = k_{\mathrm{HD}}[\mathrm{H}^*]_{t,r}[\mathrm{D}^*]_{t,r} \quad \text{(S45)}$$

The rate constants, k_{HH}, k_{HD} and k_{DD} are derived from the QPES-TST model. The isotope effect predicted by QPES-TST is shown in Fig. S9 for reactions on both Pt(111) and Pt(332) as a function of temperature. The symbol Δ_r indicates the Laplacian. In solving Eqs. S41-S45, diffusion coefficients D_{H^*} and D_{D^*} are obtained from Ref. [43]. The rate equations were solved numerically using LSODA method from the Fortran ODEPACK library implemented in the *scipy.integrate.solve_ivp* function in Python[44]. Further details on the modeling process can be found in Ref. [6].

The product formation rate is found by averaging over the spatial coordinates—Eq. S46 shows this for HD formation:

$$F^{\mathrm{HD}}(t) \equiv \frac{\mathrm{d}[\mathrm{HD}]_t}{\mathrm{d}t} = \frac{\int_0^{3\ \mathrm{mm}} \frac{\mathrm{d}[\mathrm{HD}]_{t,r}}{\mathrm{d}t} r\mathrm{d}r}{\int_0^{3\ \mathrm{mm}} r\mathrm{d}r} \quad \text{(S46)}$$

F_t^{HD} denotes the HD flux as a function of reaction time – shown as black and grey lines of Fig. 1 in the main text.

The yield, Y, of each isotope

$$Y^{\mathrm{HD}} = \int F_t^{\mathrm{HD}}\,\mathrm{d}t\,; \quad \text{(S47)}$$

$$Y^{\mathrm{H_2}} = \int F_t^{\mathrm{H_2}}\,\mathrm{d}t\,; \quad \text{(S48)}$$

$$Y^{\mathrm{D_2}} = \int F_t^{\mathrm{D_2}}\,\mathrm{d}t. \quad \text{(S49)}$$

is defined as the time integral of the product flux. The branching fraction is obtained from Eqs. S50-S52.

$$X_{\mathrm{QPES}}^{\mathrm{HD}} = \frac{Y^{\mathrm{HD}}}{Y^{\mathrm{H_2}} + Y^{\mathrm{HD}} + Y^{\mathrm{D_2}}}\ ; \tag{S50}$$

$$X_{\mathrm{QPES}}^{\mathrm{H_2}} = \frac{Y^{\mathrm{H_2}}}{Y^{\mathrm{H_2}} + Y^{\mathrm{HD}} + Y^{\mathrm{D_2}}}; \tag{S51}$$

$$X_{\mathrm{QPES}}^{\mathrm{D_2}} = \frac{Y^{\mathrm{D_2}}}{Y^{\mathrm{H_2}} + Y^{\mathrm{HD}} + Y^{\mathrm{D_2}}}. \tag{S52}$$

The QPES predicted isotopic branching ratios are shown as lines in Fig. S10.

S7. EXPERIMENTAL DETERMINATION OF ISOTOPIC BRANCHING FRACTION

The experimentally derived isotopic branching fractions, $X_{\mathrm{exp}}^{\mathrm{H_2}}$, $X_{\mathrm{exp}}^{\mathrm{HD}}$ and $X_{\mathrm{exp}}^{\mathrm{D_2}}$, are determined from measured kinetic traces at $m/z = 2, 3$ and 4. While the kinetic trace for HD reflects only reactive scattering (RS), the traces for H_2 and D_2 include contributions from both DS and RS. Furthermore, the RS contributions to $m/z = 2$ and 4 signals are rather small in comparison to DS. Fortunately, DS is most important near time-zero and it is insensitive to surface temperature; hence, RS can be distinguished from DS by its temperature and time dependence. The RS component seen at $m/z = 2$ and 4 is similar in shape to that of $m/z = 3$. This allows us to perform a simple fitting using DS and RS components applied to data obtained at $m/z = 2$ and 4.

$$h_{\mathrm{HD}}(t) = RS(t); \tag{S53}$$

$$h_{\mathrm{H_2}}(t) = A_{\mathrm{H_2}} \times DS_{\mathrm{H_2}}(t) + B_{\mathrm{H_2}} \times RS(t); \tag{S54}$$

$$h_{\mathrm{D_2}}(t) = A_{\mathrm{D_2}} \times DS_{\mathrm{D_2}}(t) + B_{\mathrm{D_2}} \times RS(t). \tag{S55}$$

Here, $RS(t)$ is derived from the analysis of the HD kinetic trace—only the parameter $B_{\mathrm{H_2}}(B_{\mathrm{D_2}})$ was optimized to the $m/z = 2(4)$ kinetic trace—furthermore, $B_{\mathrm{H_2}}(B_{\mathrm{D_2}})$ provides the ratio of H_2 (D_2) to HD. $DS_{\mathrm{H_2}}(t)$ and $DS_{\mathrm{D_2}}(t)$ are obtained experimentally using scattering data obtained close to the specular scattering angle, where DS dominates.

The experimental isotopic branching fraction is then found with help from Eqs. S56-S58.

$$X_{\mathrm{exp}}^{\mathrm{H_2}} = \frac{B_{\mathrm{H_2}}}{B_{\mathrm{H_2}} + 1 + B_{\mathrm{D_2}}}; \tag{S56}$$

$$X_{\mathrm{exp}}^{\mathrm{D_2}} = \frac{B_{\mathrm{D_2}}}{B_{\mathrm{H_2}} + 1 + B_{\mathrm{D_2}}}; \tag{S57}$$

$$X_{\mathrm{exp}}^{\mathrm{HD}} = \frac{1}{B_{\mathrm{H_2}} + 1 + B_{\mathrm{D_2}}}. \tag{S58}$$

The experimentally derived branching fractions are shown in Fig. S10 and are in good agreement with predictions of QPES-TST.

S8. SIMULATION OF TPD SPECTRA

We simulated temperature programmed desorption (TPD) spectra for H* recombination using the QPES-TST and compare to the TPD spectra of Ref. [45]. We have decided to compare to the spectra of that work because the surface used in that study had a low step density and the contribution of structural defects were clearly identified and removed. The QPES-TST rate constants are valid for the zero-coverage limit, while TPD experiments are conducted over a range of coverages. Therefore, we introduced a coverage-dependent binding energy of H_2 which is based on the scaling with coverage of previously reported isosteric heats of adsorption [34, 35]—see Fig. S8. The experimental TPD traces from Ref. [45], obtained at different initial coverages, are compared with simulated TPD spectra based on the QPES-TST rate constants but E_0^{XY} in Eq. S39 becomes coverage-dependent. The rate equations used for TPD simulation neglect the diffusion contribution that we included for simulation of kinetic traces (Section S6), but the numeric procedure remained the same.

This comparison shows that the QPES model is capable of accurately predicting the hydrogen recombination rates at much lower temperatures than in the velocity resolved kinetics experiments. In addition, although being designed to describe the recombination rates in the zero-coverage limit it can also describe the recombination rates accurately up to 0.30 ML without taking into account entropic changes resulting from higher coverage. Indeed these effects become more important when the coverages further increase, see Ref. [19].

We also compared to TPD data obtained at much lower temperatures for hydrogen recombination on Pt(553)[46], which possesses the same step type as Pt(332). Simulations of TPD spectra using a QPES-TST model of hydrogen recombination on Pt(332) yields peak temperatures within ~15 K of those experimentally observed for Pt(553) in good agreement with previous experiments. However, since the PES differs between the two facets a deeper comparison is beyond the scope of this work.

S9. QPES H* ENTROPY AT PT(111) AND PT(332)

To simulate the coverage-dependent H* entropy at Pt(111) and Pt(332) we follow closely the strategy employed by Iglesias and coworkers [19]. We provide here merely the derivation for the QPES partition function.

The canonical partition function of H* is given by:

$$Q_{\mathrm{c}}^{\mathrm{H}^*} = \frac{\left(Q_{\mathrm{QPES}}^{\mathrm{H}^*} \times Q_{\mathrm{el}}^{\mathrm{H}^*} \times n \times N_{\mathrm{cell}}\right)^N}{N!} \tag{S59}$$

We note that the single particle partition functions—$Q_{\mathrm{QPES}}^{\mathrm{H}^*} \times Q_{\mathrm{el}}^{\mathrm{H}^*}$—are defined per unit cell and N_{cell} is the number of unit cells over which the canonical partition function is defined. Here, n is the maximum number of hydrogen atoms that can be placed within a single unit cell (1 for Pt(111) and 5 for Pt(332)). Using Stirling's approximation we obtain:

$$Q_{\mathrm{c}}^{\mathrm{H}^*} = \frac{\left(Q_{\mathrm{QPES}}^{\mathrm{H}^*} Q_{\mathrm{el}}^{\mathrm{H}^*}\right)^N n^N N_{\mathrm{cell}}^N \exp(N)}{N^N} = \frac{\left(Q_{\mathrm{QPES}}^{\mathrm{H}^*} Q_{\mathrm{el}}^{\mathrm{H}^*}\right)^N \exp(N)}{\theta^N} \tag{S60}$$

where θ is the coverage of the surface. The canonical entropy is derived from:

$$S_{\mathrm{c}}^{\mathrm{H}^*} = k_{\mathrm{B}} \frac{\partial}{\partial T} T \ln\left(Q_{\mathrm{c}}^{\mathrm{H}^*}\right) \equiv S_{\mathrm{c},xy}^{\mathrm{H}^*}(\theta) + S_{\mathrm{c},z}^{\mathrm{H}^*} + S_{\mathrm{c,el}}^{\mathrm{H}^*} \tag{S61}$$

We also note that the product of the partition functions allows separability into three contributions: one coverage dependent—associated with in-plane degrees of freedom—and two coverage independent arising from z-stretch frequency and H-atom electron spin. The contribution of electron spin is temperature independent; the corresponding molar entropy is given by:

$$S_{\mathrm{c,el}}^{\mathrm{H}^*} = R \ln\left(Q_{\mathrm{el}}^{\mathrm{H}^*}\right) \tag{S62}$$

It is about 5.8 J mol^{-1} K^{-1}. The entropic contribution to the z-stretch frequency has been evaluated numerically and yields 2.3 J mol^{-1} K^{-1} at 600 K. The coverage dependent in-plane contribution to entropy is derived to be:

$$S_{\mathrm{c},xy}^{\mathrm{H}^*}(\theta) = R\left[1 + \ln\left(\frac{q_{\mathrm{QPES},xy}^{\mathrm{H}^*}}{\theta}\right) + \frac{\sum_i \frac{E_i - E_0}{k_{\mathrm{B}}T} \exp\left(-\frac{E_i - E_0}{k_B T}\right)}{q_{\mathrm{QPES},xy}^{\mathrm{H}^*}}\right] \tag{S63}$$

with $q_{\mathrm{QPES},xy}^{\mathrm{H}^*}$ as defined in Section S5c. The coverage dependent results of $S_{\mathrm{c}}^{\mathrm{H}^*}$ at 600 K are shown in Fig. 5a of the main text.

S10.SUPPLEMENTARY FIGURES

Fig S1

Fig S1: Photograph of the dual facet platinum surface used in this work.

Fig S2

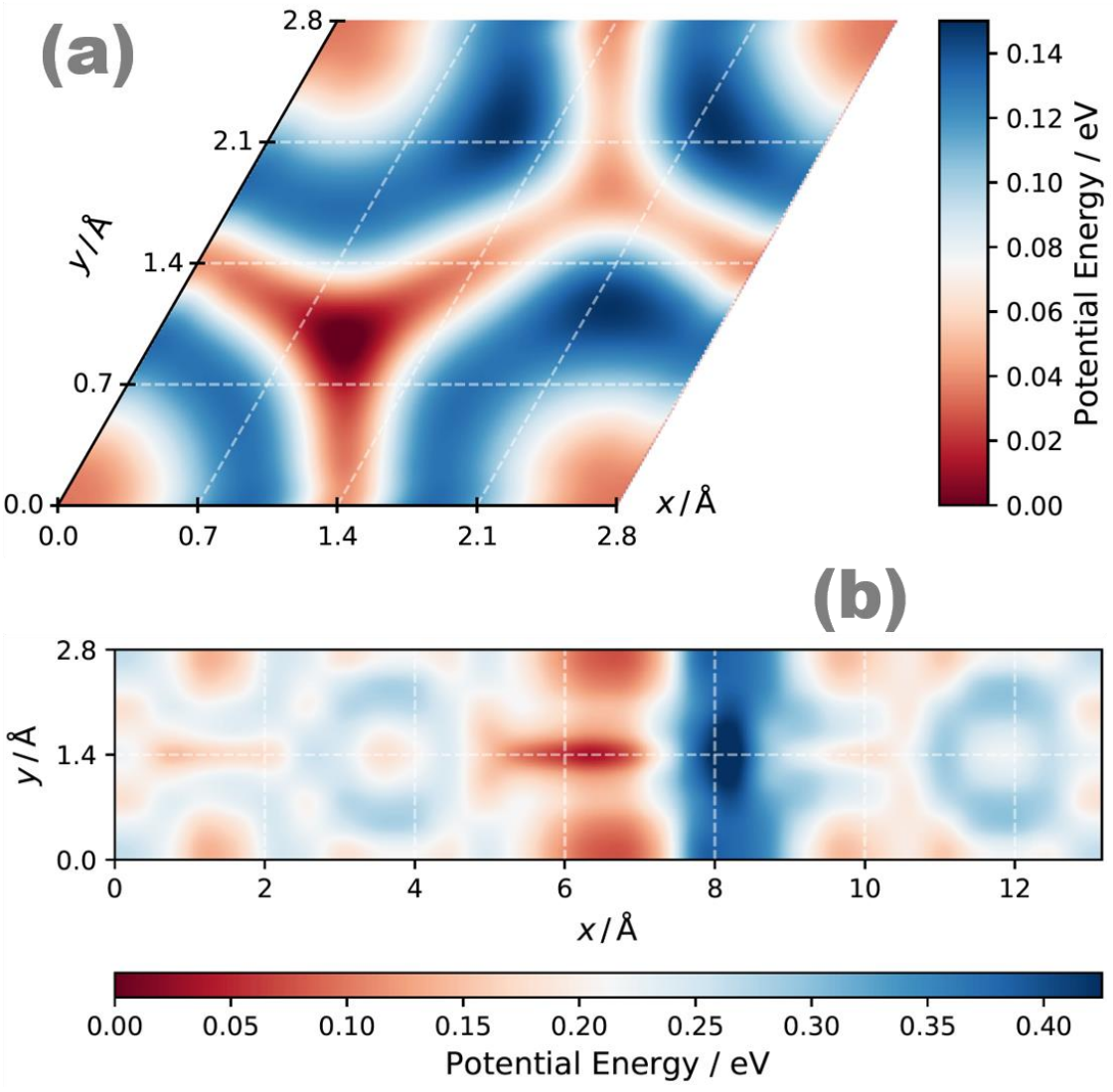

Fig S2: In-plane interaction potential $V_z^H(x,y)$ for (a) H* on Pt (111) and (b) H* on Pt(332). The zero-point energy associated with the H-Pt stretch frequency is included.

Fig S3

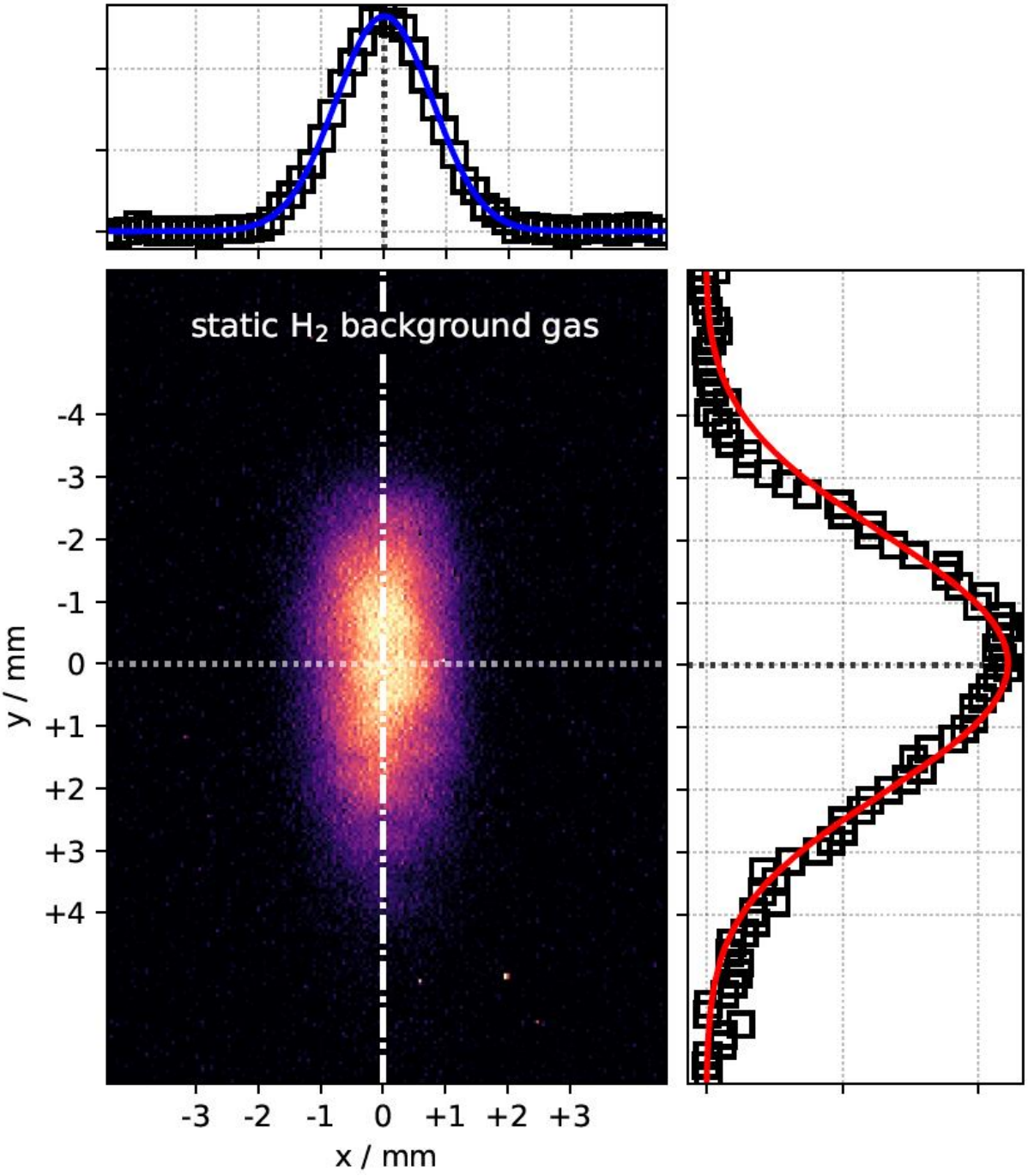

Fig S3: Ion image of the thermal H_2 background gas. The x-axis histogram is well represented by a thermal Maxwell-Boltzmann distribution—blue line. The y-axis histogram is a convolution of the thermal Maxwell-Boltzmann distribution with the ionization efficiency function, $\varepsilon_y(y)$, of H_2. The red line is a fit used to determine $\varepsilon_y(y)$, which is shown in Fig. S4.

Fig S4

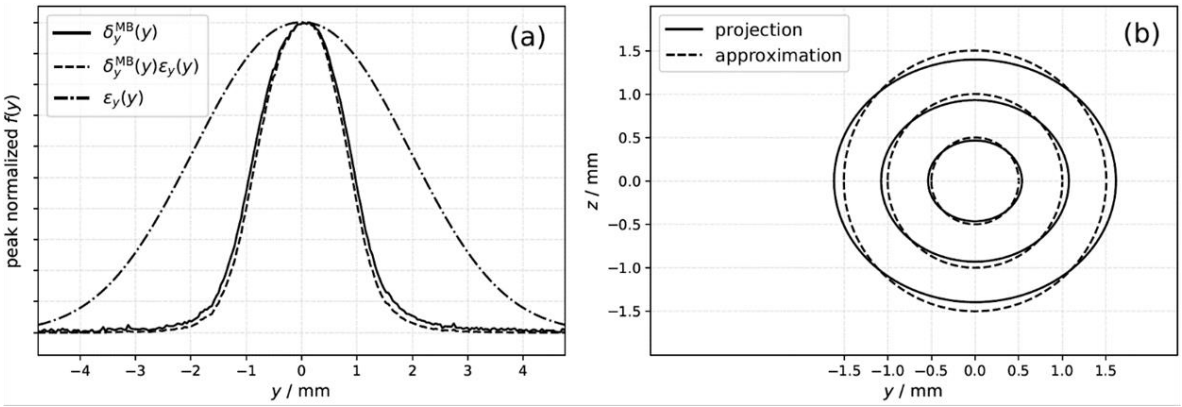

Fig S4: (a) Ionization efficiency (dash-dotted), the beams cross section (solid) and the product of both functions (dashed) is shown. (b) Projection of incident molecular beam at 30° incidence angle (solid) and its radial approximation used for the analysis (dashed).

Fig S5

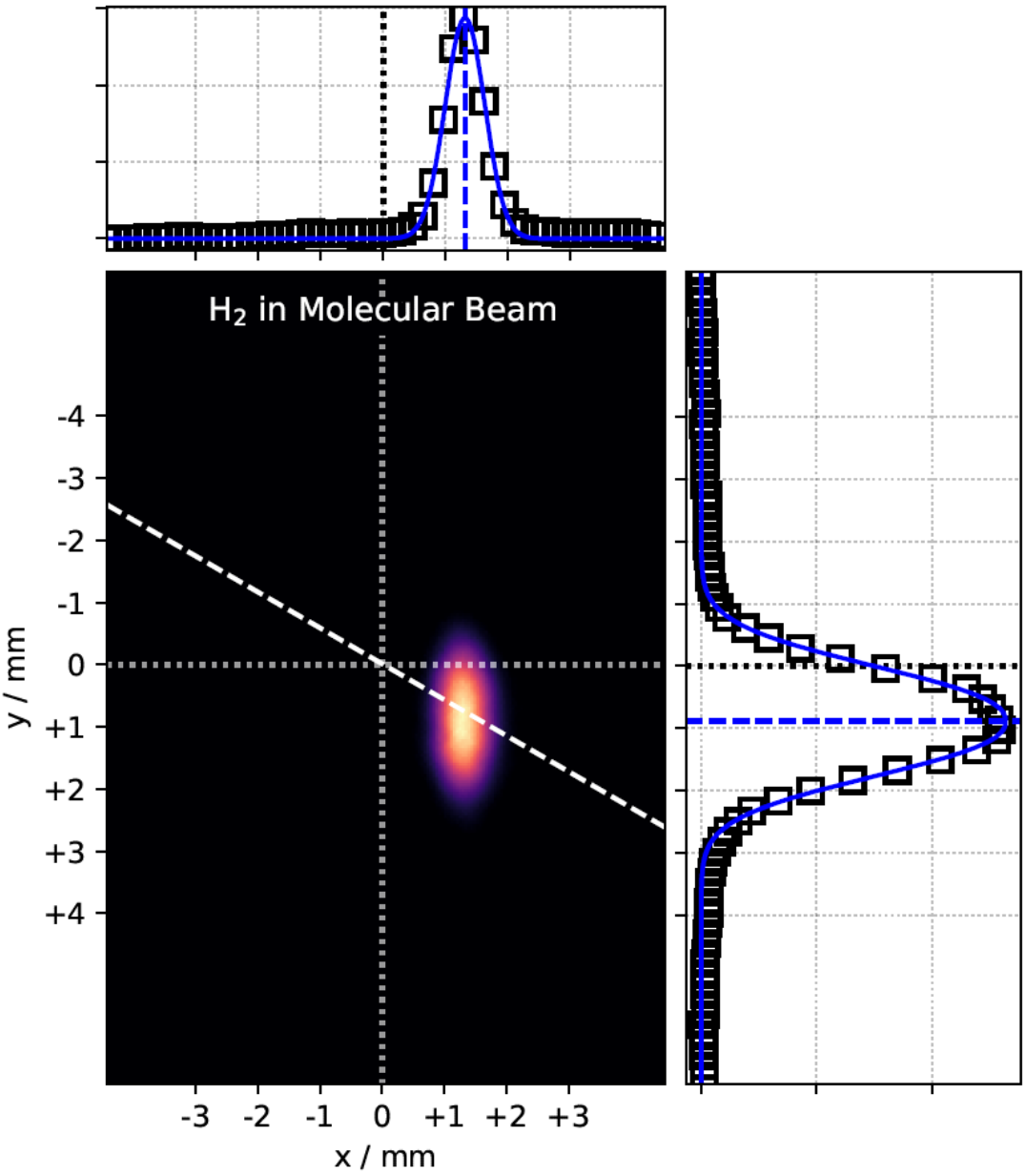

Fig S5: Ion image of H_2 from the incident molecular beam. The dashed line is the molecular beam propagation axis and dotted lines indicate the position of the laser focus. From the x- and y-axis histogram the speed of the incident molecules is derived. The y-axis histogram reflects the product of ionization efficiency and molecular beam cross section. See Fig. S4.

Fig S6

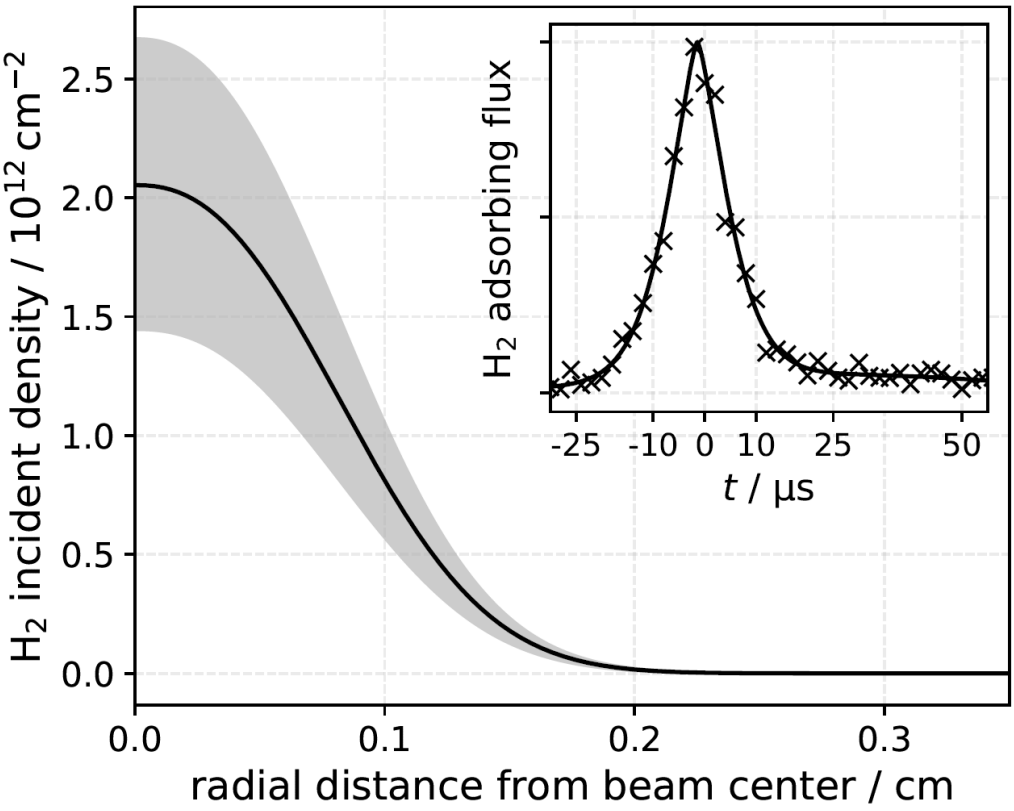

Fig S6: The radial distribution of incident H_2 density provided by a single molecular beam pulse at the surface. The shaded region indicates the error associated with the absolute flux calibration. The inset shows the temporal profile of the H_2 molecular beam pulse.

Fig S7

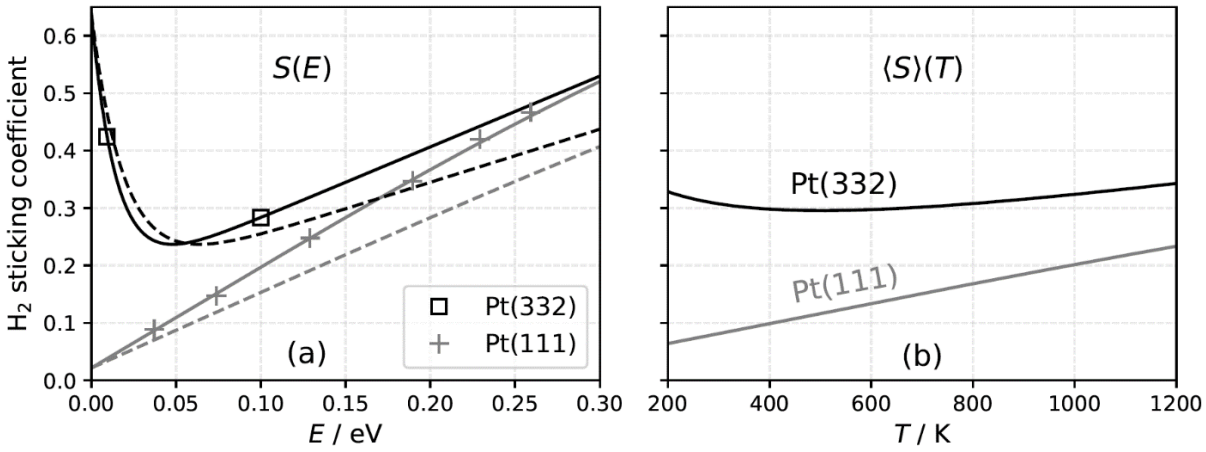

Fig S7: **(a) The sticking coefficients obtained at different Pt surfaces.** Grey solid line is an error function fit to the grey plusses. The black line is a fit of the model, developed by Juurlink and coworkers, to the corresponding squares. The black (grey) dashed line is the expected sticking coefficient at 30°incidence angle for Pt(332) (Pt(111)) assuming normal energy scaling. **(b) The angle and thermal energy averaged sticking coefficient for Pt(332) and Pt(111).**

Fig S8

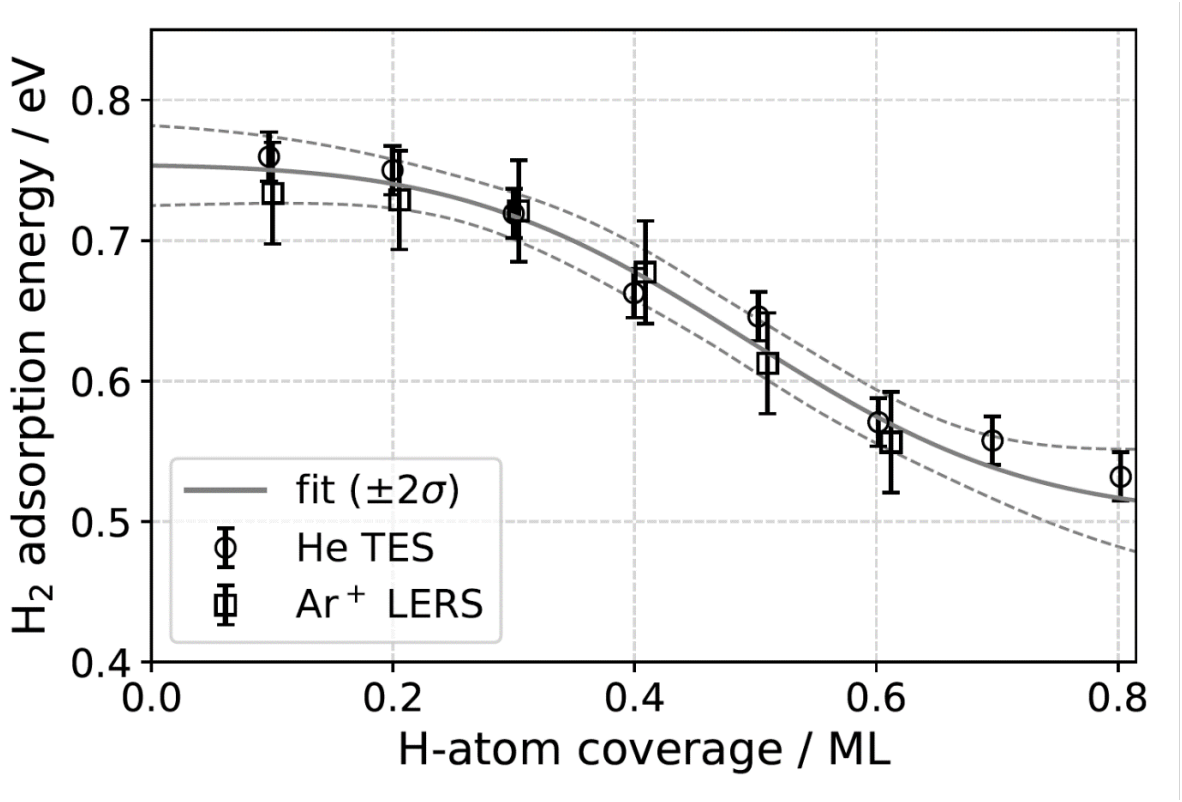

Fig S8: Determination of the H_2 Binding Energy at Pt(111) in the Zero Coverage Limit. The symbols represent isosteric heats of adsorption obtained experimentally with Ar^+-ion Low Energy Recoil Scattering[34] (LERS) and Thermal Energy He Scattering[35] (TES). The intercept with the y-axis is the H_2 adsorption energy in the zero coverage limit that we use for TST modeling at Pt(111). Note that the coverage axis of LERS experiments was in arbitrary units and we scale it to align with results of TES experiments. The solid grey line is the fit to circles and squares and the region between the gray dashed lines is its estimated 2σ uncertainty. The coverage dependence of the binding energy is estimated based on the grey line and used for TPD simulations of Fig. 1 of the main text.

Fig S9

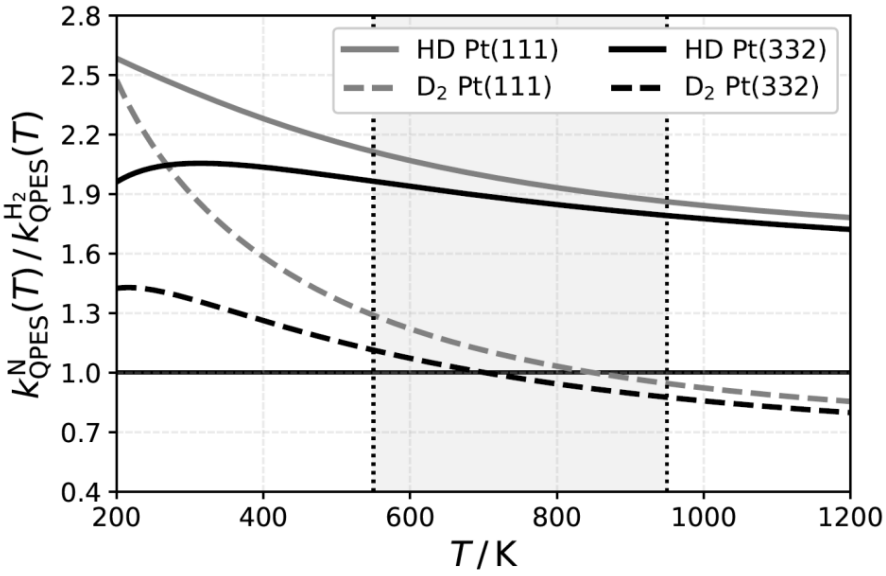

Fig S9: Isotope effect of QPES-TST model. These rate constant fractions were used to predict the rate of HD production seen in the velocity resolved kinetics experiments. The light grey region indicates the temperature range of the velocity resolved kinetics experiments.

Fig S10

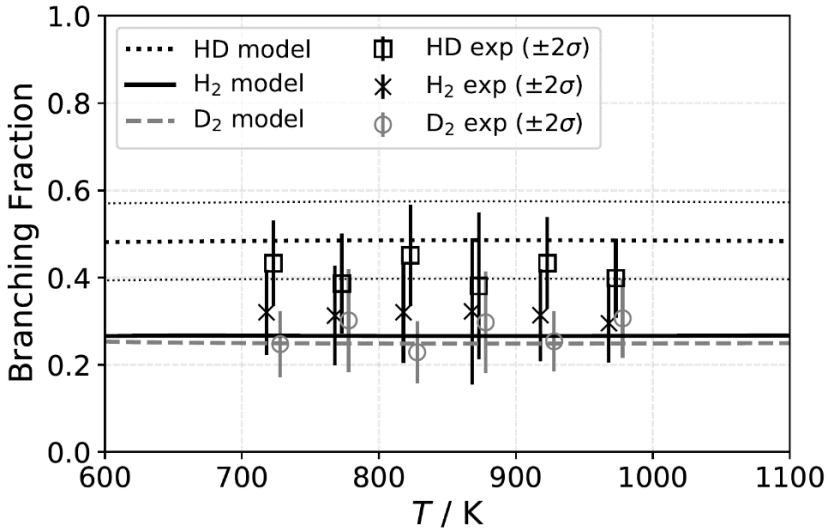

Fig S10: Isotopic branching fraction in the velocity resolved kinetics experiments (symbols, see legend) QPES model (lines, see legend). The error bars and the region between the tiny dotted lines (omitted for H_2 and D_2 for clarity) reflect 2σ uncertainty in the experiment and of the model. The data for H_2 and D_2 are shifted from experimental temperature by -5 and $+5$ K for the sake of presentation.

S11. ADDITIONAL REFFERENCES

[1] D.J. Harding, J. Neugebohren, D.J. Auerbach, T.N. Kitsopoulos, A.M. Wodtke, Using Ion Imaging to Measure Velocity Distributions in Surface Scattering Experiments, J Phys Chem A, 119 (2015) 12255-12262.

[2] D.J. Harding, J. Neugebohren, H. Hahn, D.J. Auerbach, T.N. Kitsopoulos, A.M. Wodtke, Ion and velocity map imaging for surface dynamics and kinetics, Journal of Chemical Physics, 147 (2017).

[3] J. Neugebohren, D. Borodin, H.W. Hahn, J. Altschaffel, A. Kandratsenka, D.J. Auerbach, C.T. Campbell, D. Schwarzer, D.J. Harding, A.M. Wodtke, T.N. Kitsopoulos, Velocity-resolved kinetics of site-specific carbon monoxide oxidation on platinum surfaces, Nature, 558 (2018) 280-283.

[4] J. Fingerhut, D. Borodin, M. Schwarzer, G. Skoulatakis, D.J. Auerbach, A.M. Wodtke, T.N. Kitsopoulos, The Barrier for CO2 Functionalization to Formate on Hydrogenated Pt, J Phys Chem A, (2021).

[5] K.D. Rinnen, M.A. Buntine, D.A.V. Kliner, R.N. Zare, W.M. Huo, Quantitative-Determination of H2, Hd, and D2 Internal-State Distributions by (2+1) Resonance-Enhanced Multiphoton Ionization, Journal of Chemical Physics, 95 (1991) 214-225.

[6] D. Borodin, K. Golibrzuch, M. Schwarzer, J. Fingerhut, G. Skoulatakis, D. Schwarzer, T. Seelemann, T. Kitsopoulos, A.M. Wodtke, Measuring Transient Reaction Rates from Nonstationary Catalysts, ACS Catalysis, 10 (2020) 14056-14066.

[7] G. Kresse, J. Furthmuller, Efficiency of ab-initio total energy calculations for metals and semiconductors using a plane-wave basis set, Comp Mater Sci, 6 (1996) 15-50.

[8] G. Kresse, J. Furthmuller, Efficient iterative schemes for ab initio total-energy calculations using a plane-wave basis set, Physical Review B, 54 (1996) 11169-11186.

[9] G. Kresse, J. Hafner, Ab-Initio Molecular-Dynamics Simulation of the Liquid-Metal Amorphous-Semiconductor Transition in Germanium, Physical Review B, 49 (1994) 14251-14269.

[10] G. Kresse, J. Hafner, Abinitio Molecular-Dynamics for Liquid-Metals, Physical Review B, 47 (1993) 558-561.

[11] B. Hammer, L.B. Hansen, J.K. Norskov, Improved adsorption energetics within density-functional theory using revised Perdew-Burke-Ernzerhof functionals, Physical Review B, 59 (1999) 7413-7421.

[12] P.E. Blöchl, Projector Augmented-Wave Method, Physical Review B, 50 (1994) 17953-17979.

[13] M. Methfessel, A.T. Paxton, High-Precision Sampling for Brillouin-Zone Integration in Metals, Physical Review B, 40 (1989) 3616-3621.

[14] H.J. Monkhorst, J.D. Pack, Special Points for Brillouin-Zone Integrations, Physical Review B, 13 (1976) 5188-5192.

[15] M.N. Srnec, S. Upadhyay, J.D. Madura, A Python Program for Solving Schrodinger's Equation in Undergraduate Physical Chemistry, J Chem Educ, 94 (2017) 813-815.

S32

[16] P.J. Cooney, E.P. Kanter, Z. Vager, Convenient Numerical Technique for Solving the One-Dimensional Schrodinger-Equation for Bound-States, Am J Phys, 49 (1981) 76-77.

[17] G. Kallen, G. Wahnstrom, Quantum treatment of H adsorbed on a Pt(111) surface, Physical Review B, 65 (2002).

[18] M. Kammler, S.M. Janke, A. Kandratsenka, A.M. Wodtke, Genetic algorithm approach to global optimization of the full-dimensional potential energy surface for hydrogen atom at fcc-metal surfaces, Chemical Physics Letters, 683 (2017) 286-290.

[19] M. García-Diéguez, D.D. Hibbitts, E. Iglesia, Hydrogen Chemisorption Isotherms on Platinum Particles at Catalytic Temperatures: Langmuir and Two-Dimensional Gas Models Revisited, The Journal of Physical Chemistry C, 123 (2019) 8447-8462.

[20] D.R. Olander, Heterogeneous chemical kinetics by modulated molecular beam mass spectrometry, Journal of Colloid and Interface Science, 58 (1977) 169-183.

[21] D. Borodin, M. Schwarzer, H.W. Hahn, J. Fingerhut, Y.Q. Wang, D.J. Auerbach, H. Guo, J. Schroeder, T.N. Kitsopoulos, A.M. Wodtke, The puzzle of rapid hydrogen oxidation on Pt(111), Mol Phys, (2021).

[22] R. van Lent, S.V. Auras, K. Cao, A.J. Walsh, M.A. Gleeson, L.B.F. Juurlink, Site-specific reactivity of molecules with surface defects-the case of H2 dissociation on Pt, Science, 363 (2019) 155-157.

[23] K. Cao, R. van Lent, A.W. Kleyn, L.B.F. Juurlink, A molecular beam study of D2 dissociation on Pt(111): Testing SRP-DFT calculations, Chemical Physics Letters, 706 (2018) 680-683.

[24] I.M.N. Groot, A.W. Kleyn, L.B.F. Juurlink, Separating Catalytic Activity at Edges and Terraces on Platinum: Hydrogen Dissociation, Journal of Physical Chemistry C, 117 (2013) 9266-9274.

[25] A.C. Luntz, J.K. Brown, M.D. Williams, Molecular beam studies of H2 and D2 dissociative chemisorption on Pt(111), J Chem Phys, 93 (1990) 5240-5246.

[26] C.S. Meng, M.H.M. Janssen, Measurement of the density profile of pure and seeded molecular beams by femtosecond ion imaging, Rev Sci Instrum, 86 (2015).

[27] K. Jousten, Handbook of Vacuum Technology, Wiley-VCH Verlag GmbH & Co, Weinheim, 2016.

[28] P. Samson, A. Nesbitt, B.E. Koel, A. Hodgson, Deuterium dissociation on ordered Sn/Pt(111) surface alloys, J Chem Phys, 109 (1998) 3255-3264.

[29] M.J. Murphy, A. Hodgson, Adsorption and desorption dynamics of H-2 and D-2 on Cu(111): The role of surface temperature and evidence for corrugation of the dissociation barrier, Journal of Chemical Physics, 108 (1998) 4199-4211.

[30] R.A. Olsen, D.A. McCormack, M. Luppi, E.J. Baerends, Six-dimensional quantum dynamics of H-2 dissociative adsorption on the Pt(211) stepped surface, Journal of Chemical Physics, 128 (2008).

[31] D.A. McCormack, R.A. Olsen, E.J. Baerends, Mechanisms of H-2 dissociative adsorption on the Pt(211) stepped surface, Journal of Chemical Physics, 122 (2005).

[32] C. Jansen, L. Juurlink, Absolute dissociation cross sections for D2 dissociation on Pt steps, Chemical Physics Letters, 776 (2021).

[33] G. Anger, H.F. Berger, M. Luger, S. Feistritzer, A. Winkler, K.D. Rendulic, Microfacets of the (1x2) Reconstructed Pt(110) Surface Seen in the Adsorption Dynamics of H2, Surf. Sci., 219 (1989) L583-L589.

[34] B.J.J. Koeleman, S.T. de Zwart, A.L. Boers, B. Poelsema, L.K. Verhey, Adsorption study of hydrogen on a stepped Pt(997) surface using low energy recoil scattering, Nuclear Instruments and Methods in Physics Research, 218 (1983) 225-229.

[35] B. Poelsema, K. Lenz, G. Comsa, The dissociative adsorption of hydrogen on defect-'free' Pt(111), J Phys Condens Matter, 22 (2010) 304006.

[36] D.J. Doren, J.C. Tully, Precursor Dynamics, Abstr Pap Am Chem S, 193 (1987) 11-Coll.

[37] J.C. Tully, The Dynamics of Adsorption and Desorption, Surf. Sci., 299 (1994) 667-677.

[38] M. Kratzer, J. Stettner, A. Winkler, Angular distribution of desorbing/permeating deuterium from modified Pd(111) surfaces, Surf. Sci., 601 (2007) 3456-3463.

[39] R.J. Gale, M. Salmeron, G.A. Somorjai, Variation of Surface-Reaction Probability with Reactant Angle of Incidence - Molecular-Beam Study of Asymmetry of Stepped Platinum Crystal-Surfaces for H-H Bond Breaking, Physical Review Letters, 38 (1977) 1027-1029.

S35

[40] A. Bajpai, P. Mehta, K. Frey, A.M. Lehmer, W.F. Schneider, Benchmark First-Principles Calculations of Adsorbate Free Energies, ACS Catalysis, 8 (2018) 1945-1954.

[41] M. Jørgensen, H. Grönbeck, Adsorbate Entropies with Complete Potential Energy Sampling in Microkinetic Modeling, The Journal of Physical Chemistry C, 121 (2017) 7199-7207.

[42] T.W. Hickmott, Interaction of Hydrogen with Tungsten, Journal of Chemical Physics, 32 (1960) 810-823.

[43] A.P. Graham, A. Menzel, J.P. Toennies, Quasielastic helium atom scattering measurements of microscopic diffusional dynamics of H and D on the Pt(111) surface, Journal of Chemical Physics, 111 (1999) 1676-1685.

[44] L. Petzold, Automatic Selection of Methods for Solving Stiff and Nonstiff Systems of Ordinary Differential Equations, Siam J Sci Stat Comp, 4 (1983) 136-148.

[45] S.K. Jo, Weakly-bound hydrogen on defected Pt(111), Surf. Sci., 635 (2015) 99-107.

[46] M.J.T.C. van der Niet, A. den Dunnen, L.B.F. Juurlink, M.T.M. Koper, The influence of step geometry on the desorption characteristics of O-2, D-2, and H2O from stepped Pt surfaces, Journal of Chemical Physics, 132 (2010).

Chapter 4

Molecular Desorption as a Probe for Molecule-Surface Interactions

4.1 *"NO Binding Energies to and Diffusion Barrier on Pd"*

Author contributions: The kinetic experiments were conducted by DB. Part of the experiments was conducted by JF and SH during their master and bachelor thesis, respectively. Data was analyzed by DB. The TST model was developed by DB. The paper was written by IR, AMW and DB. All authors contributed to the discussion of the results. All authors contributed to the revision of the manuscript.

THE JOURNAL OF PHYSICAL CHEMISTRY C
A JOURNAL OF THE AMERICAN CHEMICAL SOCIETY

pubs.acs.org/JPCC Article

NO Binding Energies to and Diffusion Barrier on Pd Obtained with Velocity-Resolved Kinetics

Dmitriy Borodin, Igor Rahinov, Jan Fingerhut, Michael Schwarzer, Stefan Hörandl, Georgios Skoulatakis, Dirk Schwarzer, Theofanis N. Kitsopoulos,* and Alec M. Wodtke*

Cite This: J. Phys. Chem. C 2021, 125, 11773−11781 Read Online

ACCESS | Metrics & More | Article Recommendations

ABSTRACT: We report nitric oxide (NO) desorption rates from Pd(111) and Pd(332) surfaces measured with velocity-resolved kinetics. The desorption rates at the surface temperatures from 620 to 800 K span more than 3 orders of magnitude, and competing processes, like dissociation, are absent. Applying transition state theory (TST) to model experimental data leads to the NO binding energy E_0 = 1.766 ± 0.024 eV and diffusion barrier D_T = 0.29 ± 0.11 eV on the (111) terrace and the stabilization energy for (110)-steps $\Delta E_{ST} = 0.060^{+0.015}_{-0.030}$ eV. These parameters provide valuable benchmarks for theory.

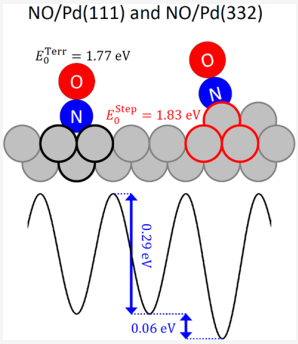

INTRODUCTION

Binding energies of molecules at surfaces serve as important descriptors, for screening heterogeneous catalysts. This exploits the well-known correlation of catalytic activity and binding strength realized in the early 20th century by Paul Sabatier.[1,2] Nowadays, the screening is done using electronic structure calculations based on density functional theory (DFT) with the generalized gradient approximation (GGA).[3−5] Although DFT-GGA often yields results in agreement with experimental binding energies,[3] there are examples where it fails. The prediction of the wrong binding site for CO on Pt(111) stands out—"The CO/Pt(111) Puzzle".[6] Exchange-correlation functionals at the GGA level predict CO to be bound at the 3-fold hollow site of Pt(111); however, CO binds to the top site. This system has been tackled by various theoreticians, and improvements have been developed,[7−9] concluding that GGA-related overbinding errors are enhanced at sites with high coordination.

This problem became apparent because CO prefers binding at low coordinated sites. It is likely that GGA calculations of chemisorption energies of NO have similar problems.[10] However, NO prefers binding at the hollow site of fcc(111) metals in agreement with predictions of DFT-GGA. Hence, GGA errors in the calculated chemisorption energies of NO can only be detected by direct comparison to precise experimental benchmarks. Although NO binding energies can be obtained from calorimetry,[11,12] competing decomposiiton has prevented any accurate experimental determinations up to now.

The interaction of NO with Pd exemplifies this situation. Here, despite earlier incorrect assignments,[13] theory and experiment now agree on the preferred binding site;[14] unfortunately, accurate experimental binding energies are not available. In previous work, NO/Pd(111) binding energies were derived from temperature-programmed desorption (TPD)[15−17] over a narrow temperature range and under conditions where the rates of NO decomposition and desorption are comparable.[15] Hence, the reported values (1.5−1.9 eV) are of little use for rigorous benchmarking of theoretical predictions.

In this work, we overcome these experimental problems using velocity-resolved kinetics and are able to use experimental desorption rates to derive the NO chemisorption energy and diffusion barrier on Pd(111) terraces as well as the stabilization energy on steps of Pd(332). Velocity-resolved kinetics is an improvement over previous methods as desorption rates are obtained at higher temperatures and over a broader temperature range. Because of this, desorption rates span over 3 orders of magnitude, and NO decomposition is absent. From the absolute magnitude and the temperature dependence of the desorption rate, we determine the binding

Received: April 1, 2021
Revised: May 10, 2021
Published: May 24, 2021

https://doi.org/10.1021/acs.jpcc.1c02965
J. Phys. Chem. C 2021, 125, 11773−11781

The Journal of Physical Chemistry C pubs.acs.org/JPCC Article

energy and the entropy of the adsorbed molecules. Using a model potential energy surface describing diffusion and step stabilization, we obtain an accurate adsorbate partition function as an input to transition state theory (TST). This leads to an accurate binding energy and diffusion barrier. Complementary experiments on a stepped Pd(332) surface clarify an open dispute between experiment and theory. Past experiments suggest that NO is more stably bound at terraces,[17] in contrast to theoretical predictions.[18] We find that NO has an energetic preference for steps.

METHODS

Similar to our previously described experiments,[19−21] an ∼30 μs long pulsed supersonic molecular beam of NO (2−20% NO in He) passed through two differential pumping stages and entered the surface-scattering chamber, at a base pressure of 2 × 10^{-10} mbar, impinging upon the Pd(111) or the Pd(332) surface (MaTeck GmbH) at an incidence angle of 30° from the surface normal. The surface was prepared by sputtering with Ar^+ (3 keV) for 10 min and subsequent annealing at 1070 K for 15 min. The cleanliness of the sample was verified with Auger electron spectroscopy. The step density of the Pd(111) crystal was determined using atomic force microscopy to be 0.4 ± 0.1%. The desorbing NO was detected, 20 mm from the surface, using nonresonant multiphoton ionization with a Ti:sapphire laser (35 fs, 0.5 W at 1 kHz). A pulsed homogeneous electric field, formed between two parallel flat meshes (repeller and extractor), projected the ions onto a time-gated MCP detector. The mass-to-charge ratio of the ions was fixed by setting the time gate on the MCP with respect to the pulsed-field extraction. The ion image appearing on the phosphor screen at the back of the MCP detector was recorded with a CCD camera.

The position of each pixel in the image relative to the intersection of the probe laser and surface normal directions corresponds to an NO velocity vector. The velocity information is used to calculate the flight time of the NO from the surface to the ionizing laser spot to more accurately determine the residence time and to convert NO density to flux. The ion images also record thermal background, which was subtracted from the signal using knowledge of the background's velocity distribution. The flux images at each beam-laser delay are integrated for velocities between 400 and 800 m/s at angles close to the surface normal, suppressing directly scattered NO's contribution to the kinetic traces. The translational energy distribution of the desorbing molecules was determined by summing all ion images from each beam-laser delay.

RESULTS

Figure 1 shows representative kinetic traces for NO desorbing from Pd(111) and Pd(332). The exponential decay is characteristic of a first-order process and is seen over the entire temperature range of this work. NO doses above ≈1 × 10^{-2} ML/pulse and below ≈1 × 10^{-3} ML/pulse are indistinguishable. As the step density of the crystal is 4 ± 1 × 10^{-3} ML, this indicates the absence of step saturation effects in the (111) experiments, seen previously for CO and NO on stepped Pt surfaces.[22,23] For experiments on the Pd(332) surface, the NO dose from each molecular beam pulse is always below the step density (0.17 ML). The absence of a biexponential kinetic trace at high NO doses indicates that

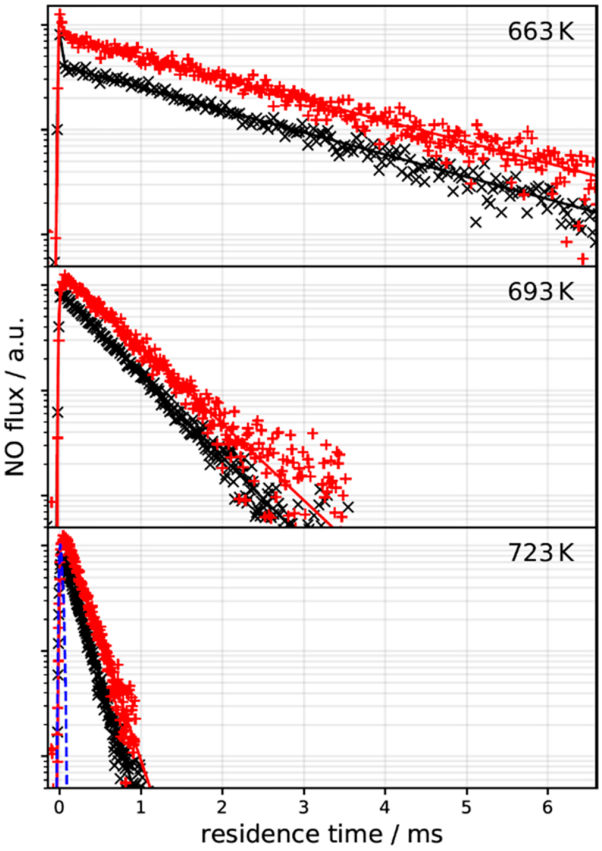

Figure 1. Kinetic traces of NO desorbing from Pd(111) (black ×, experimental data; black −, fits to eq 1) and from Pd(332) (red +, experimental data; red −, fits to eq 1) at various surface temperatures. The dashed blue line denotes the molecular beam dosing function, which determines the temporal resolution of the experiment. The kinetic traces are set apart from one another for clarity.

steps do not play a significant role for NO desorption from Pd(111). We do not observe NO decomposition or reaction. In contrast to previous work,[15,17] the experimental conditions that can be reached with velocity-resolved kinetics allow us to exclusively probe the elementary process of desorption.

To determine the desorption rate constants from the kinetic trace, we fit the flux $f(t)$ vs residence time t using a function representing two contributions

$$f(t) = a \times \mathrm{DS}(t) + b \times \mathrm{TD}(t, k_\mathrm{d}) \quad (1)$$

comprising direct scattering (DS) and a trapping desorption (TD). The DS contribution has the temporal shape of the incident molecular beam, while the TD contribution is a first-order decay convoluted with the molecular beam temporal profile. The fit yields three independent fit parameters: a, b, the amplitudes of DS and TD, and k_d, the desorption rate constant.

Desorption rate constants were derived for ∼50 surface temperatures between 620 and 800 K for both surfaces (see Figure 2). By fitting the Arrhenius equation, we find that the prefactor and the activation energy, A and E_a, differ slightly for experiments done with Pd(111) (E_a = 1.71 ± 0.03 eV, A = $10^{15.65\pm0.20}$ s^{-1}) versus Pd(332) (E_a = 1.73 ± 0.02 eV, A = $10^{15.80\pm0.15}$ s^{-1}). Using the covariance matrix of the least-

https://doi.org/10.1021/acs.jpcc.1c02965
J. Phys. Chem. C 2021, 125, 11773−11781

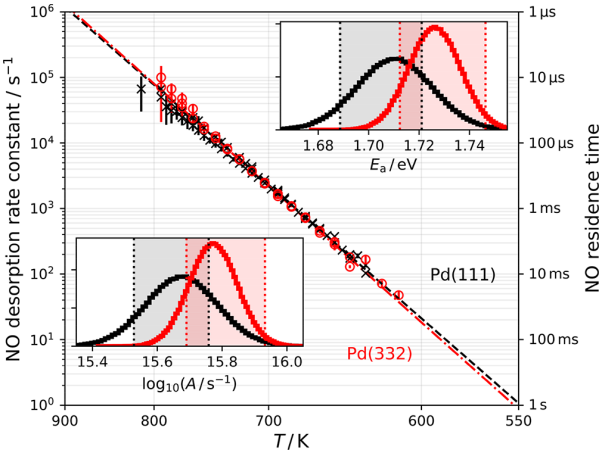

Figure 2. Arrhenius plot of NO desorption rate constants from Pd(111) (black ×, experiment; black ---, Arrhenius error-weighted fit) and Pd(332) (red ○, experiment: red ·-·, Arrhenius error-weighted fit). The error bars indicate 95% confidence intervals. The insets show the error distributions (black, Pd(111); red, Pd(332)) for the activation energy, E_a (upper right), and the prefactor, A (lower left). The red and black shaded regions in the insets are the Arrhenius rate parameter predictions from the TST model obtained between 620 and 800 K (see Section 4).

squares fit, we map out the error distribution for A and E_a, shown as red and black histograms in the insets in Figure 2.

The velocity-resolved kinetics experiment provides both the desorption rate—yielding the barrier for desorption, and, the translational energy distribution - allowing one to determine the magnitude of the barrier for adsorption. In this case the adsorption has no barrier, and therefore the barrier for desorption is the same as the NO binding energy.

Figure 3 shows translational energy distributions of NO desorbing from Pd(111) at two representative temperatures, as well as the thermal 3D Maxwell–Boltzmann distributions. The experimentally observed translational energy distributions are not hyperthermal, indicating the absence of an adsorption barrier. They are similar (within the error bars of translational energy determination) to the thermal Maxwell–Boltzmann distributions, characteristic for a chemisorbed system with high (close to unity) sticking coefficient, weakly dependent on the incident kinetic energy. This conclusion is supported by previous King and Wells measurements of the NO sticking coefficient at Pd(111) using effusive molecular beams.[15] We observe similar translational energy distributions for Pd(332) experiments (not shown).

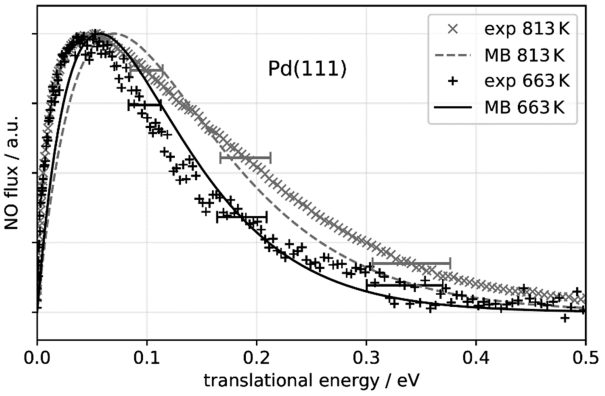

Figure 3. Translational energy distributions of NO molecules desorbing from Pd(111) at surface temperatures of 813 K (×, experiment; ---, 3D Maxwell–Boltzmann distribution at 813 K) and 663 K (+, experiment; –, 3D Maxwell–Boltzmann distribution at 663 K). The experimentally obtained translational energy distributions exhibit effective temperature close (within 10%) to the 3D Maxwell–Boltzmann distributions at the surface temperature. The horizontal error bars indicate the 2σ error of the kinetic energy determination.

DISCUSSION

The desorption kinetics of NO from Pd single-crystal surfaces has been studied previously with temperature-programmed desorption (TPD); however, the reported rate parameters vary widely, with activation energies between 1.5 and 1.9 eV and prefactors between 10^{14} and 10^{18} s^{-1}.[14,15–17] It is worth noting that despite various TPD studies arriving at different Arrhenius parameters all reported a TPD spectral peak near ~520 K for low initial coverages. This suggests that the errors in the reported values of A and E_a are correlated, a typical problem in TPD experiments which probe a narrow temperature range. Another problem with these TPD studies is decomposition of NO—measured rates do not reflect a single elementary kinetic process. Only in the work of Schmick and Wassmuth[15] has this been explicitly taken into account in the analysis of the TPD rates. The authors found that at the low temperatures of the TPD studies NO decomposes at steps of Pd(111) crystals with an efficiency of ≈50% in the low coverage limit. They estimated the rate parameters for the decomposition process—reporting a prefactor of 4×10^{11} s^{-1} and estimating the activation energy for decomposition to be ≈80% of the desorption energy.[15] In our experiments, we find no evidence of NO decomposition on Pd(111) and Pd(332). Specifically, we observe no signals from N_2, N_2O, NO_2, or O_2, reported in earlier works.[15,17,24] We also see no variation in the NO desorption rate even after long NO exposure times. Chemical change of the surface due to decomposition is absent.

This is because the fraction of NO-forming decomposition products $\varphi_{dis}(T)$ is strongly temperature dependent. Consider

$$\varphi_{dis}(T) = \frac{k_{dis}}{k_{dis} + k_d} \tag{2}$$

where k_{dis} is the rate constant for dissociation and k_d is the rate constant for desorption. Using $\frac{k_d}{s^{-1}} = 10^{15.65} \exp\left(-\frac{1.71\ \text{eV}}{k_B T}\right)$ from our experiment and $\frac{k_{dis}}{s^{-1}} = 10^{11.6} \exp\left(-\frac{1.37\ \text{eV}}{k_B T}\right)$, following the suggestions of Schmick and Wassmuth,[15] we find that at the temperatures of the TPD work φ_{dis} (400–500 K) is between 65 and 20%, whereas at the temperatures of our work, φ_{dis} (620–800 K) is 5–1%. An independent upper limit to the decomposition of NO (1%) in our experiments is found from an estimate of N_2 detection sensitivity. This upper limit is consistent with the uncertainty range of the previous work.[15]

The high quality of the NO desorption rate data made possible by our velocity-resolved methods warrants application of TST to obtain fundamental insights into the experimental observations. Thermal reaction rates are routinely obtained from TST, which places a dividing plane along the reaction coordinate and takes the equilibrium one-way flux through it as the reaction rate. Typically, TST gives an upper limit to the

https://doi.org/10.1021/acs.jpcc.1c02965
J. Phys. Chem. C 2021, 125, 11773–11781

The Journal of Physical Chemistry C pubs.acs.org/JPCC Article

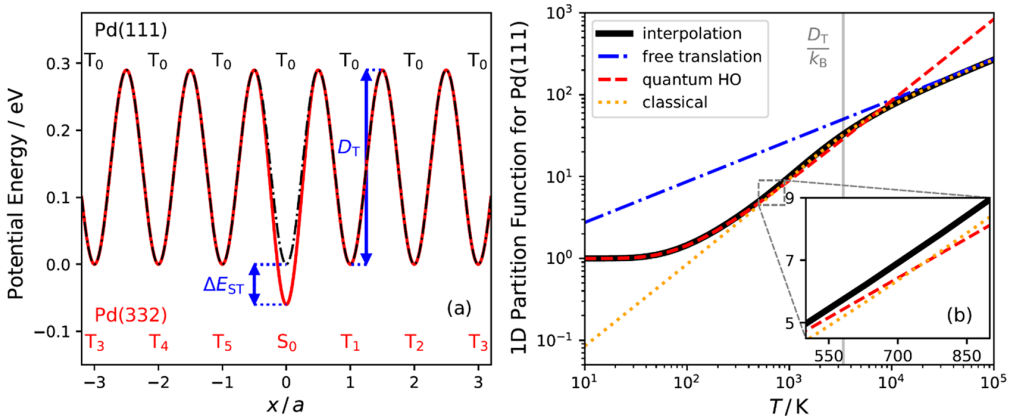

Figure 4. (a) Model potential used to describe the in-plane partition function of NO on Pd(111) (black dash-dotted line) and Pd(332) (red line). T_i denotes terrace sites, and S_i denotes step sites. The periodic unit of the potential is defined between two binding sites with the same index. The diffusion barrier between two terrace sites (D_T) and the step-terrace energy difference (ΔE_{ST}) are indicated in the plot. (b) Partition functions for NO motion parallel to a Pd(111) surface. The most accurate partition function (black line) extrapolates at low temperature to the quantum harmonic oscillator (red dashed line), at intermediate temperatures to the prediction of eq 9 (orange dotted line), and at high temperatures to the one-dimensional free translational partition function (blue dashed line). The inset shows a zoom-in of the temperature range in our analysis.

rate constant, $k_{TST}(T)$, as recrossing the dividing plane is neglected. For desorption, it is convenient to place the dividing plane at a large separation from the surface. In that case, the recrossing corrected thermal desorption rate constant is

$$k(T) = \langle S_0 \rangle \frac{k_B T}{h} \frac{Q^{\ddagger}}{Q_{ad}} \exp\left(-\frac{E_0}{k_B T}\right) = \langle S_0 \rangle k_{TST}(T) \tag{3}$$

where $Q^{\ddagger}$ and Q_{ad} are the partition functions of the desorbed gas-phase molecule and the adsorbate, respectively. E_0 is then the desorption barrier—in this case, the binding energy—and the thermal sticking coefficient $\langle S_0 \rangle$ provides the recrossing correction.[25] From the experimental velocity distributions, we surmise that the thermal sticking coefficient is close to unity, consistent with previous experiments.[15] Thus, we apply $\langle S_0 \rangle$ = 1 for the analysis of desorption rates from both surfaces, such that TST accurately represents the thermal rate.

The partition function of the desorbed gas-phase molecule is then given by

$$Q^{\ddagger} = Q_{2D}^{tr} Q^{rot} Q_{N\text{-}O}^{qHO} Q^{el} \tag{4}$$

Here, Q_{2D}^{tr} is the translational partition function of a 2D ideal gas

$$Q_{2D}^{tr} = \frac{2\pi m k_B T}{h^2} A \tag{5}$$

with m being the mass of NO. A is the area of the reference cell in which the partition function is defined. It is convenient to think of it as the area of the unit cell of the Pd surface. However, the numerical value of this area cancels out in the calculation of the TST rate constant as it enters both $Q^{\ddagger}$ and Q_{ad} in eq 3. Note that translation normal to the surface is associated with the reaction coordinate in TST and does not appear in $Q^{\ddagger}$. Q^{rot} is the classical partition function of a rigid rotor

$$Q^{rot} = \frac{k_B T}{B} \tag{6}$$

with B being the rotational constant. Q_{N-O}^{qHO} is the vibrational partition function approximated by a quantum harmonic oscillator

$$Q_{N\text{-}O}^{qHO} = \frac{1}{1 - \exp\left(-\frac{h\nu_{N-O}}{k_B T}\right)} \tag{7}$$

with ν_{N-O} being the vibrational frequency of the free molecule. Q^{el} is the electronic partition function

$$Q^{el} = 2 + 2\exp\left(-\frac{\Delta E_{1/2\to 3/2}}{k_B T}\right) \tag{8}$$

where $\Delta E_{1/2\to 3/2}$ is the energetic separation between the two spin−orbit components of the ground electronic state. Higher electronic states of NO are not populated at the temperature range of this work.

While the partition function for a diatomic in the gas phase is rather straightforward, a more careful approach is required for the adsorbate. Ignoring the surface atom motion, the number of degrees of freedom associated with the adsorbed molecule remains the same as for the gas phase. However, what was previously a free translation along x, y, and z (x and y run parallel, while z runs normal to the surface) becomes a hindered translation or vibration due to interaction with the surface. The situation is similar for degrees of freedom corresponding to gas-phase rotation. NO binds on Pd with its bond perpendicular to the surface,[10] so rotation around the NO bond axis is unimportant. The N−O stretch frequency of the molecule also changes due to interaction with the metal. While the degrees of freedom may depend weakly on binding site, we make an approximation by neglecting this dependence.

We approximate the hindered translation of NO perpendicular to the surface, the N−O stretch vibration, and the doubly degenerate hindered rotations (in xz- and yz-planes) as harmonic oscillators. Approximating hindered rotation as vibration is reasonable for chemisorbed molecules like NO and CO, which have rather high rotational isomerization barriers in their most stable configuration.[26] For the electronic partition function of the adsorbed NO, we use Q_{ad}^{el} = 2 to account for the spin states. The reduction of the electronic

https://doi.org/10.1021/acs.jpcc.1c02965
J. Phys. Chem. C 2021, 125, 11773−11781

The Journal of Physical Chemistry C pubs.acs.org/JPCC Article

Table 1. Parameters Required to Evaluate the Partition Functions for $NO_{(g)}$ and NO_{ad} at Pd(111) and Pd(332)[a]

property	$NO_{(g)}$	NO/Pd(111)	NO/Pd(332)	comment
ν_{N-O}/cm^{-1}	1904[33]	1540[13]	1540*	*value assumed to be the same as for terrace, see text
B/cm^{-1}	1.67[33]			
Q_{el}	see eq 8	2	2	
$\Delta E_{1/2\rightarrow 3/2}/cm^{-1}$	120[34]			
ν_{M-NO}/cm^{-1}		330[13]	$(\nu_{x,step}*/\nu_{x,terr}*) \times 330$	*values are obtained from the fit to Pd(111) and Pd(332)
ν_{hrot}/cm^{-1}		380*	$(\nu_{x,step}*/\nu_{x,terr}*) \times 380$	*value for hindered rotational frequency from NO/Pt(100)[35]
$\langle S_0 \rangle$		1	1	
a/Å		2.77	2.77	

[a]The frequencies of the out-of-plane hindered translation (ν_{M-NO}) and the hindered rotation frequency (ν_{hrot}) upon adsorption to steps are not reported. We assume that they scale proportionally to the in-plane hindered translation vibrational frequency (ν_x). The scaling on Pd(332) is only done if steps are the most stable binding site, which is not assumed a priori in the fitting procedure.

partition function for the adsorbate by nearly a factor of 2, compared to the gas phase, is due to the splitting of the doubly degenerate $2\pi^*$ orbital of NO into a bonding and an antibonding orbital that results from interactions with the metal orbitals.[10,27] The high energy antibonding orbital remains unpopulated at the temperatures of our work.

The proper description of NO motion parallel to the surface depends on temperature. It can be described at low temperature by vibration using the harmonic oscillator partition function or at high temperature as a hindered translation by the classical partition function given by

$$Q_x^{clas} = \frac{\sqrt{2\pi m k_B T}}{h} \int_0^{\sqrt{A}} \exp\left(-\frac{V(x)}{k_B T}\right) dx \quad (9)$$

where $V(x)$ is the molecule−surface interaction potential. In eq 9, the integration is done for the periodic unit of the surface. For the purpose of demonstration in Figure 4b, we use $\sqrt{A}$ = 2.77 Å to calculate the partition functions. Note that the harmonic oscillator will fail to describe the density of states properly when the diffusion barrier between two binding sites is low compared to the thermal energy (see the red dashed line in Figure 4b). Likewise, the classical partition function will predict unphysically low values at low temperatures (see the orange dotted line in Figure 4b).

To accurately cover all temperatures, we first construct a periodic potential for both surfaces. The one-dimensional potential for Pd(111) is modeled by

$$U_{111}(x, D_T) = \frac{D_T}{2}\left(1 - \cos\left(\frac{2\pi x}{a}\right)\right) \quad (10)$$

where the minima that represent the NO binding sites on the surface repeat, with each a = 2.77 Å being the interatomic distance of Pd atoms on the surface. The amplitude of this function, D_T, is the diffusion barrier between two binding sites. The Pd(111) potential is shown as a black dashed-dotted line in Figure 4a. The NO/Pd(111) potential along the y-axis is assumed to be identical to that along the x-axis.

To construct the potential for Pd(332), we define the x-axis as the coordinate perpendicular to the steps of Pd(332). The one-dimensional Pd(332) potential along this axis is given by

$$U_{332}(x, D_T, \Delta E_{ST}) = g(x) \times U_{111}(x, D_T) + (1 - g(x)) \times (U_{111}(x, D_T + \Delta E_{ST}) - \Delta E_{ST}) \quad (11)$$

Here ΔE_{ST} is the energy difference between the step and terrace site, and $g(x)$ is a cutoff function that is used to smoothly stitch the two basis functions at the step. A Pd(332) one-dimensional potential, generated in this way, is shown in Figure 4a as the red solid line. The NO/Pd(332) potential along the y-axis (parallel to the steps) is identical to the NO/Pd(111) potential.

Therefore, we define the in-plane (two-dimensional) potential for Pd(111) as

$$V_{111}(x, y, D_T) = U_{111}(x, D_T) + U_{111}(y, D_T) \quad (12)$$

and for Pd(332) as

$$V_{332}(x, y, D_T, \Delta E_{ST}) = U_{332}(x, D_T, \Delta E_{ST}) + U_{111}(y, D_T) \quad (13)$$

We note that the potential functions defined in this way do not reproduce the symmetry of the Pd(111) surface; however, we expect this simplification has no effect on the calculated entropy.[28] With this potential expression, the in-plane partition function, Q_{xy}, becomes separable and is given by the product of two one-dimensional partition functions Q_x and Q_y, associated with the corresponding potential energy contribution.

The construction of an accurate one-dimensional partition function (black line of Figure 4b), Q_x (or equivalently Q_y), is done following the procedure originally suggested for describing the heat capacity contribution of the hindered rotation of ethane in the gas phase.[29,30] This approach has been suggested earlier for applications of surface reactions,[28] and it is considered an accurate method to describe the partition function.[31] We define Q_x as

$$Q_x = \frac{Q_x^{qHO} Q_x^{clas}}{Q_x^{cHO}} \quad (14)$$

where Q_x^{cHO} is the partition function of the classical harmonic oscillator for hindered translation (eq 9). As mentioned above, Q_x^{qHO} is a poor approximation of Q_x at high temperatures, while Q_x^{clas} is not an appropriate approach at low temperatures. Dividing the product of Q_x^{qHO} and Q_x^{clas} by the Q_x^{cHO} is used as a trick to circumvent the inaccuracies associated with the partition function at different temperature limits. At high temperatures, the quantum harmonic oscillator partition function becomes its classical counterpart, while at low temperatures the classical partition function becomes equal to the classical oscillator partition function. Note that the hindered translation frequencies, ν_x, used in Q_x^{qHO} and Q_x^{cHO} are determined from $V(x)$ used to calculate Q_x^{clas}—this is required for self-consistency of the interpolation function Q_x. Using this approach, it is only the diffusion barrier that determines the magnitude of Q_x. In Figure 4b, we show that Q_x (black bold line) is converging to the correct limiting cases at

https://doi.org/10.1021/acs.jpcc.1c02965
J. Phys. Chem. C 2021, 125, 11773−11781

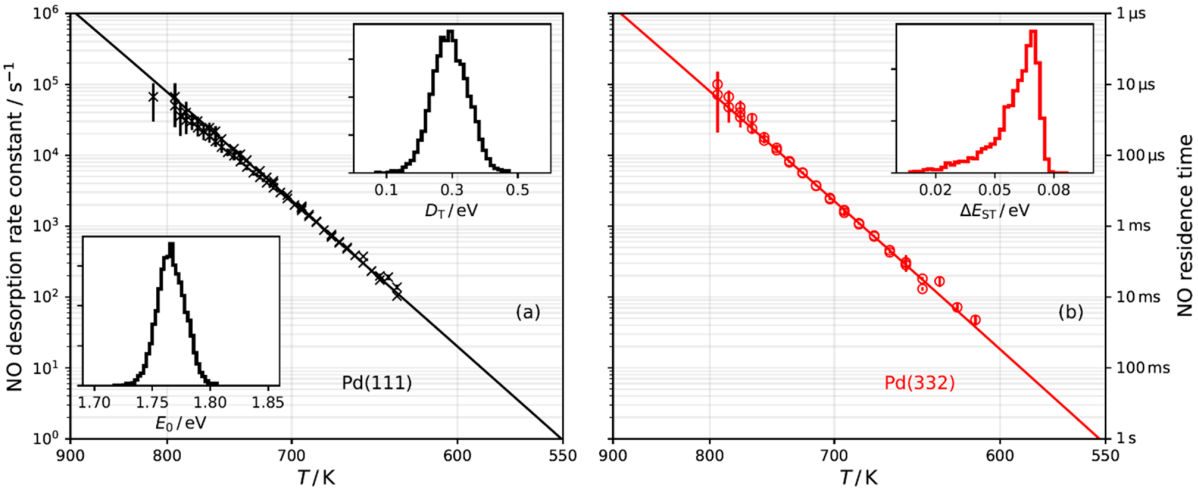

Figure 5. (a) Desorption rate constants from Pd(111) (black ×) are shown with the corresponding TST model fit (black −). The parameter distributions obtained from the fit to the data, NO binding energy E_0, and NO diffusion barrier D_T are shown in the insets. (b) Desorption rate constants from Pd(332) (red ○) are shown with the corresponding TST model fit (red −). The obtained distribution of the NO step-terrace energy difference at Pd(332) is shown in the inset.

low (Q_x^{qHO}, red-dashed line) and high temperatures (Q_x^{clas}, orange-dotted line). The total partition function for the adsorbed NO is given by

$$Q_{ad} = Q_x Q_y Q_{M-NO}^{qHO} (Q_{hrot}^{qHO})^2 Q_{N-O_{ad}}^{qHO} Q_{ad}^{el} \quad (15)$$

All the parameters needed to evaluate the partition function of $NO_{(g)}$ and NO_{ad} are summarized in Table 1. We note in passing that the partition functions presented here are valid only in the zero-coverage limit relevant to our experiments. Detailed discussion of partition functions and the derived thermodynamic state functions capturing the effects of surface coverage can be found in refs 28 and 32.

Next we use these partition functions to construct the TST rate expression, with which we fit the measured NO desorption rates. For desorption rates from Pd(111), we fit using only two parameters, the diffusion barrier, D_T, and the binding energy on the terrace, E_0. The best fit of the TST model (black line) to the measured rate constants (black crosses) is shown in Figure 5a. To evaluate uncertainty, the parameter distribution of D_T and E_0 is sampled by random numbers from a multivariate Gaussian distribution using the covariance matrix that was obtained from the least-squares fit. The parameter distributions are shown as insets in Figure 5a. This analysis leads to our final results, D_T = 0.29 ± 0.11 eV and E_0 = 1.766 ± 0.024 eV, where the error bars represent 95% confidence intervals.

For our analysis, we use the hindered rotational frequency of NO that had been observed on Pt(100) earlier.[35] It is known that CO on transition metal surfaces has hindered rotational frequencies that are similar within ~40 cm^{-1}.[36−38] We expect the same to be valid for NO. We have investigated the introduced error by modifying the hindered rotational frequency by ±40 cm^{-1} for the fit and find that D_T and E_0 remain within the reported error range.

We also analyzed the Pd(332) rate data with the TST model. We used the correlated distribution of D_T and E_0 obtained from the least-squares fitting of the Pd(111) rate data to determine the distribution of step-terrace stabilization energies ΔE_{ST} from a fit to Pd(332) rate data. The results are shown in the inset of Figure 5b. The best fit to the Pd(332) rate data is shown in Figure 5b as a red solid line. The results of this analysis show that NO is energetically stabilized at steps of Pd(332) by $\Delta E_{ST} = 0.060^{+0.015}_{-0.030}$ eV. Table 2 summarizes all of the results of the TST-based desorption rate analysis.

Table 2. Rate and Energy Parameters Determined in This Work for the NO/Pd(111) and the NO/Pd(332) Systems[a]

property	Pd(111)	Pd(332)	comment
A/s^{-1}	$10^{15.65\pm0.20}$	$10^{15.80\pm0.15}$	Arrhenius fit
$E_{a,d}$/eV	1.71 ± 0.03	1.73 ± 0.02	Arrhenius fit
E_0/eV	1.766 ± 0.024	1.766 ± 0.024	binding energy at the terrace, TST fit to Pd(111) data
D_T/eV	0.29 ± 0.11	0.29 ± 0.11	TST fit to Pd(111) data
ΔE_{ST}/eV	–	$0.060^{+0.015}_{-0.030}$	TST fit to Pd(332) data
ν_x/cm^{-1}	82 ± 16	90 ± 18	hindered translational frequency from D_T and ΔE_{ST}
ν_y/cm^{-1}	82 ± 16	82 ± 16	hindered translational frequency from D_T

[a]The hindered translational frequencies (ν_x and ν_y) result from the one-dimensional potential and the fitted diffusion barrier. The uncertainties indicate a 95% confidence interval.

It is worth noting that that the difference in the activation energies (~0.02 eV) obtained from Arrhenius fits to the NO desorption rates on Pd(111) and Pd(332) in Figure 2 might lead one to believe that that the energy preference for steps is negligible. However, this naïve conclusion neglects entropy considerations. Our modeling approach, self-consistently, links the energetic difference between two binding sites with the associated change in the density of states. Thus, energetic stabilization of NO at the step leads to a decrease in the local density of states, compared to a terrace site. As a consequence, ΔE_{ST} is substantially larger than the difference of activation energies, as the entropic contribution to the desorption rate also differs between terraces and steps. We emphasize that the absolute upper limit of NO step preference on Pd(332) is 0.08

https://doi.org/10.1021/acs.jpcc.1c02965
J. Phys. Chem. C 2021, 125, 11773−11781

eV—higher energy values cannot be compensated by entropic arguments.

For quantitative comparison, we have used our TST predicted rates to obtain Arrhenius activation energies and prefactors using

$$E_a^{mod} = k_B T^2 \frac{\partial \ln(k(T))}{\partial T} \quad (16)$$

$$A^{mod} = k(T) \exp\left(\frac{E_a^{mod}}{k_B T}\right) \quad (17)$$

We obtain E_a^{mod} and A^{mod} for Pd(111) and Pd(332) between 800 and 620 K and show the predicted values as gray and red shaded regions in the insets of Figure 2. Our results are consistent with the small difference of activation energies and prefactors obtained from the Arrhenius fits, indicating the high fidelity of the TST analysis.

CONCLUSIONS

In this work, we have reported experimental desorption rates of nitric oxide from Pd(111) and Pd(332) between 620 and 800 K. We employed molecular-beam surface scattering with velocity-resolved kinetics, which allowed us to work at conditions where NO decomposition is substantially suppressed compared to desorption. We have applied TST analysis to the accurate desorption rate data to determine the NO binding energy to Pd(111) (1.766 ± 0.024 eV), its diffusion barrier on (111) terraces (0.29 ± 0.11 eV), and the NO stabilization energy at steps of Pd(332) ($0.060^{+0.015}_{-0.030}$ eV). While it is well-known that the prediction of binding site preference for CO at transition metal surfaces can only be achieved with DFT methods beyond the GGA level,[6−10,23] little effort has been made to investigate similar effects on chemisorption energies for NO. DFT functionals at the GGA level predict a broad range of binding energies: 2.07−2.34 eV (PW91),[39−41] 2.21 eV (PBE),[10] and 1.49−1.84 eV (RPBE).[39−41] The work of Huang and Mason[10] suggests, that by using the DFT+U method, the GGA chemisorption energies of NO at Pd(111) are corrected by 10−15%.[10] With this correction, they suggest a binding energy of 1.95 eV (initially using the PBE functional, 2.21 eV) which is still 0.16 eV higher than the upper boundary of the binding energy derived from our measurements.

These differences likely underestimate the error in the DFT-GGA binding energies. The NO binding energy determined in this work applies to the low NO coverage limit, whereas most DFT-GGA calculations were conducted for 0.25 ML coverage, where NO−NO repulsion energies are important.[15,40] Hence, the calculations presented above will yield somewhat higher values of the binding energy in the limit of low NO coverage, making the agreement between theory and experiment even less satisfying.

We have also been able to estimate the NO diffusion barrier on Pd(111) to be 0.29 ± 0.11 eV. To the best of our knowledge, this is the first experimental report of this parameter. DFT calculations report values of 0.22 eV (PBE with DFT+U),[10] 0.32 eV (PBE and RPBE),[40,41] and 0.36 eV (PW91).[41] All are in good agreement with our results. While binding energies are very sensitive to the choice of the functional, diffusion barriers show little dependence, indicating that the GGA overbinding clearly demonstrated by the comparison to our experimental binding energy is approximately independent of the position along the diffusion pathway.

We have determined the step-terrace energy preference for NO at Pd(332) to be $0.060^{+0.015}_{-0.030}$ eV. Despite this energy preference, the desorption rates on Pd(111) and Pd(332) are very similar. The reason for this is that with the energetic stabilization of NO at steps also the local density of states is consequently reduced. These two effects cancel mutually and lead to similar magnitude of the desorption rates with weak differences in their temperature dependence. Small energetic preference for steps, such as in the NO/Pd(332) system, tends thus to be missed in the analysis of experimental desorption data.

The energetic stabilization on steps is contrasted by previous experimental work that concluded stronger binding of NO at terraces.[17] However, we note that those experiments rely on an assumed assignment of HREELS vibrational spectra, and furthermore, the step type associated with the (211) crystal used in that work was different than the step type found on (332) crystals. So far, there have been no DFT calculations that can be directly compared to our work. However, DFT calculations on similar step sites find that NO binding is stabilized by 0.06 eV compared to the terrace site,[39] quite close in magnitude to our reported value of ΔE_{ST}.

AUTHOR INFORMATION

Corresponding Authors

Theofanis N. Kitsopoulos − *Institute for Physical Chemistry, Georg-August University of Goettingen, 37077 Goettingen, Germany; Department of Dynamics at Surfaces, Max Planck Institute for Biophysical Chemistry, 37077 Goettingen, Germany; Department of Chemistry, University of Crete, Heraklion, Greece; Institute of Electronic Structure and Laser − FORTH, Heraklion, Greece;* orcid.org/0000-0001-6228-1002; Email: theo.kitsopoulos@mpibpc.mpg.de

Alec M. Wodtke − *Institute for Physical Chemistry, Georg-August University of Goettingen, 37077 Goettingen, Germany; Department of Dynamics at Surfaces, Max Planck Institute for Biophysical Chemistry, 37077 Goettingen, Germany; International Center for Advanced Studies of Energy Conversion, Georg-August University of Goettingen, 37077 Goettingen, Germany;* orcid.org/0000-0002-6509-2183; Email: alec.wodtke@mpibpc.mpg.de

Authors

Dmitriy Borodin − *Institute for Physical Chemistry, Georg-August University of Goettingen, 37077 Goettingen, Germany; Department of Dynamics at Surfaces, Max Planck Institute for Biophysical Chemistry, 37077 Goettingen, Germany*

Igor Rahinov − *Department of Natural Sciences, The Open University of Israel, 4353701 Raanana, Israel*

Jan Fingerhut − *Institute for Physical Chemistry, Georg-August University of Goettingen, 37077 Goettingen, Germany*

Michael Schwarzer − *Institute for Physical Chemistry, Georg-August University of Goettingen, 37077 Goettingen, Germany*

Stefan Hörandl − *Institute for Physical Chemistry, Georg-August University of Goettingen, 37077 Goettingen, Germany*

Georgios Skoulatakis − *Department of Dynamics at Surfaces, Max Planck Institute for Biophysical Chemistry, 37077 Goettingen, Germany*

https://doi.org/10.1021/acs.jpcc.1c02965
J. Phys. Chem. C 2021, 125, 11773−11781

Dirk Schwarzer − *Department of Dynamics at Surfaces, Max Planck Institute for Biophysical Chemistry, 37077 Goettingen, Germany;* orcid.org/0000-0003-3838-2211

Complete contact information is available at: https://pubs.acs.org/10.1021/acs.jpcc.1c02965

Notes

The authors declare no competing financial interest.

■ ACKNOWLEDGMENTS

D.B. thanks the BENCh graduate school, funded by the DFG (389479699/GRK2455). I.R. gratefully acknowledges the support by Israel Science Foundation, ISF (grant no. 2187/19), and by the Open University of Israel Research Authority (grant no. 31044). T.N.K., G.S., M.S., and J.F. acknowledge support from the European Research Council (ERC) under the European Union's Horizon 2020 research and innovation programme (grant agreement no. [833404]).

■ REFERENCES

(1) Sabatier, P. *Catalysis in Organic Chemistry*; D. Van Nostrand Company: New York, 1922.
(2) Che, M. Nobel Prize in Chemistry 1912 to Sabatier: Organic Chemistry or Catalysis? *Catal. Today* **2013**, *218*, 162−171.
(3) Norskov, J. K.; Bligaard, T.; Rossmeisl, J.; Christensen, C. H. Towards the Computational Design of Solid Catalysts. *Nat. Chem.* **2009**, *1*, 37−46.
(4) Medford, A. J.; Vojvodic, A.; Hummelshoj, J. S.; Voss, J.; Abild-Pedersen, F.; Studt, F.; Bligaard, T.; Nilsson, A.; Norskov, J. K. From the Sabatier Principle to a Predictive Theory of Transition-Metal Heterogeneous Catalysis. *J. Catal.* **2015**, *328*, 36−42.
(5) Hammer, B.; Norskov, J. K. Theoretical Surface Science and Catalysis - Calculations and Concepts. *Adv. Catal.* **2000**, *45*, 71−129.
(6) Feibelman, P. J.; Hammer, B.; Norskov, J. K.; Wagner, F.; Scheffler, M.; Stumpf, R.; Watwe, R.; Dumesic, J. The CO/Pt(111) Puzzle. *J. Phys. Chem. B* **2001**, *105*, 4018−4025.
(7) Ren, X. G.; Rinke, P.; Scheffler, M. Exploring the Random Phase Approximation: Application to CO Adsorbed on Cu(111). *Phys. Rev. B: Condens. Matter Mater. Phys.* **2009**, *80*, 045402.
(8) Kresse, G.; Gil, A.; Sautet, P. Significance of Single-Electron Energies for the Description of CO on Pt(111). *Phys. Rev. B: Condens. Matter Mater. Phys.* **2003**, *68*, 073401.
(9) Gil, A.; Clotet, A.; Ricart, J. M.; Kresse, G.; Garcia-Hernandez, M.; Rosch, N.; Sautet, P. Site Preference of CO Chemisorbed on Pt(111) from Density Functional Calculations. *Surf. Sci.* **2003**, *530*, 71−86.
(10) Huang, X.; Mason, S. E. DFT-GGA Errors in NO Chemisorption Energies on (111) Transition Metal Surfaces. *Surf. Sci.* **2014**, *621*, 23−30.
(11) Lew, W.; Lytken, O.; Farmer, J. A.; Crowe, M. C.; Campbell, C. T. Improved Pyroelectric Detectors for Single Crystal Adsorption Calorimetry from 100 to 350 K. *Rev. Sci. Instrum.* **2010**, *81*, 024102.
(12) Fischer-Wolfarth, J. H.; Hartmann, J.; Farmer, J. A.; Flores-Camacho, J. M.; Campbell, C. T.; Schauermann, S.; Freund, H. J. An Improved Single Crystal Adsorption Calorimeter for Determining Gas Adsorption and Reaction Energies on Complex Model Catalysts. *Rev. Sci. Instrum.* **2011**, *82*, 024102.
(13) Bertolo, M.; Jacobi, K. NO Adsorption on Pd(111) in the Temperature-Range between 20 and 300 K. *Surf. Sci.* **1990**, *226*, 207−220.
(14) Loffreda, D.; Simon, D.; Sautet, P. Vibrational Frequency and Chemisorption Site: A DFT-Periodic Study of NO on Pd(111) and Rh(111) Surfaces. *Chem. Phys. Lett.* **1998**, *291*, 15−23.
(15) Schmick, H. D.; Wassmuth, H. W. Adsorption, Desorption and Reaction-Kinetics of Nitric-Oxide on a Stepped Pd(111) Surface. *Surf. Sci.* **1982**, *123*, 471−490.
(16) Wickham, D. T.; Banse, B. A.; Koel, B. E. Adsorption of Nitrogen-Dioxide and Nitric-Oxide on Pd(111). *Surf. Sci.* **1991**, *243*, 83−95.
(17) Ramsier, R. D.; Gao, Q.; Waltenburg, H. N.; Lee, K. W.; Nooij, O. W.; Lefferts, L.; Yates, J. T. NO Adsorption and Thermal-Behavior on Pd Surfaces - a Detailed Comparative-Study. *Surf. Sci.* **1994**, *320*, 209−237.
(18) Hammer, B.; Norskov, J. K. Adsorbate Reorganization at Steps: NO on Pd(211). *Phys. Rev. Lett.* **1997**, *79*, 4441−4444.
(19) Harding, D. J.; Neugebohren, J.; Hahn, H.; Auerbach, D. J.; Kitsopoulos, T. N.; Wodtke, A. M. Ion and Velocity Map Imaging for Surface Dynamics and Kinetics. *J. Chem. Phys.* **2017**, *147*, 013939.
(20) Neugebohren, J.; et al. Velocity-Resolved Kinetics of Site-Specific Carbon Monoxide Oxidation on Platinum Surfaces. *Nature* **2018**, *558*, 280−283.
(21) Borodin, D.; Golibrzuch, K.; Schwarzer, M.; Fingerhut, J.; Skoulatakis, G.; Schwarzer, D.; Seelemann, T.; Kitsopoulos, T.; Wodtke, A. M. Measuring Transient Reaction Rates from Nonstationary Catalysts. *ACS Catal.* **2020**, *10*, 14056−14066.
(22) Serri, J. A.; Tully, J. C.; Cardillo, M. J. The Influence of Steps on the Desorption Kinetics of NO from Pt(111). *J. Chem. Phys.* **1983**, *79*, 1530−1540.
(23) Golibrzuch, K.; Shirhatti, P. R.; Geweke, J.; Werdecker, J.; Kandratsenka, A.; Auerbach, D. J.; Wodtke, A. M.; Bartels, C. CO Desorption from a Catalytic Surface: Elucidation of the Role of Steps by Velocity-Selected Residence Time Measurements. *J. Am. Chem. Soc.* **2015**, *137*, 1465−75.
(24) Hirsimaki, M.; Suhonen, S.; Pere, J.; Valden, M.; Pessa, M. Adsorption, Desorption and Surface Reactions of CO and NO on Pd (320). *Surf. Sci.* **1998**, *402*, 187−191.
(25) Tully, J. C. The Dynamics of Adsorption and Desorption. *Surf. Sci.* **1994**, *299*, 667−677.
(26) Borodin, D.; et al. Following the Microscopic Pathway to Adsorption through Chemisorption and Physisorption Wells. *Science* **2020**, *369*, 1461−1465.
(27) Zeng, Z. H.; Da Silva, J. L.; Li, W. X. Theory of Nitride Oxide Adsorption on Transition Metal (111) Surfaces: A First-Principles Investigation. *Phys. Chem. Chem. Phys.* **2010**, *12*, 2459−2470.
(28) Sprowl, L. H.; Campbell, C. T.; Arnadottir, L. Hindered Translator and Hindered Rotor Models for Adsorbates: Partition Functions and Entropies. *J. Phys. Chem. C* **2016**, *120*, 9719−9731.
(29) Kemp, J. D.; Pitzer, K. S. The Entropy of Ethane and the Third Law of Thermodynamics Hindered Rotation of Methyl Groups. *J. Am. Chem. Soc.* **1937**, *59*, 276−279.
(30) McClurg, R. B.; Flagan, R. C.; Goddard, W. A. The Hindered Rotor Density-of-States Interpolation Function. *J. Chem. Phys.* **1997**, *106*, 6675−6680.
(31) Bajpai, A.; Mehta, P.; Frey, K.; Lehmer, A. M.; Schneider, W. F. Benchmark First-Principles Calculations of Adsorbate Free Energies. *ACS Catal.* **2018**, *8*, 1945−1954.
(32) Campbell, C. T.; Sprowl, L. H.; Árnadóttir, L. Equilibrium Constants and Rate Constants for Adsorbates: Two-Dimensional (2d) Ideal Gas, 2d Ideal Lattice Gas, and Ideal Hindered Translator Models. *J. Phys. Chem. C* **2016**, *120*, 10283−10297.
(33) Huber, K. P., Herzberg, G. *Constants of Diatomic Molecules. In: Molecular Spectra and Molecular Structure*; Springer: Boston, MA, 1979.
(34) Brown, J. M.; Cole, A. R. H.; Honey, F. R. Magnetic Dipole Transitions in Far Infrared-Spectrum of Nitric-Oxide. *Mol. Phys.* **1972**, *23*, 287−295.
(35) Pirug, G.; Bonzel, H. P.; Hopster, H.; Ibach, H. Vibrational-Spectra of Nitric-Oxide Chemisorbed on Pt(100). *J. Chem. Phys.* **1979**, *71*, 593−598.
(36) Over, H.; Gierer, M.; Bludau, H.; Ertl, G. Anisotropic Thermal Displacements of Adsorbed Atoms and Molecules on Surfaces Studied by Low-Energy Electron Diffraction. *Phys. Rev. B: Condens. Matter Mater. Phys.* **1995**, *52*, 16812−16829.

(37) Lahee, A. M.; Toennies, J. P.; Woll, C. Low-Energy Adsorbate Vibrational-Modes Observed with Inelastic Helium Atom Scattering - CO on Pt(111). *Surf. Sci.* **1986**, *177*, 371−388.
(38) Ha, J. S.; Sibener, S. J. Measurement of Low-Energy Frustrated Vibrational-Modes of CO on Ni(111) Via Inelastic Electron-Scattering. *Surf. Sci.* **1991**, *256*, 281−287.
(39) Hammer, B. The NO+CO Reaction Catalyzed by Flat, Stepped, and Edged Pd Surfaces. *J. Catal.* **2001**, *199*, 171−176.
(40) Gajdos, M.; Hafner, J.; Eichler, A. Ab Initio Density-Functional Study of NO on Close-Packed Transition and Noble Metal Surfaces: I. Molecular Adsorption. *J. Phys.: Condens. Matter* **2006**, *18*, 13−40.
(41) Herron, J. A.; Tonelli, S.; Mavrikakis, M. Atomic and Molecular Adsorption on Pd(111). *Surf. Sci.* **2012**, *606*, 1670−1679.

https://doi.org/10.1021/acs.jpcc.1c02965
J. Phys. Chem. C 2021, 125, 11773−11781

4.2 *"Following CO's Microscopic Pathways to Adsorption on Au(111)"*

Author contributions: PRS and IR performed the experiments. The initial idea for the model came from IR. The initial analysis was done by PRS and IR. MH and HG developed the PES. TZ and DS conducted the TPD experiments at Au(332). The analysis methods were developed by AK, DJA and DB. All experimental data was reanalyzed by DB. TST rate constants and sticking coefficients were modeled by DB. The paper was written by IR, AMW and DB. All authors contributed to the discussion of the results. All authors contributed to the revision of the manuscript.

SURFACE CHEMISTRY

Following the microscopic pathway to adsorption through chemisorption and physisorption wells

Dmitriy Borodin[1,2], Igor Rahinov[3], Pranav R. Shirhatti[4], Meng Huang[5], Alexander Kandratsenka[2], Daniel J. Auerbach[2], Tianli Zhong[1,2], Hua Guo[5], Dirk Schwarzer[2], Theofanis N. Kitsopoulos[1,2,6,7], Alec M. Wodtke[1,2,8]*

Adsorption involves molecules colliding at the surface of a solid and losing their incidence energy by traversing a dynamical pathway to equilibrium. The interactions responsible for energy loss generally include both chemical bond formation (chemisorption) and nonbonding interactions (physisorption). In this work, we present experiments that revealed a quantitative energy landscape and the microscopic pathways underlying a molecule's equilibration with a surface in a prototypical system: CO adsorption on Au(111). Although the minimum energy state was physisorbed, initial capture of the gas-phase molecule, dosed with an energetic molecular beam, was into a metastable chemisorption state. Subsequent thermal decay of the chemisorbed state led molecules to the physisorption minimum. We found, through detailed balance, that thermal adsorption into both binding states was important at all temperatures.

Adsorption of molecules to metal surfaces initiates most heterogeneous chemistry; yet, the precise way it occurs is difficult to study. When hot molecules collide with a surface, they must lose translational and internal energy, ultimately reaching equilibrium with the solid. This process may involve forming transient chemical bonds to the surface, leading to chemisorption (*1*) or, alternatively, noncovalent (physisorption) interactions. Furthermore, which interactions prevail can strongly influence surface chemistry (*2*, *3*); for example, chemisorbed O_2 on Pt(111) can dissociate producing highly reactive adsorbed atoms (*4*), whereas physisorbed O_2 desorbs, remaining unreactive (*5*).

Generally, molecules adsorb through both physisorption and chemisorption interactions (*5*). Hence, adsorption generally involves passage through multiple binding states before equilibrium is achieved. This process represents a complex and fundamental problem that is not well understood. For example, one might think that physisorption is more important for accommodation of impinging molecules. For the CO/Au(111) system, density functional theory (DFT) calculations suggest that when chemisorbed, CO binds with a fixed (OC-Au) orientation and at specific sites; but when physisorbed, CO is nearly a free rotor and weakly bound at every surface site (*6*). When a molecule collides randomly at different surface sites and with random orientation, physisorption is statistically favored. But this scenario ignores that rates of equilibration depend strongly on the nature of the interactions. For example, the vibrational relaxation time of chemisorbed CO to Cu is ~2 ps (*7*) but is 49 ps for CO physisorbed to Au (*8*).

The intricate interplay between physisorption and chemisorption states is believed to take place in precursor-mediated adsorption (*9*–*11*) and bear on a broad variety of surface science applications, ranging from catalytic steam reforming (*10*, *11*) to designing molecular switches (*12*). Despite being central to a dynamical picture of surface chemistry, predicting and probing adsorption pathways exceeds our current understanding. Not only is electronic structure theory challenged to provide accurate, simultaneous descriptions of covalent and noncovalent interactions, but also no experiments so far have been reported that directly follow adsorption pathways through chemisorption and physisorption wells. Recently, we observed that vibrationally excited CO can trap to a gold surface, equilibrating

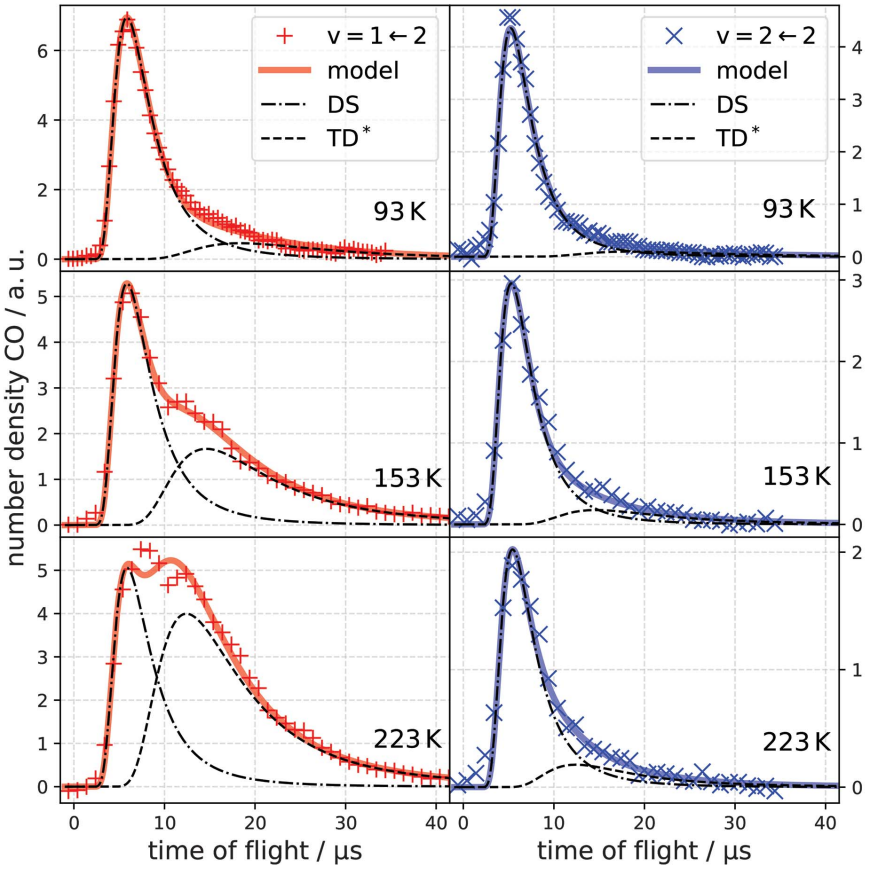

Fig. 1. State-specific time of flight traces. Measured TOF traces of CO(v = 1) (+ symbols) and CO(v = 2) (× symbols) at different surface temperatures along with their global fits (solid lines) revealing the DS (dash-dotted lines) and TD* (dashed lines) components. The incidence energy is E_i = 0.32 eV. The surface temperature is indicated in each panel. The method for decomposing the data into DS and TD* components is explained in the supplementary materials, section 1.

[1]Institute for Physical Chemistry, Georg-August University of Göttingen, Tammannstraße 6, 37077 Göttingen, Germany. [2]Department of Dynamics at Surfaces, Max Planck Institute for Biophysical Chemistry, Am Faßberg 11, 37077 Göttingen, Germany. [3]Department of Natural Sciences, The Open University of Israel, 4353701 Raanana, Israel. [4]Tata Institute of Fundamental Research, 500046 Hyderabad, India. [5]Department of Chemistry and Chemical Biology, University of New Mexico, Albuquerque, NM 87131, USA. [6]Department of Chemistry, University of Crete, 71003 Heraklion, Greece. [7]Institute of Electronic Structure and Laser, FORTH, 71110 Heraklion, Greece. [8]International Center for Advanced Studies of Energy Conversion, Georg-August University of Göttingen, Tammannstraße 6, 37077 Göttingen, Germany.
*Corresponding author. Email: alec.wodtke@mpibpc.mpg.de

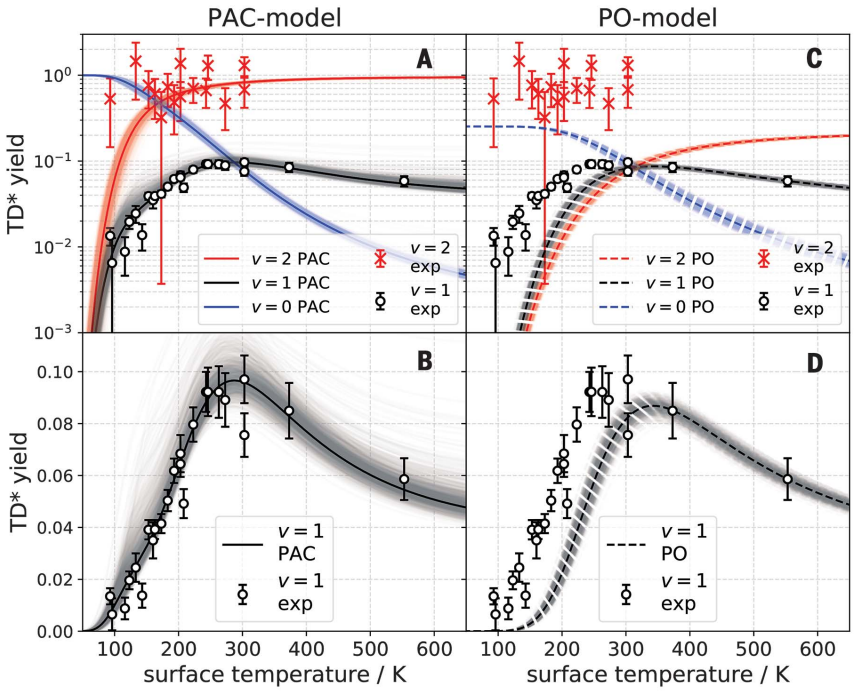

Fig. 2. Vibrational state–specific yields of desorbing molecules. (**A** to **D**) Experimentally observed CO(v = 1) (open circles) and CO(v = 2) (× symbols) passing through the TD* channel. The error bars indicate a 90% confidence interval. Black and red solid lines are results of fits to the PAC model. (A) Logarithmic scale. (B), Linear scale. Black and red dashed lines represent the PO model. (C) Logarithmic scale. (D) Linear scale. Blue solid line (PAC) and blue dashed line (PO) represent the desorbing yield of CO(v = 0) stemming from ultimate vibrational relaxation of CO(v = 2). The shading represents the uncertainty of the fit determined by random number sampling of the fit parameter distribution (supplementary materials, section 4).

both its rotational and translational motion but without vibrational equilibration (*13*). As we will show below, this feature provided a distinctive opportunity to follow the microscopic pathways of adsorption and equilibration on the surface, using the vibrational relaxation time as an internal clock.

Specifically, we have demonstrated that the adsorption of energetic CO to Au(111) involves pathways through a chemisorption state recently predicted by theory (*6*) as well as the known physisorption state (*8*, *14*). We showed that although the overall free-energy minimum is the physisorbed state, when an energized molecule collides with the surface, it first becomes trapped in a metastable chemisorption state, in which it rapidly loses its vibrational and translational energy to the solid. We were able to derive the adsorption energies of the two states and the height of the energy barrier separating them. Application of the principle of detailed balance allowed us to use the information obtained in this molecular beam experiment to probe the pathway to thermal adsorption. This analysis showed that thermal adsorption involves substantial contributions from both chemisorption and physisorption at all temperatures.

The experiment involved scattering a molecular beam of optically prepared CO(v = 2, J = 1) from Au(111) (where v is a vibrational quantum number and J is a rotational quantum number) and state-selectively detecting, at controlled surface temperature (T_S), the time of flight (TOF) of the thermally desorbing molecules in v = 1 and v = 2, in addition to directly scattered ones (supplementary materials, materials and methods) (*13*). We were inspired by recent theoretical predictions of a metastable chemisorption state with a short vibrational relaxation lifetime (*6*). We knew that the physisorbed molecule undergoes slow vibrational relaxation (*8*, *15*). So, it was clear that by varying T_S and thereby controlling the molecule's surface residence time, the

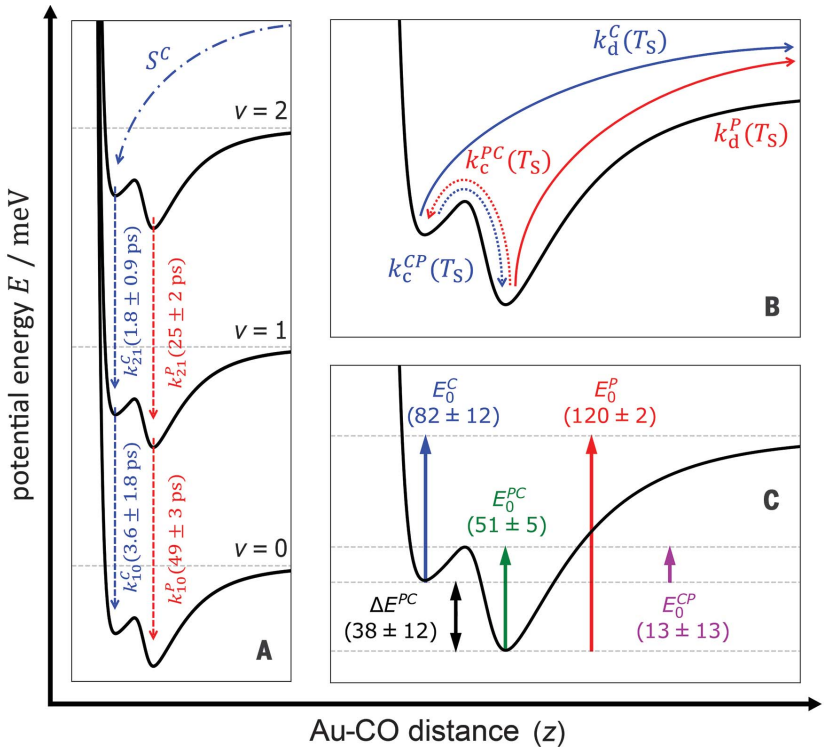

Fig. 3. The PAC model. (**A** and **B**) Rate processes describing the competition between (A) vibrational relaxation (dashed arrows) and (B) desorption (solid arrows) and interconversion between the chemisorbed and physisorbed states (dotted arrows). (**C**) Features of the Au(111)-CO interaction potential, derived from a fit of the PAC model to the experimental data.

temperature-independent vibrational relaxation lifetime could act as an internal clock, sensitive to the type of interaction that the molecule had experienced at the surface. Our goal was to obtain quantitative insight into the pathways to adsorption from measured populations of thermally desorbing CO in v = 1 and 2, which depend on the branching ratio between vibrational relaxation and desorption.

Examples of these TOF experiments are shown in Fig. 1. The traces comprise a high-speed direct scattering (DS) component and a slower component owing to thermal desorption (TD*) of CO(v = 1 or 2). We use the notation TD* to indicate that the vibrational relaxation is not complete despite all other degrees of freedom (rotation and translation) being thermalized with the surface (*13*).

We fit data such as that of Fig. 1 to a simple model on the basis of the principle of detailed balance (supplementary materials, section 1). Hence, the fitting also yields the sticking probability versus incidence kinetic energy for CO on Au(111), which agrees well with a previous report (*16*). This procedure also yielded vibrational state–specific populations of desorbing molecules in the TD* channel (Fig. 2). CO (v = 2) (Fig. 2, × symbols) dominated the TD* channel, but some CO also desorbed in v = 1 (Fig. 2, open circles). Desorption yield varied strongly with T_S and can be fit with a kinetic model involving physisorption and chemisorption states (PAC model).

The PAC model is shown schematically in Fig. 3, A and B, and is described further in the supplementary materials, section 2. The important rate processes are thermal desorption from the chemisorbed (k_d^C) and physisorbed (k_d^P) states; thermal conversion between the two states (k_c^{PC} and k_c^{CP}); and vibrational relaxation of chemisorbed (k_{ij}^C) and physisorbed (k_{ij}^P) molecules. Here, i and j are vibrational quantum numbers.

We have fit the vibrational state–specific quantities of Fig. 2, the × symbols and open circles, to the PAC model, optimizing only five parameters: k_{10}^C, the relaxation rate constant of chemisorbed CO(v = 1); ΔE^{PC}, the energy of the chemisorbed state relative to the physisorbed state; E_0^{PC}, the barrier to convert physisorbed molecules to the chemisorbed state; $A_c^{PC}(T_S)$, the Arrhenius prefactor to convert physisorbed molecules to the chemisorbed state; and S^C, the fraction of CO(v = 2) molecules that initially trap into the chemisorbed state. The values of parameters that result from the fits are provided in table S4.

Other constants in the model are known independently from temperature-programmed desorption (TPD) (*17*) or pump-probe measurements of vibrational lifetimes (*8*) or can be derived with the help of first-principles electronic structure calculations (*6*) and transition state theory (supplementary materials, section 3) (*18*–*20*).

The best fit is shown in Fig. 2, A and B, as black and red lines; all of the relevant rate constants are tabulated in the supplementary materials, section 3. A host of useful information emerges from the fitting. The derived energy landscape for adsorption is shown in Fig. 3C; this includes an analysis of TPD data yielding E_0^P, the desorption barrier from the physisorbed state (supplementary materials, section 3). We emphasize that S^C = 0.98 ± 0.02, indicating nearly exclusive initial population of the metastable chemisorption well in the molecular beam experiment and that molecules initially trapped in the chemisorbed state need only pass over a small barrier (of E_0^{CP} = 13 meV) to reach the physisorbed state, which is qualitatively consistent with predictions of first-principles electronic structure theory (*6*).

We also attempted to fit our results to models that neglect the chemisorption state (supplementary materials, section 5). In a physisorption-only (PO) model, adsorption occurs into a single physisorption well, and vibrational relaxation competes with thermal desorption. The PO model (Fig. 2, C and D, dashed black and red lines) failed to reproduce the experimental observations. Thermal desorption from the physisorbed state was much slower than from the chemisorbed state ($k_d^P \ll k_d^C$) (table S3); therefore, vibrationally excited molecules that were physisorbed relaxed more rapidly than they desorbed. This is mainly due to adsorbate entropy; the physisorbed state has the high entropy of a two-dimensional ideal gas, and the chemisorbed state has the low entropy of a hindered translator. By contrast, in the PAC model, rapid thermal desorption from the chemisorption well allowed CO (v = 2) to survive, which is in agreement with experiment. We also tried a third model that was based on the hypothesis that vibrational relaxation from v = 2 → 1 occurred during the subpicosecond interaction time of a DS event and that a fraction of these nascent CO(v = 1) molecules became trapped in the physisorption well (supplementary materials, section 5). This model also fails to describe the experimental observations.

The PAC model was supported by first-principles predictions of the coexistence of chemisorbed and physisorbed states (*6*). The precise energies of these states, the height of the energy barrier separating them, and the predicted vibrational relaxation lifetimes all depend on the specific assumptions of the theory and the chosen functional. Nevertheless, they were consistent with the experimentally derived values (supplementary materials, section 6).

Calculated microscopic pathway fluxes obtained from the experimentally validated PAC model are shown in Fig. 4. This includes pathways leading to CO(v = 1) desorption (Fig. 4A) and adsorption to the lowest energy physisorption minimum (Fig. 4B). Details on how pathway fluxes were determined are provided in the supplementary materials, section 7. At all temperatures, the first step toward equilibrium involved trapping of CO(v = 2) into the chemisorption well. This state can then undergo vibrational relaxation, thermal

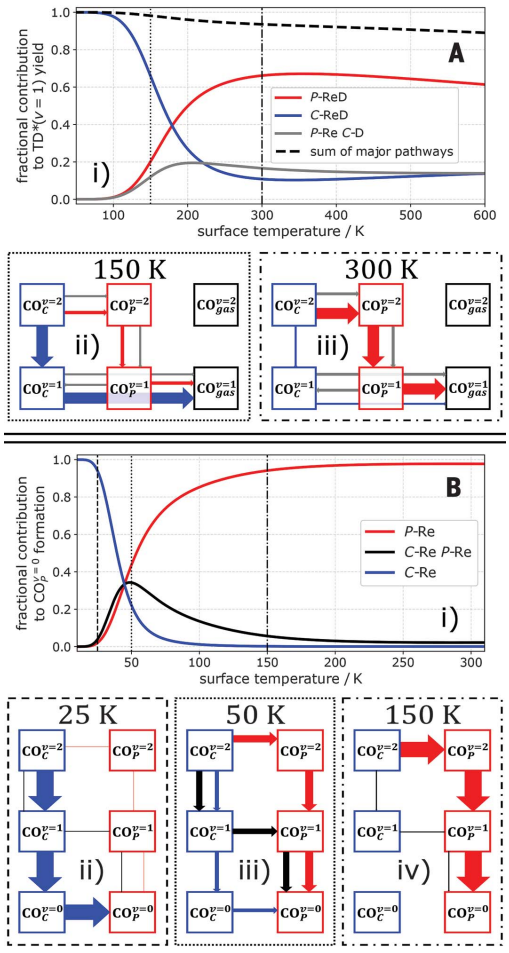

Fig. 4. Pathway fluxes for adsorption and desorption. (**A**) (Top) (i) Relative contribution of the most prominent pathways to CO(v = 1) desorption flux. (Bottom) Schematics illustrating the relative contributions of three most prominent pathways at (ii) low (150 K) and (iii) high (300 K) surface temperatures. (**B**) (Top) (i) Relative contribution of most prominent pathways of CO(v = 2) ultimate relaxation and formation of physisorbed CO(v = 0) on the surface. (Bottom) (ii to iv) Schematic representations of the most prominent pathways at different surface temperature regimes. The arrow thickness is proportional to the relative importance of the formation pathways.

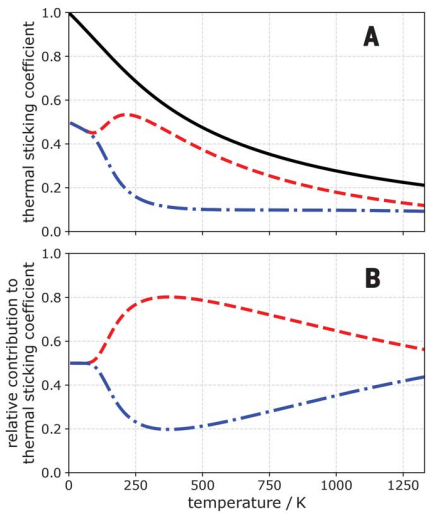

Fig. 5. Thermal adsorption into chemisorbed and physisorbed states. (**A**) Thermal sticking coefficients. (**B**) Relative contributions. Colored lines denote thermal adsorption into the physisorption (dashed, red) and chemisorption (dash-dotted, blue) wells. The black line is the total thermal adsorption coefficient.

desorption, and/or thermal conversion to the physisorbed state. At low temperatures (Fig. 4, blue lines and blue arrows), vibrational relaxation dominated because it required no thermal activation. At high temperature (Fig. 4, red lines and red arrows), conversion to the physisorbed species was rapid, followed by either desorption or vibrational relaxation. At intermediate temperatures, the physisorbed state could even transfer back to the chemisorption well.

Although the observations of these experiments are specific to vibrationally inelastic pathways to adsorption, the conclusions of this work are not. Vibrational motion has little influence on adsorption (*21*), and by applying the principle of detailed balance (supplementary materials, section 8) we can use the quantities derived from these molecular beam experiments to better understand thermal adsorption of CO to Au(111). Key results are shown in Fig. 5.

Thermal adsorption occurred initially into both the chemisorbed and physisorbed states, with similar probabilities at all temperatures. At low temperatures, adsorption into the two states was equally important. At intermediate temperatures, the higher-entropy physisorbed state increased in relative importance. But at the highest surface temperatures, the translational and rotational entropy of the chemisorbed CO approached that of the physisorbed CO and the chemisorbed CO again grew in importance. This increased entropy of the chemisorbed CO resulted from a greater sampling of higher-energy chemisorption states at different binding sites of the surface.

We also reconcile in Fig. 5 the seemingly contradictory observations that the molecular beam experiments exclusively probed the chemisorption state, but low-temperature thermal dosing experiments have never shown evidence of the chemisorption state (*8*, *14*). In the molecular beam experiments that used high-energy CO, the chemisorption state could be initially and selectively populated; these states were the same ones that became increasingly important in the high temperature range shown in Fig. 5. The high-temperature thermal adsorption still populated both states because of the large width of the Maxwell-Boltzmann distribution, while the width of the energy distribution in the molecular beam was orders of magnitude narrower (supplementary materials, section 8). For low-temperature dosing, it is clear now that both binding states were initially populated. But when we consider the small barrier to interconversion, it turns out that experiments have never been done at low enough temperatures to suppress thermal interconversion of the chemisorption to the physisorption state (supplementary materials, section 9). This analysis suggests an interesting experiment that could be carried out in the future. If a molecular beam with 0.3 eV incidence energy is used to selectively populate the chemisorption state and the surface is cooled below 5 K, it may be possible to suppress interconversion to the physisorbed state long enough to observe directly the metastable chemisorbed state.

Last, we highlight the implications of our work within the context of an industrially important class of catalytic reactions. Catalytic oxidation is initiated on a variety of metals through the reaction $O_{2(g)} \rightarrow O_2^*$, where O_2^* can be either physisorbed or chemisorbed. Hence, catalytic activation of oxygen, similar to many other examples in heterogeneous catalysis, is a complex network of thermal rate processes that includes adsorption into, desorption from, and interconversion between physisorbed and chemisorbed molecular states (*5*). Although these qualitative statements are long established, it has never before been possible to construct a model that accurately describes such a kinetic adsorption network. As a result, there has also never been a way to test to what extent theory is capable of describing such an intricately balanced set of rate processes. With the results presented here, we successfully determined the rate constants of a thermal adsorption network, revealing the fundamental energetic and entropic characteristics of adsorption and desorption. We also showed that the results can be understood from first principles by comparison with a multidimensional potential energy surface constructed with DFT (*6*). This result strengthens the foundation on which a predictive theory of surface chemistry and heterogeneous catalysis may continue to be developed.

REFERENCES AND NOTES

1. H. Jiang *et al.*, *Science* **364**, 379–382 (2019).
2. D. A. King, M. G. Wells, *Surf. Sci.* **29**, 454–482 (1972).
3. D. A. King, M. G. Wells, *Proc. R. Soc. London Ser. A* **339**, 245–269 (1974).
4. T. Zambelli, J. V. Barth, J. Wintterlin, G. Ertl, *Nature* **390**, 495–497 (1997).
5. C. T. Rettner, C. B. Mullins, *J. Chem. Phys.* **94**, 1626–1635 (1991).
6. M. Huang *et al.*, *Phys. Rev. B* **100**, 201407 (2019).
7. M. Morin, N. J. Levinos, A. L. Harris, *J. Chem. Phys.* **96**, 3950–3956 (1992).
8. S. Kumar *et al.*, *Phys. Rev. Lett.* **123**, 156101 (2019).
9. D. E. Brown, D. J. Moffatt, R. A. Wolkow, *Science* **279**, 542–544 (1998).
10. E. Dombrowski, E. Peterson, D. Del Sesto, A. L. Utz, *Catal. Today* **244**, 10–18 (2015).
11. R. Moiraghi *et al.*, *J. Phys. Chem. Lett.* **11**, 2211–2218 (2020).
12. W. Liu, S. N. Filimonov, J. Carrasco, A. Tkatchenko, *Nat. Commun.* **4**, 2569 (2013).
13. P. R. Shirhatti *et al.*, *Nat. Chem.* **10**, 592–598 (2018).
14. J. Pischel, A. Pucci, *J. Phys. Chem. C* **119**, 18340–18351 (2015).
15. I. Lončarić, M. Aldučin, J. I. Juaristi, D. Novko, *J. Phys. Chem. Lett.* **10**, 1043–1047 (2019).
16. C. T. Rettner, *J. Chem. Phys.* **99**, 5481–5489 (1993).
17. D. P. Engelhart, R. J. V. Wagner, A. Meling, A. M. Wodtke, T. Schäfer, *Surf. Sci.* **650**, 11–16 (2016).
18. J. C. Tully, *Surf. Sci.* **299-300**, 667–677 (1994).
19. T. L. Hill, *Introduction to Statistical Thermodynamics* (Dover Publication, 1986).
20. M. Jørgensen, H. Grönbeck, *J. Phys. Chem. C* **121**, 7199–7207 (2017).
21. A. M. Wodtke, H. Yuhui, D. J. Auerbach, *Chem. Phys. Lett.* **413**, 326–330 (2005).
22. D. Borodin, CO(v=2) scattering on Au(111) (TPD, TOF and TD*(v=1,2)). Zenodo (2020).

ACKNOWLEDGMENTS

Funding: A.M.W. acknowledges support from the SFB1073 under project A04, from the Deutsche Forschungsgemeinschaft (DFG), and financial support from the Ministerium für Wissenschaft und Kultur (MWK) Niedersachsen and the Volkswagenstiftung under grant INST 186/901-1 to build parts of the experimental apparatus. A.M.W. and A.K. also acknowledge the Max Planck Society for the Advancement of Science. I.R. and A.M.W. acknowledge support from the Niedersächsisch-Israelische Gemeinschaftsvorhaben under project 574 7 022. T.N.K. acknowledges the European Research Council (ERC) under the European Union's Horizon 2020 research and innovation program (grant agreement 833404). D.B. thanks the BENCh graduate school, funded by the DFG (389479699/GRK2455). M.H. and H.G. acknowledge support from the National Science Foundation (grant CHE-1462109). H.G. also acknowledges the Alexander von Humboldt Foundation for a Humboldt Research Award. **Author contributions:** D.B., I.R., P.R.S., D.J.A., and A.K. developed the PAC kinetic model and carried out the analysis. I.R. and D.B. wrote the supplementary materials. I.R. and P.R.S. performed experiments that led to the data presented in this work. M.H. and H.G. performed the theoretical calculations and analyzed the results. T.Z. and D.S. carried out TPD measurements that were essential to the application of the PAC model. D.S. and T.N.K. participated in discussion of the results, analysis, data interpretation, and revisions. D.J.A. had major conceptual contributions to data interpretation and supplementary materials and manuscript revisions. A.M.W. wrote the manuscript and participated in revisions. All authors provided critical input to the writing of the paper. **Competing interests:** None declared. **Data and materials availability:** There are no restrictions on materials used in this work. All data needed to evaluate the conclusions in the paper are present in the paper or the supplementary materials and are publicly available in the repository (*22*).

SUPPLEMENTARY MATERIALS

science.sciencemag.org/content/369/6510/1461/suppl/DC1
Materials and Methods
Supplementary Text
Figs. S1 to S13
Tables S1 to S4
References (*23*–*41*)

24 May 2020; accepted 14 July 2020
10.1126/science.abc9581

science.sciencemag.org/content/369/6510/1461/suppl/DC1

Supplementary Material for

Following the microscopic pathway to adsorption through chemisorption and physisorption wells

Dmitriy Borodin, Igor Rahinov, Pranav R. Shirhatti, Meng Huang, Alexander Kandratsenka, Daniel J. Auerbach, Tianli Zhong, Hua Guo, Dirk Schwarzer, Theofanis N. Kitsopoulos, Alec M. Wodtke*

*Corresponding author. Email: alecwodtke@googlemail.com

Published 18 September 2020, *Science* **369**, 1461 (2020)
DOI: 10.1126/science.abc9581

This PDF file includes:

Materials and Methods

Experimental

The experimental setup has been previously described (*13*, *23*, *24*). The molecular beam scattering apparatus consisted of four interconnected chambers. In the source chamber, a gas mixture of CO seeded in H_2 was expanded in a supersonic jet from a home-built, piezo-driven pulsed valve (3 bar backing pressure, 298 K operating temperature, 1 mm diameter orifice). The beam passed through a 1.5 mm diameter skimmer and two differential pumping chambers before entering the ultra-high vacuum scattering chamber (base pressure $\sim 2 \times 10^{-10}$ Torr). The experiments were carried out at incidence energy of ~ 0.32 eV obtained by supersonic expansion of 20% CO in H_2. Vibrationally excited CO($v = 2$) molecules were prepared using infrared light from a high power nanosecond laser system with nearly Fourier transform limited (150 MHz) bandwidth that provided 10 mJ/pulse. This preparation was enough to efficiently pump the overtone CO($v = 0 \rightarrow 2$) R(0) transition at 4263.835 cm^{-1}. The incident and scattered CO molecules in $v = 2{,}1$ were state specifically detected by (2+1) REMPI using the two-photon $B\ ^1\Sigma^+ \leftarrow X\ ^1\Sigma^+$ system. The resulting ions were collected to and detected by two Multi-Channel Plates in Chevron configuration. The incident CO molecules were pumped via overtone pumping to $v = 2$ at ~0.5 mm from the surface and the scattered molecules were detected at 8.4 or 5.9 mm from the Au(111) surface. State-to-state TOF distributions were obtained by recording the ion signal as function of the delay between IR-PUMP and REMPI-PROBE laser pulses.

The Au(111) surface (orientation accuracy better than 0.1°, purity 99.999 %, MaTeck GmbH), mounted on a 4-axis (x, y, z, Θ) translation stage, was positioned approximately 180 mm from the nozzle. Before every set of experiments, the surface was prepared by sputtering with Ar ions (3 keV, 30 min), followed by annealing at surface temperature T_S > 950K for ~ 60 min. Cleanliness of the surface was checked using Auger electron spectroscopy.

DFT calculations

The DFT calculations were performed with the BEEF-vdW functional (*25*) using the Vienna Ab Initio Simulation Package (VASP) (*26*, *27*). In these calculations, the Au(111) surface is represented by a four-layer slab model in a 3×3 unit cell and only the two top layers of Au atoms are allowed to move. The kinetic energy cut-off of the basis set is 450 eV and a 5×5×1 Monkhorst-Pack grid is used to sample the Brilliouin zone. More details of the calculations can be found elsewhere (*6*).

The fitting of the TOF experiments (TOF traces and TD* yields) was done using the LMFIT package (*28*) (Version 0.9.14) in python (Version 3.7.4). The numerical simulation of the TPD experiment is done using LSODA from the ODEPACK library wrapped in the scipy (Version 1.4.1) module solve_ivp.

Supplementary Text

1. Fitting the TOF Data

The solid lines of Fig. 1 in the main text were derived by a fitting procedure that we now describe. Both CO(v=2) and CO(v=1) TOF traces are composed of direct scattering (DS) and trapping-desorption (TD*) components:

$$TOF(t) = DS(t) + TD^*(t), \quad (1)$$

where the direct scattering is modelled as a streaming Maxwell-Boltzmann distribution, which has been previously shown to be a realistic model of direct scattering (*29*).

$$DS(t) = \frac{A}{t^4}\exp\left(-\frac{\left(\frac{l}{t}-v_0\right)^2}{\alpha^2}\right). \quad (2)$$

Here, t is the flight time over l, the distance from the surface to the detection laser beam. v_0 is the streaming velocity, α is the width parameter and A is the amplitude of direct scattering. The surface-residence time is negligible compared to t.

According to the principle of detailed balance, the observed trapping desorption component of the translational energy distribution, $TD^*(E, T_S)$, can be expressed as the product of the sticking coefficient, $S_0(E, \theta)$, and the Maxwell Boltzmann distribution $F(E, T_S)$:

$$TD^*(E, T_S) = S_0(E, \theta) \times F(E, T_S). \quad (3)$$

We use an empirical form where the sticking probability decays exponentially with the normal component of translational energy, $E_n = E\cos(\theta)$:

$$S_0(E, \theta) = \exp(-\gamma \times E_n) = \exp\big(-\gamma \times E\cos(\theta)\big), \quad (4)$$

This leads to Eq (5) where the TD^* component is expressed in the time domain as:

$$TD^*(t) = \frac{B}{t^4}\exp\left(-\frac{m\left(\frac{l}{t}\right)^2}{2k_B} \times \left(\frac{1}{T_S} + \gamma\cos(\theta)\right)\right). \quad (5)$$

Here B is the amplitude of the trapping-desorption component and m is the mass of the CO molecule.

We performed a fit to both CO(v=2) and CO(v=1) data sets simultaneously where A and B and v_0 vary with surface temperature and $S_0(E, \theta)$ and α do not. With this procedure and a knowledge of the REMPI laser intensity and transition strengths (*30*), we extract CO(v=2 & v=1) relative populations (Fig. 2 of the main text). This procedure also yields the sticking coefficient as a function of the normal component of the incidence translational energy, $S_0(E_n)$, which agrees well with results of Rettner (*16*) in Fig. S1. We emphasize that the empirical parameter γ is optimized by fitting the TOF data of this work, yet it is in excellent agreement with the absolute sticking probabilities obtained in Ref. (*16*) using the King & Wells method. Strictly speaking, the sticking coefficient from TOF data can be determined only over a limited range of energies (solid

line of Fig. S1). Nevertheless, the (perhaps fortuitous) agreement with Ref. (2) over a wider range (dotted line of Fig. S1) allows us to use this Eq. (4), unrestricted by considerations of limited energy ranges. This is elaborated further in SM Section 8.

2. The PAC Model for Trapping-Desorption

In order to describe the observed T_S dependence of the TD* yields of CO(v=1) and CO(v=2), we constructed a microkinetic model involving two binding states within which CO can be found in one of three vibrational states v=2, 1, or 0. This was inspired by a recently published DFT potential energy surface (PES) (*6*) – see Figure S2.

According to the PAC model, the CO(v=2) arriving to the surface can initially land in one of two states;

(1) Chemisorption well, ***C***, where relaxation from v=2→1 and from v=1→0 can occur. Note that according to DFT calculations with the BEEF-vdW functional (*6*) the PES for CO/Au(111) interaction possesses chemisorption wells at several binding sites. These include ***metastable*** chemisorption wells (***mC***), at the hollow sites and bridge sites (red and blue curves in Fig. S2), situated, at ~ 2.2 Å from the surface, as well as a ***stable*** chemisorption well (***sC***) at the top site located ~ 2.8 Å from the surface plane (black curve in Fig. S2). Due to the very low barrier from the metastable to stable chemisorption wells (< 20 meV) the initial population of the metastable chemisorption well results in a fast conversion to the stable chemisorption well. Back-conversion will be unimportant due to the large barrier ($>$ 160 meV).

For the sake of simplicity in our kinetic model, we assume there is only one chemisorption well corresponding the lowest energy well. In DFT, this well is stable (lower in energy than the physisorption well) but we treat the well depth of the chemisorption well, and the barrier to the physisorption well as adjustable parameters. As we shall see, in the PAC model, ***C*** turns out to be metastable. Using one chemisorption well amounts to ignoring the elementary step of fast interconversion from the higher lying metastable states and desorption from these states. Further discussion of the higher lying DFT metastable states is given in SM Section 8.

(2) A physisorption well ***P*** is located at 4.5 Å from the surface plane. The CO(v=1→0) vibrational lifetime in this state was recently determined experimentally to be 49±3 ps by direct PUMP-PROBE experiments (*8*). This is consistent with a small electron transfer from the surface to the 2π* orbital of CO. In general, the partial occupation of CO 2π* orbital increases and, consequently, the adsorbate vibrational lifetime decreases at shorter distances to the surface (*6, 15*).

We emphasize that there is no prior assumption as to the partitioning of the initially trapped CO(v=2) between the ***chemisorption*** and ***physisorption*** wells – this partitioning is fitted in the PAC model. Once adsorbed in either ***C*** or ***P,*** CO(v=2) can desorb back to the gas-phase or undergo vibrational relaxation to produce CO(v=1), which can, in turn, desorb or further relax to the vibrational ground state CO(v=0). Conversion between ***C*** and ***P*** for both CO(v=2 and 1) is also considered.

Tables S1 and S2 summarize the energy barriers and the rate constants of the processes considered in the microkinetic model used in this work.

Figure S3 shows a flow-chart of the optimization procedure used to fit the PAC model to the experimental data. The output of this algorithm includes the quantities listed in Tables S1 and S2.

We construct the rate equations governing the populations in the four states of interest:

- $[\mathrm{CO}_C^{v=2}]$ (CO in v=2 at the chemisorption well),
- $[\mathrm{CO}_P^{v=2}]$ (CO in v=2 at the physisorption well),
- $[\mathrm{CO}_C^{v=1}]$ (CO in v=1 at the chemisorption well), and
- $[\mathrm{CO}_P^{v=1}]$ (CO in v=1 at the physisorption well).

The incoming flux of CO(v=2) is represented by dosing function $\rho(t)$ and is partitioned between the chemisorption - $S^C\rho(t)$ – and physisorption wells – $(1-S^C)\rho(t)$. S^C denotes the fraction of CO(v=2) molecules that initially trap into the chemisorption well and is used along with the parameters listed in Table S1 and S2 to fit the scattering data shown in Fig. 2 of the main text. The rate equations are:

$$\frac{\mathrm{d}[\mathrm{CO}_C^{v=2}]}{\mathrm{d}t} = -\left(k_{\mathrm{c}}^{CP} + k_{21}^{C} + k_{\mathrm{d}}^{C}\right)[\mathrm{CO}_C^{v=2}] + k_{\mathrm{c}}^{PC}[\mathrm{CO}_P^{v=2}] + S^C\rho(t), \quad (6)$$

$$\frac{\mathrm{d}[\mathrm{CO}_P^{v=2}]}{\mathrm{d}t} = k_{\mathrm{c}}^{CP}[\mathrm{CO}_C^{v=2}] - \left(k_{\mathrm{c}}^{PC} + k_{\mathrm{d}}^{P} + k_{21}^{P}\right)[\mathrm{CO}_P^{v=2}] + (1-S^C)\rho(t), \quad (7)$$

$$\frac{\mathrm{d}[\mathrm{CO}_C^{v=1}]}{\mathrm{d}t} = k_{21}^{C}[\mathrm{CO}_C^{v=2}] - \left(k_{\mathrm{c}}^{CP} + k_{\mathrm{d}}^{C} + k_{10}^{C}\right)[\mathrm{CO}_C^{v=1}] + k_{\mathrm{c}}^{PC}[\mathrm{CO}_P^{v=1}], \quad (8)$$

$$\frac{\mathrm{d}[\mathrm{CO}_P^{v=1}]}{\mathrm{d}t} = k_{21}^{P}[\mathrm{CO}_P^{v=2}] + k_{\mathrm{c}}^{CP}[\mathrm{CO}_C^{v=1}] - \left(k_{\mathrm{c}}^{PC} + k_{\mathrm{d}}^{P} + k_{10}^{P}\right)[\mathrm{CO}_P^{v=1}], \quad (9)$$

and can be rewritten as a rate matrix, column vector of time-dependent populations and a column vector of time-dependent incoming flux:

$$\frac{\mathrm{d}}{\mathrm{d}t}\begin{pmatrix}[\mathrm{CO}_C^{v=2}]\\ [\mathrm{CO}_P^{v=2}]\\ [\mathrm{CO}_C^{v=1}]\\ [\mathrm{CO}_P^{v=1}]\end{pmatrix} = \begin{pmatrix} -\left(k_{\mathrm{c}}^{CP} + k_{21}^{C} + k_{\mathrm{d}}^{C}\right) & k_{\mathrm{c}}^{PC} & 0 & 0\\ k_{\mathrm{c}}^{CP} & -\left(k_{\mathrm{c}}^{PC} + k_{\mathrm{d}}^{P} + k_{21}^{P}\right) & 0 & 0\\ k_{21}^{C} & 0 & -\left(k_{\mathrm{c}}^{CP} + k_{\mathrm{d}}^{C} + k_{10}^{C}\right) & k_{\mathrm{c}}^{PC}\\ 0 & k_{21}^{P} & k_{\mathrm{c}}^{CP} & -\left(k_{\mathrm{c}}^{PC} + k_{\mathrm{d}}^{P} + k_{10}^{P}\right)\end{pmatrix}\begin{pmatrix}[\mathrm{CO}_C^{v=2}] + S^C\rho(t)\\ [\mathrm{CO}_P^{v=2}] + (1-S^C)\rho(t)\\ [\mathrm{CO}_C^{v=1}]\\ [\mathrm{CO}_P^{v=1}]\end{pmatrix}. \quad (10)$$

The total ***time-dependent desorbing flux*** of CO(v=1) and CO(v=2) is given by Eq. (11) and Eq. (12), respectively:

$$F_{\mathrm{d}}(\mathrm{CO}^{v=1}) = k_{\mathrm{d}}^{C}[\mathrm{CO}_C^{v=1}](t) + k_{\mathrm{d}}^{P}[\mathrm{CO}_P^{v=1}](t), \quad (11)$$

$$F_{\mathrm{d}}(\mathrm{CO}^{v=2}) = k_{\mathrm{d}}^{C}[\mathrm{CO}_C^{v=2}](t) + k_{\mathrm{d}}^{P}[\mathrm{CO}_P^{v=2}](t). \quad (12)$$

To obtain the ***time-integrated desorbing flux (desorption yields)***, there is no need to derive the flux first and then integrate it. In general, systems of coupled first-order differential equations, such as the one presented here, obey analytical solutions and so do the corresponding yields. In the general case, the kinetics of these systems is defined by:

$$\dot{\boldsymbol{n}} = \underline{\boldsymbol{\mathcal{K}}}\,\boldsymbol{n} + \boldsymbol{b}(t), \quad (13)$$

where $\boldsymbol{n}$ is the column vector of populations, $\dot{\boldsymbol{n}}$ its time derivative, $\underline{\boldsymbol{\mathcal{K}}}$ is the rate matrix, and the column vector $\boldsymbol{b}(t)$ is the time-dependent incoming flux. By integrating the left- and right-hand sides of Eq. (13):

$$\int_0^\infty \dot{\boldsymbol{n}} dt = \underline{\boldsymbol{\mathcal{K}}} \int_0^\infty \boldsymbol{n} dt + \int_0^\infty \boldsymbol{b}(t) dt, \qquad (14)$$

we have:

$$\boldsymbol{n}_\infty - \boldsymbol{n}_0 = \underline{\boldsymbol{\mathcal{K}}}\, \boldsymbol{\zeta} + \boldsymbol{a}, \qquad (15)$$

where $\boldsymbol{\zeta} = \int_0^\infty \boldsymbol{n}\, dt$ is a column-vector of the time-integrated populations, $\boldsymbol{a} = \int_0^\infty \boldsymbol{b}(t)\, dt$ is a column-vector of the time-integrated incoming flux, and $\int_0^\infty \dot{\boldsymbol{n}}\, dt = \boldsymbol{n}_\infty - \boldsymbol{n}_0$. Because Eq. (15) is a system of ***algebraic*** equations, it can be analytically solved for $\boldsymbol{\zeta}$:

$$\boldsymbol{\zeta} = \underline{\boldsymbol{T}}\, (\boldsymbol{n}_\infty - \boldsymbol{n}_0 - \boldsymbol{a}). \qquad (16)$$

If the rate matrix $\underline{\boldsymbol{\mathcal{K}}}$ is not singular, then $\underline{\boldsymbol{T}} = \underline{\boldsymbol{\mathcal{K}}}^{-1}$. Because an open system is considered, $\boldsymbol{n}_\infty = \boldsymbol{0}$, and therefore:

$$\boldsymbol{\zeta} = -\underline{\boldsymbol{T}}\, (\boldsymbol{n}_0 + \boldsymbol{a}). \qquad (17)$$

The solution (Eq. (17)) for the system of algebraic equations shows the equivalence of populating the states either by the incoming beam ($\boldsymbol{a}$) or by defining the initial conditions ($\boldsymbol{n}_0$). Having the solution yields analytical expressions for the total desorbing yields (time-integrated desorbing fluxes, specified in Eqs. (11) and (12)). More importantly, having the analytical expressions allows to run the fitting routine faster and thus more reliably when finding the global minimum for the underlying problem – fitting the total desorption yields obtained in scattering experiments.

This fit enables us to extract:

1) S^C – the fractional initial population of the chemisorbed state,
2) ΔE^{PC} – the energy difference between physisorption and chemisorption energy well minima,
3) E_0^{PC} and $A_c^{PC}(T_S)$ – the *barrier* and the *pre-factor* for the conversion from physisorption to chemisorption well, respectively and
4) τ_{21}^C & τ_{10}^C, the vibrational relaxation times in chemisorption well for v=2→1 and for v=1→0, respectively.

For the vibrational lifetimes for v=2→1 and v=1→0 in the physisorption well, values obtained in the very recent PUMP-PROBE experiment (*8*) and harmonic oscillator scaling (*31*, *32*) were used. See Figure S3 and Tables S1 and S2 for further details and overview of the parameters and the analysis protocol. The explicit expressions for the pre-exponential factors of the rate constants and the desorption barrier in the physisorption well were obtained based on the TPD data and DFT PES with the BEEF-vdW functional (*6*), as elaborated in further details in SM Section 3.

3. <u>Determining Rate Constants</u>

Many rate constants are needed to implement the PAC model. Fortunately, many of them are known or can be found from experimental data. For example, the lifetime of CO(v =1) in the physisorption well has been directly measured (*8*). Other rate constants can be found using first principles electronic structure theory to obtain reactant and transition state entropies – then with transition state theory, activation barriers can be derived from experiment. We describe this in the following subsections.

<u>Modelling elementary rate constants using first principles entropies</u>

We have used Transition State Theory (TST) (*18*) to help determine some of the rate constants used in this work. For desorption, the TST expression is the following.

$$k(T_S) = \langle S_0 \rangle \frac{k_B T_S}{h} \frac{Q^{\neq}}{Q_{ad}} \exp\left(-\frac{E_0}{k_B T_S}\right). \qquad (18)$$

Here, k_B is the Botlzmann constant, E_0 is the desorption barrier, $\langle S_0 \rangle$ is the mean sticking coefficient and Q_{ad} is the partition function for the adsorbate. Because adsorption of CO to Au(111) has no barrier, E_0 is equal to the adsorption energy and $Q^{\neq}$ is the partition function of the gas-phase CO molecule reduced by one translational degree of freedom to account for the desorption coordinate.

We used information from DFT to obtain Q_{ad} for both the chemisorbed and physisorbed species (*6*). We then used the calculated Q_{ad} to fix the rate constants' pre-factors and we fit energy barriers to match experimental data. We do not use the DFT energies – they are not accurate enough. In the next sections, we systematically explain how the partition functions of the chemisorbed and physisorbed molecules were obtained for different degrees of freedom.

Hindered and unhindered translation across the surface plane

DFT shows that chemisorbed CO preferably binds to the top site and has a diffusion barrier of at least 0.15 eV to a neighboring top site (see Figure S4). At the low surface temperatures of our experiments, we use a 2D hindered translation partition function (*19, 20*) to describe the motion of the chemisorbed CO molecules parallel to the surface.

$$Q_{HT}(T_S) = \frac{2\pi m k_B T_S}{h^2} A \int_0^1 \int_0^1 \exp\left(-\frac{V(x,y)}{k_B T_S}\right) \mathrm{d}x\mathrm{d}y. \qquad (19)$$

Here, m is the mass of the CO molecule, T_S the surface temperature, A the area of the reference cell and $V(x,y)$ the potential energy for CO in the up-right configuration across the surface obtained from first principles electronic structure calculations – see Fig.S4. For the physisorbed CO, DFT energies vary by only about 5 meV across the surface plane – hence, we use a partition function for 2D free translation for the physisorbed state.

$$Q_{FT}(T_S) = Q_{HT}(T_S; V(x,y) = 0) = \frac{2\pi m k_B T_S}{h^2} A. \qquad (20)$$

In passing we note that this can be derived from Eq. (19) assuming that $V(x,y) = 0$.

CO hindered rotation

DFT calculations show that the barrier for rotation of the chemisorbed CO molecule perpendicular to its bond axis (characterized by the polar angle θ) is at least 0.4 eV irrespective of binding site. Therefore, we treat this hindered rotation as a vibration, approximated by a harmonic oscillator. Because the CO molecule is bound with its bond axis perpendicular to the surface plane, we may ignore azimuthal rotation around its bond axis. The vibrational force constants of the hindered rotation are determined from the curvature of the DFT PES vs. θ for the top, bridge and hollow sites (see Figure S5). The resulting vibrational frequencies are 49.5, 90.4 and 98.9 cm^{-1} for top, hollow and bridge site, respectively, for which partition function we used a harmonic oscillator form without correction for zero-point energy:

$$Q_{\mathrm{HO}}(T_{\mathrm{S}}) = \frac{1}{1-\exp\left(-\frac{h\nu}{k_{\mathrm{B}}T_{\mathrm{S}}}\right)}. \qquad (21)$$

This means that all barriers resulting from our fits are automatically zero-point energy corrected.

DFT data for physisorbed CO shows that rotation perpendicular to its bond axis has a barrier of only 30 meV. Yet it is not a free rotor. The total energy of the rotating molecule will be given by:

$$H_{\mathrm{HR}} = \frac{L_\theta^2}{2I} + \frac{L_\phi^2}{2I\sin^2(\theta)} + V(\theta,\phi), \qquad (22)$$

where L_ϕ and L_θ are the angular momenta for the two angles and *I* is the moment of inertia for the CO molecule bound to the surface. $V(\theta,\phi)$ is teh potential energy along the polar angle θ and azimuthal angle ϕ again obtained from DFT. Integration of Eq. (23), the classical partition function for hindered rotation,

$$Q_{\mathrm{HR}}(T_{\mathrm{S}}) = \frac{1}{h^2}\int_{\phi=0}^{2\pi}\int_{\theta=0}^{\pi}\int_{L_\phi=-\infty}^{+\infty}\int_{L_\theta=-\infty}^{+\infty}\exp\left(-\frac{H_{\mathrm{HR}}}{k_{\mathrm{B}}T_{\mathrm{S}}}\right)\mathrm{d}L_\theta\mathrm{d}L_\phi\mathrm{d}\theta\mathrm{d}\phi. \qquad (23)$$

leads to Eq. (24)

$$Q_{\mathrm{HR}}(T_{\mathrm{S}}) = \frac{k_{\mathrm{B}}T_{\mathrm{S}}}{4\pi B}\int_{\theta=0}^{\pi}\int_{\phi=0}^{2\pi}\sin(\theta)\exp\left(-\frac{V(\theta,\phi)}{k_{\mathrm{B}}T_{\mathrm{S}}}\right)\mathrm{d}\phi\mathrm{d}\theta, \qquad (24)$$

where *B* is the rotational constant of physisorbed CO. Potential energy along the azimuthal angle ϕ is smooth within 4 meV and, therefore, is approximated as uniform. The configuration integral thus does not depend on ϕ and thus Eq. (24) can be simplified to:

$$Q_{\mathrm{HR}}(T_{\mathrm{S}}) = \frac{k_{\mathrm{B}}T_{\mathrm{S}}}{2B}\int_{\theta=0}^{\pi}\sin(\theta)\exp\left(-\frac{V(\theta)}{k_{\mathrm{B}}T_{\mathrm{S}}}\right)\mathrm{d}\theta. \qquad (25)$$

The CO external stretch

DFT also provides information on the surface-adsorbate vibration (M-CO) in the chemisorption and physisorption wells. The potential energy in the chemisorption well is fitted with a Morse function (see Figure S6 blue curve). The harmonic vibrational frequencies (ω_e) are

171, 180 and 186 cm^{-1} for top, hollow and bridge site, respectively. The anharmonic vibrational frequencies ($\omega_e x_e$) are 12.4, 7.31 and 8.91 cm^{-1} for top, hollow and bridge site, respectively.

Eq. (26) presents the partition function for the external CO stretch degree of freedom.

$$Q_{\mathrm{discr}}(T_{\mathrm{S}}) = \sum_{v=0}^{v_{\max}} \exp\left(-\frac{G(v)-G(0)}{k_{\mathrm{B}}T_{\mathrm{S}}}\right), \qquad (26)$$

where $G(v)$ is the energy associated with the vibrational quantum state v from the Morse-oscillator and $v_{\max}$ is the last bound vibrational state.

For the physisorbed molecule, a harmonic oscillator function fits the DFT PES well – See Fig. S6 red curve). The corresponding harmonic vibrational frequencies are 60.2, 71.5 and 69.1 cm^{-1} for top, hollow and bridge site, respectively. For the hollow and bridge site we use Eq. (26) and truncate the series at at 0.12 eV above the minimum. This truncation energy is determined self-consistently by comparing to the TPD fits. For the physisorbed molecule at the top site, we truncate the series at the barrier for physisorption-to-chemisorption conversion.

Constructing the total partition function

The CO has different vibrational frequencies when it is adsorbed to different binding sites. The probability of populating the respective binding site will influence the contribution of each frequency towards the total vibrational partition function. To account for this, we use weighted contributions of each binding site for the total vibrational partition function. For the chemisorbed CO, the vibrational partition function at the binding site *m* is given by its contribution of hindered rotation (doubly degenerated mode) and the surface-adsorbate mode resulting in:

$$Q^{C}_{\mathrm{vib},m} = \left(Q^{\mathrm{HR},C}_{\mathrm{HO},m}\right)^{2} Q^{\mathrm{M-CO}_C}_{\mathrm{discr},m}. \qquad (27)$$

The weighting follows the following formulation:

$$Q^{C}_{\mathrm{vib}} = \prod_m \left(Q^{C}_{\mathrm{vib},m}\right)^{\frac{g_m \exp\left(-\frac{E_m}{k_{\mathrm{B}}T_{\mathrm{S}}}\right)}{\sum_m g_m \exp\left(-\frac{E_m}{k_{\mathrm{B}}T_{\mathrm{S}}}\right)}}, \qquad (28)$$

where g_m is the degeneracy of the binding site *m* (g_m =1, 2 and 3 for top, hollow and bridge site respectively) in the reference cell and E_m its relative energy (0, 0.14 and 0.185 eV for top, hollow and bridge site respectively) derived from the DFT PES. Using this formulation, the individual contributions to the partition function remain multiplicative. Accordingly, the vibrational partition function for the physisorbed molecule is:

$$Q^{P}_{\mathrm{vib}} = \prod_m \left(Q^{\mathrm{M-CO}_P}_{\mathrm{discr},m}\right)^{\frac{g_m}{\sum_m g_m}}. \qquad (29)$$

The energetic contribution is absent from the weighting because all binding sites are isoenergetic. The corresponding total partition function for the chemisorbed CO is then given by Eq. (30)

$$Q^{C} = Q^{C}_{\mathrm{HT}} Q^{C}_{\mathrm{vib}}, \qquad (30)$$

and that for the physisorbed CO by Eq. (31)

$$Q^P = Q^P_{\mathrm{FT}} Q^P_{\mathrm{HR}} Q^P_{\mathrm{vib}}. \quad (31)$$

Construction of rate constant expressions

As discussed above, the adsorbate entropies are obtained from DFT input data to simple classical partition functions. Top obtain transition state theory rate constants, we also need the partition function of the transition state. For desorption, this can be expressed as

$$Q^{\neq}_{\mathrm{d}} = Q_{\mathrm{FT}} Q_{\mathrm{FR}}, \quad (32)$$

where Q_{FT} is the 2D free translational partition function and Q_{FR} is the free rotational partition function for CO in the gas phase. The desorption rate constant for the physisorbed CO on Au(111) is then given by Eq. (33),

$$k^P_{\mathrm{d}}(T_{\mathrm{S}}) = \langle S_0 \rangle \frac{k_{\mathrm{B}} T_{\mathrm{S}}}{h} \frac{Q^{\neq}_{\mathrm{d}}(T_{\mathrm{S}})}{Q^P(T_{\mathrm{S}})} \exp\left(-\frac{E^P_0}{k_{\mathrm{B}} T_{\mathrm{S}}}\right), \quad (33)$$

and that for chemisorbed CO by Eq. (34)

$$k^C_{\mathrm{d}}(T_{\mathrm{S}}) = \langle S_0 \rangle \frac{k_{\mathrm{B}} T_{\mathrm{S}}}{h} \frac{Q^{\neq}_{\mathrm{d}}(T_{\mathrm{S}})}{Q^C(T_{\mathrm{S}})} \exp\left(-\frac{E^C_0}{k_{\mathrm{B}} T_{\mathrm{S}}}\right). \quad (34)$$

We emphasize here that with the approach taken, only E^P_0 and E^C_0 are varied in the fitting procedure described above. We also take into account that adsorbed CO converts between the physisorbed and the chemisorbed states. Using the partition functions of each adsorbed state we can directly express the equilibrium constant as

$$K^{PC}_{\mathrm{eq}}(T_{\mathrm{S}}) = \frac{Q^C(T_{\mathrm{S}})}{Q^P(T_{\mathrm{S}})} \exp\left(-\frac{\Delta E^{PC}}{k_{\mathrm{B}} T_{\mathrm{S}}}\right), \quad (35)$$

where $\Delta E^{PC} = E^P_0 - E^C_0$. The equilibrium constant is related to the rate constants for inter-conversion by Eq. (36),

$$K^{PC}_{\mathrm{eq}} = \frac{k^{PC}_{\mathrm{c}}}{k^{CP}_{\mathrm{c}}}, \quad (36)$$

where k^{PC}_{c} is the rate constant for conversion from physisorption to chemisorption and k^{CP}_{c} the rate constant of the reverse process. The TST expression for k^{PC}_{c} is shown in Eq. (37).

$$k^{PC}_{\mathrm{c}}(T_{\mathrm{S}}) = \frac{k_{\mathrm{B}} T_{\mathrm{S}}}{h} \frac{Q^{\neq}_{\mathrm{c}}}{Q^P} \exp\left(-\frac{E^{PC}_0}{k_{\mathrm{B}} T_{\mathrm{S}}}\right), \quad (37)$$

where E^{PC}_0 is the barrier to interconversion from physisorption to chemisorption, and $Q^{\neq}_{\mathrm{c}}$ is the partition function of the transition state. We assume that $Q^{\neq}_{\mathrm{c}}$ can be expressed by a weighted

average between the partition function for physisorption and chemisorption (divided by its respective partition function for M-CO vibration, see Section 3.1.3). This gives Eq. (38).

$$Q_{\mathrm{C}}^{\neq} = \left(\frac{Q^{P}}{Q_{\mathrm{vib}}^{P}}\right)^{\eta} \left(\frac{Q^{C}}{\prod_m \left(Q_{\mathrm{discr},m}^{\mathrm{M-CO}_C}\right)^{\frac{g_m \exp\left(-\frac{E_m}{k_{\mathrm{B}} T_{\mathrm{S}}}\right)}{\sum_m g_m \exp\left(-\frac{E_m}{k_{\mathrm{B}} T_{\mathrm{S}}}\right)}}} \right)^{1-\eta} . \qquad (38)$$

The division by the M-CO vibration partition function is required as this mode represents the interconversion reaction coordinate. The parameter η is a weighting parameter in the range between 0 and 1 which is fitted in the optimization routine to the experimentally observed TD*($v = 1,2$) yields.

In the conversion process we deal with a distribution of transition states because the molecules can convert from chemisorption to physisorption at different binding sites, thus a well-defined transition state does not exist. In addition, the barrier for conversion between chemisorption and physisorption is strongly dependent on the underlying DFT functional. By using this formulation and optimizing the weighting parameter we constrain the available range of pre-factors for the conversion process to physically meaningful values and keeping the temperature dependence reasonable.

Having discussed the ways in which TST is used to augment our knowledge of rate constants, we now show how we found the adsorption energy of the physisorbed state using experimental TPD results.

TPD desorption rate modelling – The physisorption binding energy

The desorption rate of CO from Au(111) was previously measured with temperature programmed desorption (TPD) (*17*). The authors observed a double peaked structure in the desorption spectrum of CO which was attributed to the repulsive interactions associated with a densely packed phase of CO, present at high coverages. Although this explanation is consistent with the explanations suggested by Gottfried *et al.* on an Au(110) surface (*33*), new TPD results at Au(111) and Au(332) suggests a more likely explanation. We attribute the double peaked structure to the influence of steps.

Even nominally defect-free single crystal surfaces have step-densities from 0.1 to 5%. An energetic preference of the adsorbates for steps will dramatically influence the observed desorption rates – see TPD work for CO from stepped Pt surfaces (*34, 35*). The influence of steps appears in three ways:

1) at initial CO coverages lower than the step-density the desorption trace shows a single peak,
2) at CO coverages slightly higher than the step-density the desorption trace has a major peak at high temperatures with a growing shoulder at lower surface temperatures, and
3) at CO coverages close to saturation coverage the TPD trace shows two well separated peaks.

The peak at low temperatures is associated with desorption from terraces, and the high temperature peak is associated with desorption influenced by steps. The separation of these two peaks is

dependent on the magnitude of the adsorbate stabilization at steps. Published TPD spectra of CO on Au(111) (*17*) where the crystal had an estimated 5% step density, resemble the behavior just described. We have performed new TPD measurements on a Au(111) surface with ~1% step-density as well as from Au(332) single crystal surface (step density 16.7%).

In Figure S7-A, TPD spectra resulting from our measurements on Au(111) (1% step-density) and Au(332) (16.7% step-density) surfaces are compared with those obtained on Au(111) in Ref. (*17*) (5% step-density). The TPD spectra were recorded with 1K/s heating rate and at full monolayer initial CO coverage.

To describe the observed desorption rates for CO from Au(111), we set-up a kinetic model involving step and terrace binding sites. We follow the approach of Serri, Tully and Cardillo (*36*). We approximate the surface structure as steps separated by uniformly sized terraces. We treat the surface as a 1D array of binding sites with periodic boundary conditions. The size of the reference cell depends on the underlying step-density, e.g., when the crystal has 5% step density then 20 atom rows are treated explicitly, from which one atom row is the step site and the rest are terrace sites. We introduce four elementary rate constants: k_{H} describes hops between adjacent terrace sites and hops from terrace sites to steps, k_{S} is for hops from steps to adjacent terrace sites, k_{d}^{P} is for desorption from terrace sites and $k_{\mathrm{d(S)}}^{P}$ is the rate constant for desorption from step sites. No adsorbate-adsorbate interactions are taken into account.

For the desorption rate from the terrace, we rely on the DFT PES based estimations for the desorption "pre-factor" of the physisorbed CO molecule bound to Au(111). Due to the flat PES for the physisorbed CO we estimate the k_{H} from the time required for an ideal 2D gas to move by one lattice constant ($\approx 5 \times 10^{11}\mathrm{s}^{-1}$). The k_{S} is estimated from $k_{\mathrm{H}}/K_{\mathrm{eq}}^{TS}$, where K_{eq}^{TS} is the equilibrium constant $\exp(-\Delta E^{TS}/k_B T)$ containing ΔE^{TS} representing the energetic preference of CO for step sites (fit parameter in the kinetic model). The advantage of our kinetic model is that due to explicit treatment of terrace and step sites, the configuration entropy is directly described and does not need to be included in the equilibrium constant.

In Figure S7-A, we show a comparison of the kinetic model (solid lines) with experimental data (dashed lines). The model also reliably predicts the heating rate (Figure S7-B) and initial coverage (Figure S7-C) dependence of the measured TPD.

We find the best agreement between the data (between 40 and 60 K) from three different surfaces and model with a terrace desorption barrier of 120 ± 2 meV and an energy preference for steps of 23 ± 1 meV. The small energy difference between CO at terraces and steps indicates a physisorbed CO species associated with the step. Previous work has showed that also chemisorbed CO is found at the steps (*37, 38*). With our model we can quantitatively explain the desorption rates from surfaces with different step-densities between 40 and 60 K, however we cannot determine the "location" of the here modeled step-related CO molecules, i.e., we cannot say if CO is directly bound to the step or located close nearby.

The previously deduced desorption rate constant for physisorbed CO (*13, 17*) at Au(111) differs substantially from that determined in this work – see Fig. S8. This is due to the fact that the previous analysis ognored the infleucne of steps. In our analysis, we take the full shape of the TPD traces into account by simulating the rate equations—previous work used a simple *peak maximum* method, which cannot descirbe anything more than the simplest desortption systems.

Summary of the kinetic parameters determined in this work

It is common that Arrhenius rate constant expressions determined at low temperatures have limited validity when extrapolated to high temperatures. This is primarily due to the temperature

dependent entropy difference between reactant and the transition state. In this work we have modeled these entropies based on a DFT PES—this provides applicability of the rate constants over a wide range of surface temperatures with high accuracy.

The rate constants were determined numerically and in most cases do not have a trivial analytical expression. However, their numerical values can be reproduced using an extended Arrhenius form shown in Eq. (39) that we applied between 5 and 1330 K.

$$k_{\mathrm{e}}(T) \;=\; A_{\mathrm{e}} \left(\frac{\mathrm{K}}{T}\right)^{m} \exp\left(-\frac{E_{\mathrm{e}}}{k_{\mathrm{B}}T}\right) \quad (39)$$

Here, *T* is given in Kelvin (K) and the terms in parentheses are unit-less. Unlike a simple Arrhenius equation, this function takes the temperature dependence of the pre-factor into account, allowing a better description of the rate constant over a large temperature range. The parameters of Eq. (39) are summarized in Table S3.

4. Determination of the Uncertainty Range of the Microkinetic Model Fit

The uncertainty range of the fit obtained with the microkinetic model was derived using the covariance matrix, determined from the least squares fit, in the following way:

1) Random vectors of fitted parameters are drawn from the underlying multivariate Gaussian distribution; this directly accounts for parameter correlation.
2) Only physically realistic parameter vectors were used. That is, vectors producing negative activation energies and/or relaxation rates were discarded. The model is re-evaluated with the random parameter vector and is shown (with high transparency) in Fig. 2 of the main text.
3) The procedure was performed 10000 times resulting in ≈ 7000 physically meaningful vectors. The distribution spanned by the physically meaningful vectors is referred to as the filtered parameter distribution.

The filtered distributions are used for the final parameter and error determination. The model with fitted values and the model with the expectation value of the filtered distribution have a relative standard deviation $<5\%$ across the entire experimental temperature range. The values of the fitting parameters are given in Table S4.

5. Evaluating alternatives to the proposed PAC mechanism

We are interested to know if alternatives to the proposed relaxation trapping and desorption mechanism can be found that explain the observations of this work. We explored two alternative mechanisms. In the PO model, we assume no chemisorption state exists. In this case trapping occurs directly into the physisorption state and vibrational relaxation competes with desorption. In another "direct trapping" (DT) model, we consider the fact that incident CO($v = 2$) molecules indeed undergo direct v=2→1 vibrational relaxation in a direct scattering process and that it is generally believed that the strongest interaction resulting in vibrational quantum number change occurs at the repulsive wall; that is, close to the turning point of a direct scattering trajectory. The DT model poses the question: is it possible that some directly scattered molecules, after being converted to CO($v = 1$) at the inner turning point of the trajectory, could be trapped into the

physisorption well before escaping. After a finite residence time these molecules could desorb and contribute to the observed CO($v = 1$) desorption yield. This model would offer an alternative explanation to our observations that would not require trapping into a chemisorbed state.

To test both of these hypotheses, we need only modify the initial conditions vector—Eq. (10)—used in the PAC model to have the form:

$$\begin{pmatrix} (1-r^C)S^C\rho(t) \\ (1-r^P)(1-S^C)\rho(t) \\ S^C r^C \rho(t) \\ r^P(1-S^C)\rho(t) \end{pmatrix}. \qquad (40)$$

The additional terms, r^C and r^P, are instantaneous relaxation probabilities that determine together with S^C, the initial population of $\boldsymbol{C}$ and $\boldsymbol{P}$ in v=1, respectively. The PO model obtains when all CO(v=2) molecules initially trap in $\boldsymbol{P}$, $S^C = 0$, and the conversion rate constant to $\boldsymbol{C}$, k_c^{PC}, is set to zero in addition $r^C = r^P = 0$. The DT model obtains when $S^C$is fixed to be 0 and $r^P > 0$.

Figure S9 shows the outcome of simulations, fixing elements of the initial conditions vector and specific rate constants to define the mechanism. Panels A and E show the optimized fits of the PO and PAC models, respectively (similar to Figure 2 in the main text). The PO model clearly fails. Panel C shows the PAC model, forcing all initial trapping to occur in the physisorption state. This result is barely distinguishable from the PO model. PAC model with CO($v = 2$) initially populating the physisorption well and 2% of direct $v = 2 \rightarrow 1$ vibrational relaxation and trapping ($S^C = 0$, $r^P = 0.02$; not shown here) yields a prediction virtually identical to the case Fig. S9-C. Panels B and D show models where direct trapping into the physisorption state plays a large role – in panel B the chemisorption state is eliminated whereas in panel D, the chemisorption state can be populated after initial population of the physisorption state. Again, these models do not reproduce experimental observation.

Finally, we extend the PAC model to include direct trapping with CO(v=2) initially populating the chemisorption well ($S^C = 1$) and allowing a large fraction to directly relax to CO(v=1) and trap in the chemisorption well. The extent of direct trapping ($0 \leq r^C \leq 0.25$) is varied – see Fig. S9-F. The experimental observations are reproduced in the limit that direct trapping disappears. Strictly speaking, we cannot rule out that perhaps 2% of the scattering events follow this mechanism.

In summary, the presence of the chemisorbed state is essential to reproducing the observed surface temperature dependence of both CO(v=1) and CO(v=2) desorption yields, and direct, sub-ps v=2→1 relaxation followed by trapping cannot serve as an alternative explanation.

6. Comparison of Parameters Derived from PAC Model and Theoretical Work

A comprehensive comparison to first principles predictions (*6, 15*) and PAC model results is presented in Fig. S10 along with recent findings of PUMP-PROBE experiments (*8*). Theory is in semi-quantitative agreement with experiment. For example, bit find that the vibrational lifetime of the chemisorbed state is 1-2 orders of magnitude shorter that of the physisorbed state. However, most reported predictions are too large for the vibrational lifetimes of CO($v = 1$) on Au(111), be it in the chemisorbed or physisorbed sate (see the upper panel of Fig. S10).

Only the relaxation rate of the CO($v = 1 \rightarrow 0$ coming from perturbation theory with DFT-calculated interaction potential using the PBE functional (*15*) yields a vibrational lifetime of 2.3-3.8 ps, in excellent agreement with the values extracted from our kinetic model. However, this same approach predicts a much stronger chemisorption interaction for CO than can be justified from experimental observation. In fact, there is no physisorption well in this calculation.

This clearly illustrates how DFT-calculated energy differences between physisorption and chemisorption states are subject to uncertainty and depend strongly on the underlying DFT functional and the dispersion correction used for the description of the physisorbed state. For this reason, we have used the relative energies within one single state, since in this case the binding sites will all be similarly affected by the absolute error of the binding energy and, therefore, less sensitive to the choice of the functional. In light of the above-mentioned limitations of DFT, we find it remarkable that combination of BEEF functional and dispersion correction used in the work of Huang *et al.* (*6*) comes so close to the final outcome of the kinetic model and the experiment.

The experimentally derived energetics reveal a value of $\Delta E^{PC} = 38 \pm 12$ meV for the energetically lowest chemisorption state. While being less common, the formation of metastable (or weakly bound) chemisorption state is not without precedent: for example some alkenthioles have a stronger bound physisorption state than a chemisorption state (*39*). A positive ΔE^{PC} value is also consistent with the absence of a chemisorbed state in the sum frequency generation study from Kumar *et al*. (*8*) – see SM, Section 9.

7. Analysis of the Pathways Fluxes to Desorption and Thermalization

The yield contribution of each pathway is evaluated by determining the transition probability of each participating elementary step. The probability, P_i, for the process *i*, is determined from the rate constant for process *i* (k_i), divided by the total rate ($\sum_j k_j$) de-populating the state of interest in the following way,

$$P_i = \frac{k_i}{\sum_j k_j}. \qquad (41)$$

The transition probabilities of all participating elementary steps in the sequence are multiplied to yield the pathway-specific flux (*PSF*). It can be illustrated with the following exemplary pathway of TD* (v=1) formation (red arrows and lines in Fig. 4A of the main text):

1. Conversion from ***C*** to ***P*** in v=2,
2. Relaxation from ***P*** v=2 to ***P*** v=1
3. Desorption from ***P*** in v=1

For such pathway, the probabilities from Eq. (41) will be explicitly combined to yield Eq. (42).

$$PSF(T_S) = \frac{k_c^{CP}}{k_c^{CP}+k_d^{C}+k_{21}^{C}} \times \frac{k_{21}^{P}}{k_c^{PC}+k_d^{P}+k_{21}^{P}} \times \frac{k_d^{P}}{k_c^{PC}+k_d^{P}+k_{10}^{P}} \qquad (42)$$

PSF for other channels can be understood by analogy to this.

8. Analysis of the Thermal Adsorption of CO to Au(111) and the role of DFT metastable chemisorbed states not included in the PAC model

The PAC model provides a good description of the observations of the T_S dependence of the flux of CO(v=1) trapping desorption observed when CO(v=2) is incident on a Au(111) surface at $E_i = 0.32$ eV. An essential result of the model is that initial adsorption of the incident CO(v=2) occurs almost exclusively into the chemisorption state. In this section we address the broader question of whether the chemisorbed state plays an important role in thermal adsorption of CO on Au(111). We also discuss why at high incdnece energy, CO adsorbs predominantly into the chemisorption state.

We begin using the principle of detailed balance to obtain information about the relative contributions of the physisorption and chemisorption states to adsorption of CO. We then augment the information provided by the PAC-model analysis with information from first principles electronic structure theory describing the chemisorption of CO on Au(111). This allows us to estimate additional contributions to adsorption from features of the chemisorption interaction that are not included in the PAC model.

8.1 Detailed balance analysis of the contribution of chemisorption and physisorption to thermal adsorption in the PAC model

We have already seen in SM Section 1 that a detailed balance analysis of the TOF data for the TD* component of CO(v=1) desorption yields a sticking probability for CO(v=1) that is consistent with previous measurements of the sticking probability of CO(v=0) on Au(111) (*16*). That the sticking probability is independent of the vibrational state agrees with previous observations for other systems (*21*). Thus, we can use what we learn from the PAC model based on incident CO(v=2) to analyze the role of the chemisorption state in adsorption of CO in a thermal distribution of vibrational states.

We approach this question using the principle of detailed balance. We use the PAC kinetic model to calculate the temperature dependent relative fluxes for desorption from chemisorption (***C***) and physisorption (***P***) states under thermal equilibrium. To do this, we simply integrate the rate equations of the PAC model over time using the equilibrium population in ***C*** and ***P*** as initial conditions. We consider all the processes in the PAC model: the conversion of ***C*** to ***P*** (k_{c}^{CP}), the conversion of ***P*** to ***C*** (k_{c}^{PC}), desorption from ***C*** (k_{d}^{C}) and desorption from ***P*** (k_{d}^{P}).

The corresponding rate matrix formulation is the following.

$$\frac{\mathrm{d}}{\mathrm{d}t}\begin{pmatrix}[\mathrm{CO}_C]\\ [\mathrm{CO}_P]\end{pmatrix} = \begin{pmatrix} -\left(k_{\mathrm{c}}^{CP} + k_{\mathrm{d}}^{C}\right) & k_{\mathrm{c}}^{PC} \\ k_{\mathrm{c}}^{CP} & -\left(k_{\mathrm{c}}^{PC} + k_{\mathrm{d}}^{P}\right)\end{pmatrix}\begin{pmatrix}[\mathrm{CO}_C]\\ [\mathrm{CO}_P]\end{pmatrix}. \qquad (43)$$

The initial populations of CO in ***C*** and ***P*** is then calculated from the equilibrium constant between ***P*** and ***C***, K_{eq}^{PC}, which is also available from the PAC analysis.

$$\frac{1}{[\mathrm{CO}_C]_0+[\mathrm{CO}_P]_0}\begin{pmatrix}[\mathrm{CO}_C]_0\\ [\mathrm{CO}_P]_0\end{pmatrix} = \begin{pmatrix} 1 - \frac{1}{1+K_{\mathrm{eq}}^{PC}(T_S)} \\ \frac{1}{1+K_{\mathrm{eq}}^{PC}(T_S)}\end{pmatrix} \qquad (44)$$

Due to detailed balance, the time integrated desorption flux from ***C*** and ***P***, $\varphi_C(T)$ and $\varphi_P(T)$ respectively, are identical to the thermal adsorption branching to ***C*** and ***P***. Because we use normalized concentrations in Eq. (44), $\varphi_C(T)$ and $\varphi_P(T)$ are equal to the fractional contributions

of ***C*** and ***P*** to thermal adsorption, respectively. The temperature dependence of $\varphi_C(T)$ and $\varphi_P(T)$ is shown in Fig. S11.

At low temperature the contributions of the chemisorption and physisorption states are equal, because the interchange between ***P*** and ***C*** is fast compared to desorption. As the temperature increases the relative contribution of ***C*** decreases due to a faster increase in the entropy of ***P*** at these temperatures**.** Above 500 K, the relative contribution again increases due to the increased entropy and consequent delocalization of ***C.***

8.2 <u>The contribution of additional chemisorption wells seen in DFT to adsorption</u>

In the construction of the PAC model we considered only a single chemisorption state, ***C,*** and a physisorption state, ***P***. DFT calculations for CO interacting with Au(111) reveal a more complicated situation with multiple chemisorption wells present (*6*). See SM Section 2.

The lowest energy DFT chemisorption well is characteristic of CO binding at the top site. In DFT this well is deeper than the physisorption well so it supports stable adsorption. We denote this state ***DFT-sC.*** Note that this stability differs from PAC ***C*** state, which is metastable with respect to physisorption. DFT also predicts other higher energy metastable chemisorption wells, denoted hereafter, ***DFT-mC***. These wells exist at other surface sites such as hollow and bridge sites as shown in Figure S2 and S4.

The simplification of the PAC model to a single chemisorbed state ***C*** is justified by the very low barrier(< 20 meV) between the ***DFT-mC*** wells and the lowest lying DFT chemisorption state which facilitates fast ***DFT-mC*** $\rightarrow$ ***DFT-sC*** conversion; reverse conversion is hindered by a larger barrier (> 160 meV). Furthermore, the PAC treats many features of the DFT multiple well PES by doing integrations over the PES in the calculation of the partition functions that go into the PAC rates.

Importantly, however, the PAC model does not include desorption from ***DFT-mC*** states. By detailed balance, adsorption into these states is also not included. Thus, the ***DFT-mC*** states provide additional channels for adsorption which have important implications for both understanding thermal adsorption and adsorption at high incident energy. We now turn to a discussion of these implications.

As shown in Fig. S2, adsorption into the ***DFT-mC*** states proceeds over an energy barrier, and adsorption into the PAC ***C*** and ***P*** states (Fig. 3 in the main text) has no barrier. Thus, we can get an idea of the relative contribution to adsorption of the ***DFT-mC*** states, so far omitted from our analysis, to that of the PAC ***C*** and ***P*** states if we can decompose the sticking probability vs. energy curve into activated and non-activated components.

8.3 <u>Separating the sticking probability into activated and non-activated components</u>

To decompose the sticking probability into activated and non-activated contributions, we construct a model function describing the energy dependence of sticking for these two components and fit it to the measured sticking probability data.

For the non-activated component we use the following function motivated by the Hard-Cube model (*29*)

$$S_{\mathrm{nA}}(E) = \frac{1}{1 + \exp(\alpha E + \beta)}, \qquad (45)$$

17

where α and β are adjustable parameters.

For activated adsorption we note that the sticking probability will go to zero below the barrier. Furthermore, when the incidence energy is high compared to the well depth, sticking will also be suppressed. Such behavior can be described as

$$S_{\mathrm{A}}(E) = A \times \exp(-\gamma E) \times \left[\mathrm{erf}\left(\frac{E - \langle E \rangle}{\sigma}\right) + 1\right]. \quad (46)$$

In Eq. (46), we describe the onset for the activated adsorption by an error function rather than a step function, to account for the distribution of barrier heights that results from various incidence sites and angles and surface thermal motion (*40*); $\langle E \rangle$ is the center of a supposed Gaussian barrier height distribution and σ is the distributions width. The error function is multiplied by an exponential function to account for the decay (described by γ) at higher incidence energy.

The total sticking probability is the sum of these two (nA for non-activated and A for activated) components: We call this the two-component model (TCM):

$$S_{\mathrm{TCM}}(E) = S_{\mathrm{nA}}(E) + S_{\mathrm{A}}(E). \quad (47)$$

We fit the sticking data of Rettner (*16*) using Eq. (47). We estimated and fixed values of $\langle E \rangle$ (150 meV) and σ (40 meV) based on the DFT data (*6*). We also constrained the fit so that the sticking probability is unity for $E = 0$.

The fit using the TCM is shown as a solid blue line in Fig. S12A. The non-activated ($S_{\mathrm{nA}}(E)$, dotted blue line) and activated ($S_{\mathrm{A}}(E)$, dashed blue line) contributions are also shown. The sticking coefficient extracted from TOF data using an empirical exponential expression (EEE) for the sticking coefficient (Eq. (4), SM Section 1) is also shown for comparison (red line).

Both the TCM and EEE are consistent with the experimental TOF observations but only the TCM is compatible with the result of the PAC model that adsorption of CO(v=2) at $E_i = 0.32$ eV results in nearly exclusive population of the chemisorbed state. From Fig. S12A, one can see that when CO($v = 2$) collides with Au(111) at $E_i = 0.32$ eV—the green solid line shows the incident molecular beam's energy distribution—only activated adsorption is possible. According to the TCM, 96% of the adsorption of CO comes from activated adsorption, i.e. from the contribution of the ***DFT-mC*** states to adsorption. Due to very small barriers these states will relax to the lower lying PAC ***C*** state quasi-instantaneously. In essence, at high incidence energies the ***DFT-mC*** states act as a "hook" to capture the approaching CO into the ***C*** state.

8.4 Relative contributions of chemisorption and physisorption to thermal adsorption including the role of DFT metastable chemisorbed states.

We can use the decomposition of sticking into activated and non-activated components to calculate the effect of the ***DFT-mC*** states on the relative contributions of chemisorption and physisorption to thermal adsorption.

We first calculate the total thermal sticking coefficient from $S_{\mathrm{TCM}}(E)$ defined by Eq. (47). This is done by integrating over the Maxwell-Boltzmann energy distributions, $F(E, T)$ associated with temperature T.

$$\langle S\rangle(T) = \frac{\int_0^\infty S_{\mathrm{TCM}}(E)F(E,T)\mathrm{d}E}{\int_0^\infty F(E,T)\mathrm{d}E} = \frac{\int_0^\infty S_{\mathrm{nA}}(E)F(E,T)\mathrm{d}E}{\int_0^\infty F(E,T)\mathrm{d}E} + \frac{\int_0^\infty S_{\mathrm{A}}(E)F(E,T)\mathrm{d}E}{\int_0^\infty F(E,T)\mathrm{d}E}$$
$$= \langle S\rangle_{\mathrm{nA}}(T) + \langle S\rangle_{\mathrm{A}}(T), \qquad (48)$$

Here, $\langle S\rangle_{\mathrm{nA}}(T)$ and $\langle S\rangle_{\mathrm{A}}(T)$ are the thermal sticking coefficients arising from the non-activated and activated contributions, respectively.

The activated part of thermal sticking is due to ***DFT-mC*** states.

$$\langle S\rangle_{\mathrm{A}}(T) = \langle S\rangle_{\mathrm{DFT}-mC}(T). \qquad (49)$$

The non-activated part of the thermal sticking coefficient comprises sticking into both the PAC model ***C*** and ***P*** states.

$$\langle S\rangle_{\mathrm{nA}}(T) = \langle S\rangle_{C}(T) + \langle S\rangle_{P}(T), \qquad (50)$$

From the detailed calculation given in SM Section 7.1, we know that fractional contributions of $\langle S\rangle_{\boldsymbol{C}}$ and $\langle S\rangle_{\boldsymbol{P}}$ to $\langle S\rangle_{\mathrm{nA}}(T)$ are $\varphi_C(T)$ and $\varphi_P(T)$, respectively. Therefore, we can partition the non-activated part of the thermal sticking coefficient into ***C*** and ***P*** components as follows:

$$\langle S\rangle_{C}(T) = \varphi_C(T)\,\langle S\rangle_{\mathrm{nA}}(T), \quad (51)$$
$$\langle S\rangle_{P}(T) = \varphi_P(T)\langle S\rangle_{\mathrm{nA}}(T). \quad (52)$$

Finally, we must add in activated adsorption involving the ***DFT-mC*** state to obtain the complete thermal sticking coefficient involving chemisorption. See Eq. (53).

$$\langle S\rangle_{\mathrm{total}\,C}(T) = \varphi_C(T)\langle S\rangle_{\mathrm{nA}}(T) + \langle S\rangle_{\mathrm{DFT}-mC}(T). \qquad (53)$$

This is what is shown as the blue dashed line in in Fig. 5A of the main text.

The total thermal sticking coefficient decreases with surface temperature as does the $\langle S\rangle_{\mathrm{total}\,C}(T_S)$ contribution. The fraction of thermal sticking proceeding directly through ***P***, ($\langle S\rangle_{P}(T)$), peaks at around 250 K and decays at higher and lower temperatures. The absolute magnitude of the component of thermal sticking proceeding directly through ***DFT-mC***, $\langle S\rangle_{\mathrm{DFT}-mC}(T)$, increases above 250 K with temperature, but does not exceed 5% up to the melting temperature of gold. Nevertheless, the contribution to thermal sticking occurring through the ***DFT-mC*** state and the PAC ***C*** state constitute ~ 40 % of the total thermal sticking at surface temperatures above 1100 K. The reason for this is that at high temperatures, CO in the chemisorbed states becomes more mobile parallel to the surface, more closely resembling the high entropy physisorbed state. With increasing temperature, the translational and rotational entropy of ***C*** approaches the high entropy of ***P***, becoming nearly equal at the highest temperatures. We note that this is consistent with an expectation based on the equipartition theorem.

9. Consistency of the Data Fit to the PAC Model with the PUMP-PROBE Experiments

In the PUMP-PROBE experiment by Kumar *et al.* (*8*) conducted at a surface temperature of 35 K, where the Au(111) surface was dosed with static CO gas, there was no evidence for a

coexisting chemisorbed state of CO on Au(111). This observation is also consistent with the value of the energy difference between the physisorption and chemisorption states, derived in this work, that is $\Delta E^{PC} = 38 \pm 12$ meV. Figure S13 depicts the equilibrium constant between chemisorption and the physisorption calculated using the fitted energy difference between the two states. At 35 K it has a value of 10^{-9}, indicating that physisorbed CO molecules are exclusively present at the surface.

Figures for Supplementary Material

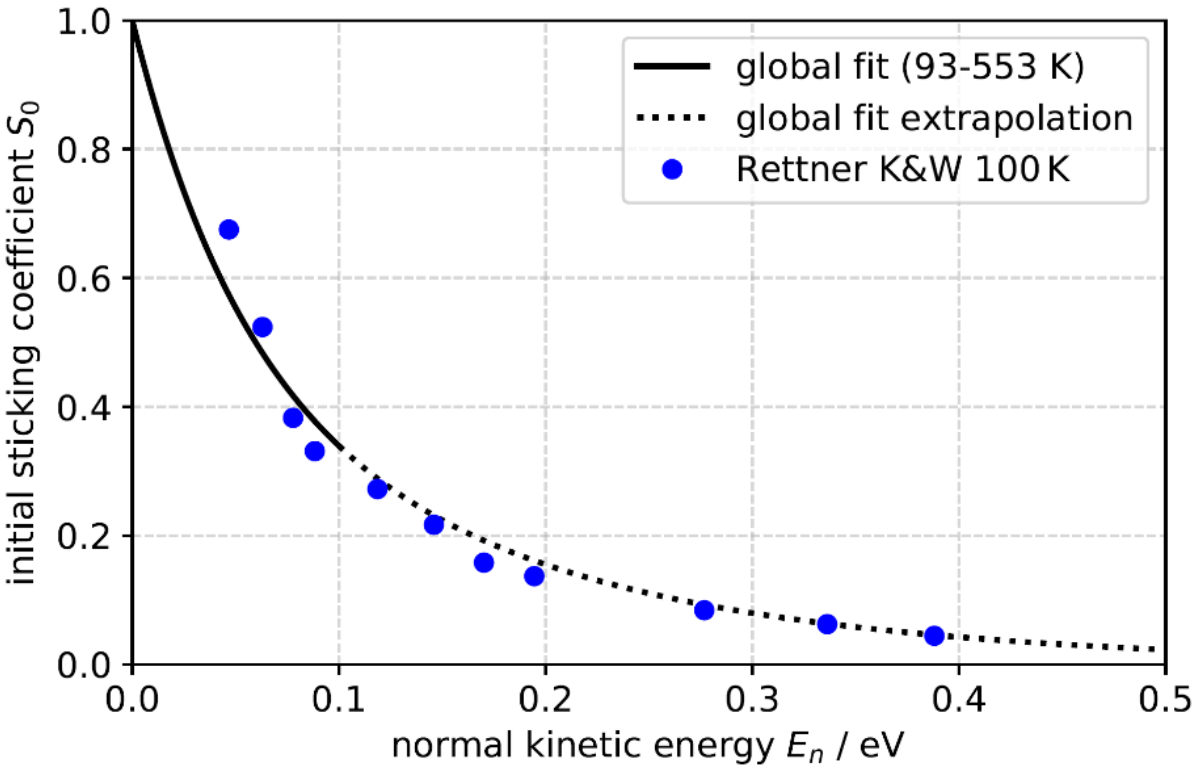

Figure S1 | CO sticking probability to Au(111): $S_0(E_n)$ - the dependence of initial sticking probability on the normal component of the incidence energy resulting from the fit to the TOF traces of CO(v=2) and CO(v=1) scaled to independent measurements reported by Rettner (*16*) for CO(v=0) sticking on Au(111) (blue dots) determined with the method of King and Wells (K&W). The solid line indicates the range over which our experiments are sensitive. The dotted line shows the extrapolated values of the optimized sticking coefficient function using Eq. (4). The excellent agreement indicates that: 1) the sticking probability is independent of the vibrational state, consistent with observations on other systems (3) and 2) desorbing CO(v=2) and CO(v=1) are translationally equilibrated with the surface.

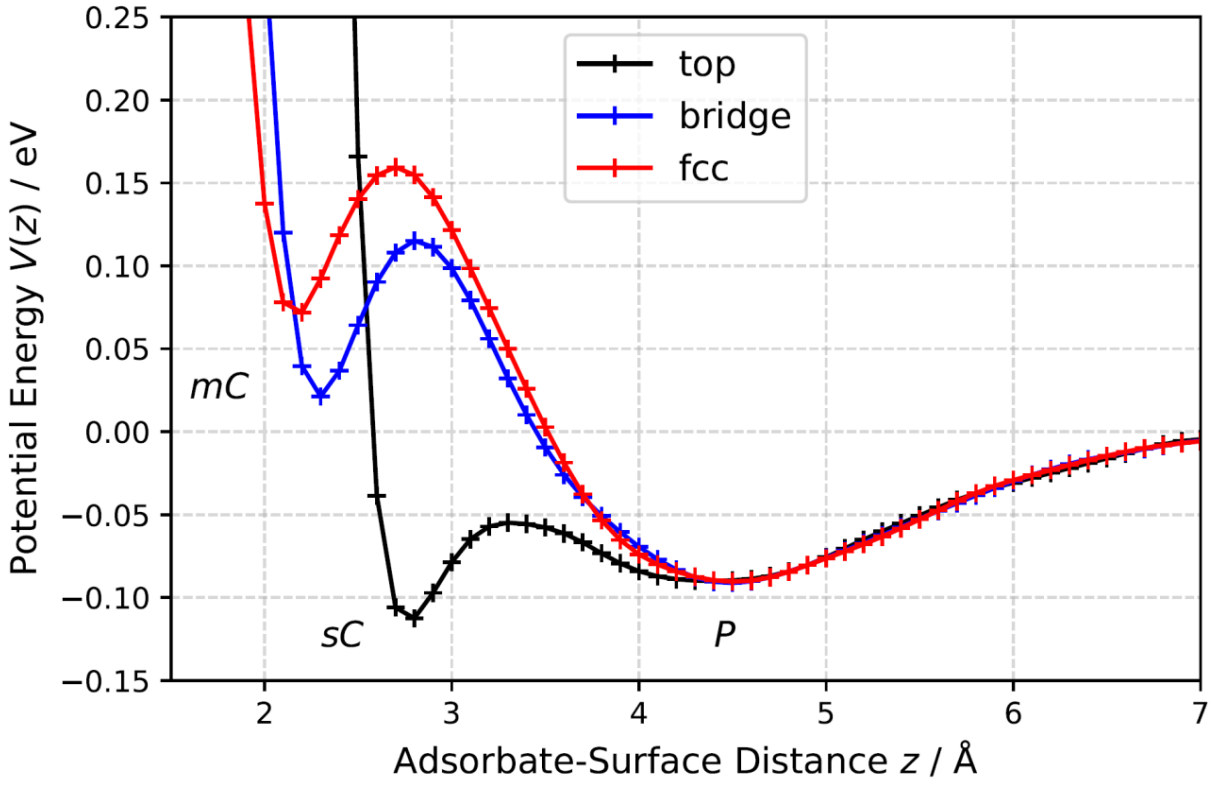

Figure S2 | One-dimensional DFT PES for CO on Au(111): One-dimensional cuts through a potential energy function calculated by density functional theory (DFT) with the BEEF-vdW functional for the Au(111)-CO system (*6*). Interaction potentials for top, fcc and bridge sites are depicted. The interaction potentials are for CO that is oriented with its C-end to the surface and CO bond which is oriented parallel to the surface normal.

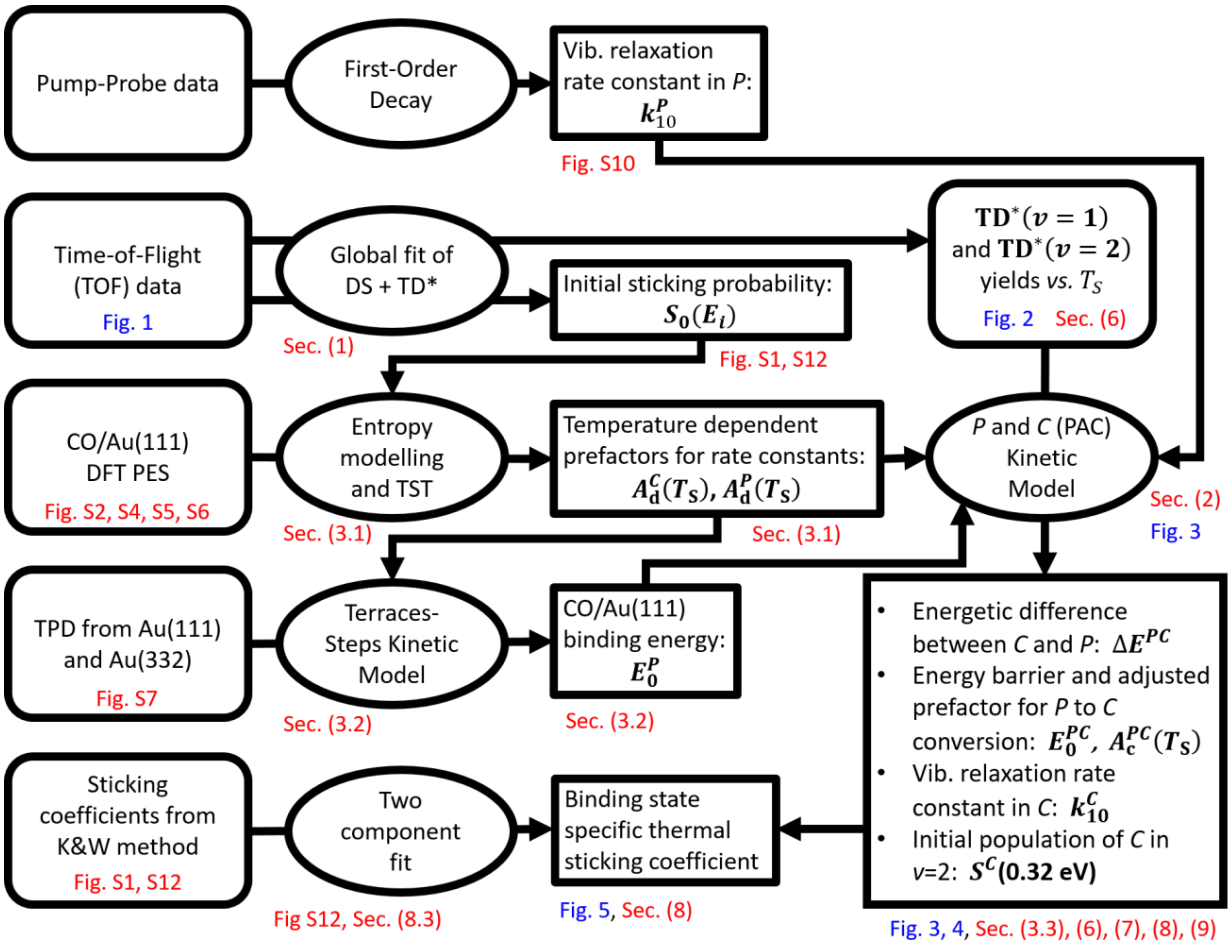

Figure S3 | Flow-chart of the data analysis in this work: Flow-chart of the data analysis yielding the energies, barriers and rate constants listed in Tables S1 and S2. The section and figure numbers of the SM (red label) and figure numbers of the main paper (blue label) devoted to the corresponding parts of the analysis protocol are shown in the flow-chart. For references see text.

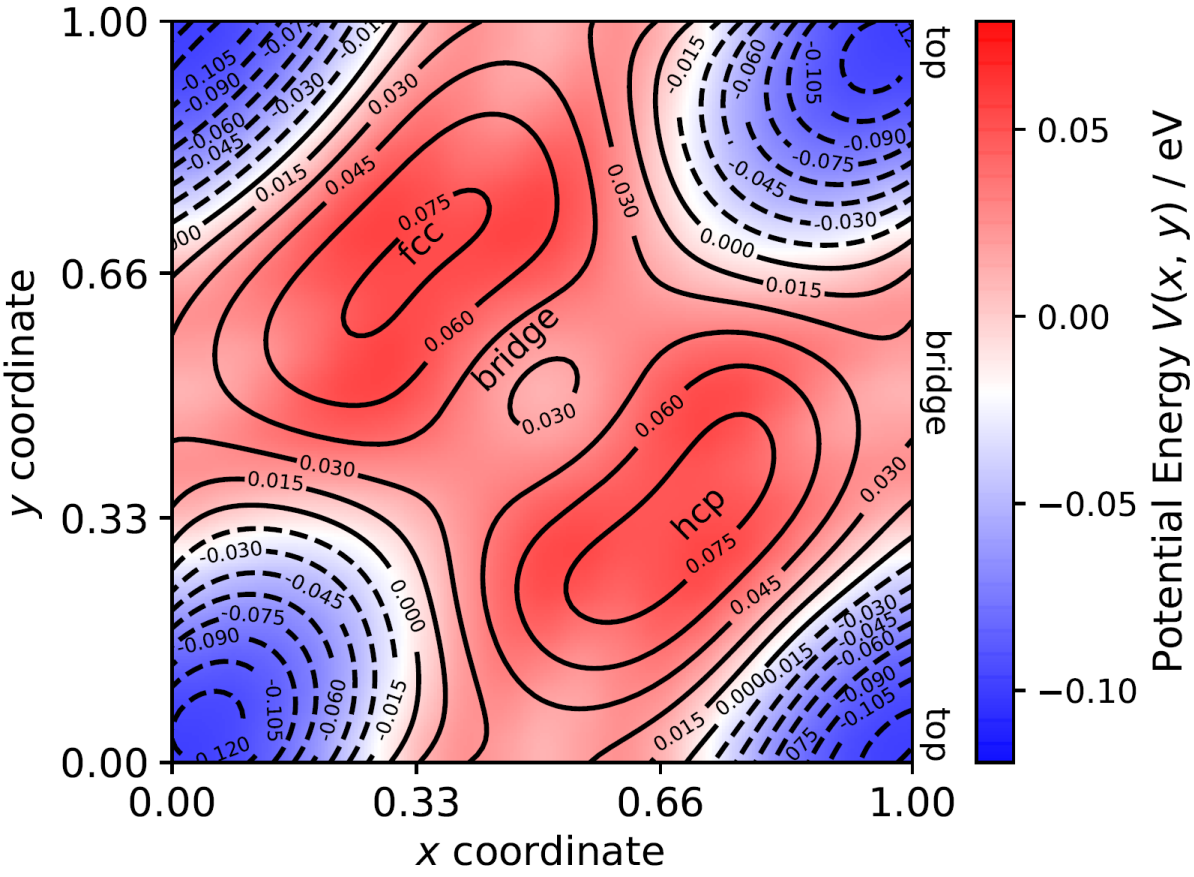

Figure S4 | Two-dimensional DFT PES for chemisorbed CO: DFT-calculated $V(x,y)$ potential energy of chemisorbed CO in the up-right configuration across the Au(111) unit cell.

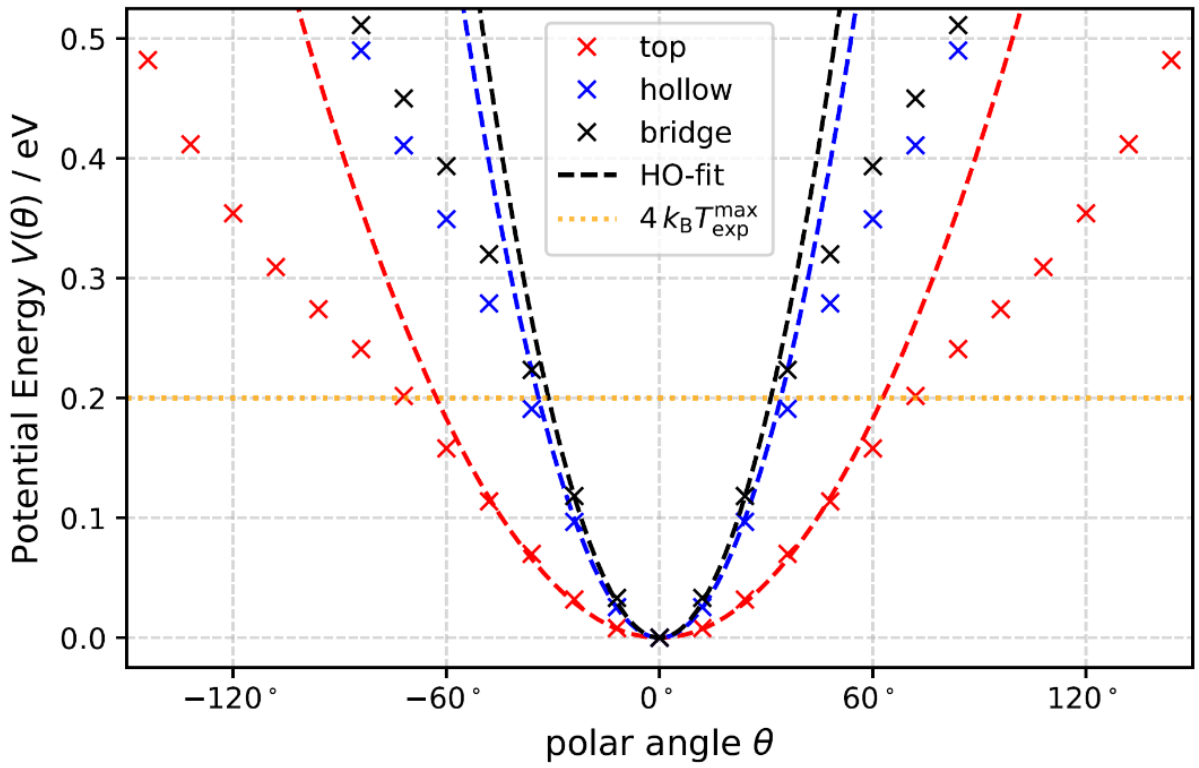

Figure S5 | DFT PES for hindered rotation of chemisorbed CO: Potential energy of the Au-CO interaction in top, hollow and bridge chemisorption sites. Crosses: the DFT PES, dashed lines: harmonic oscillator fits. Horizontal dotted line represents the value of $4\,k_B T_S$ for maximum surface temperature of the experiments T_S=550 K – confirming that for the temperature range of the experiment $V(\theta)$ can be described by a parabolic function of harmonic oscillator.

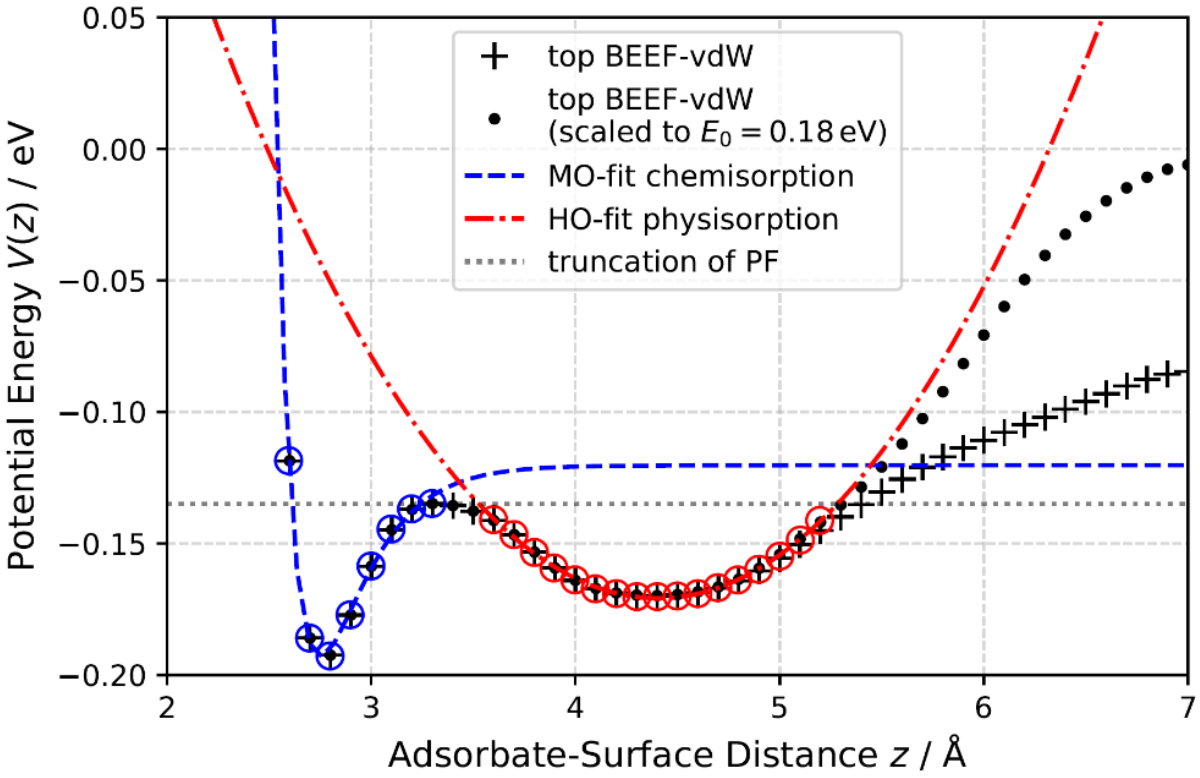

Figure S6 | One-dimensional DFT PES cut for CO on the top-site of Au(111): The Au(111)-CO interaction potential along the z-axis on the top site is shown. Black pluses represent the calculated PES and black dots is the PES that is modified to match previously reported CO binding energies (*17*) from Ref. (*6*). The blue dashed line is the Morse potential fit to DFT data points (points chosen for the fit are surrounded by blue circles) for the chemisorption well, red dash-dot line is the harmonic oscillator potential fit to physisorption well (points chosen for this fit are surrounded by red circles). Grey horizontal dotted line at -0.13 eV correspond to truncation values of the partition function (PF) corresponding to $v_{\max}$ (see Eq. (26)) of chemisorption well (Morse potential fit) and physisorption well (harmonic oscillator fit).

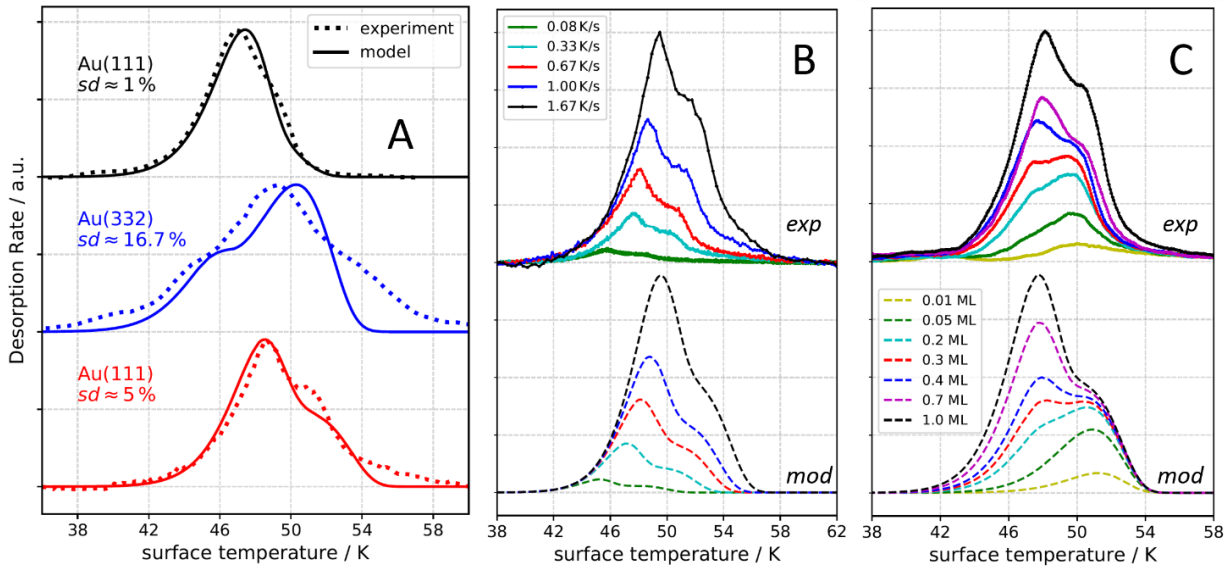

Figure S7 | CO TPD measurements at Au(111) and Au(332) with Model: (A) Step-density influence on desorption rates of CO measured from three different Au surfaces: Au(111) of this work (dotted line, black), Au(332) of this work (dotted line, blue) and Au(111) from Engelhart *et al.* (*17*) (dotted line, red) with different step-densities (*sd*) at initial coverage of 1.0 ML and a heating rate of 1 K/s. The peak temperatures of the two Au(111) datasets appear to be shifted by 1-2 K with respect to each other. We attribute this shift to temperature calibration uncertainties at low temperatures (up to $\pm$2K between 10 and 100 K) (*41*).The model output (solid line) is shifted for Au(332) by -2 K and for Au(111) from Engelhart *et al.* (*17*) by $+1$ K to match the maxima of the experimental datasets.. **(B)** The heating rate dependence of TPD traces determined by Engelhart *et al.* (*17*) (solid line) and the corresponding (shifted by $+1$ K) prediction of the model (dashed line). The experimental and model heating rates are given in the legend with the initial coverage of 1.0 ML. **(C)** The initial CO coverage dependence of TPD traces determined by Engelhart *et al.* (*17*) (solid line) and the corresponding prediction of the model (dashed line). The initial coverage used as an input to the model is given in the legend with a heating rate of 0.5 K/s. Because in the case of two contributing states to desorption the determination of initial coverages from the integral of the TPD trace is no longer possible, the experimental initial coverages might deviate from those used as an input to the model.

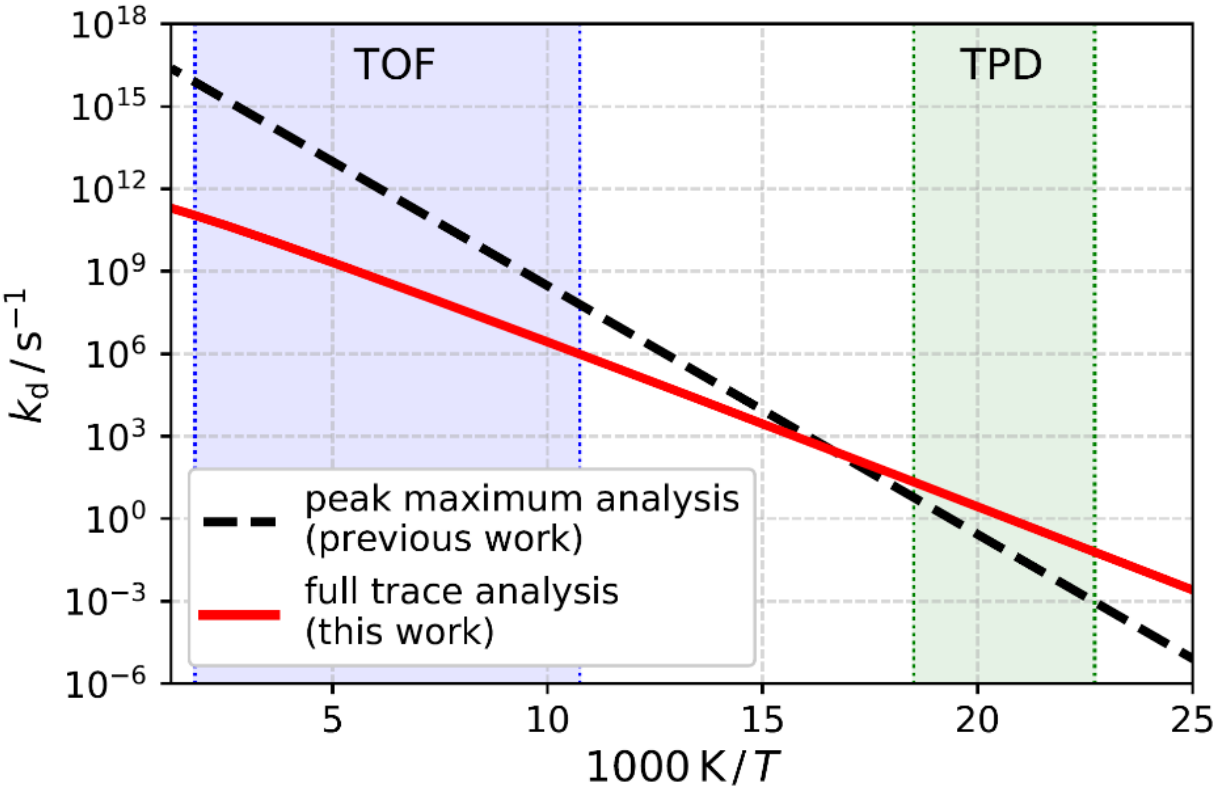

Figure S8 | CO desorption rate constant from TPD: The rate constant for desorption of the physisorbed CO determined in this work (red line) and previously estimated desorption rate constant (*13*, *17*) (black, dashed line) in an Arrhenius plot. Previous work used the heating rate variation method, and in this work we fitted the full TPD trace with a kinetic mechanism. The green shaded region indicates the temperature range of the TPD experiments, and the blue shaded region indicates the temperature range where the molecular beam TOF experiments, probing CO(v=2 and 1) desorption yields were conducted.

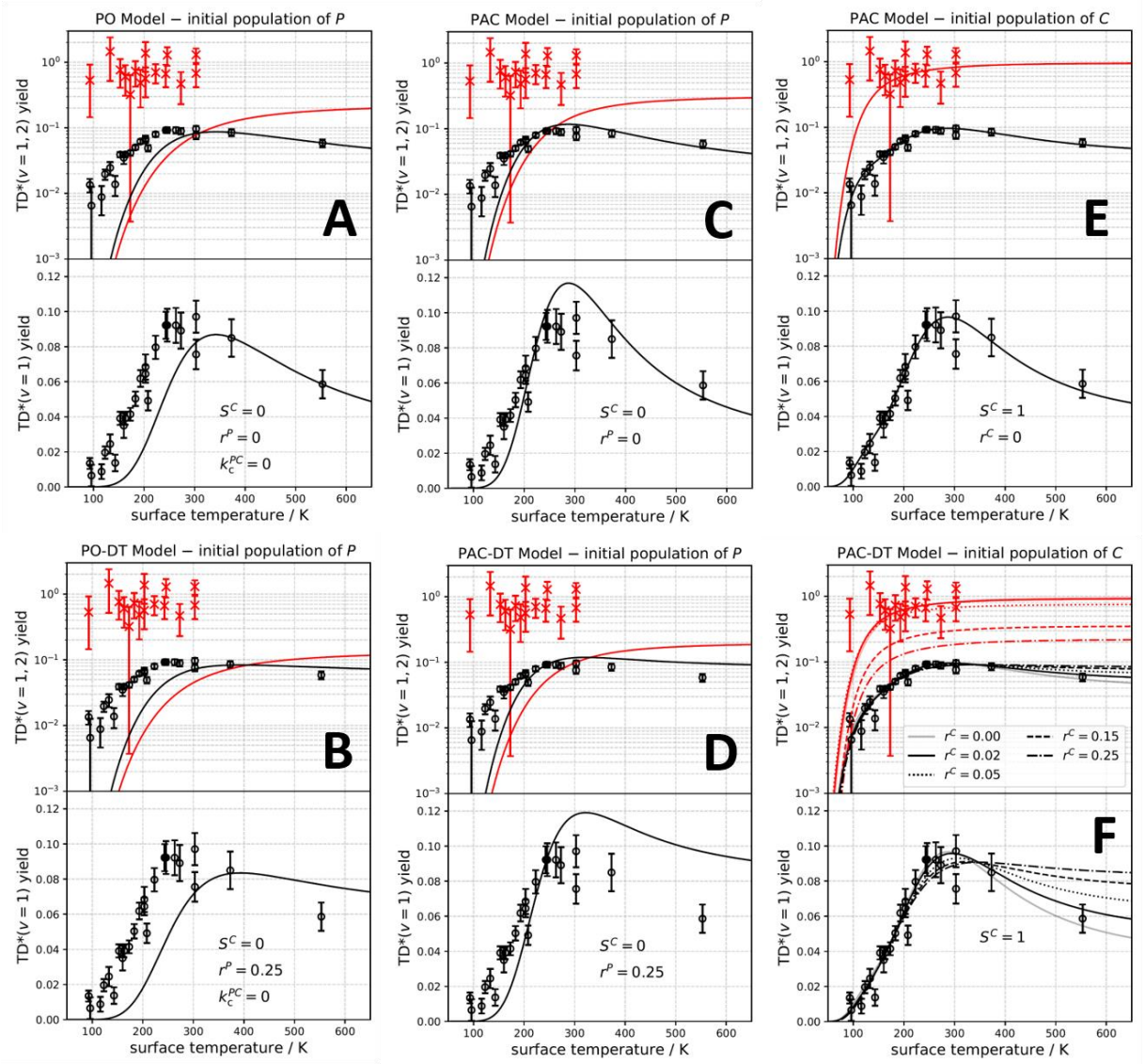

Figure S9 | Various scenarios of PO, DT and PAC simulations: All labelled panels are split horizontally. The lower half shows the CO(v=1) desorption yield on a linear scale and the upper half shows both CO(v=2 and 1) desorption yields on a logarithmic scale. Experimentally determined yields, TD*(v=2) and TD*(v=1), are shown as red crosses and black circles, respectively. The model result for TD*(v=2) and TD*(v=1) are shown as red and black lines, respectively. See further details in the legend and in the text. Error bars indicate a 90% confidence interval.

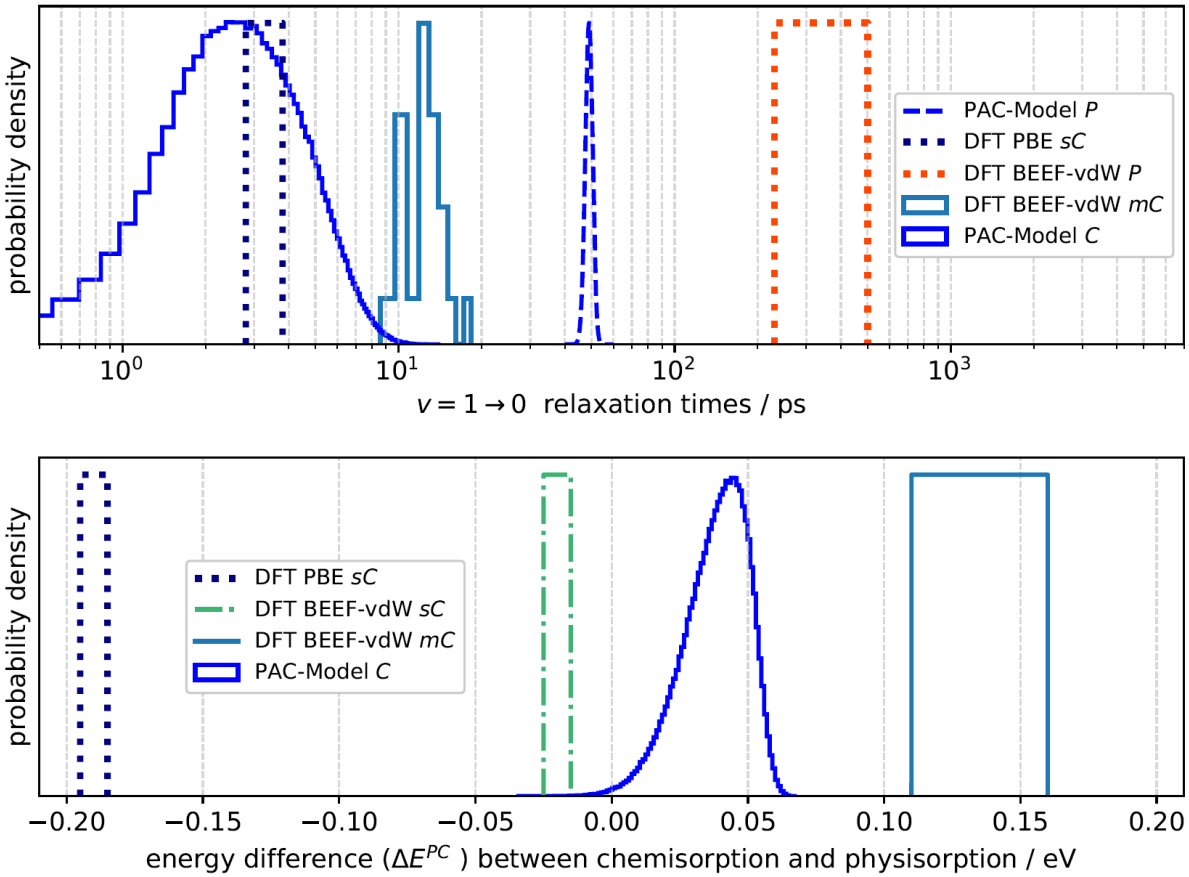

Figure S10 | Comparison of vibrational relaxation times and *C*-*P* energy differences: Upper panel: vibrational relaxation v=1→0 lifetimes in chemisorption and physisorption wells derived based on comprehensive analysis of the experimental data-set along with theory predictions based on DFT calculated PES with the PBE (Novko and coworkers, refers for stable chemisorption (*sC*) (*15*)) and BEEF-vdW (Guo and coworkers, refers to metastable chemisorption (*mC*) (*6*) and Novko and coworkers, refers to physisorption (*P*) (*15*)) functionals. The relaxation lifetime for *P* used in the PAC-Model was fixed to experimental results from Ref. (*8*). Lower panel: energetic difference between the minima of chemisorption and physisorption well based on the rate-equation analysis of the experimental data along with DFT-predictions.

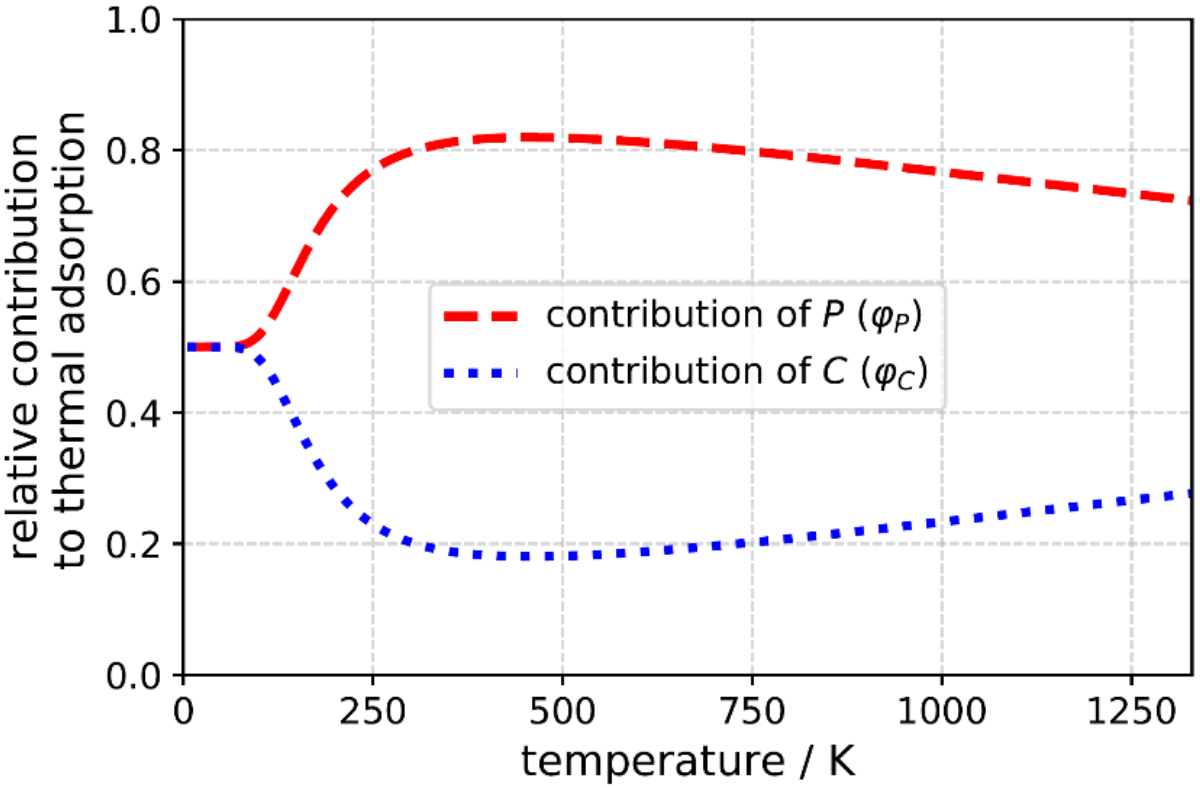

Figure S11 | The dependence of φ_C and φ_P on the surface temperature. The contributions to the thermal sticking coefficient trough C and P derived from the PAC model.

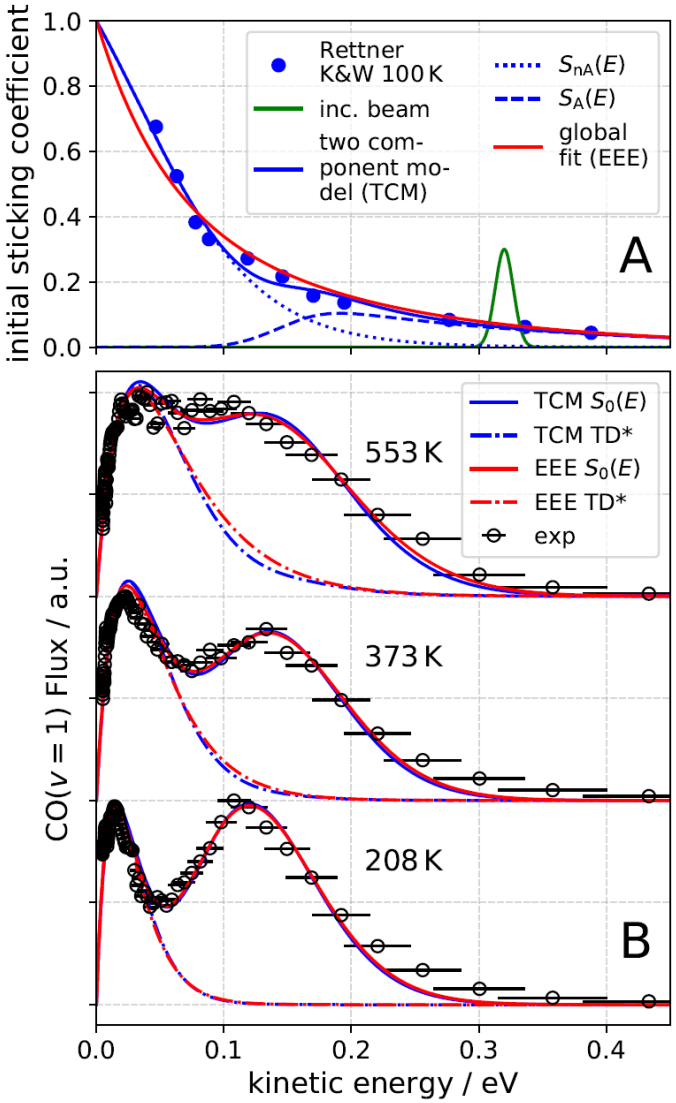

Figure S12 | Sticking coefficients models and their consistency with TOF data: (A) Fit of Rettner's sticking data (*16*) (blue solid circles): two component model (TCM, Eq. (47) – blue solid line) - and its contributions – non-activated component, describing the low energy part (Eq. (45), blue dotted line) and activated component, describing the high energy part (Eq. (46) -blue dashed line). The empirical exponential expression (EEE) used in the global fit of the TOF data (red solid line) is shown for comparison – see SM Section 1. The green solid line shows the kinetic energy distribution of the incident beam at $E_i = 0.32$ eV. (B) CO($v = 1$) TOF data at different surface temperatures converted to energy domain (empty circles) are fitted with two components: Direct Scattering component (DS) and Trapping Desorption component (TD*). The red solid lines represent the global fits that were determined using the empiric exponential expression (EEE, Eq. (4) – see SM Section 1) for the sticking coefficient and red dash-dot lines represent the TD* component extracted using EEE. The blue solid lines represent the TOF fits obtained using sticking coefficient determined with the TCM model fit (Eq. (49)) to Rettner's data (*16*). The blue dash-dot lines represent the TD* component extracted using TCM. Both EEE and TCM approaches lead to virtually equal quality of the resulting TOF fits. The error bars indicate a 95% confidence interval

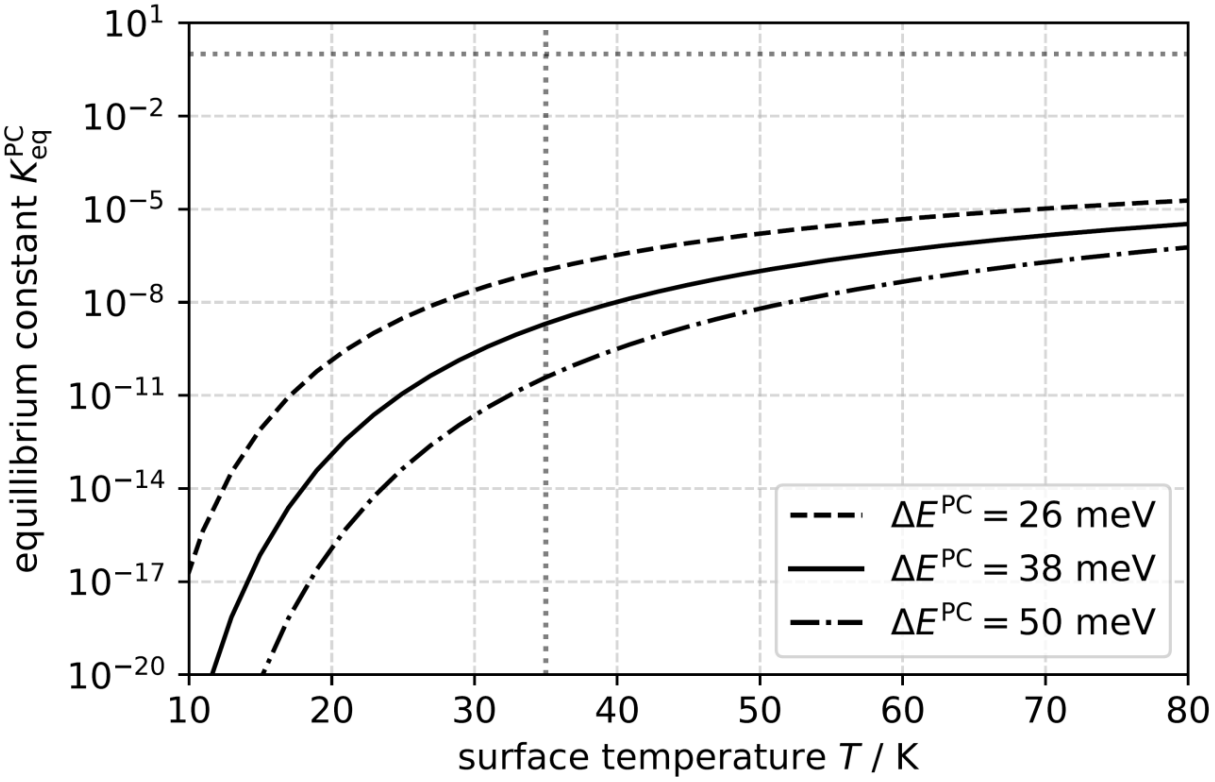

Figure S13 | Equilibrium constant between the physisorbed and chemisorbed CO: The equilibrium constant between the physisorbed and chemisorbed states plotted as a function of the surface temperature using the fitted value of their energy difference, $\Delta E^{PC} = 38 \pm 12$ meV . The solid line depicts the value of equilibrium constant; dashed and dashed-dotted lines show the error margins calculated assuming ± 12 meV uncertainty in the value of energy difference between ***P*** and ***C*** obtained from the PAC model fit. Vertical dotted line marks the surface temperature of 35 K used in the PUMP-PROBE experiments of Kumar *et al.* (*8*), and horizontal dotted line indicates the equilibrium constant, at which ***P*** and ***C*** would have equal population.

Tables for Supplementary Material

Table S1. Energies and barriers (see Fig. 3 in the main text)

Parameter	**Description**	**How it was determined**
$\boldsymbol{E_0^P}$	Desorption barrier from the physisorption well	from a fit to temperature programmed desorption (TPD) data – this work (SI, Section 3.2) and Ref. (*17*)
$\boldsymbol{\Delta E^{PC}}$	Energy difference between physisorption and chemisorption minima, $\Delta E^{PC} = E_0^P - E_0^C$	from a fit to the TD*(v=2,1) scattering data *vs.* T_S
$\boldsymbol{E_0^{PC}}$	Barrier for conversion between physisorption and chemisorption wells	from the fit to the TD*(v=2,1) scattering data *vs.* T_S
$\boldsymbol{E_0^C}$	Desorption barrier from the chemisorption well	from $E_0^C = E_0^P - \Delta E^{PC}$
$\boldsymbol{E_0^{CP}}$	Barrier for conversion between chemisorption and physisorption wells	from $E_0^{CP} = E_0^{PC} - \Delta E^{PC}$

Table S2. Rate constants for elementary processes of the PAC model

Rate constant	**Description**	**Value**
$\boldsymbol{k_{\mathrm{d}}^{C}}$	Desorption from the chemisorption well	$k_{\mathrm{d}}^{C} = A_{\mathrm{d}}^{C}(T_S)\exp(-E_0^C/k_{\mathrm{B}}T_S)$; $A_{\mathrm{d}}^{C}(T_S)$ is derived from partition functions on the DFT PES [#]
$\boldsymbol{k_{\mathrm{d}}^{P}}$	Desorption from the physisorption well	$k_{\mathrm{d}}^{P} = A_{\mathrm{d}}^{P}(T_S)\exp(-E_0^P/k_{\mathrm{B}}T_S)$; $A_{\mathrm{d}}^{P}(T_S)$ is derived from partition functions on the DFT PES [#]
$\boldsymbol{k_{\mathrm{c}}^{PC}}$	Conversion from the physisorption to the chemisorption well	$k_{\mathrm{c}}^{PC} = A_{\mathrm{c}}^{PC}(T_S)\exp(-E_0^{PC}/k_{\mathrm{B}}T_S)$; the range of the pre-exponent, $A_{\mathrm{c}}^{PC}(T_S)$, is derived from classical partition functions on the DFT PES. We allow constrained optimization of this parameter during the fit to TD* (v=2,1) scattering data [#]
$\boldsymbol{k_{\mathrm{c}}^{CP}}$	Conversion from the chemisorption to the physisorption well	$k_{\mathrm{c}}^{CP} = k_{\mathrm{c}}^{PC}/K_{\mathrm{eq}}^{PC}$. The relative energies ΔE^{PC} were obtained from the fit to TD* (v=2,1) scattering data vs. T_S. The entropies came from the DFT PES [#]
$\boldsymbol{k_{10}^{C} = \frac{1}{\tau_{10}^{C}}}$	v=1→0 vibrational relaxation in the chemisorption well	from the fit to the TD* (v=2,1) scattering data vs. T_S
$\boldsymbol{k_{10}^{P} = \frac{1}{\tau_{10}^{P}}}$	v=1→0 vibrational relaxation in the physisorption well	$\tau_{10}^{P} = 49$ ps from Ref. (*8*)
$\boldsymbol{k_{21}^{C} = \frac{1}{\tau_{21}^{C}}}$	v=2→1 vibrational relaxation in the chemisorption well	$\tau_{10}^{C} = 2\tau_{21}^{C}$ [§]
$\boldsymbol{k_{21}^{P} = \frac{1}{\tau_{21}^{P}}}$	v=2→1 vibrational relaxation in the physisorption well	$\tau_{21}^{P} = \tau_{10}^{P}/2 = 24.5$ ps [§]

[#]. See SI Section 3.
[§]. Expected behavior for harmonic oscillators. See Refs. (*31*, *32*).

Table S3. Rate constants determined in this work, parametrized according to $k_e(T) = A_e \left(\frac{\mathrm{K}}{T}\right)^m \exp\left(-\frac{E_e}{k_B T}\right)$. The deviation of the parametrized rate constants, compared to the numerical result, is $\leq 15\%$ between 40 and 1330 K. The numerical rate constants are parametrized and validated between 40 and 560 K.

Rate constant	$\boldsymbol{A_e}$ **/** $\mathbf{s^{-1}}$	$\boldsymbol{m}$	$\boldsymbol{E_e}$ **/ meV**
$\boldsymbol{k_d^P}$	3.24×10^{13}	0.498	121.4
$\boldsymbol{k_d^C}$	5.07×10^{18}	1.55	84.8
$\boldsymbol{k_c^{PC}}$	4.42×10^{7}	-1.21	50.8
$\boldsymbol{k_c^{CP}}$	6.92×10^{12}	-0.156	14.3
$\boldsymbol{k_{10}^P}$	2.04×10^{10}	0	0
$\boldsymbol{k_{10}^C}$	2.76×10^{11}	0	0
$\boldsymbol{k_{21}^P}$	4.08×10^{10}	0	0
$\boldsymbol{k_{21}^C}$	5.52×10^{11}	0	0
$\boldsymbol{k_{d(S)}^P}$	3.24×10^{13}	0.498	144.4
$\boldsymbol{k_H}$	7.50×10^{10}	-0.50	0
$\boldsymbol{k_S}$	7.50×10^{10}	-0.50	23.0

Table S4. Values of parameters of the PAC determined from fits.

Parameter	**Description & Remarks**
$\boldsymbol{\tau_{10}^{C} = 3.6 \pm 1.8\ ps}$	Lifetime of v=1→0 vibrational relaxation in the chemisorption well
$\boldsymbol{\Delta E^{PC} = 38 \pm 12\ meV}$	Energy difference between physisorption and chemisorption minima.
$\boldsymbol{E_0^{PC} = 51 \pm 5\ meV}$	Barrier for conversion between physisorption and chemisorption wells
$\boldsymbol{\eta = 0.303 \pm 038}$	Weighting parameter in the expression for partition function of transition state between physisorption and chemisorption (see Eq. 38). The weighting parameter $\boldsymbol{\eta}$ is related to the $\boldsymbol{A_c^{PC}(T_S)}$, the Arrhenius pre-factor to convert physisorbed molecules to the chemisorbed state.
$\boldsymbol{S^C = 1}$	The fraction of CO($v = 2$) molecules that initially trap into the chemisorbed state. In all the fits the parameter $\boldsymbol{S^C}$ always approaches 1. To estimate the covariance matrix in the minimum of the parameter space we fixed $\boldsymbol{S^C}$ to 1. Based on the analysis of sticking probability data we estimated the $\boldsymbol{S^C}$ to be ~ 0.96 – see SI Section 8.3. Value of $\boldsymbol{S^C}$ = 0.98±0.02 is reported in the main text.

References and Notes

1. H. Jiang, M. Kammler, F. Ding, Y. Dorenkamp, F. R. Manby, A. M. Wodtke, T. F. Miller 3rd, A. Kandratsenka, O. Bünermann, Imaging covalent bond formation by H atom scattering from graphene. *Science* **364**, 379–382 (2019). doi:10.1126/science.aaw6378 Medline

2. D. A. King, M. G. Wells, Molecular beam investigation of adsorption kinetics on bulk metal targets: Nitrogen on tungsten. *Surf. Sci.* **29**, 454–482 (1972). doi:10.1016/0039-6028(72)90232-4

3. D. A. King, M. G. Wells, Reaction mechanism in chemisorption kinetics: Nitrogen on the {100} plane of tungsten. *Proc. R. Soc. London Ser. A* **339**, 245–269 (1974). doi:10.1098/rspa.1974.0120

4. T. Zambelli, J. V. Barth, J. Wintterlin, G. Ertl, Complex pathways in dissociative adsorption of oxygen on platinum. *Nature* **390**, 495–497 (1997). doi:10.1038/37329

5. C. T. Rettner, C. B. Mullins, Dynamics of the chemisorption of O_2 on Pt(111): Dissociation via direct population of a molecularly chemisorbed precursor at high incidence kinetic energy. *J. Chem. Phys.* **94**, 1626–1635 (1991). doi:10.1063/1.459966

6. M. Huang, X. Zhou, Y. Zhang, L. Zhou, M. Alducin, B. Jiang, H. Guo, Adiabatic and nonadiabatic energy dissipation during scattering of vibrationally excited CO from Au(111). *Phys. Rev. B* **100**, 201407 (2019). doi:10.1103/PhysRevB.100.201407

7. M. Morin, N. J. Levinos, A. L. Harris, Vibrational energy transfer of CO/Cu(100): Nonadiabatic vibration/electron coupling. *J. Chem. Phys.* **96**, 3950–3956 (1992). doi:10.1063/1.461897

8. S. Kumar, H. Jiang, M. Schwarzer, A. Kandratsenka, D. Schwarzer, A. M. Wodtke, Vibrational relaxation lifetime of a physisorbed molecule at a metal surface. *Phys. Rev. Lett.* **123**, 156101 (2019). doi:10.1103/PhysRevLett.123.156101 Medline

9. D. E. Brown, D. J. Moffatt, R. A. Wolkow, Isolation of an intrinsic precursor to molecular chemisorption. *Science* **279**, 542–544 (1998). doi:10.1126/science.279.5350.542 Medline

10. E. Dombrowski, E. Peterson, D. Del Sesto, A. L. Utz, Precursor-mediated reactivity of vibrationally hot molecules: Methane activation on Ir(111). *Catal. Today* **244**, 10–18 (2015). doi:10.1016/j.cattod.2014.10.025

11. R. Moiraghi, A. Lozano, E. Peterson, A. Utz, W. Dong, H. F. Busnengo, Nonthermalized precursor-mediated dissociative chemisorption at high catalysis temperatures. *J. Phys. Chem. Lett.* **11**, 2211–2218 (2020). doi:10.1021/acs.jpclett.0c00260 Medline

12. W. Liu, S. N. Filimonov, J. Carrasco, A. Tkatchenko, Molecular switches from benzene derivatives adsorbed on metal surfaces. *Nat. Commun.* **4**, 2569 (2013). doi:10.1038/ncomms3569 Medline

13. P. R. Shirhatti, I. Rahinov, K. Golibrzuch, J. Werdecker, J. Geweke, J. Altschäffel, S. Kumar, D. J. Auerbach, C. Bartels, A. M. Wodtke, Observation of the adsorption and desorption of vibrationally excited molecules on a metal surface. *Nat. Chem.* **10**, 592–598 (2018). doi:10.1038/s41557-018-0003-1 Medline

14. J. Pischel, A. Pucci, Low-temperature adsorption of carbon monoxide on gold surfaces: IR spectroscopy uncovers different adsorption states on pristine and rough Au(111). *J. Phys. Chem. C* **119**, 18340–18351 (2015). doi:10.1021/acs.jpcc.5b05051

15. I. Lončarić, M. Alducin, J. I. Juaristi, D. Novko, CO stretch vibration lives long on Au(111). *J. Phys. Chem. Lett.* **10**, 1043–1047 (2019). doi:10.1021/acs.jpclett.9b00069 Medline

16. C. T. Rettner, The search for direct vibrational excitation in gas-surface collisions of CO with Au(111). *J. Chem. Phys.* **99**, 5481–5489 (1993). doi:10.1063/1.465965

17. D. P. Engelhart, R. J. V. Wagner, A. Meling, A. M. Wodtke, T. Schäfer, Temperature programmed desorption of weakly bound adsorbates on Au(111). *Surf. Sci.* **650**, 11–16 (2016). doi:10.1016/j.susc.2015.06.010

18. J. C. Tully, The dynamics of adsorption and desorption. *Surf. Sci.* **299-300**, 667–677 (1994). doi:10.1016/0039-6028(94)90688-2

19. T. L. Hill, *Introduction to Statistical Thermodynamics* (Dover Publication, 1986).

20. M. Jørgensen, H. Grönbeck, Adsorbate entropies with complete potential energy sampling in microkinetic modeling. *J. Phys. Chem. C* **121**, 7199–7207 (2017). doi:10.1021/acs.jpcc.6b11487

21. A. M. Wodtke, H. Yuhui, D. J. Auerbach, Insensitivity of trapping at surfaces to molecular vibration. *Chem. Phys. Lett.* **413**, 326–330 (2005). doi:10.1016/j.cplett.2005.06.031

22. D. Borodin, CO(v=2) scattering on Au(111) (TPD, TOF and TD*(v=1,2)). Zenodo (2020); doi:10.5281/zenodo.3932143.

23. M. Forsblom, M. Persson, Vibrational lifetimes of cyanide and carbon monoxide on noble and transition metal surfaces. *J. Chem. Phys.* **127**, 154303 (2007). doi:10.1063/1.2794744 Medline

24. K. Golibrzuch, P. R. Shirhatti, J. Altschäffel, I. Rahinov, D. J. Auerbach, A. M. Wodtke, C. Bartels, State-to-state time-of-flight measurements of NO scattering from Au(111): Direct observation of translation-to-vibration coupling in electronically nonadiabatic energy transfer. *J. Phys. Chem. A* **117**, 8750–8760 (2013). doi:10.1021/jp403382b Medline

25. J. Wellendorff, K. T. Lundgaard, A. Møgelhøj, V. Petzold, D. D. Landis, J. K. Nørskov, T. Bligaard, K. W. Jacobsen, Density functionals for surface science: Exchange-correlation model development with Bayesian error estimation. *Phys. Rev. B Condens. Matter Mater. Phys.* **85**, 235149 (2012). doi:10.1103/PhysRevB.85.235149

26. G. Kresse, J. Furthmüller, Efficient iterative schemes for ab initio total-energy calculations using a plane-wave basis set. *Phys. Rev. B Condens. Matter* **54**, 11169–11186 (1996). doi:10.1103/PhysRevB.54.11169 Medline

27. G. Kresse, J. Furthmuller, Efficiency of ab initio total energy calculations for metals and semiconductors using plane wave basis set. *Comput. Mater. Sci.* **6**, 15–50 (1996). doi:10.1016/0927-0256(96)00008-0

28. M. Newville *et al.*, lmfit/lmfit-py 1.0.1. Zenodo (2020); doi:10.5281/zenodo.3814709.

29. C. T. Rettner, E. K. Schweizer, C. B. Mullins, Desorption and trapping of argon at a 2H–W(100) surface and a test of the applicability of detailed balance to a nonequilibrium system. *J. Chem. Phys.* **90**, 3800–3813 (1989). doi:10.1063/1.455838

30. R. E. Imhof, F. H. Read, S. T. Beckett, Determination of the transition moment of the $B^1\Sigma^+$-$X^1\Sigma^+$transition in CO. *J. Phys. B* **5**, 896–902 (1972). doi:10.1088/0022-3700/5/4/025

31. S. Monturet, P. Saalfrank, Role of electronic friction during the scattering of vibrationally excited nitric oxide molecules from Au(111). *Phys. Rev. B Condens. Matter Mater. Phys.* **82**, 075404 (2010). doi:10.1103/PhysRevB.82.075404

32. K. Golibrzuch, A. Kandratsenka, I. Rahinov, R. Cooper, D. J. Auerbach, A. M. Wodtke, C. Bartels, Experimental and theoretical study of multi-quantum vibrational excitation: NO(v = 0→1,2,3) in collisions with Au(111). *J. Phys. Chem. A* **117**, 7091–7101 (2013). doi:10.1021/jp400313b Medline

33. J. M. Gottfried, K. J. Schmidt, S. L. M. Schroeder, K. Christmann, Adsorption of carbon monoxide on Au(110)-(1×2). *Surf. Sci.* **536**, 206–224 (2003). doi:10.1016/S0039-6028(03)00595-8

34. K. Golibrzuch, P. R. Shirhatti, J. Geweke, J. Werdecker, A. Kandratsenka, D. J. Auerbach, A. M. Wodtke, C. Bartels, CO desorption from a catalytic surface: Elucidation of the role of steps by velocity-selected residence time measurements. *J. Am. Chem. Soc.* **137**, 1465–1475 (2015). doi:10.1021/ja509530k Medline

35. B. Tränkenschuh, N. Fritsche, T. Fuhrmann, C. Papp, J. F. Zhu, R. Denecke, H. P. Steinrück, A site-selective in situ study of CO adsorption and desorption on Pt(355). *J. Chem. Phys.* **124**, 74712 (2006). doi:10.1063/1.2168441 Medline

36. J. A. Serri, J. C. Tully, M. J. Cardillo, The influence of steps on the desorption kinetics of NO from Pt(111). *J. Chem. Phys.* **79**, 1530–1540 (1983). doi:10.1063/1.445946

37. C. Ruggiero, P. Hollins, Interaction of CO molecules with the Au(332) surface. *Surf. Sci.* **377-379**, 583–586 (1997). doi:10.1016/S0039-6028(96)01451-3

38. C. D. Feldt, R. Moreira, E. Meyer, P. Clawin, W. Riedel, T. Risse, L. Moskaleva, W. Dononelli, T. Klüner, CO adsorption on Au(332): Combined Infrared spectroscopy and density functional theory study. *J. Phys. Chem. C* **123**, 8187–8197 (2019). doi:10.1021/acs.jpcc.8b08406

39. D. J. Lavrich, S. M. Wetterer, S. L. Bernasek, G. Scoles, Physisorption and chemisorption of alkanethiols and alkyl sulfides on Au(111). *J. Phys. Chem. B* **102**, 3456–3465 (1998). doi:10.1021/jp980047v

40. S. Kaufmann, Q. Shuai, D. J. Auerbach, D. Schwarzer, A. M. Wodtke, Associative desorption of hydrogen isotopologues from copper surfaces: Characterization of two reaction mechanisms. *J. Chem. Phys.* **148**, 194703 (2018). doi:10.1063/1.5025666 Medline

41. H. Schlichting, D. Menzel, Techniques for attainment, control, and calibration of cryogenic temperatures at small single-crystal samples under ultrahigh vacuum. *Rev. Sci. Instrum.* **64**, 2013–2022 (1993). doi:10.1063/1.1143992

4.3 *"NH_3 Desorption and Diffusion on Pt: Implications for the Ostwald Process"*

Author contributions: The experiments were performed by DB. Parts of the experiments were performed by JF during his bachelor thesis. OG conducted the DFT calculations. KG provided and analyzed parts of the Pt(332) data. Data was analyzed by DB. The kinetic model was developed by DB. TST modelling was done by DB based on DFT data from OG. The paper was written by IR, AMW and DB. All authors contributed to the discussion of the results. All authors contributed to the revision of the manuscript.

JACS
JOURNAL OF THE AMERICAN CHEMICAL SOCIETY
pubs.acs.org/JACS
Article

Kinetics of NH_3 Desorption and Diffusion on Pt: Implications for the Ostwald Process

Dmitriy Borodin, Igor Rahinov, Oihana Galparsoro, Jan Fingerhut, Michael Schwarzer, Kai Golibrzuch, Georgios Skoulatakis, Daniel J. Auerbach, Alexander Kandratsenka, Dirk Schwarzer, Theofanis N. Kitsopoulos,* and Alec M. Wodtke*

Cite This: J. Am. Chem. Soc. 2021, 143, 18305−18316

ABSTRACT: We report accurate time-resolved measurements of NH_3 desorption from Pt(111) and Pt(332) and use these results to determine elementary rate constants for desorption from steps, from (111) terrace sites and for diffusion on (111) terraces. Modeling the extracted rate constants with transition state theory, we find that conventional models for partition functions, which rely on uncoupled degrees of freedom (DOFs), are not able to reproduce the experimental observations. The results can be reproduced using a more sophisticated partition function, which couples DOFs that are most sensitive to NH_3 translation parallel to the surface; this approach yields accurate values for the NH_3 binding energy to Pt(111) (1.13 ± 0.02 eV) and the diffusion barrier (0.71 ± 0.04 eV). In addition, we determine NH_3's binding energy preference for steps over terraces on Pt (0.23 ± 0.03 eV). The ratio of the diffusion barrier to desorption energy is ∼0.65, in violation of the so-called 12% rule. Using our derived diffusion/desorption rates, we explain why established rate models of the Ostwald process incorrectly predict low selectivity and yields of NO under typical reactor operating conditions. Our results suggest that mean-field kinetics models have limited applicability for modeling the Ostwald process.

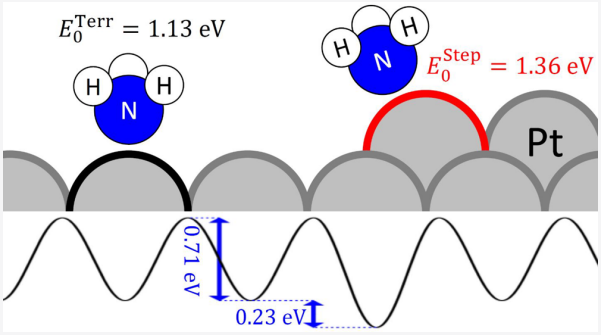

1. INTRODUCTION

The Ostwald process is a critically important stepping stone for industrial production of artificial fertilizers, converting ammonia (NH_3) to nitric acid (HNO_3) in the presence of oxygen and water. The key to its success is the efficient oxidation of NH_3 to nitric oxide (NO) on a Pt catalyst. In industry, the Ostwald process is conducted at temperatures of 1050−1250 K and total pressures between 1 and 12 bar with an ammonia to air ratio of 1:10.[1] To initiate the oxidation, NH_3 adsorbs with high probability to the majority terrace site and must then diffuse to low-coordination step sites, where it is able to react with oxygen.[2−8] Thus, the competition between desorption and diffusion and the equilibrium between adsorption at step and terrace sites are critical factors in determining reaction probability; yet the competition between NH_3 desorption and diffusion on Pt has never been investigated. There is not even an experimental consensus concerning such a basic parameter as the binding energy of NH_3 at Pt(111). Molecular beam relaxation spectrometry (MBRS)[9] yielded a binding energy of 0.68 eV, whereas analysis of collision-induced desorption (CID) experiments[10] led to a value of 1.1 eV. Laser-induced desorption (LID)[11] studies suggest a binding energy of ∼0.8 eV, consistent with results obtained with temperature-programmed desorption (TPD).[12,13] Analysis of TPD data also reveals a weakening NH_3−Pt bond with increasing NH_3 coverage and contradicts the expectation one might infer from MBRS, conducted at low coverages, and CID, conducted at high coverages. Obviously, the uncertainty among the experimental determinations of the binding energy precludes any serious comparison with theory. This is presumably the reason why the NH_3 binding energy at Pt(111), despite its importance, is still missing from experimental benchmark tables.[14] Furthermore, real catalysts exhibit a diversity of active sites, including steps and kinks, and the relative binding strengths of molecules to different sites can determine the reactant's ability to compete with other molecules to occupy the active site(s). Sadly, no reliable site-specific binding energies of NH_3 on Pt have yet been reported.

The lack of reliable quantitative information concerning NH_3/Pt interactions led to surrogate empirically optimized models, which unfortunately lack universality and trans-

Received: September 1, 2021
Published: October 21, 2021

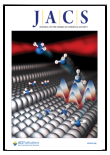

ferability. Nevertheless, the Ostwald process has been modeled using transition state theory (TST) and density functional theory (DFT) to calculate the relevant rate parameters on single crystal model catalysts like Pt(111),[2,15] Pt(100),[16] and Pt(211)[2,4,17] that are then used to elucidate the optimum process conditions. Such models have rarely been validated by comparison to experiment, of which there are few. One of the best known models, frequently used in reactor simulations of the Ostwald process, was developed by Kraehnert and Baerns[18] (KB). The KB kinetics model relies on a mechanism derived from DFT calculations on Pt(111) by Offermans et al.[15] and optimizing the rate parameters to achieve agreement with the experimental rates of NH_3 oxidation on polycrystalline Pt at 1 mbar and 600 K. Experimental observations could only be explained assuming that adsorbed NH_3 (NH_3*) and O* occupy different binding sites. These sites were assigned to those found on Pt(111) single crystals—on top for NH_3* and fcc hollow for O* and NO*.[18] Other structural features like steps, which are known to be more reactive than terraces,[2,6,7] were not considered. Scheuer et al. pointed out that the KB mechanism lacks quantitative transferability to the ammonia slip[19] regime, where NH_3 reacts with O_2, forming predominantly N_2 and H_2O. The lack of transferability is likely due to the use of rate constants, which do not reflect the correct elementary processes. For example, the KB mechanism includes a 0.65 eV adsorption barrier for NO on Pt, in contradiction to our current understanding that NO−Pt adsorption is barrierless.[20,21] Beyond this, the rate parameters used to describe NH_3 desorption in the KB model include an unphysically low prefactor in the Arrhenius expression, suggesting the entropy of Pt-adsorbed NH_3 is higher than that of the gas-phase molecule. Clearly, there is a pressing need for reliable information on site-specific binding energies and entropies of NH_3 and other molecules on Pt surfaces.

In this work, we report elementary thermal rate constants for NH_3 desorption from and diffusion on Pt(111) and Pt(332) at surface temperatures $430 \leq T \leq 620$ K, derived from kinetic data obtained with the velocity-resolved kinetics method.[22] We find that the kinetic traces for the desorption rate of NH_3 from a Pt(111) surface do not follow first-order kinetics but are instead biexponential. This is attributed to the exceptionally high diffusion barrier of NH_3 on the (111) terrace that slows down the diffusion across the terraces toward the steps: molecules that desorb from the terrace prior to reaching the steps comprise the fast component of the biexponential, whereas molecules that make contact with the steps comprise the slow component. We globally fit desorption data from Pt(111)—step density 0.4 ± 0.2% monolayer (ML)—and Pt(332)—step density 16.7%ML—using a kinetics model that includes NH_3* desorption from terraces and steps, hopping across terraces and hopping from steps to terraces. From the derived rate constants, we can accurately compute the desorption rate of NH_3 from Pt surfaces as well as the population of step and terrace sites as a function of step density, pressure, and temperature.

The high quality of the kinetic data over a wide range of temperatures provides a great deal of information through application of TST, but the most common implementations of TST reported so far cannot reproduce our results. This problem is solved by developing a semiempirical partition function of adsorbed ammonia that includes the coupling between several modes that actively participate in diffusion. Using this form of TST, we obtain an excellent fit to the measured rate constants as well as NH_3's binding energy on terraces of Pt(111) (1.13 ± 0.02 eV), the diffusion barrier between binding sites of Pt(111) (0.71 ± 0.04 eV), and the degree of energetic stabilization of NH_3 at steps compared to terraces (0.23 ± 0.03 eV). These results are in good agreement with DFT calculations that we also report here. Note the diffusion barrier for this system is ∼65% of the binding energy, a strong violation of the so-called 12% rule,[23,24] postulating that diffusion barrier constitutes a rather small fraction of a binding energy. Clearly, the 12% rule should be used with caution.

We also used DFT calculations to investigate the coverage dependence of the NH_3 desorption rate; our results are able to reproduce previously reported TPD experiments carried out for NH_3/Pt(111),[12] conducted at much lower surface temperatures. This success of our approach over such a wide temperature range justifies modeling catalyst NH_3 coverages at high temperatures and pressures typical for Ostwald catalysis reactors. Our model predicts NH_3 coverages below ∼10%, whereas established reactor models predict fully covered catalysts at all conditions relevant to the Ostwald process. We believe this explains why some of the established reactor models tend to overestimate the degree of NH_3 slippage at process-relevant conditions.[18] Finally, we find that the derived desorption and diffusion rates from this work suggest that the mean-field approximation, frequently employed to model reaction rates, is not appropriate for description of NH_3 reactivity on Pt under industrially relevant conditions.

2. RESULTS

The velocity-resolved kinetics technique has been described in detail elsewhere.[22,25,26] Compared to other kinetics methods applied to surface processes, it has the advantage of providing time-resolved desorption flux directly, as NH_3's velocity- and angle-resolved density is obtained as a function of its surface residence time using ion imaging. Briefly, NH_3 is deposited at a Pt surface of known temperature using a short (∼35 μs) molecular beam pulse to initiate the thermal desorption process. The flux of desorbing ammonia ($\propto d[NH_3^*]/dt$) is obtained as a function of residence time by scanning the delay between the molecular beam pulse and an ionization laser pulse. The beam-laser delay is easily converted to surface residence time through knowledge of the molecule's speed. Together this yields the kinetic trace, defined as the flux of ammonia leaving the surface versus residence time. At each value of time, velocity-resolved kinetics provides not only the kinetic trace but also, in addition, the speed and angular distributions of the desorbing ammonia molecules. See section 5.1 for further details of the methods used for these measurements.

We obtained the speed distributions for NH_3 desorption from both Pt(111) and (332) at several surface temperatures, T_S (Supporting Information (SI), section S1). We fit these to Maxwell−Boltzmann distributions, extracting an effective translational temperature for the desorbing molecules, T_{tr}. For experiments with Pt(332), T_{tr} was found to be equal to T_S; whereas, for Pt(111) T_{tr} was less than T_S. Based on detailed balance,[27] these results immediately indicate that NH_3 adsorption to Pt has no activation barrier and, therefore, that the binding energy is equal to the desorption energy. Furthermore, we also obtain the shape of the sticking probability curve as a function of kinetic energy $S(E_{tr})$, and by assuming $S(E_{tr} = 0)$ to be 1,[28] we obtain the absolute

https://doi.org/10.1021/jacs.1c09269
J. Am. Chem. Soc. 2021, 143, 18305−18316

Journal of the American Chemical Society pubs.acs.org/JACS Article

quantity $S(E_{tr})$. This is used to obtain the thermal sticking probability $\langle S_0 \rangle(T)$ between 0 and 2000 K, which is shown in section S2 in the SI. A previous report at a single temperature[9] agrees well with our results.

We also obtained kinetic traces for NH_3 desorption from Pt(111) and Pt(332), which are shown on a logarithmic scale at nine surface temperatures in Figure 1. The sharp, early time

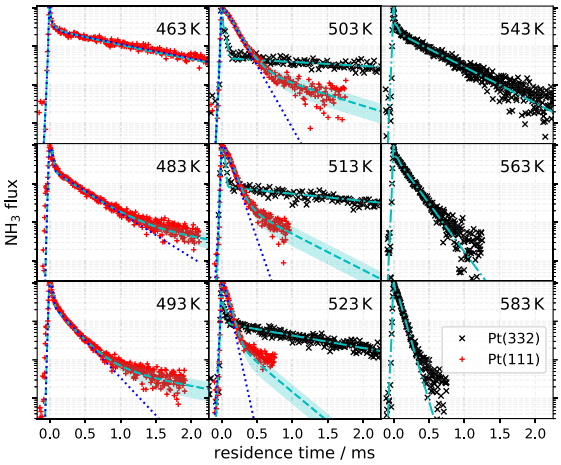

Figure 1. Kinetic traces of NH_3 desorbing from Pt(111) (+) and Pt(332) (×) for surface temperatures between 463 and 583 K. The step density of the Pt(111) is 0.4 ± 0.2%ML and of Pt(332) is 16.7% ML. The light blue dashed (− −) and dash-dotted (− · −) lines show the global fit to the experimental kinetic data for Pt(111) and Pt(332), respectively. The shaded regions indicate the model uncertainty associated with the step density of the Pt(111) surface. The blue dotted line (···) indicates the model's prediction for NH_3 desorption rate from a step-free (ideal) Pt(111) surface.

(first 0.1 ms) feature is a residual NH_3 background from the directly scattered beam. It is independent of surface temperature and exhibits a narrow angular distribution peaking close to the specular angle. The dominant contribution to the observed signal is temperature-dependent and arises from thermally desorbing NH_3. It has a broad angular distribution ($\sim\cos(\theta)$), where θ is the angle with respect to the surface normal. The NH_3 desorption rate from Pt(332) follows first-order kinetics as expected for a simple desorption process; however, NH_3 desorbing from Pt(111) with 0.4 ± 0.2% steps is biexponential, with a fast (major) and a slow (minor) component. We repeated the desorption experiments at a Pt(111) surface with fewer steps and found that the slow component could be even further reduced (see section S3 in the SI). Notice that, when compared at the same temperature, the major component of Pt(111) data is faster than desorption from Pt(332). This indicates that NH_3 has an increased residence time on highly stepped surfaces.

Figure 2 shows schematically the energy landscape and key elementary processes, with their rate constants, of a kinetics model capable of describing NH_3 diffusion and desorption at Pt surfaces as a function of step density. The model is one-dimensional describing diffusion perpendicular to steps only. Each rate constant is parametrized in an Arrhenius form. The short time behavior of the kinetic trace, representing the direct scattering, is modeled with a temperature-independent model based on the arrival time distribution of the NH_3 at the surface. We use periodic boundary conditions and make the model

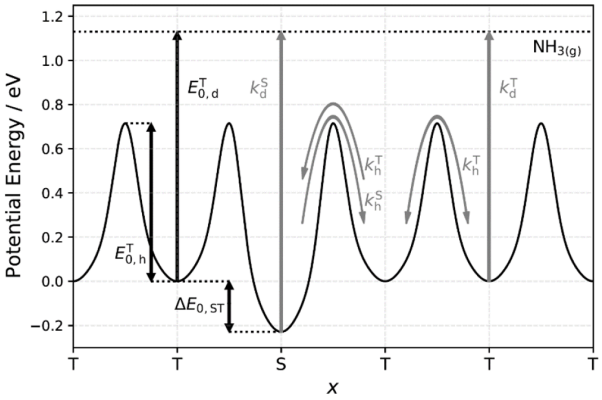

Figure 2. Schematic overview of the elementary processes (gray) included and energy parameters (black) extracted from the desorption−diffusion kinetics model. Steps and terraces are indicated by the letter S and T, respectively. The NH_3 binding energy at (111) terraces of Pt is $E^T_{0,d}$ = 1.13 ± 0.02 eV, the site-to-site hopping barrier is $E^T_{0,h}$ = 0.71 ± 0.04 eV, and the energy preference for steps is ΔE_{ST} = 0.23 ± 0.03 eV. Following a similar strategy as described in ref 20, we include five elementary processes with first-order rate constants: (1) hopping between adjacent terrace sites, k^T_h; (2) hopping from terrace to step sites, which is assumed to be the same as k^T_h; (3) hopping from step to terrace sites, k^S_h; (4) desorption from terrace sites k^T_d; and (5) desorption from step sites, k^S_d. We note that k^S_d describing process (5) is not an independent rate constant, $k^S_d = k^T_d k^S_h / k^T_h$; see section S4.1 of the SI.

applicable to different step densities by varying the number of terrace sites separating the steps. Using this diffusion−desorption kinetics model (see section S4.2 of the SI for details), we fit the measured desorption rates from Pt(111) and Pt(332) simultaneously at all temperatures (see section S4.3 of the SI for details). The fit, shown as dashed (− −) and dash-dotted (− · −) lines in Figure 1, is excellent. The six independently derived Arrhenius rate parameters and their uncertainties are presented in Table 1.

Using the values of Table 1, we simulated how NH_3 desorption would look in the absence of steps (blue dotted

Table 1. Rate Constants for Desorption and Diffusion of Ammonia on Platinum[a,b]

elementary rate constants	fitted parameters	fit results
$k^T_d(T)$	$E^T_{a,d}$/eV	1.09 ± 0.02
	$\log_{10}(A^T_d/s^{-1})$	14.8 ± 0.2
$k^S_h(T)$	ΔE_{ST}/eV[c]	0.23 ± 0.03
	$\log_{10}(A^S_h/s^{-1})$	13.7 ± 0.6
$k^T_h(T)$	$E^T_{a,h}$/eV	0.73 ± 0.04
	$\log_{10}(A^T_h/s^{-1})$	13.6 ± 0.4
	derived quantities	
$k^S_d(T) = k^T_d k^S_h / k^T_h$	$E^S_{a,d}$/eV	1.32 ± 0.04
	$\log_{10}(A^S_d/s^{-1})$	14.9 ± 0.6
$D^T(T)$[d]	$\log_{10}(D^T_0/cm^2\ s^{-1})$	−1.9 ± 0.4

[a]Results were obtained from the global fit of the kinetics model to experimental desorption rates from Pt(111) and Pt(332). [b]The elementary rate constants are parametrized according to the Arrhenius equation: $k(T) = A \exp(-E_a/k_BT)$. [c]$E^S_{a,h} = E^T_{a,h} + \Delta E_{ST}$. Since $A^S_h \approx A^T_h$, the difference of activation energies ΔE_{ST} is nearly equal to the difference of binding energies $\Delta E_{0,ST}$. [d]$D^T(T) = D^T_0 \exp\left(-\frac{E^T_{a,h}}{k_BT}\right)$, where D^T_0 is derived from A^T_h following ref 29.

https://doi.org/10.1021/jacs.1c09269
J. Am. Chem. Soc. 2021, 143, 18305−18316

lines (···) in Figure 1). This shows that the fast component of the biexponential decay reflects direct desorption from terrace sites. In light of the relatively large step stabilization energy ΔE_{ST} also shown in Table 1, it becomes clear why desorption from Pt(332) is slower than the fast component of desorption from Pt(111). Table 1 also shows the computed prefactor for the terrace diffusion constant $D^T(T)$ derived from the hopping rate constant $k_h^T(T)$ following ref 29 as well as the rate constant for direct desorption from steps $k_d^S(T)$, which is derived from the other rate constants. Notice that the Arrhenius prefactor for terrace desorption and direct step desorption are nearly equal; that is, the entropy of the NH_3 is nearly the same for these two binding sites. This is a striking result and means that the ammonia molecule is highly localized at terrace sites, a conclusion that is consistent with the large activation energy found for terrace hopping $E_{a,h}^T = 0.73 \pm 0.04$ eV.

Combining kinetic data with DFT parametrized TST can be highly useful. Thus, we performed a variety of DFT calculations using the Perdew–Burke–Ernzerhof (PBE) exchange-correlation functional.[30] Our experiments are relevant to the zero-coverage limit; hence, we relied most heavily on DFT calculations carried out using a periodic 4 × 4 unit cell. We find that the on-top site is the most stable binding site for NH_3* at Pt(111) with a (zero-point energy corrected) binding energy of 0.86 eV at 0.06 ML. In addition, we performed calculations with 2–4 NH_3* molecules placed in the cell to produce coverages from 0.12 to 0.25 ML. We calculated the NH_3* binding energy at Pt(111) in each case and find it to decreases linearly with increasing coverage with a slope of $\alpha = -1.61$ eV/ML. Based on this finding, we determine a zero-coverage binding energy of 0.95 eV (see section S5 of the SI). Similarly, we calculate the binding energy at Pt(332) and, by comparison to Pt(111), find that the step stabilization is 0.30 eV.

In addition to the binding energy calculations, we performed analysis of the minimum energy pathway for hopping between on-top binding sites of Pt(111). We use the climbing image nudged elastic band (CI-NEB) method[31] to locate the TS that we found at the bridge site. We obtain a zero-point energy corrected hopping barrier of 0.70 eV (0.52 eV) for the 4 × 4 (2 × 2) supercell. We also performed calculations of the harmonic frequencies at the on-top most stable binding site and for the transition states found at the bridge site (see Table 2).

3. FURTHER ANALYSIS AND DISCUSSION

3.1. Two Approaches to the Adsorbate Partition Function. In this section, we analyze the derived thermal rate constants in terms of transition state theory. This allows us to derive fundamental quantities such as the desorption energy and the diffusion barrier height. We elaborate detailed expressions for the adsorbate partition function in two ways. The partition function is normally considered a product of partition functions for the individual degrees of freedom (DOFs). We show here that this uncoupled TST approach fails to reproduce our experimental results. We then introduce a partition function which makes a better accounting of the state count when some of the DOFs are coupled (coupled TST). Coupled modes are identified through DFT calculations of NH_3's minimum energy pathway for hopping where we find that hindered translation and frustrated rotational modes are actively participating in the site-to-site exchange. This is reflected by an increase of surface–molecule distance and tilting of NH_3's symmetry axis along the minimum energy pathway. Also the associated vibrational frequencies decrease at the transition state for hopping by a factor of 2 to 3 (see Table 2), reflecting their importance for accurate description of the adsorbate entropy. This approach allows us to explain the temperature dependence of the rate constants precisely over the entire temperature range. This then provides the most accurate energy barriers for NH_3 site-to-site hopping and desorption from Pt(111) presently available.

Table 2. Results of DFT Calculations Performed for This Work: Harmonic Frequencies for NH_3* at the Most Stable Binding Site (On-Top) and on the Transition State (TS) for Hopping (Bridge) Obtained from a 4 × 4 [2 × 2] Supercell Using the PBE Exchange-Correlation Functional[a]

mode		calculated harmonic frequencies/cm^{-1}	
ν_i (ν_{gas})	description	on-top	TS for hopping (bridge)
ν_1 (3a)	asym. stretch	3483.1 [3484.4]	3546.7 [3550.5]
ν_2 (3b)	asym. stretch	3481.5 [3482.8]	3540.1 [3545.6]
ν_3 (1)	sym. stretch	3356.8 [3342.7]	3400.6 [3397.4]
ν_4 (4a)	asym. bending	1572.5 [1551.3]	1583.3 [1586.8]
ν_5 (4b)	asym. bending	1571.5 [1549.7]	1581.3 [1577.9]
ν_{umb} (2)	umbrella mode	1142.0 [1055.2]	930.0 [856.2]
	free C_3-axis rotation	- [-]	- [-]
R_x	frustrated rotation	672.7 [636.3]	325.8 [131.3]
R_y	frustrated rotation	672.4 [636.3]	269.9 [109.5]
T_z	hindered translation	357.8 [338.3]	127.5 [45.9]
T_x	hindered translation	122.8 [109.5]	190.9i [176.4i]
T_y	hindered translation	119.9 [109.5]	68.2 [-]

[a]The imaginary frequency in T_x at the TS emerges from the degeneracy with the hopping coordinate. In this work we numbered the internal modes of adsorbed NH_3 from high to low frequency. The conventional nomenclature from gas-phase vibrational spectroscopy is provided in parentheses for convenience.

The general expression for the TST rate constant for desorption or diffusion is

$$k_{TST}(T) = \frac{k_B T}{h}\frac{Q^{\ddagger}}{Q_{ad}}\exp\left(-\frac{E_0}{k_B T}\right) \quad (1)$$

where Q_{ad} is the partition functions of the ammonia adsorbate, $Q^{\ddagger}$ is the partition function for the transition state, and E_0 is the zero-point energy corrected barrier height. Highly accurate evaluation of Q_{ad} is often unnecessary in analyzing surface desorption rate data as the uncertainty in the experimental prefactor often exceeds an order of magnitude[32] or in many cases is not measured at all.[8] When analyzing high-quality kinetic data as obtained with velocity-resolved kinetics, Q_{ad} becomes a sensitive probe of the NH_3/Pt interactions. Inappropriate approximations lead to detectable deviations from the measured desorption rates. In the following, we demonstrate the deficiencies of uncoupled TST and the advantages of coupled TST for the computation of Q_{ad}.

The first approach, uncoupled TST (uTST), uses a sophisticated and established approach. Here, we base it on the approximation of a hindered translator,[33] which is considered as one of the more accurate ways to compute Q_{ad}.[34] Here, the partition functions for $T_{x,y}$ are described using a model potential, parametrized using DFT-calculated hindered translational frequencies (see Table 2) and the

https://doi.org/10.1021/jacs.1c09269
J. Am. Chem. Soc. 2021, 143, 18305–18316

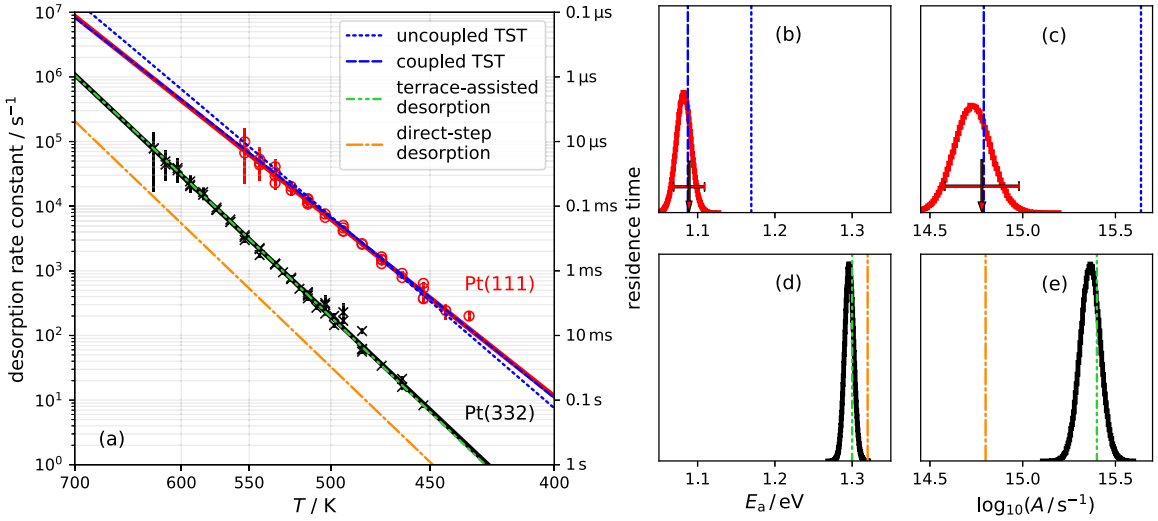

Figure 3. (a) NH_3 desorption rate constants from Pt(111) terrace obtained from global kinetics model fit (red line) and from individual fits of the kinetic traces (red circles with error bars; see section S7 of the SI). The red line is *not* the Arrhenius fit to the circles. Terrace desorption rate constants are compared to the uTST (blue dotted) and cTST (blue dashed) models. The first-order desorption rate constants from Pt(332) (black crosses with error bars) and the corresponding Arrhenius fit (solid black line) are compared with a model assuming that desorption happens directly from steps (k_d^S from Table 1, orange dash-dotted line) and a model that describes desorption as a "terrace-assisted" process including desorption from terraces and steps (eq 4, green dash-dot-dotted line). (b,c) Comparison of experimentally derived Arrhenius activation energy and prefactor for terrace desorption from Pt(111) and Arrhenius parameters predicted based on uTST (dotted blue line) and cTST (blue dashed line) models at 530 K (average temperature of present experiments). The red arrows with error bars result from global fit of diffusion−desorption kinetics model to experimental data (see SI section S4.3) and are represented by the red line in panel (a). The red histograms are parameter distributions emerging from Arrhenius fit (not shown for clarity) to red circles of panel (a). (d,e) Comparison of the Arrhenius parameter obtained from first-order desorption rate constants from Pt(332) to rate parameters based on direct-step and "terrace-assisted" desorption model at 530 K.

experimentally derived terrace hopping barriers (see section 3.3). The hindered translational partition function exploits an established interpolation scheme, ensuring its proper behavior at low and high temperatures.[21,33,35] We treat NH_3 rotation around its symmetry axis as a free rotation, justified by our DFT results and in agreement with previous theoretical work.[36] The remaining DOFs are described by harmonic oscillators. For uTST, we use DFT-calculated frequencies for NH_3 bound at its most stable binding site (see Table 2), consistent with how this approach is conventionally applied (for further details, see section S6.1 of the SI).

The uTST assumes that all DOFs are decoupled, making Q_{ad} a product of the partition functions of each DOF sensitive only to the structure of the molecule at the on-top binding site. However, when NH_3* migrates over a diffusion barrier, its binding strength at the surface weakens, and consequently, the vibrational modes, especially those that strongly influence the oriented molecule−surface binding ($R_{x,y}$, T_z, and ν_{umb}), soften substantially (see Table 2). Since these modes have low frequencies, further frequency reduction has a large impact on the thermally accessible density of states.

To account for this effect, we developed a second approach, dubbed hereafter as the coupled TST (cTST) model. Briefly, cTST allows translation parallel to the surface to explicitly soften several of ammonia's vibrational frequencies. This precludes a product form for Q_{ad}. Instead, we construct a partition function where the vibrational frequencies of several modes (ν_{umb}, R_x, R_y, and, T_z) vary along the minimum energy pathway for site-to-site hopping. This approach describes more faithfully the bond softening induced by the motion toward the diffusion barrier. Other DOFs are described as in uTST model. The construction of Q_{ad} for the cTST is described in detail in the SI section S6.2. In the next section, we apply uTST and cTST for the description of desorption and hopping rates of NH_3 at Pt(111).

3.2. Analysis of the Desorption Rate Constants Using TST. To obtain desorption rate constants from TST, we must compute $Q^{\ddagger}$. The modern formulation of TST prescribes a dividing plane that separates reactants from products such that every trajectory that originates in the reactant region of configuration space and evolves to the product region must pass through the dividing plane at least once. The choice of the position of the dividing plane can influence the probability for recrossing, which introduces a recrossing error to the TST rate. For NH_3 desorption from Pt, it is convenient to place the dividing plane far from the surface, where the gas-phase NH_3 molecule becomes the transition state. This choice of the transition state is convenient, as the thermal sticking coefficient $\langle S_0 \rangle(T_S)$ obtained above serves as the exact recrossing correction.[37] Furthermore, $Q^{\ddagger}$ is easily computed using tabulated gas-phase vibrational frequencies and rotational constants. We carried out this procedure in a similar way to a recent report for NO desorption from Pd;[21] also, see section S6.3 of the SI.

We may then write down a highly accurate formula for the experimentally derived desorption rate constants:

$$k_d(T) = \langle S_0 \rangle(T) k_{TST}(T) \quad (2)$$

Using eq 2, we optimized E_0 to fit the cTST and uTST model to the experimentally derived terrace desorption rate constants—red circles with error bars and solid red line in Figure 3a. The red line is the terrace desorption rate constant that we extract from the global kinetics model fit (see also Table 1). Complementary to the global fit results, we analyze

https://doi.org/10.1021/jacs.1c09269
J. Am. Chem. Soc. 2021, 143, 18305−18316

the fast decay of each NH_3 kinetic trace from Pt(111) that we assigned to reflect the terraces' desorption (see Figure 1) and derive the red circles from Figure 3a; see section S7 of the SI for details. The cTST (uTST) yields the blue dashed (dotted) line in Figure 3a with $E^{T}_{0,d}$ = 1.13 ± 0.02 (1.17) eV. Figure 3b,c offers a clear comparison of the cTST and uTST models to the derived Arrhenius rate parameters, which accurately represent the experimental rate constants. Here, the red arrow with the error bar represents the experimental uncertainty of the Arrhenius activation energy (Figure 3b) and Arrhenius prefactor (Figure 3c) for terrace desorption obtained from the global kinetics model fit to the experimental data, see section S4.3 of the SI for details. Complementing this, the red histograms display the uncertainty of the terrace desorption Arrhenius rate parameters that we derive from an Arrhenius fit (omitted in Figure 3a for clarity) to the red circles from Figure 3a. Both rate parameters are accurately reproduced by the cTST model (blue dashed vertical line), while the uTST model (blue dotted vertical line) clearly fails. Specifically, the uTST predicts an adsorbate entropy that is too low, and thus the resulting prefactor is too high (Figure 3c). The activation energy is then forced to be artificially high to compensate for this error in the prefactor (Figure 3b).

Based on this analysis, we recommend the results of the cTST model ($E^{T}_{0,d}$ = 1.13 ± 0.02 eV) for future use as the ammonia desorption energy on Pt(111). This value agrees with results from CID[10] (1.1 ± 0.1 eV), although the error bar of that work was far outside chemical accuracy. Results from LID (0.8 eV) are clearly incompatible with the present work.[11] This is likely due to the fact that those experiments were done at relatively high coverages. Despite working at low coverages, previous MBRS results (0.68 eV) are also incompatible with our results. The value of $E^{T}_{0,d}$ found with velocity-resolved kinetics is in poor agreement with DFT calculations when a PBE exchange-correlation functional is used—0.95 eV—see section S5 of the SI. Previous work with the PW91 functional[38] yielded a value of ∼1.0 eV, which agrees only slightly better with the present results, confirming similarities between the PBE and the PW91 functionals.[14]

In the global fit of the kinetics model, we have also derived ΔE_{ST}, the activation energy difference between desorption of NH_3 at steps and terraces of Pt. As these two processes exhibit nearly the same prefactor, the difference of activation energies can be set equal to the difference in binding energies, $\Delta E_{0,ST}$ = 0.23 ± 0.03 eV. This compares well to previous TPD work (∼0.2 eV)[8] and our DFT calculations, which predict an energy preference at steps of 0.3 eV. These results also have implications for the mechanism of desorption from steps. In Figure 3a, we compare a model that naively assumes desorption from a stepped surface, like Pt(332), that occurs directly—that is, diffusion from steps to terraces is unimportant. This clearly fails to capture the experimental observations (orange lines in Figure 3a,d,e). This suggests a more intricate step desorption mechanism, where both steps and terraces play a role. This is discussed further in section 3.5.1.

3.3. Analysis of the Hopping Rate Constants Using TST. We also used the cTST and uTST models to describe NH_3 site-to-site hopping on Pt(111). Here, we require the partition function of the hopping TS. To compute that, we approximate all but two DOFs as simple harmonic oscillators (with frequencies from Table 2). The exceptions are the NH_3* rotation around its symmetry axis, which is again assumed to be a free rotation, and T_y, which is treated as described in section S6.4 of the SI. Note that translation along x drops out, as this is the hopping coordinate. We first carry out this calculation using the DFT-derived and zero-point energy corrected hopping barrier of 0.70 eV presented above. The modeled cTST and uTST hopping rate constants at Pt(111) are shown as blue dashed and blue dotted lines of Figure 4, respectively, and are compared to the experimentally derived hopping rate constant (black solid line).

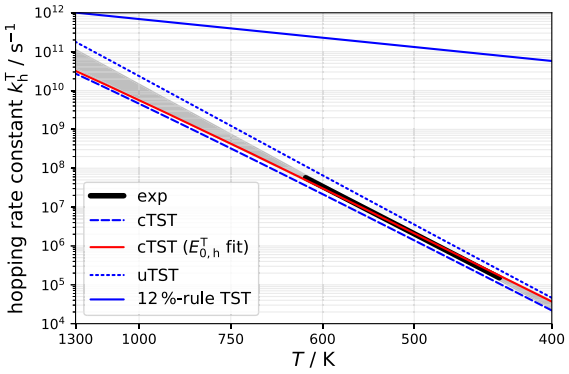

Figure 4. Broad black line shows the derived hopping rate constants in the temperature range of our experiments. The extrapolation of the derived hopping rate constant based on its Arrhenius parameters is shown as the gray shaded region that indicates the uncertainty of extrapolation. The blue solid line is the result of the hopping rate constant that is estimated based on the 12% rule (eq 3) suggested by Mavrikakis and co-workers.[23,24] The blue dashed (dotted) line is the result of cTST (uTST) modeling of hopping rate constant using DFT-calculated hopping barriers. The red solid line is the cTST model using the hopping barrier fitted to the experimental rate constant. The residual mismatch between experiment and the cTST model can be explained with uncertainties in the assumptions of the TS partition functions (see text).

Again, cTST results are within ∼30% of the experimental values. The uTST model predicts rate constants that are systematically ∼2× too large. We note that the residual error in the cTST rate constant is not necessarily due to an error in the DFT barrier height. Instead, it could be an indication that a coupled partition function for the transition state is also required, something that is beyond the scope of this work. Coupling DOFs in the TS would increase TS state densities and increase the hopping rate constant, possibly leading to better agreement with the experiment. The use of an uncoupled partition function for the TS is also likely to be the reason why the deviation of uTST from experiment is only a factor of ∼2—due to a compensation of errors taking place in Q_{ad} and $Q^{‡}$.

We used two approaches to attempt an experimental determination of the hopping barrier. In the first, we optimized $E^{T}_{0,h}$ in the cTST model to fit our experimental hopping rate constant (black solid line of Figure 4). This led to 0.68 eV, which represents a lower limit. See also the red solid line in Figure 4. In the second approach, we used the DFT hopping barrier and determined the difference between activation energy and barrier height for hopping, based on the cTST model; $E^{T}_{a,h}$(500 K) − $E^{T}_{0,h}$ = 0.017 eV, which we subtracted from the experimentally obtained activation energy for hopping ($E^{T}_{a,h}$ = 0.73 ± 0.04; see Table 1). For the estimation of the activation energy, we used an average temperature of our

https://doi.org/10.1021/jacs.1c09269
J. Am. Chem. Soc. 2021, 143, 18305−18316

Pt(111) experiments (500 K, which are most important to extraction of diffusion rates). This yielded an estimate of the hopping energy barrier: $E_{0,h}^{T}$ = 0.71 ± 0.04 eV, which also compares well with the DFT-derived hopping barrier obtained with the PBE functional and the estimated lower limit.

3.4. Comment about the 12% Rule for Diffusion Barriers. We notice that the Arrhenius expression-based prefactor derived for NH_3 hopping—$A_h^T = 10^{13.6\pm0.4}$ s^{-1}—is higher than values considered "common", i.e., $10^{<13}$ s^{-1}. However, this high value not only is in good agreement with DFT and cTST prediction of $10^{13.3}$ s^{-1} but also is physically reasonable. When a molecule is positioned at a weakly bound site, like the TS for hopping, its interaction with the surface is weakened, and thus the molecule is more likely to have an enhanced density of states and concomitant higher entropy. When the hopping barrier is very high, the TS is actually similar to a gas-phase molecule. Hence, the hopping prefactor will approach the prefactor for desorption, and the hopping of the molecule can be imagined to resemble transient or partial desorption, which is the case for NH_3 on Pt(111). Contrasting this to the case of a small hopping barrier, the adsorbates' density of states hardly changes at the hopping transition state compared to the molecule at its initial binding site. Therefore, the TST rate constant can be expressed using only the information about the molecule's hindered translational frequency, here, ∼120 cm^{-1}:

$$k(T) = \frac{k_B T}{h}\frac{1}{Q_x^{qHO}}\exp\left(-\frac{E_{hop,low}}{k_B T}\right) \xrightarrow{@500\ K} 10^{12.5} s^{-1}\exp\left(-\frac{E_{hop,low}}{k_B T}\right) \quad (3)$$

The associated prefactor will be in the range of 10^{12-13} s^{-1}, considered to be "typical". A similar conclusion was reached by Mavrikakis and co-workers[23,24] in developing the so-called 12% rule ($=E_{hop}/E_{bind}$) for diffusion barriers who argued that not only is the ratio of E_{hop} to E_{bind} likely to be about 0.12 but that the prefactors for hopping are commonly 10^{12-13} s^{-1}. Ammonia binding to and diffusion on Pt(111) is an illustrative example, emphasizing that one has to be cautious with drawing universal conclusions about scaling relations based on stable site binding energies alone, without considering the nuances of molecular structure. In Figure 4, we show for comparison the hopping rate constant with barrier estimated based on the 12% rule with the corresponding hopping prefactor from eq 3, where the failure of this estimate becomes evident.

It had been realized earlier that the choice of the adsorbate entropy[33,34,39,40] models and inclusion of anharmonic corrections[41] has a substantial impact on the prediction of thermodynamic state functions relevant for the description of reaction rates. However, coupling of different DOFs, which we clearly show to be important for NH_3 at Pt, is normally not considered. While these problems could, of course, be solved by demanding construction of a full dimensional potential energy surface, it is useful to develop a systematic hierarchy of correction schemes to provide an accurate description of thermal reaction rates using TST beyond the harmonic approximation. In that spirit, the application of the cTST model, incorporating the coupling of in-plane coordinates to different DOFs is a good step forward, especially as it requires little more input information from DFT than is already used for the less sophisticated approaches.

3.5. Implications for Modeling of the Ostwald Process. The ability of ammonia to find its way to steps is critical to it becoming chemically activated in the Ostwald process.[2,4,5,7] In principle, this may happen by either direct adsorption and desorption to and from steps or by adsorption at terraces followed by diffusion to steps in competition with desorption. The complexity of the adsorption/diffusion/desorption often goes unappreciated. In this section, we take up this matter.

3.5.1. Desorption Involving Multiple Active Sites. We have shown that NH_3 desorption from Pt(111) is primarily due to desorption from terraces, whereas the desorption rate from Pt(332) is strongly influenced by steps. In Figure 3a, we show the extracted first-order rate constants of NH_3 desorption from Pt(332) (black crosses) and compare them to the elementary rate constants for direct desorption from steps, k_d^S (orange dash-dotted line)—direct desorption from steps fails to explain experiment. This is easily understood as molecules bound at steps can readily hop first to a terrace site, where desorption is much faster. Simply put, hopping from steps to terraces with subsequent desorption from terraces involves two low barrier processes, whereas direct desorption from steps involves one high barrier process. By assuming a steady-state concentration of ammonia at terraces (conditions that are ensured for Pt(332) experiments; see section 3.5.2) and including competitive desorption from terraces and steps, we can derive the effective first-order desorption rate constant of NH_3 from a stepped surface (see section S8 of the SI for further details):

$$k_{eff}(T) = k_d^S + k_h^S(1-\mu)\times\frac{k_d^T}{k_h^T\mu + k_d^T} \quad (4)$$

where $k_{eff}(T)$ describes the "terrace-assisted" desorption of molecules (at low coverages) from surfaces with the step density, μ, which is defined as steps per unit cell length. The first term of eq 4 is the contribution of direct desorption from steps; the second term consists of a product between the hopping rate from steps to terraces, followed by the probability to desorb from terraces. For the derivation of this equation, we assumed that the total NH_3 population at Pt(332) is well described by the population at steps. This assumption is justified, as NH_3 has a high energy preference for steps, and entropic gain from binding at terraces is small due to a small number of terraces. See the SI section S8 for detailed derivation of this equation. The results of this "terrace-assisted" model are shown in Figure 3a as the green line, which agrees very well with the experimentally derived first-order desorption rate constants from Pt(332). In addition, the model reproduces the experimentally derived activation energy and prefactor for NH_3 desorption from Pt(332) quite well (see Figure 3d,e).

Figure 3a shows that desorption rates from an Ostwald catalyst with multiple active sites cannot be adequately described if exchange between steps and terraces is not explicitly considered. However, very often, kinetics modeling of the desorption process does not consider multiple binding sites even though they are present at the stepped model catalysts. Most commonly, single binding sites are assumed that have the characteristic energies and prefactors that are associated with the most stable binding site.[2,17,18] Clearly, this approach will underestimate the rate of actual desorption, where the adsorbate might exchange between binding sites and leave the surface through the less stable binding site. In fact, such

https://doi.org/10.1021/jacs.1c09269
J. Am. Chem. Soc. 2021, 143, 18305−18316

errors, even if the rate constants are modeled correctly, may lead to erroneous conclusions about the efficiency of a catalyst at the desired reaction conditions.

3.5.2. Limited Applicability of Mean-Field Approximation for NH_3 Chemistry at Pt. We have observed that the NH_3 desorption rate from Pt(111) with a step density of 0.4 ± 0.2% has a biexponential behavior, emerging from the competition between NH_3 desorption from terraces and its slow diffusion to steps. At Pt(332), we observe a single-exponential desorption rate, indicating that NH_3 equilibrates between steps and terraces, demonstrating that the competition between diffusion and desorption depends on the step density. Obviously, it will also depend on the temperature. Using the derived elementary process rate constants, we next investigate the competition between diffusion to steps and desorption from terraces as a function of the step density and temperature, including conditions relevant to Ostwald process.

For the purpose of demonstration, we determine NH_3's probability to reach a step after landing at the center of a terrace. To do so, we place a low initial concentration of NH_3 at the center of the terrace and solve the desorption−diffusion rate equations. We set $k_h^S = 0$, "freezing" the NH_3 molecule once it reaches a step. After all the NH_3 molecules have either desorbed from the terrace or diffused to the steps, we determine the fraction of molecules that remained at steps. The results of this analysis are shown in Figure 5.

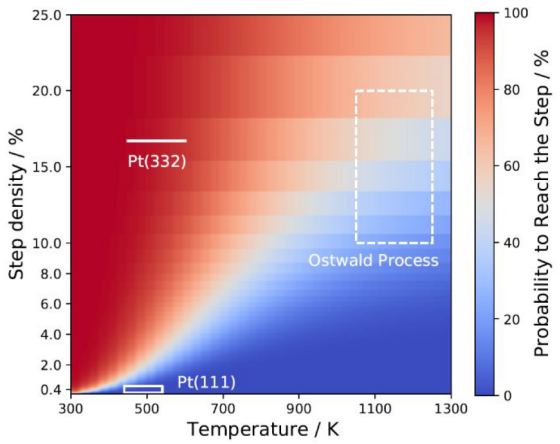

Figure 5. Probability of NH_3 molecules that landed in the center of the terrace to reach the steps before desorption as a function of step density and catalyst temperature. The temperature ranges (1050−1250 K) and associated step densities of our experimental (solid box) and Ostwald process (dashed box) conditions are indicated in the plot. The step densities for the Ostwald catalyst are not known, but we consider typical step/edge densities found on catalytic nanoparticles[42,43] as representative for real catalysts.

At low temperatures, diffusion to steps is fast compared to NH_3 desorption, and all molecules can reach the step. At high temperatures, NH_3 is less likely to reach the steps prior to desorption because the site-to-site hopping event approaches a time scale similar to that of the desorption event. Although the probability to reach the step increases with higher step densities, it can be clearly seen that at conditions typical for the Ostwald process not all molecules landing at majority terrace sites are able to reach the step prior to their desorption. It means that NH_3 must adsorb on or very close to a step site in order to react. Under typical Ostwald conditions, the reactants (NH_3* and O* at steps) are not able to encounter one another on a time scale faster than desorption, and as a consequence, the reactants cannot be assumed to be homogeneously mixed. This calls in question the basic assumption of the mean-field rate equations commonly used to model the Ostwald process.

The slow hopping rates and the previously observed preference for reaction at steps suggests that kinetics modeling of NH_3 chemistry at Pt needs to explicitly account for different active sites and accurately describe the exchange between them—factors that have not been considered in kinetics modeling of Ostwald process so far. Notice that under catalytically relevant conditions, other adsorbates like NO* and O* will be present at the catalyst and likely decrease NH_3's mobility even further. These results suggest that the key reaction in the Ostwald process may, in fact, be diffusion-limited, contradicting current models that assume fast diffusion.[2,4,5,18]

3.5.3. NH_3 Coverages at a Pt Catalyst under Ostwald Process Conditions. Current kinetics models for NH_3 oxidation at Pt lack transferability to reaction conditions different from those at which they were optimized. One possible reason for this is that the rate parameters employed do not describe elementary steps in the reaction. Using the experimentally derived desorption rates of this work, we can estimate the stationary NH_3 isosteres as a function of temperature and pressure at steps and terraces of a stepped Pt catalyst at conditions typical for the Ostwald process. We compare those with predictions of the KB[18] model that is frequently used for Ostwald process reactor simulations.[44−46]

This requires considering the coverage dependence of the ammonia desorption energy and prefactor. We use a coverage-dependent desorption barrier which we parametrize based on the experimentally derived NH_3 binding energy (in the zero-coverage limit) and the scaling of the binding energy with coverage derived from DFT calculations (see sections S5 and S9 of the SI). We have performed harmonic frequency and hopping barrier calculations with DFT at 0.06 and 0.25 ML NH_3 coverages, which allows us to estimate the coverage dependence of the prefactor. We assume that the logarithm of the prefactor—proportional to the entropy difference between the initial and transition state—scales linearly with coverage (see section S9 of the SI for further details). To test the constructed coverage-dependent desorption rate constant, we simulated TPD spectra from Pt(111) and compared them to results from previous works.[12] Earlier TPD studies[12] found broad NH_3 desorption peaks, indicating substantial adsorbate−adsorbate interactions, influencing the desorption rate. We find that our model predicts the right temperature ranges for the TPD spectra and accounts correctly for the coverage dependence, which is reflected by the shape of the TPD trace (see section S9 of the SI).

Next, we used the desorption−diffusion model to determine the steady-state NH_3 coverage at terraces and steps at surface temperatures and NH_3 partial pressures characteristic of the Ostwald process (see section S9 of the SI for details). We chose the highly stepped Pt(332) surface as a model catalyst for the Ostwald process. The results are shown in Figure 6 and compared to the KB model predictions.

We find that the steady-state coverage of NH_3 is strongly temperature- and pressure-dependent, whereas the KB model predicts saturated coverage under all conditions. Our model predicts rather low NH_3 coverages (blue color in Figure 6)

https://doi.org/10.1021/jacs.1c09269
J. Am. Chem. Soc. 2021, 143, 18305−18316

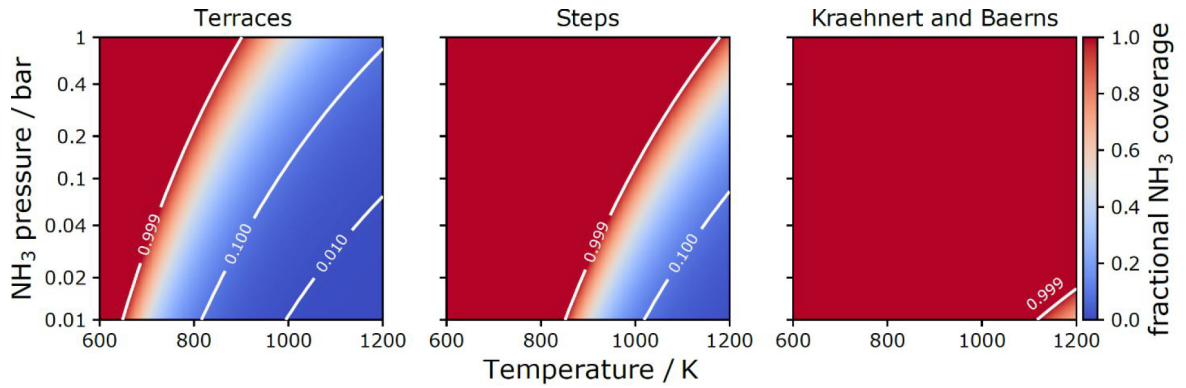

Figure 6. Fractional NH_3 coverages at terraces (left) and steps (middle) of a Pt(332) model catalyst at temperatures and NH_3 partial pressures typical for the Ostwald process. We compare our results (left and center panels) to the predictions of the KB model (right panel) which assumes one single active site for NH_3. Note that the Ostwald process is conducted at total pressures of ≥1 bar with NH_3 partial pressures of ∼10% of the total pressure.

over a broad range of Ostwald process conditions. We hasten to point out that NH_3 coverage will be strongly affected by coadsorbed O*, which can react to remove NH_3 but also may induce stronger ammonia binding to the surface. Still the comparisons shown in Figure 6 suggest that it is likely that the commonly applied kinetics model overpredicts the coverage of NH_3, which will lead to a higher degree of NH_3 slippage (where less nitrogen ends up as NO—the desired product of the Ostwald process). This is consistent with the fact that the KB model under-predicts the NO yield and tends to overestimate the N_2 yield at Ostwald process conditions.[18]

4. SUMMARY AND CONCLUSIONS

In this work, we have investigated the desorption kinetics of NH_3 from Pt(111) and Pt(332) between 430 and 620 K using velocity-resolved kinetics. Detailed analysis of NH_3 desorption kinetics using a diffusion−desorption kinetics model enabled us to extract rate constants for four elementary processes: direct desorption from terraces and from steps, site-to-site hopping at terraces, and hopping from steps to adjacent terrace sites. The measurement of a velocity-resolved kinetic trace provides simultaneously the speed distributions of desorbing molecules, from which we derive NH_3 thermal sticking coefficients to Pt using the principle of detailed balance.

The rate constants of the elementary processes of desorption and diffusion have been further analyzed using TST with DFT input parameters. The conventional TST models, which describe the partition function of the adsorbate with uncoupled DOFs, fail to reproduce the experimental results. A correction scheme to the partition function is implemented that allows NH_3 vibrational frequencies, associated with the molecule−surface interaction, to soften when displaced away from the most stable binding site. This approach faithfully reproduces the experimental kinetic data, and we derive accurate interaction energies for NH_3 at Pt surfaces, which we summarize in Table 3.

Our work provides compelling evidence that NH_3 diffusion on Pt(111) must pass over a large barrier, which is ∼65% of its binding energy. This is an exception to the so-called 12% rule. Instead of relying on such simple rules, our comparison with DFT calculations shows that the minimum energy path of diffusion appears to be highly accurate.

Table 3. Most Important Results for Ammonia Interactions at Pt Surfaces

NH_3/Pt interaction		recommended value
(111) desorption energy	$E^{T}_{0,d}$	1.13 ± 0.02 eV
(111) site-to-site hopping barrier	$E^{T}_{0,h}$	0.71 ± 0.04 eV
step preference over terrace	$\Delta E_{0,ST}$	0.23 ± 0.03 eV

Having a quantitatively accurate kinetics model for ammonia desorption and diffusion, we were able to critically evaluate the approximations commonly employed in kinetics modeling of the Ostwald process. It is known from previous work that NH_3 reacts efficiently with oxygen atoms at steps,[2,6,7] while reaction at terraces is less efficient. We show that at temperatures typical for the Ostwald process, the NH_3 hopping rate is close to its desorption rate, indicating that NH_3 landing at terrace sites is unlikely to reach the steps, where it may react prior to its desorption. This implies that mean-field kinetics models have limited applicability for prediction of NH_3 conversion rates and NO selectivity under Ostwald process conditions. Furthermore, by careful analysis of NH_3's desorption from Pt(332), we show that it is not possible to model the desorption rate from catalysts with multiple active sites by considering only the direct desorption from steps, an approach which is nevertheless persistently employed in kinetics modeling literature.[2,17]

With the help of DFT calculations, we extend the desorption rate constants beyond the zero-coverage limit of our experiment, which allows us to reproduce previously observed TPD spectra and to estimate NH_3 coverages at Ostwald process conditions. The comparison of our results with a kinetics model commonly used for reactor simulations provides a simple explanation why established models tend to overpredict the extent of NH_3 slip under Ostwald process conditions. We showed that this is a direct result of the model's prediction of high NH_3 coverages, which favor the formation of N_2 and N_2O and reduce the efficiency of NO formation.

In summary, the demonstrated approach exemplifies how the combination of high-quality kinetic data with TST analysis yields highly accurate elementary step rate constants, potentially capable of constructing mechanisms possessing high transferability without relying on empirical optimization within narrow range of experimental conditions.

https://doi.org/10.1021/jacs.1c09269
J. Am. Chem. Soc. 2021, 143, 18305−18316

5. METHODS

5.1. Experimental. The Pt surfaces (MaTeck GmbH) were prepared by sputtering with Ar^+ (3 keV) for 10 min and subsequent annealing at 1300 K for 20 min, and its cleanliness was verified with Auger electron spectroscopy. We employed two Pt(111) crystals with different step densities: the first had a step density quantified with atomic force microscopy of 0.4 ± 0.2% and the second a step density of 0.15 ± 0.05% estimated from the surface cut angle accuracy. We also used a Pt(332) crystal with a step density of 16.7%. Similar to previous work,[21,22,26] a 20−50 μs long pulsed molecular beam of NH_3 (0.5−2% NH_3 in He) passed from the source chamber through two differential pumping chambers before entering a surface-scattering chamber, with a base pressure of 2×10^{-10} mbar. The incidence kinetic energy of NH_3 in the beam was ∼0.25 eV. The NH_3 pulses (repetition rate 20−40 Hz) strike the Pt at an incidence angle of 30° from the surface normal. The dose provided by each NH_3 pulse was between 2×10^{-4} and 1×10^{-3} monolayer (ML).

Before investigating NH_3 desorption from Pt, we verified that NH_3 does not react under our conditions. We find no detectable H_2 or N_2 produced under our conditions. Isotopic exchange (e.g., NH_2D and HD, using NH_3 dosing of a D atom precovered Pt surfaces) was also absent. Furthermore, after dosing Pt(111) and Pt(332) surfaces with ∼2000 ML NH_3, no nitrogen signal could be detected in the Auger spectrum.

The desorbing and the directly scattered NH_3 were detected 2 cm from the surface using nonresonant multiphoton ionization (pulse duration 35 fs, average power 0.2 W, repetition rate 1 kHz). A pulsed homogeneous electric field, formed between two parallel flat meshes, projected the ions onto a time-gated MCP detector. The mass-to-charge ratio of the ions was selected with a time-gate on the microchannel plate (MCP), applied at a delay after pulsed extraction of the ions from the ionization region. The MCP amplified the ion signal, producing electrons that impinge upon a phosphor screen, emitting light recorded with a CCD camera. The pixel position provides information on the NH_3 velocity, which is used to convert NH_3 density to flux and to calculate the molecule's flight times to the surface and from surface to the ionizing laser spot. We integrated the flux images from 400 and 1200 m/s at angles close to the surface normal, which strongly suppresses the background from direct scattering, which peaks at an angle of ∼30° and a velocity of 1500 m/s. This integral was determined at many beam laser delays, which we correct to surface residence time, t_{res}, by subtracting the flight time, and we yield the kinetic trace $d[NH_3]/dt$ versus t_{res}. The translational energy distribution of the molecules could be obtained by summing ion images over all measured timings.

A fraction of the NH_3/Pt(332) data, from 453 to 553 K, was obtained in the 1 kHz detection setup and analyzed as has been described previously in detail.[25]

5.2. Computational. NH_3 binding energies, diffusion barriers, and frequencies at Pt(111) and Pt(332) have been obtained using the Vienna Ab-initio Simulation Package.[47−51] Periodic DFT calculations were performed at the level of generalized-gradient approximation using the PBE[30] exchange-correlation functional.

The core−electron interactions were described by the projector-augmented wave potentials,[52,53] with a cutoff energy of 400 eV for the plane-wave basis. The surfaces were modeled by a four-layer periodic slab, with each layer containing a 2 × 2 or a 4 × 4 supercell for Pt(111) and a 4 × 6 supercell for Pt(332). Two bottom layers were fixed during optimization. A 24 Å vacuum region was added to the slab to avoid interaction in the z-direction. The Brillouin zone was sampled with a 8 × 8 × 1 and a 5 × 5 × 1 with Γ-centered Monkhorst−Pack grids of special k-points for Pt(111) and Pt(332), respectively.

To predict adsorption energies, the two topmost surface layers and the NH_3 molecule were allowed to relax until forces were lower than 0.02 eV/Å. Accounting for the same amount of DOFs, the reaction paths and transition states for diffusion and desorption were located by the CI-NEB method.[31] The calculation was considered converged when forces were <0.05 eV/Å. The harmonic frequencies and normal modes were obtained solving the Hessian matrix for the DOFs of the NH_3 molecule, applying two central finite differences with displacements of 0.02 Å.

■ ASSOCIATED CONTENT

Supporting Information

The Supporting Information is available free of charge at https://pubs.acs.org/doi/10.1021/jacs.1c09269.

NH_3 speed distributions, analysis of sticking coefficients, comparison of desorption rates from Pt(111) with different step densities, equations for the diffusion−desorption kinetics model, coverage dependence of DFT-derived binding energies, construction of the partition functions for TST rate constant modeling, determination of first-order rate constants from experimental data, derivation of the terrace-assisted desorption model, construction of coverage-dependent desorption rate constants, and additional references (PDF)

■ AUTHOR INFORMATION

Corresponding Authors

Theofanis N. Kitsopoulos − *Institute for Physical Chemistry, Georg-August University of Goettingen, 37077 Goettingen, Germany; Department of Dynamics at Surfaces, Max Planck Institute for Biophysical Chemistry, 37077 Goettingen, Germany; Department of Chemistry, University of Crete, 71003 Heraklion, Greece; Institute of Electronic Structure and Laser − FORTH, 71110 Heraklion, Greece;* orcid.org/0000-0001-6228-1002; Email: theo.kitsopoulos@mpibpc.mpg.de

Alec M. Wodtke − *Institute for Physical Chemistry, Georg-August University of Goettingen, 37077 Goettingen, Germany; Department of Dynamics at Surfaces, Max Planck Institute for Biophysical Chemistry, 37077 Goettingen, Germany; International Center for Advanced Studies of Energy Conversion, Georg-August University of Goettingen, 37077 Goettingen, Germany;* orcid.org/0000-0002-6509-2183; Email: alec.wodtke@mpibpc.mpg.de

Authors

Dmitriy Borodin − *Institute for Physical Chemistry, Georg-August University of Goettingen, 37077 Goettingen, Germany; Department of Dynamics at Surfaces, Max Planck Institute for Biophysical Chemistry, 37077 Goettingen, Germany*

Igor Rahinov − *Department of Natural Sciences, The Open University of Israel, 4353701 Raanana, Israel*

Oihana Galparsoro − *Donostia International Physics Center (DIPC), 20018 Donostia-San Sebastián, Spain; Kimika Fakultatea, Euskal Herriko Unibertsitatea UPV/EHU, P.K. 1072 Donostia-San Sebastián, Spain*

Jan Fingerhut − *Institute for Physical Chemistry, Georg-August University of Goettingen, 37077 Goettingen, Germany*

Michael Schwarzer − *Institute for Physical Chemistry, Georg-August University of Goettingen, 37077 Goettingen, Germany*

Kai Golibrzuch − *Department of Dynamics at Surfaces, Max Planck Institute for Biophysical Chemistry, 37077 Goettingen, Germany*

Georgios Skoulatakis − *Department of Dynamics at Surfaces, Max Planck Institute for Biophysical Chemistry, 37077 Goettingen, Germany*

https://doi.org/10.1021/jacs.1c09269
J. Am. Chem. Soc. 2021, 143, 18305−18316

Daniel J. Auerbach − *Department of Dynamics at Surfaces, Max Planck Institute for Biophysical Chemistry, 37077 Goettingen, Germany*

Alexander Kandratsenka − *Department of Dynamics at Surfaces, Max Planck Institute for Biophysical Chemistry, 37077 Goettingen, Germany;* orcid.org/0000-0003-2132-1957

Dirk Schwarzer − *Department of Dynamics at Surfaces, Max Planck Institute for Biophysical Chemistry, 37077 Goettingen, Germany;* orcid.org/0000-0003-3838-2211

Complete contact information is available at: https://pubs.acs.org/10.1021/jacs.1c09269

Funding

Open access funded by Max Planck Society.

Notes

The authors declare no competing financial interest.

■ ACKNOWLEDGMENTS

D.B. and M.S. thank the BENCh graduate school, funded by the DFG (389479699/GRK2455). I.R. gratefully acknowledges the support by Israel Science Foundation, ISF (Grant No. 2187/19), and by the Open University of Israel Research Authority (Grant No. 31044). O.G. acknowledges financial support by the Spanish Ministerio de Ciencia e Innovación (Grant No. PID2019-107396GB-I00/AEI/10.13039/501100011033). T.N.K., G.S., M.S., and J.F. acknowledge support from the European Research Council (ERC) under the European Union's Horizon 2020 research and innovation program (Grant Agreement No. 833404).

■ REFERENCES

(1) Bartholomew, C. H.; Farrauto, R. J. *Fundamentals of Industrial Catalytic Processes*; Wiley, 2005; Vol. 2, pp 570−575.
(2) Ma, H. Y.; Schneider, W. F. Structure- and Temperature-Dependence of Pt-Catalyzed Ammonia Oxidation Rates and Selectivities. *ACS Catal.* **2019**, *9* (3), 2407−2414.
(3) Rafti, M.; Vicente, J. L.; Albesa, A.; Scheibe, A.; Imbihl, R. Modeling ammonia oxidation over a Pt (533) surface. *Surf. Sci.* **2012**, *606* (1−2), 12−20.
(4) Imbihl, R.; Scheibe, A.; Zeng, Y. F.; Gunther, S.; Kraehnert, R.; Kondratenko, V. A.; Baerns, M.; Offermans, W. K.; Jansen, A. P. J.; van Santen, R. A. Catalytic ammonia oxidation on platinum: mechanism and catalyst restructuring at high and low pressure. *Phys. Chem. Chem. Phys.* **2007**, *9* (27), 3522−3540.
(5) Weststrate, C. J.; Bakker, J. W.; Rienks, E. D. L.; Vinod, C. P.; Matveev, A. V.; Gorodetskii, V. V.; Nieuwenhuys, B. E. Ammonia oxidation on Pt(410). *J. Catal.* **2006**, *242* (1), 184−194.
(6) Gland, J. L.; Woodard, G. C.; Korchak, V. N. Ammonia Oxidation on the Pt(111) and Pt(S)-12(111) x (111) Surfaces. *J. Catal.* **1980**, *61* (2), 543−546.
(7) Gland, J. L.; Korchak, V. N. Ammonia Oxidation on a Stepped Platinum Single-Crystal Surface. *J. Catal.* **1978**, *53* (1), 9−23.
(8) Gland, J. L. Adsorption and Decomposition of Nitric-Oxide and Ammonia on a Stepped Platinum Single-Crystal Surface. *Surf. Sci.* **1978**, *71* (2), 327−350.
(9) Guthrie, W. L.; Sokol, J. D.; Somorjai, G. A. The Decomposition of Ammonia on the Flat (111) and Stepped (557) Platinum Crystal-Surfaces. *Surf. Sci.* **1981**, *109* (2), 390−418.
(10) Szulczewski, G.; Levis, R. J. Collision-Induced Desorption of Ammonia Chemisorbed on Pt(111) - from Direct Measurement of the Threshold Energy to Determination of the Surface-Adsorbate Bond Strength. *J. Chem. Phys.* **1995**, *103* (23), 10238−10251.
(11) Cai, L.; Xiao, X. D.; Loy, M. M. T. Desorption of polyatomic molecules from the Pt(111) surface by femtosecond laser radiation. *J. Chem. Phys.* **2001**, *115* (20), 9490−9495.
(12) Mieher, W. D.; Ho, W. Thermally Activated Oxidation of NH3 on Pt(111) - Intermediate Species and Reaction-Mechanisms. *Surf. Sci.* **1995**, *322* (1−3), 151−167.
(13) Sexton, B. A.; Mitchell, G. E. Vibrational-Spectra of Ammonia Chemisorbed on Platinum (111) 0.1. Identification of Chemisorbed States. *Surf. Sci.* **1980**, *99* (3), 523−538.
(14) Wellendorff, J.; Silbaugh, T. L.; Garcia-Pintos, D.; Norskov, J. K.; Bligaard, T.; Studt, F.; Campbell, C. T. A benchmark database for adsorption bond energies to transition metal surfaces and comparison to selected DFT functionals. *Surf. Sci.* **2015**, *640*, 36−44.
(15) Offermans, W. K.; Jansen, A. P. J.; van Santen, R. A. Ammonia activation on platinum {111}: A density functional theory study. *Surf. Sci.* **2006**, *600* (9), 1714−1734.
(16) Novell-Leruth, G.; Ricart, J. M.; Perez-Ramirez, J. Pt(100)-catalyzed ammonia oxidation studied by DFT: Mechanism and microkinetics. *J. Phys. Chem. C* **2008**, *112* (35), 13554−13562.
(17) Ma, H. Y.; Schneider, W. F. DFT and microkinetic comparison of Pt, Pd and Rh-catalyzed ammonia oxidation. *J. Catal.* **2020**, *383*, 322−330.
(18) Kraehnert, R.; Baerns, M. Kinetics of ammonia oxidation over Pt foil studied in a micro-structured quartz-reactor. *Chem. Eng. J.* **2008**, *137* (2), 361−375.
(19) Scheuer, A.; Votsmeier, M.; Schuler, A.; Gieshoff, J.; Drochner, A.; Vogel, H. NH3-Slip Catalysts: Experiments Versus Mechanistic Modelling. *Top. Catal.* **2009**, *52* (13−20), 1847−1851.
(20) Serri, J. A.; Tully, J. C.; Cardillo, M. J. The influence of steps on the desorption kinetics of NO from Pt(111). *J. Chem. Phys.* **1983**, *79* (3), 1530−1540.
(21) Borodin, D.; Rahinov, I.; Fingerhut, J.; Schwarzer, M.; Hörandl, S.; Skoulatakis, G.; Schwarzer, D.; Kitsopoulos, T. N.; Wodtke, A. M. NO Binding Energies to and Diffusion Barrier on Pd Obtained with Velocity-Resolved Kinetics. *J. Phys. Chem. C* **2021**, *125* (21), 11773−11781.
(22) Neugebohren, J.; Borodin, D.; Hahn, H. W.; Altschaffel, J.; Kandratsenka, A.; Auerbach, D. J.; Campbell, C. T.; Schwarzer, D.; Harding, D. J.; Wodtke, A. M.; Kitsopoulos, T. N. Velocity-resolved kinetics of site-specific carbon monoxide oxidation on platinum surfaces. *Nature* **2018**, *558* (7709), 280−283.
(23) Peng, G. W.; Mavrikakis, M. Adsorbate Diffusion on Transition Metal Nanoparticles. *Nano Lett.* **2015**, *15* (1), 629−634.
(24) Nilekar, A. U.; Greeley, J.; Mavrikakis, M. A simple rule of thumb for diffusion on transition-metal surfaces. *Angew. Chem., Int. Ed.* **2006**, *45* (42), 7046−7049.
(25) Borodin, D.; Golibrzuch, K.; Schwarzer, M.; Fingerhut, J.; Skoulatakis, G.; Schwarzer, D.; Seelemann, T.; Kitsopoulos, T.; Wodtke, A. M. Measuring Transient Reaction Rates from Nonstationary Catalysts. *ACS Catal.* **2020**, *10* (23), 14056−14066.
(26) Harding, D. J.; Neugebohren, J.; Hahn, H.; Auerbach, D. J.; Kitsopoulos, T. N.; Wodtke, A. M. Ion and velocity map imaging for surface dynamics and kinetics. *J. Chem. Phys.* **2017**, *147* (1), 013939.
(27) Rettner, C. T.; Schweizer, E. K.; Mullins, C. B. Desorption and Trapping of Argon at a 2H-W(100) Surface and a Test of the Applicability of Detailed Balance to a Nonequilibrium System. *J. Chem. Phys.* **1989**, *90* (7), 3800−3813.
(28) Borodin, D.; Rahinov, I.; Shirhatti, P. R.; Huang, M.; Kandratsenka, A.; Auerbach, D. J.; Zhong, T.; Guo, H.; Schwarzer, D.; Kitsopoulos, T. N.; Wodtke, A. M. Following the microscopic pathway to adsorption through chemisorption and physisorption wells. *Science* **2020**, *369* (6510), 1461−1465.
(29) King, D. A. Surface-Diffusion of Adsorbed Species - a Review. *J. Vac. Sci. Technol.* **1980**, *17* (1), 241−247.
(30) Perdew, J. P.; Burke, K.; Ernzerhof, M. Generalized gradient approximation made simple. *Phys. Rev. Lett.* **1996**, *77* (18), 3865−3868.

(31) Henkelman, G.; Uberuaga, B. P.; Jonsson, H. A climbing image nudged elastic band method for finding saddle points and minimum energy paths. *J. Chem. Phys.* **2000**, *113* (22), 9901−9904.
(32) Engelhart, D. P.; Wagner, R. J. V.; Meling, A.; Wodtke, A. M.; Schafer, T. Temperature programmed desorption of weakly bound adsorbates on Au(111). *Surf. Sci.* **2016**, *650*, 11−16.
(33) Sprowl, L. H.; Campbell, C. T.; Arnadottir, L. Hindered Translator and Hindered Rotor Models for Adsorbates: Partition Functions and Entropies. *J. Phys. Chem. C* **2016**, *120* (18), 9719−9731.
(34) Jørgensen, M.; Grönbeck, H. Adsorbate Entropies with Complete Potential Energy Sampling in Microkinetic Modeling. *J. Phys. Chem. C* **2017**, *121* (13), 7199−7207.
(35) McClurg, R. B.; Flagan, R. C.; Goddard, W. A. The hindered rotor density-of-states interpolation function. *J. Chem. Phys.* **1997**, *106* (16), 6675−6680.
(36) Garcia-Hernandez, M.; Lopez, N.; Moreira, I. D.; Paniagua, J. C.; Illas, F. Ab initio cluster model approach to the chemisorption of NH3 on Pt(111). *Surf. Sci.* **1999**, *430* (1−3), 18−28.
(37) Tully, J. C. The Dynamics of Adsorption and Desorption. *Surf. Sci.* **1994**, *299* (1−3), 667−677.
(38) Novell-Leruth, G.; Valcarcel, A.; Clotet, A.; Ricart, J. M.; Perez-Ramirez, J. DFT characterization of adsorbed NHx species on Pt(100) and Pt(111) surfaces. *J. Phys. Chem. B* **2005**, *109* (38), 18061−18069.
(39) Bajpai, A.; Mehta, P.; Frey, K.; Lehmer, A. M.; Schneider, W. F. Benchmark First-Principles Calculations of Adsorbate Free Energies. *ACS Catal.* **2018**, *8* (3), 1945−1954.
(40) Campbell, C. T.; Sprowl, L. H.; Árnadóttir, L. Equilibrium Constants and Rate Constants for Adsorbates: Two-Dimensional (2D) Ideal Gas, 2D Ideal Lattice Gas, and Ideal Hindered Translator Models. *J. Phys. Chem. C* **2016**, *120* (19), 10283−10297.
(41) Amsler, J.; Plessow, P. N.; Studt, F.; Bucko, T. Anharmonic Correction to Adsorption Free Energy from DFT-Based MD Using Thermodynamic Integration. *J. Chem. Theory Comput.* **2021**, *17* (2), 1155−1169.
(42) Groot, I. M. N.; Kleyn, A. W.; Juurlink, L. B. F. Separating Catalytic Activity at Edges and Terraces on Platinum: Hydrogen Dissociation. *J. Phys. Chem. C* **2013**, *117* (18), 9266−9274.
(43) García-Diéguez, M.; Hibbitts, D. D.; Iglesia, E. Hydrogen Chemisorption Isotherms on Platinum Particles at Catalytic Temperatures: Langmuir and Two-Dimensional Gas Models Revisited. *J. Phys. Chem. C* **2019**, *123* (13), 8447−8462.
(44) Shrestha, S.; Harold, M. P.; Kamasamudram, K. Experimental and modeling study of selective ammonia oxidation on multifunctional washcoated monolith catalysts. *Chem. Eng. J.* **2015**, *278*, 24−35.
(45) Scheuer, A.; Hirsch, O.; Hayes, R.; Vogel, H.; Votsmeier, M. Efficient simulation of an ammonia oxidation reactor using a solution mapping approach. *Catal. Today* **2011**, *175* (1), 141−146.
(46) Wiser, A. Investigation of the industrial NH3 oxidation by CFD simulations including detailed surface kinetics. Ph.D. Thesis, TU Darmstadt, 2020.
(47) Kresse, G.; Hafner, J. Abinitio Molecular-Dynamics for Liquid-Metals. *Phys. Rev. B: Condens. Matter Mater. Phys.* **1993**, *47* (1), 558−561.
(48) Kresse, G.; Hafner, J. Ab-Initio Molecular-Dynamics Simulation of the Liquid-Metal Amorphous-Semiconductor Transition in Germanium. *Phys. Rev. B: Condens. Matter Mater. Phys.* **1994**, *49* (20), 14251−14269.
(49) Kresse, G.; Hafner, J. Norm-Conserving and Ultrasoft Pseudopotentials for First-Row and Transition-Elements. *J. Phys.: Condens. Matter* **1994**, *6* (40), 8245−8257.
(50) Kresse, G.; Furthmuller, J. Efficient iterative schemes for ab initio total-energy calculations using a plane-wave basis set. *Phys. Rev. B: Condens. Matter Mater. Phys.* **1996**, *54* (16), 11169−11186.
(51) Kresse, G.; Furthmuller, J. Efficiency of ab-initio total energy calculations for metals and semiconductors using a plane-wave basis set. *Comput. Mater. Sci.* **1996**, *6* (1), 15−50.
(52) Blöchl, P. E. Projector Augmented-Wave Method. *Phys. Rev. B: Condens. Matter Mater. Phys.* **1994**, *50* (24), 17953−17979.
(53) Kresse, G.; Joubert, D. From ultrasoft pseudopotentials to the projector augmented-wave method. *Phys. Rev. B: Condens. Matter Mater. Phys.* **1999**, *59* (3), 1758−1775.

https://doi.org/10.1021/jacs.1c09269
J. Am. Chem. Soc. 2021, 143, 18305−18316

The Kinetics of NH_3 Desorption and Diffusion on Pt: Implications for the Ostwald Process

Dmitriy Borodin[1,2], Igor Rahinov[3], Oihana Galparsoro[4,5], Jan Fingerhut[1], Michael Schwarzer[1], Kai Golibrzuch[2], Georgios Skoulatakis[2], Daniel J. Auerbach[2], Alexander Kandratsenka[2], Dirk Schwarzer[2], Theofanis N. Kitsopoulos[1,2,6,7]* and Alec M. Wodtke[1,2,8]**

[1]Institute for Physical Chemistry, Georg-August University of Goettingen, Tammannstraße 6, 37077 Goettingen, Germany.

[2]Department of Dynamics at Surfaces, Max Planck Institute for Biophysical Chemistry, Am Fassberg 11, 37077 Goettingen, Germany.

[3]Department of Natural Sciences, The Open University of Israel, 4353701 Raanana, Israel.

[4]Donostia International Physics Center (DIPC), Paseo Manuel de Lardizabal 4, 20018 Donostia-San Sebastián, Spain.

[5]Kimika Fakultatea, Euskal Herriko Unibertsitatea UPV/EHU, P.K. 1072 Donostia-San Sebastián, Spain.

[6]Department of Chemistry, University of Crete, Heraklion, Greece

[7]Institute of Electronic Structure and Laser – FORTH, Heraklion, Greece

[8]International Center for Advanced Studies of Energy Conversion, Georg-August University of Goettingen, Tammannstraße 6, 37077 Goettingen, Germany.

Email: *theo.kitsopoulos@mpibpc.mpg.de, **alec.wodtke@mpibpc.mpg.de

S1. Speed Distributions of desorbing NH3 from Pt(111) and Pt(332)

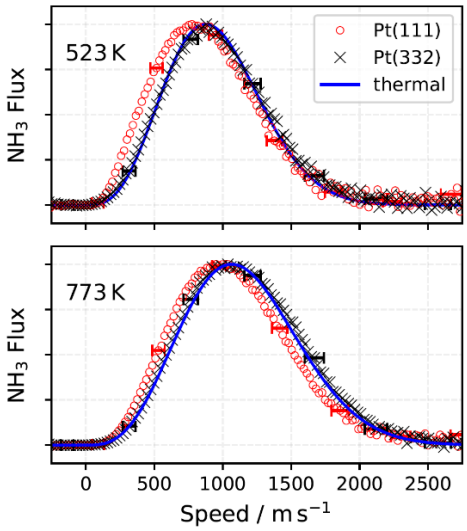

Figure S1: Speed distributions of desorbing NH_3 from Pt(111) (◦) and Pt(332) (×) detected at $\pm 5°$ from surface normal at two surface temperatures. The horizontal error bar indicates the uncertainty in the speed calibration. The blue line is the thermal Maxwell-Boltzmann flux distribution at the temperature of the surface shown for comparison.

S2. Determination of the thermal sticking coefficient of NH3 at Pt(111)

The thermal sticking coefficient on Pt(111) is derived from the experimentally obtained translational energy distributions of desorbing NH_3 molecules using the principle of detailed balance. From detailed balance, the relation between the desorbing flux distribution (E, T_S) , the Maxwell-Boltzmann thermal (3D) distribution $F_{MB}(E, T_S)$, and the initial sticking probability function $S_0(E)$ is:

$$F(E, T_S) \propto S_0(E) F_{MB}(E, T_S), \tag{S1}$$

We observe that the desorbing NH_3 is subthermal, which indicates a decreasing sticking coefficient with increasing translational energy. The experimentally derived translational energy distributions of NH_3 desorbing from Pt(111) at 473-873 K are fitted globally to an empirical temperature independent $S_0(E)$. After fitting, the resulting sticking probability is obtained.

$$S_0(E) = 0.40 \times \exp(-30.95\ E/\text{eV}) + 0.60 \times \exp(-1.160\ E/\text{eV}). \tag{S2}$$

The corresponding fits are shown in Fig. S2.

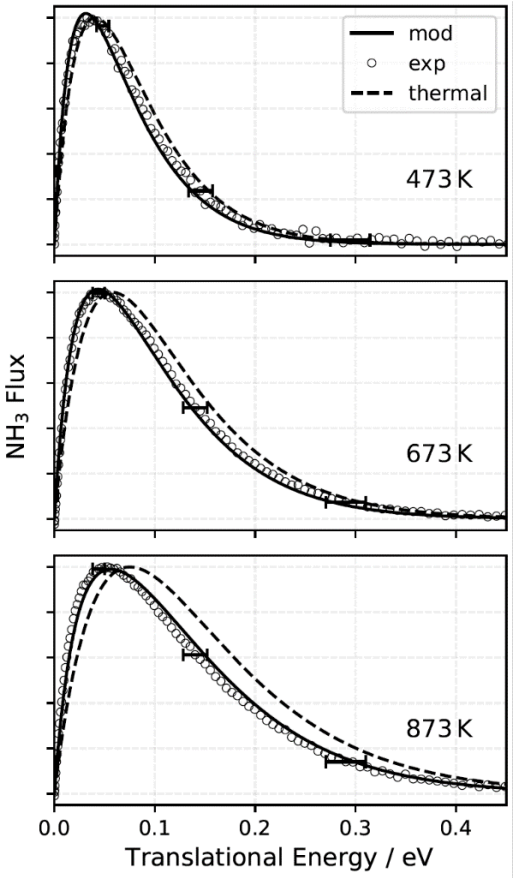

Figure S2: Experimentally derived translational energy distributions of NH_3 desorbing from Pt(111) are shown for surface temperatures between 473 and 873 K. The horizontal error bars indicate the uncertainty of the translational energy measurement. The black dashed line is the thermal Maxwell-Boltzmann distribution at the surface temperature. The black solid lines are the fit results of Eq. S1 and S2.

This approach gives the shape but not the absolute value of the sticking probability curve. We establish the absolute value using $S_0(E = 0) = 1$, an excellent assumption for a non-activated adsorption system like this one[1]. Figure S3 (left panel) shows the $S_0(E)$ found in this way. The thermal sticking coefficient $\langle S_0 \rangle(T)$ is then obtained from $S_0(E)$, by integrating over the Maxwell-Boltzmann energy distribution at temperature T:

$$\langle S_0 \rangle(T) = \frac{\int_0^\infty S_0(E) F_{MB}(E, T) \mathrm{d}E}{\int_0^\infty F_{MB}(E, T) \mathrm{d}E}. \tag{S3}$$

This is shown in Fig. S3 (right panel) along with the a previous report of $\langle S_0 \rangle (300\ \mathrm{K})$[2].

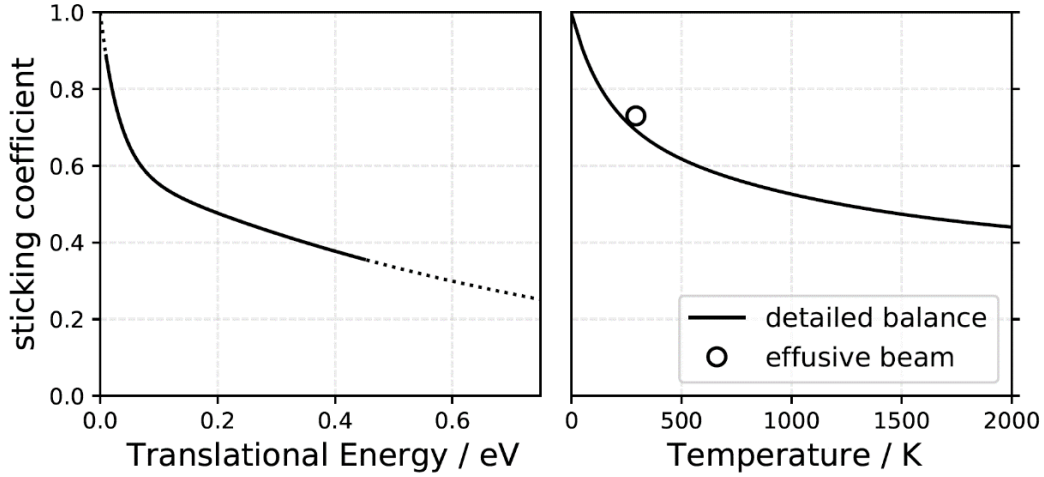

Figure S3: The sticking coefficient for NH_3 on Pt(111). Left panel as a function of NH_3's translational energy and right panel as a function of temperature. The empty circle is the experimental value of $\langle S_0 \rangle (T)$ found in Ref. [2]. The solid line in left figure shows the region over which the data constrains the fit. The NH_3 sticking coefficient on Pt(332) is unity for all translational energies and temperatures.

S3. Comparison of NH3 desorption rate from Pt(111) with different step densities

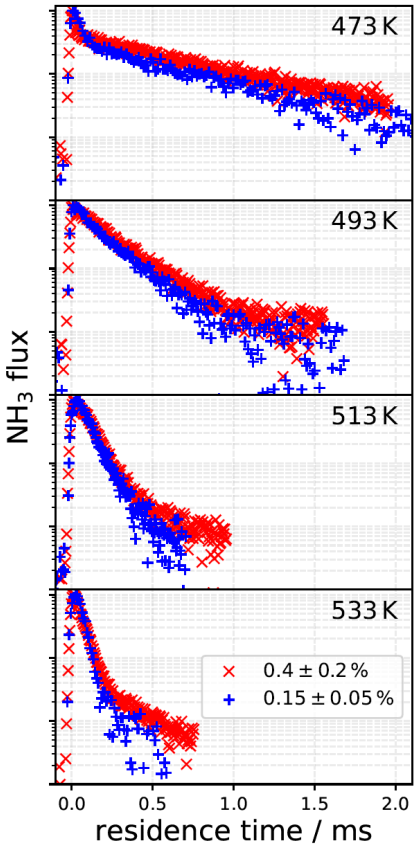

Figure S4: The kinetic traces of NH_3 desorption are shown for two Pt(111) crystals with different step densities: 0.15 ± 0.05 % (+) and 0.4 ± 0.2 % (×). At reduced step density the trace resembles more closely a single exponential. This shows that the slow component of the bi-exponential kinetic trace arises due to NH_3 interactions with steps.

S4. The Diffusion-Desorption Kinetic Model

S4.1. The relationship between $k_{\mathrm{d}}^{\mathrm{S}}$, $k_{\mathrm{h}}^{\mathrm{T}}$, $k_{\mathrm{h}}^{\mathrm{S}}$ and $k_{\mathrm{d}}^{\mathrm{T}}$

The elementary rate constant for direct desorption from steps $k_{\mathrm{d}}^{\mathrm{S}}$ can be obtained from the other three elementary rate constants, $k_{\mathrm{h}}^{\mathrm{T}}$, $k_{\mathrm{h}}^{\mathrm{S}}$, and $k_{\mathrm{d}}^{\mathrm{T}}$. Consider the TST rate expressions for these three elementary processes:

$$k_{\mathrm{h}}^{\mathrm{T}} = \frac{k_{\mathrm{B}}T}{h}\frac{Q_{\mathrm{hop}}^{\ddagger}}{Q_{\mathrm{T}}}\exp\left(-\frac{E_{0,\mathrm{h}}^{\mathrm{T}}}{k_{\mathrm{B}}T}\right), \tag{S4}$$

$$k_{\mathrm{h}}^{\mathrm{S}} = \frac{k_{\mathrm{B}}T}{h}\frac{Q_{\mathrm{hop}}^{\ddagger}}{Q_{\mathrm{S}}}\exp\left(-\frac{E_{0,\mathrm{h}}^{\mathrm{T}} + \Delta E_{0,\mathrm{ST}}}{k_{\mathrm{B}}T}\right), \tag{S5}$$

$$k_{\mathrm{d}}^{\mathrm{T}} = \frac{k_{\mathrm{B}}T}{h}\frac{Q_{\mathrm{des}}^{\ddagger}}{Q_{\mathrm{T}}}\exp\left(-\frac{E_{0,\mathrm{d}}^{\mathrm{T}}}{k_{\mathrm{B}}T}\right). \tag{S6}$$

Here, Q_{T} and Q_{S} are the partition functions for NH_3 adsorbed at terraces and steps, respectively, while $Q_{\mathrm{hop}}^{\ddagger}$ and $Q_{\mathrm{des}}^{\ddagger}$ are the TS partition functions for hopping and desorption, respectively. The following can then easily be shown

$$k_{\mathrm{d}}^{\mathrm{T}}\frac{k_{\mathrm{h}}^{\mathrm{S}}}{k_{\mathrm{h}}^{\mathrm{T}}} = \frac{k_{\mathrm{B}}T}{h}\frac{Q_{\mathrm{des}}^{\ddagger}}{Q_{\mathrm{S}}}\exp\left(-\frac{E_{0,\mathrm{d}}^{\mathrm{T}} + \Delta E_{\mathrm{ST}}}{k_{\mathrm{B}}T}\right) = k_{\mathrm{d}}^{\mathrm{S}}. \tag{S7}$$

We recognize that, within our approximations, expression S7 is nothing else but the TST expression for direct desorption from steps. We notice that this approximation is only valid for our setup of the kinetic model as we assume that the TS for terrace hopping is the same as for hopping between terrace and step sites.

S4.2. Kinetic rate equations in a non-uniform spatial grid

Our approach follows closely the work reported in Ref. [3], where it was shown how to account for surface diffusion by sequential hopping events between adjacent binding sites. The method employs periodic boundary conditions. For a step density of 0.4% this requires solving 250 coupled differential equations numerically, which is time consuming especially when employed within an optimization routine designed to obtain fits to the experimental data. However, in order to describe diffusion accurately, we do not need to treat each terrace site individually. The only unique binding sites that must be treated individually are the steps—the individual binding sites at the terraces can be coarse-grained into spatial regions that include multiple atomic rows, where the diffusion equation is solved. This dramatically reduces the number of coupled differential equations that need to be solved. We use spatial grids with atomic rows close to the steps, which increase in size when approaching the center of the terrace.

The diffusion-desorption rate equations are as follows:

$$\begin{aligned}\dot{c}_0 = {} & S_0^{\mathrm{S}}(1-c_0)F_{\mathrm{B}}(t) - k_{\mathrm{h}}^{\mathrm{S}}c_0(1-c_{m-1}) - k_{\mathrm{h}}^{\mathrm{S}}c_0(1-c_1) + k_{\mathrm{h}}^{\mathrm{T}}c_{m-1}(1-c_0) \\ & + k_{\mathrm{h}}^{\mathrm{T}}c_1(1-c_0) - k_{\mathrm{d}}^{\mathrm{S}}c_0,\end{aligned} \tag{S8}$$

$$\begin{aligned}\dot{c}_1 = {} & S_0^{\mathrm{T}}(1-c_1)F_{\mathrm{B}}(t) - k_{\mathrm{h}}^{\mathrm{T}}c_1(1-c_0) - k_{\mathrm{h}}^{\mathrm{T}}c_1(1-c_2) + k_{\mathrm{h}}^{\mathrm{S}}c_0(1-c_1) \\ & + k_{\mathrm{h}}^{\mathrm{T}}c_2(1-c_1) - k_{\mathrm{d}}^{\mathrm{T}}c_1,\end{aligned} \tag{S9}$$

$$\begin{aligned}\dot{c}_2 = {} & S_0^{\mathrm{T}}(1-c_2)F_{\mathrm{B}}(t) - k_{\mathrm{h}}^{\mathrm{T}}c_2(1-c_1) - k_{\mathrm{h}}^{\mathrm{T}}c_2(1-c_3) + k_{\mathrm{h}}^{\mathrm{T}}c_1(1-c_2) \\ & + k_{\mathrm{h}}^{\mathrm{T}}c_3(1-c_2) - k_{\mathrm{d}}^{\mathrm{T}}c_2,\end{aligned} \tag{S10}$$

...

$$\begin{aligned}\dot{c}_i = {} & S_0^{\mathrm{T}}(1-c_i)F_{\mathrm{B}}(t) + \frac{2D^{\mathrm{T}}}{d_i(d_{i+1}+d_i)}c_{i+1}(1-c_i) - \frac{2D^{\mathrm{T}}}{d_i(d_{i+1}+d_i)}c_i(1-c_{i+1}) \\ & - \frac{2D^{\mathrm{T}}}{d_i(d_i+d_{i-1})}c_i(1-c_{i-1}) + \frac{2D^{\mathrm{T}}}{d_i(d_i+d_{i-1})}c_{i-1}(1-c_i) - k_{\mathrm{d}}^{\mathrm{T}}c_i,\end{aligned} \tag{S11}$$

...

$$\begin{aligned}\dot{c}_{m-1} = {} & S_0^{\mathrm{T}}(1-c_{m-1})F_{\mathrm{B}}(t) - k_{\mathrm{h}}^{\mathrm{T}}c_{m-1}(1-c_0) - k_{\mathrm{h}}^{\mathrm{S}}c_{m-1}(1-c_{m-2}) \\ & + k_{\mathrm{h}}^{\mathrm{T}}c_{m-2}(1-c_{m-1}) + k_{\mathrm{h}}^{\mathrm{S}}c_0(1-c_{m-1}) - k_{\mathrm{d}}^{\mathrm{T}}c_{m-1}.\end{aligned} \tag{S12}$$

NH_3's fractional occupation of the binding site is given by c. Index i=0 indicates the step site, while indices 1 and $m-1$ indicates the terrace sites adjacent to the step. Indices 2 until $m-2$ are terrace sites. In the first term F_t is the flux of

molecules impinging on the surface, which is described by the molecular beam dosing function. For terrace sites, we use the sticking probabilities (S_0^{T}) from Fig. S3 and for step sites, we set the sticking probability (S_0^{S}) to unity. This is justified as the measured speed distributions of NH_3 desorbing from Pt(332) is thermal with $T_{\mathrm{tr}} = T_{\mathrm{S}}$ and exhibits a $\cos(\vartheta)$ angular distribution. In the equations above, $k_{\mathrm{h}}^{\mathrm{T/S}}$ are the hopping rate constants between adjacent atomic rows and D^T is the diffusion constant for NH_3 at terraces. The terms in parentheses are needed to account for effect of binding site occupation.

The terrace sites further away from steps are treated in non-uniform spatial elements with the width d_i. The definition of the spatial elements is shown in Fig. S5(a). In these regions, the terrace diffusion constant D^T is used. The resulting diffusion equations are in agreement with previously reported schemes[4]. We compare the desorption rates emerging from our non-uniform grid model to the model with only atomic rows, as suggested in Ref. [3], using a broad range of rate parameters and choose appropriate grids to reach a relative accuracy of at least 0.04% when modelling the desorption rate. This allows especially for low step density crystals, to reduce the evaluation time to a minimum, while having accurate results suitable for the kinetic model to fit the experimental data.

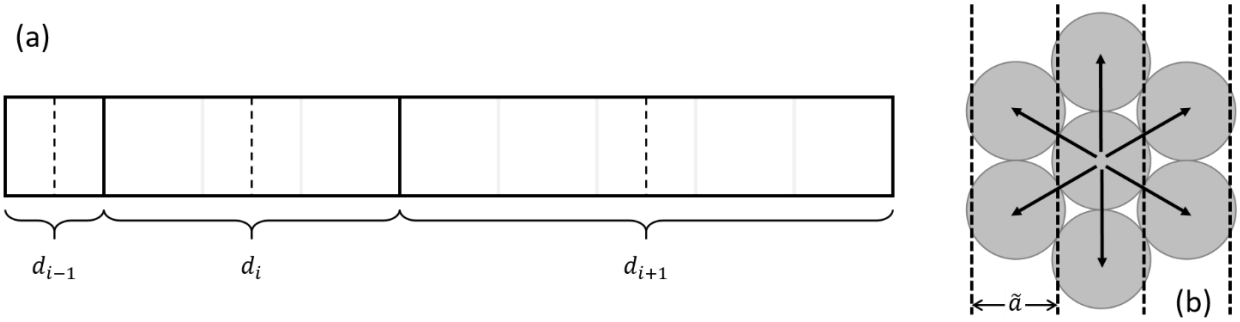

Figure S5: (a) Width definitions used for construction of diffusion equations in a non-uniform grid. (b) Sketch of degeneracy of pathways on a (111)-facet with black dashed lines indicating the step alignment on a Pt(332) crystal.

The diffusion constant D^T can be derived from the hopping rate constant between adjacent atomic rows following Ref. [5] or from the well-known formula for mean-square displacement. However, we have to account for the fact that hopping between adjacent rows on a Pt(111) will have degenerate pathways, as sketched in Fig. S5(b). Thus, D^T is given by:

$$D^T = \tilde{a}^2 k_h^T, \tag{S13}$$

where $\tilde{a}$ is the distance between two adjacent atomic rows (see Figure S5). When the width of spatial elements, d_i, is expressed in units of atomic rows as:

$$d_i = \tilde{a} n_i. \tag{S14}$$

Then Eq. S11 is reduced to:

$$\begin{aligned}\dot{c}_i = S_0^{\mathrm{T}}(1-c_i)F_t + \frac{2k_h^T}{n_i(n_{i+1}+n_i)}c_{i+1}(1-c_i) - \frac{2k_h^T}{n_i(n_{i+1}+n_i)}c_i(1-c_{i+1}) \\ - \frac{2k_h^T}{n_i(n_i+n_{i-1})}c_i(1-c_{i-1}) + \frac{2k_h^T}{n_i(n_i+n_{i-1})}c_{i-1}(1-c_i) - k_d^T c_i.\end{aligned} \tag{S15}$$

The differential equations are solved following the protocol described in Ref. [6] and the corresponding desorption flux is obtained from:

$$F_t^{\mathrm{NH_3}} = k_d^S c_{0,t} + \sum_{i=1}^{m-1} n_i k_d^T c_{i,t}\,. \tag{S16}$$

S4.3. Fitting procedure and uncertainty estimation

The global optimization routine is based on least-square minimization of the residual, error-weighted difference between experiment and model – see Ref. [1] for details. After the initial guess of the six globally optimized rate parameters the global fitting employs a cyclical two step procedure.

1. First, the desorption rate is numerically calculated (Eq. S16) based on the initial guess or the optimized rate parameter values established in the previous execution of step 2. Then, the amplitudes of the direct scattering and the trapping-desorption channel are fitted (locally) to each individual kinetic trace. For description of direct scattering we use a function proportional to the incident molecular beam $F_{\mathrm{B}}(t)$ in Eq. S8 and Eq. S9. The residual over the total dataset is calculated.
2. The local fitting procedure of the direct-scattering and trapping desorption amplitudes ensures the lowest possible residual or the present set of rate parameters. The rate parameters are modified following the least squares procedure and step 1 is repeated until convergence of the residual is reached.

The uncertainties of the fitted parameters were estimated by displacing the rate parameter of interest from its best fit value in small increments, fixing it and re-optimizing the remaining five parameter globally until a noticeable mismatch (deviations beyond the noise level of the data) between the re-fitted model and the data was observed. The parameter values between which an accurate fit could be obtained define the uncertainty range (see arrow with error-bar of Figure 3(b) and 3(c)). From the present analysis, we find that the strongest parameter correlation is the correlation between A and E_{a} of the individual rate constants (increasing prefactor leads to increasing activation energy). We also find a strong correlation between $A_{\mathrm{h}}^{\mathrm{T}}$ and $A_{\mathrm{h}}^{\mathrm{S}}$ (which have an almost constant ratio). Correlations for other parameters are less pronounced. For terrace desorption (see Figure 3(b) and (c)) the error analysis compares well with a complementary error estimation (see Section 3.2 of the main text) reflecting its reasonability.

S5. Coverage dependence of NH3 binding energies at Pt(111)

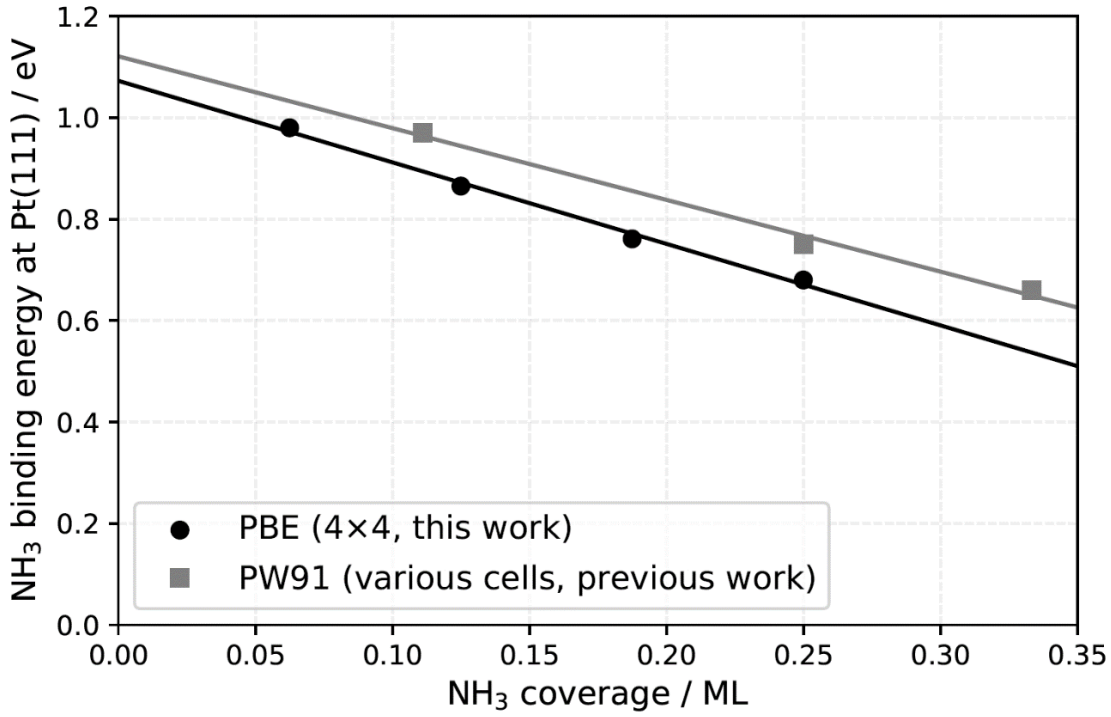

Figure S6: Calculated coverage dependence of NH_3 binding energies at Pt(111). The black points were obtained by placing 1, 2, 3 and 4 molecules inside a 4×4 unit cell and minimizing the energy. DFT energies were calculated with the PBE functional (the zero-point energy amounts ~0.12 eV at 0.06 ML but is not included for the energies shown in the plot). The grey squares are results from previously reported DFT calculations with the PW91 functional[7]. While the energies are different, the slopes of the fitted black and grey lines are very similar. The lines are linear extrapolations to zero-coverage for comparison to results derived from velocity-resolved kinetic experiments. The zero point energy correction on the binding energy at 0 and 0.06 ML, given in the main text, is included based of calculated frequencies at 0.06 ML. The scaling of the binding energy with the coverage was used for TPD and for isotherm simulations.

S6. The partition functions used in this work for TST modelling

S6.1. NH3* - uncoupled partition function for uTST model

The uncoupled TST (uTST) model used in this work employs the following adsorbate partition function $Q_{\mathrm{ad}}^{\mathrm{uTST}}$

$$Q_{\mathrm{ad}}^{\mathrm{uTST}} = \left(\prod_{i=1}^{5} Q_{\nu_i}^{\mathrm{qHO}}\right) Q_{\nu_{\mathrm{umb}}}^{\mathrm{qHO}} Q_{R_x}^{\mathrm{qHO}} Q_{R_y}^{\mathrm{qHO}} Q_{T_z}^{\mathrm{qHO}} Q_{C_3}^{\mathrm{rot}} \times \frac{2\pi m k_{\mathrm{B}} T}{h^2} \int_{-a/2}^{a/2}\int_{-b/2}^{b/2} \exp\left(-\frac{U_{n,\gamma}(x,y)}{k_{\mathrm{B}}T}\right) \mathrm{d}x\mathrm{d}y \left(\frac{Q_{T_x}^{\mathrm{qHO}}}{Q_{T_x}^{\mathrm{cHO}}}\right)\left(\frac{Q_{T_y}^{\mathrm{qHO}}}{Q_{T_y}^{\mathrm{cHO}}}\right). \quad \text{(S17)}$$

Here the vibrational partition function of individual DOFs appear in an overall product form. NH_3*'s possesses six internal modes—ν_{1-5} and ν_{umb} that correlate to the normal modes of the gas-phase molecule. Due to adsorption to the surface, ν_{umb} no longer inverts and two of rotational DOFs with rotation axes perpendicular to NH_3*'s symmetry axis, become frustrated rotations—R_x and R_y—and translation perpendicular to the surface—T_z—correlates to the external stretch of the adsorbate. All of these modes are treated as simple quantum harmonic oscillators,

$$Q^{\mathrm{qHO}} = \frac{1}{1-\exp\left(-\frac{h\nu}{k_{\mathrm{B}}T}\right)}, \quad \text{(S18)}$$

where, ν is the harmonic frequency of the mode at the most stable binding site (see Table 2 of the main text).

The rotation around NH_3* symmetry axis remains free, validated from previous work[8], and is described by the 1D-rotational partition function:

$$Q_{C_3}^{\mathrm{rot}} = \frac{\sqrt{\pi}}{\sigma}\sqrt{\frac{k_B T}{C}}, \quad \text{(S19)}$$

where C is the rotational constant and σ is the corresponding symmetry number.

NH_3*'s two translational DOFs parallel to the surface $T_{x,y}$ are treated within the hindered translator model[9-11], using a periodic interaction potential $U_{n,\gamma}(x,y)$, which we write in the following form:

$$U_{n,\gamma}(x,y) = f(x;n,\gamma) + f(y;n,\gamma). \quad \text{(S20)}$$

$f(x;n,\gamma)$ and $f(y;n,\gamma)$ contain adjustable parameters, n and γ, that are used to reproduce the harmonic frequency of T_x and T_y obtained from DFT, and the experimentally derived energy barrier for site-to-site hopping. To match both of these quantities, the commonly employed 1D model potential functions[9-10, 12] are better replaced by functions of the following form:

$$f(\xi;n,\gamma) = (1-\gamma)E_{0,\mathrm{h}}^{\mathrm{T}}\left(1-\cos^2\frac{\xi\pi}{a}\right) + \gamma E_{0,\mathrm{h}}^{\mathrm{T}}\left(1-\cos^2\frac{\xi\pi}{a}\right)^n, \quad \text{(S21)}$$

where, ξ is x or y, a is the length of the unit cell (2.77 Å), $E_{0,\mathrm{h}}^{\mathrm{T}}$ is the experimentally derived hopping barrier (0.71 eV). The hindered translation potential used in uTST $f(\xi;n=2,\gamma=0.47)$ is shown in Figure S7. The configuration integral above is classical and converges to 0 at low temperatures. We ensure proper quantum behavior of the partition function—i.e. $Q \geq 1$—at low temperature by including the term $Q_{T_\xi}^{\mathrm{qHO}}/Q_{T_\xi}^{\mathrm{cHO}}$. This correction term is described in Ref. [10] in detail.

S6.2. NH_3* - coupled Q_{ad} for use in the coupled TST model

Despite energy sampling of a multidimensional potential energy surface for NH_3 at Pt(111) would be the most straightforward approach it is computationally demanding. Thus, we require clever approximative methods for the description of the potential energy going beyond the harmonic approximation and the assumption of normal modes.

Because the coupling of DOFs for partition functions in TST is not common and there are many ways this might be implemented, we first illustrate our idea using a 2D toy system. Consider an atom on a one-dimensional catalyst surface, which exhibits displacement over a diffusion barrier along x and harmonic vibration normal to the surface along z. For motion along x, the harmonic frequency in the z direction varies due to the changing interaction with the catalyst. This can be expressed as an x-dependent force constant $k_z(x)$, where the total energy expression is then approximated by:

$$H_{\mathrm{toy}}(p_x,p_z,x,z) = \frac{p_x^2}{2m} + \frac{p_z^2}{2m} + V(x) + \frac{1}{2}k_z(x)z^2. \quad \text{(S22)}$$

Here, the first two terms describe the kinetic energy along x and z, the third term describes the potential energy along the minimum energy pathway for diffusion, while the fourth term describes the potential energy for z displacement. This

formulation explicitly introduces coupling of x and z as k_z depends on x. The classical partition function for the toy system then becomes:

$$Q_{\mathrm{ad}}^{\mathrm{toy}} = \frac{1}{h^2} \int_{z=-\infty}^{\infty} \int_{x=0}^{a} \int_{p_z=-\infty}^{\infty} \int_{p_x=-\infty}^{\infty} \exp\left(-\frac{H_{\mathrm{toy}}(p_x, p_z, x, z)}{k_{\mathrm{B}}T}\right) \mathrm{d}p_x \mathrm{d}p_z \mathrm{d}x \mathrm{d}z, \tag{S23}$$

where a is the length of the unit cell. Combining Eq. S22 and S23 leads to:

$$Q_{\mathrm{ad}}^{\mathrm{toy}} = \frac{\sqrt{2\pi m k_{\mathrm{B}}T}}{h} \int_{-a/2}^{a/2} \exp\left(-\frac{V(x)}{k_{\mathrm{B}}T}\right) \frac{k_B T}{h\nu_z(x)} \mathrm{d}x = \frac{\sqrt{2\pi m k_{\mathrm{B}}T}}{h} \int_{-a/2}^{a/2} \exp\left(-\frac{V(x)}{k_{\mathrm{B}}T}\right) Q_z^{\mathrm{cHO}}(x) \mathrm{d}x. \tag{S24}$$

Here, $\nu_z(x)$ is the harmonic stretch frequency and the coupling between x and z manifests itself by a modification of the configurational integral over x, which now includes the z-coordinate stretch frequency in the x-dependent vibrational partition function $Q_z^{\mathrm{cHO}}(x)$. Since $k_B T \ll h\nu$, we replace $Q_z^{\mathrm{cHO}}(x)$ by its quantum mechanical counterpart:

$$\begin{aligned} Q_z^{\mathrm{cHO}}(x) &= \frac{k_B T}{h\nu_z(x)} \\ &\Downarrow \\ Q_z^{\mathrm{qHO}}(x) &= \frac{1}{1 - \exp\left(-\frac{h\nu_z(x)}{k_B T}\right)}. \end{aligned} \tag{S25}$$

While this approach is certainly *ad hoc*, it represents a useful step beyond uTST, that can be taken without significantly increasing the effort beyond the established methods and with a more realistic accounting of the adsorbate entropy.

In the NH_3 Pt system, we couple four DOFs—ν_{umb}, R_x, R_y, T_z—to hindered translation parallel to the Pt surface. The frequencies of these DOFs change most when moving along the hindered translation coordinate from the on-top binding site to the hopping transition state (see Table 2). Then, in analogy to the toy system described above, we write $Q_{\mathrm{ad}}^{\mathrm{cTST}}$ in the following form:

$$\begin{aligned} Q_{\mathrm{ad}}^{\mathrm{cTST}} = &\left(\prod_{i=1}^{5} Q_{\nu_i}^{\mathrm{qHO}}\right) Q_{C_3}^{\mathrm{rot}} \frac{2\pi m k_{\mathrm{B}}T}{h^2} \times \\ &\int_{-a/2}^{a/2} \int_{-b/2}^{b/2} Q_{\nu_{\mathrm{umb}}}^{\mathrm{qHO}}(x,y) Q_{R_x}^{\mathrm{qHO}}(x,y) Q_{R_y}^{\mathrm{qHO}}(x,y) Q_{T_z}^{\mathrm{qHO}}(x,y) \exp\left(-\frac{U_{n,\gamma}(x,y)}{k_{\mathrm{B}}T}\right) \mathrm{d}x \mathrm{d}y \left(\frac{Q_{T_x}^{\mathrm{qHO}}}{Q_{T_x}^{\mathrm{cHO}}}\right) \left(\frac{Q_{T_y}^{\mathrm{qHO}}}{Q_{T_y}^{\mathrm{cHO}}}\right). \end{aligned} \tag{S26}$$

The first six terms before the integral are identical to those used in uTST and represent vibrational partition functions that are independent of x and y. As a consequence of coupling, the minimum energy pathway emerging from a linear combination of multiple normal modes, cannot be described by hindered translational frequencies of the initial state, as we have done in uTST approach. The in-plane interaction potential, $U_{n,\gamma}(x,y)$ is parametrized similarly as described for uTST with the difference that here $f(\xi; n, \gamma)$ are fitted to the shape of the minimum energy path for hopping obtained from CI-NEB. See Figure S7, which shows the DFT minimum energy path as crosses and the best fit $f(\xi; n = 4.5, \gamma = 0.64)$ as a black solid line. The configuration integral now includes x- and y-dependent vibrational partition functions for the four DOFs whose frequencies change most dramatically when NH_3 translates from the on-top site to the diffusion transition state, according to DFT calculations.

These four partition functions are then parametrized as follows:

$$Q_{\nu_i}^{\mathrm{qHO}}(x,y) = \frac{1}{1 - \exp\left(-\frac{h\nu_i(x,y)}{k_B T}\right)}, \tag{S27}$$

with

$$\nu_i(x,y) = \nu_{i,\mathrm{bri}} + \left(\nu_{i,\mathrm{top}} - \nu_{i,\mathrm{bri}}\right) \exp\left(-\frac{x^2 + y^2}{\sigma_\nu^2}\right). \tag{S28}$$

$\nu_i(x,y)$ now describes the softening of the modes as the NH_3 molecule moves away from the atop binding site. Note, that we only use DFT frequency information for two structures: $\nu_{\mathrm{i,top}}$ for the top site and $\nu_{i,\mathrm{bri}}$ for the bridge site, which is the TS for hopping. The scaling with the in-plane coordinates is done assuming radial symmetry around the top site, which is a sensible approximation due to a localized bond formation between NH_3 and the top site of Pt. We have optimized σ_ν such that $\nu(x,y)$ at the bridge site does not deviate by more than 0.1% from ν_{bri} and yields good agreement with the temperature dependence of the desorption rate from Pt(111). The $\nu_i(x,y)$ functions are shown as blue solid lines in Fig. S7. The

uncertainties of NH_3* binding energy, that were derived from the cTST fit to the data, emerge from uncertainties associated with σ_ν. We have investigated the sensitivity of derived binding energies to σ_ν values that appeared reasonable in shape ($\nu_i(x,y)$ with FWHM between 0.5 and 2.0 Å) and estimated the uncertainty based on this.

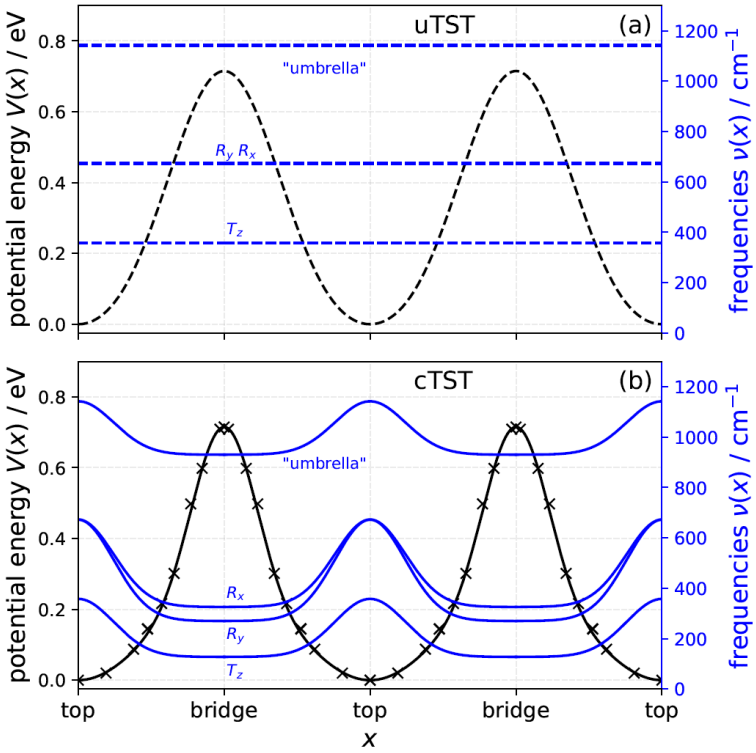

Figure S7: Coupling degrees of freedom in the TST of ammonia desorption and diffusion. (a) NH_3-Pt(111) interaction potential (black line) as a function of parallel translation x used to construct Q_{ad} within the uTST. It is parametrized based on the hindered translational frequency found from DFT at the top site and the experimentally derived hopping barrier. The blue dashed lines present the harmonic frequencies of vibrational modes that are associated with the molecule surface interaction. In this uncoupled picture the frequencies are independent of x. (b) NH_3-Pt(111) interaction potential (black line) as a function of parallel translation x used to construct Q_{ad} within the cTST. The crosses are the minimum energy path for diffusion derived from DFT calculations but scaled to match the experimental hopping barrier. Eq. S21 was used to generate the black solid line with optimized values of n and γ. The parallel translational dependence of the harmonic frequencies of four coupled modes is shown as blue solid lines. The region between two bridge sites characterizes the partition function for the adsorbate.

S6.3. Transition state for desorption

The desorbed gas-phase molecule is taken as the transition state for desorption in this entire work. Its partition function is given by:

$$Q^{\ddagger} = Q_{\mathrm{2D}}^{\mathrm{tr}} Q_{\mathrm{3D}}^{\mathrm{rot}} \left(\prod_{i=1}^{5} Q_{\nu_i}^{\mathrm{qHO}} \right) Q_{\mathrm{umb}}. \tag{S29}$$

Here, $Q_{\mathrm{2D}}^{\mathrm{tr}}$ is the partition function for free translation of a 2D ideal gas:

$$Q_{\mathrm{2D}}^{\mathrm{tr}} = \frac{2\pi m k_{\mathrm{B}} T}{h^2} A, \tag{S30}$$

with m being the mass of NH_3. A is the area of the Pt(111) unit cell, in which the partition function is defined. Note that translation normal to the surface is associated with the reaction coordinate in TST and is not part of $Q^{\ddagger}$.

$Q_{\mathrm{3D}}^{\mathrm{rot}}$ is the classical rotational partition function of a symmetric top:

$$Q_{\mathrm{3D}}^{\mathrm{rot}} = \frac{\sqrt{\pi}}{\sigma} \sqrt{\frac{(k_{\mathrm{B}} T)^3}{B^2 C}}, \tag{S31}$$

where B and C are the rotational constants and σ is the associated symmetry number.

The vibrational partition function can be accurately approximated by a simple quantum harmonic oscillator partition function $Q_{v_i}^{\mathrm{qHO}}$ for five DOFs: the symmetric and two asymmetric stretches as well as two asymmetric bends, conventionally referred to as $v_1 - v_5$. $Q_{v_i}^{\mathrm{qHO}}$ takes the usual form:

$$Q_{v_i}^{\mathrm{qHO}} = \frac{1}{1 - \exp\left(-\frac{h\nu_i}{k_{\mathrm{B}}T}\right)}. \tag{S32}$$

Here, ν_i is the harmonic frequency of mode v_i. The umbrella mode is treated by explicit counting of the first ten vibrational levels, E_i^{umb}, to account for its complex quantum structure.

$$Q_{\mathrm{umb}} = \sum_{i=1}^{10} \exp\left(-\frac{E_i^{\mathrm{umb}}}{k_{\mathrm{B}}T}\right). \tag{S33}$$

All parameters needed to evaluate the partition function can be found in Refs. [13-15].

S6.4. Transition state for hopping

The transition state for hopping is described with the following partition function:

$$Q_{\mathrm{hop}}^{\ddagger} = \left(\prod_i^5 Q_{\nu_i'}^{\mathrm{qHO}}\right) Q_{\nu_{umb}'}^{\mathrm{qHO}} Q_{R_x'}^{\mathrm{qHO}} Q_{R_y'}^{\mathrm{qHO}} Q_{T_z'}^{\mathrm{qHO}} Q_{C_3}^{\mathrm{rot}} \frac{\sqrt{2\pi m k_{\mathrm{B}}T}}{h} \int_{-b/2}^{b/2} \exp\left(-\frac{h(y)}{k_{\mathrm{B}}T}\right) \mathrm{d}y \left(\frac{Q_{y'}^{\mathrm{qHO}}}{Q_{y'}^{\mathrm{cHO}}}\right). \tag{S34}$$

The first nine partition functions describes the internal NH_3* vibrations, the frustrated rotations and translation (along the surface normal) as quantum harmonic oscillator with TS frequencies from Table 2. NH_3*'s rotation around its symmetry axis is assumed to be free. Since we find a rather low hindered translational frequency along the y-coordinate (x is taken as the reaction coordinate) we treat it by a hindered translator. Based on DFT generated harmonic frequencies, we estimate the shape of $h(y)$ using the commonly applied model potential energy function from Ref. [9]. We also include the low temperature correction to the partition function, previously described in Section 8.6.1.

We emphasize that this partition function does not take coupling of different DOFs into account. Including coupling would require vibrational frequencies of NH_3 along y while x would be fixed at the TS. Including coupling corrections would result in a somewhat higher value of the partition function than offered by the present approach.

S7. Extraction of First-Order rate constants from the desorption rates

We determine the first-order rate constants for NH_3 desorption from Pt(332) and the fast component in Pt(111) by fitting the flux $f(t)$ vs. residence time t using a function with two contributions,

$$f(t) = a \times \mathrm{DS}(t) + b \times \mathrm{TD}(t, k_{\mathrm{des}}), \tag{S35}$$

comprising direct scattering (DS) and a trapping-desorption (TD) with k_{des} as the desorption constant. The DS contribution has the temporal shape of the incident molecular beam, while the TD contribution is an exponential decay convoluted with the molecular beam temporal profile. For Pt(332) analysis, the full trace is fitted with Eq. S35, while for Pt(111) we cut the slow part off for the fit. The corresponding fits to the kinetic traces are shown in Fig. S8, while the fitted rate constants are shown in Fig. 3(a) (as red circles and black crosses) of the main text.

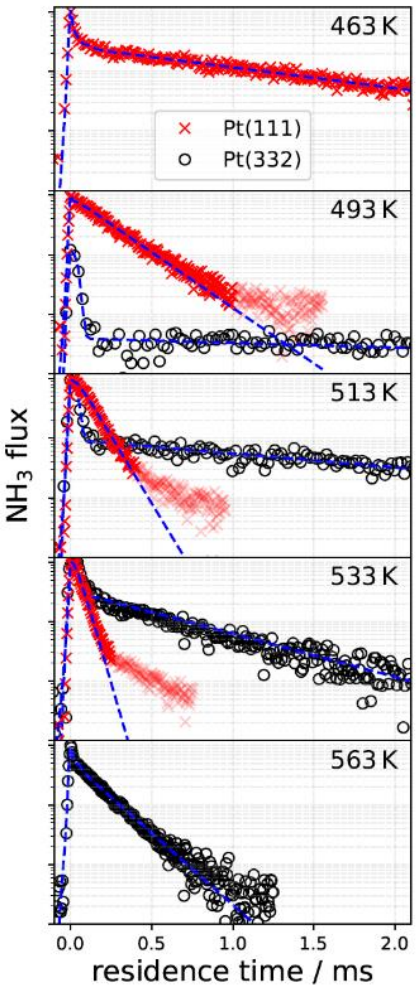

Figure S8: Desorption rate analysis with first-order rate constant extraction. Data from Pt(332), black circles, are fitted completely with Eq. S35, while Pt(111) data, red crosses, are fitted partially, with the excluded region shown in light red. The fits of Eq. S35 to the individual kinetic traces are shown by the blue dashed lines.

S8. Terrace-assisted desorption model from stepped surfaces

Here we derive the formula for the terrace-assisted desorption (TAD) model given in Eq. 4 of the main text. We assume a steady state between NH_3 at steps and terraces including the possibility to desorb from terraces and steps. An effective first-order desorption rate constant for NH_3 desorption from a stepped surface can be derived. We assume the following processes:

$$\mathrm{NH}_{3,\mathrm{T}}^{*} \underset{k_{\mathrm{h}}^{\mathrm{S}}(1-\mu)}{\overset{k_{\mathrm{h}}^{\mathrm{T}}\mu}{\rightleftarrows}} \mathrm{NH}_{3,\mathrm{S}}^{*}\,, \tag{S36}$$

$$\mathrm{NH}_{3,\mathrm{T}}^{*} \xrightarrow{k_{\mathrm{d}}^{\mathrm{T}}} \mathrm{NH}_3\,, \tag{S37}$$

$$\mathrm{NH}_{3,\mathrm{S}}^{*} \xrightarrow{k_{\mathrm{d}}^{\mathrm{S}}} \mathrm{NH}_3\,, \tag{S38}$$

where μ reflects the step density of the crystal. We define the total desorption rate and the effective first-order desorption rate constant as follows:

$$\frac{\mathrm{d}[\mathrm{NH}_3]}{\mathrm{d}t} = k_{\mathrm{d}}^{\mathrm{T}}\left[\mathrm{NH}_{3,\mathrm{T}}\right] + k_{\mathrm{d}}^{\mathrm{S}}[\mathrm{NH}_{3,\mathrm{S}}] \equiv k_{\mathrm{eff}}[\mathrm{NH}_{3,\mathrm{S}}] \tag{S39}$$

Since NH_3 has a big energy preference for steps, after a short induction period, the total desorption rate will be characteristic of the concentration pool at steps with the corresponding effective desorption rate constant. Assuming steady-state for $\left[\mathrm{NH}_{3,\mathrm{T}}\right]$, which is justified as shown in Section 3.5.2 of the main text we obtain:

$$\left[\mathrm{NH}_{3,\mathrm{T}}\right]_t = \frac{k_{\mathrm{h}}^{\mathrm{S}}(1-\mu)}{k_{\mathrm{h}}^{\mathrm{T}}\mu + k_{\mathrm{d}}^{\mathrm{T}}}\left[\mathrm{NH}_{3,\mathrm{S}}\right]_t\,. \tag{S40}$$

Combining Eq. S39 and S40 we obtain k_{eff}, shown as Eq. 4 of the main text and below:

$$k_{\mathrm{eff}} = k_{\mathrm{d}}^{\mathrm{S}} + k_{\mathrm{h}}^{\mathrm{S}}(1-\mu)\frac{k_{\mathrm{d}}^{\mathrm{T}}}{k_{\mathrm{h}}^{\mathrm{T}}\mu + k_{\mathrm{d}}^{\mathrm{T}}}. \tag{4}$$

We emphasize that the present model is kept simple and thus works only at stepped surfaces and adsorbates with strong energy preference. The results of the TAD model are shown in Fig. S9 as a black solid line in excellent agreement with experiment rate constants ($\chi^2 = 2.9$) obtained for NH_3 desorption from Pt (332) (black crosses). We also compare the results of an earlier model from Serri, Tully and Cardillo[3] (STC model) where no direct step desorption was considered (black dashed line). Neglecting direct step desorption degrades the fit ($\chi^2 = 16.3$) somewhat underestimating the experimental rate constants.

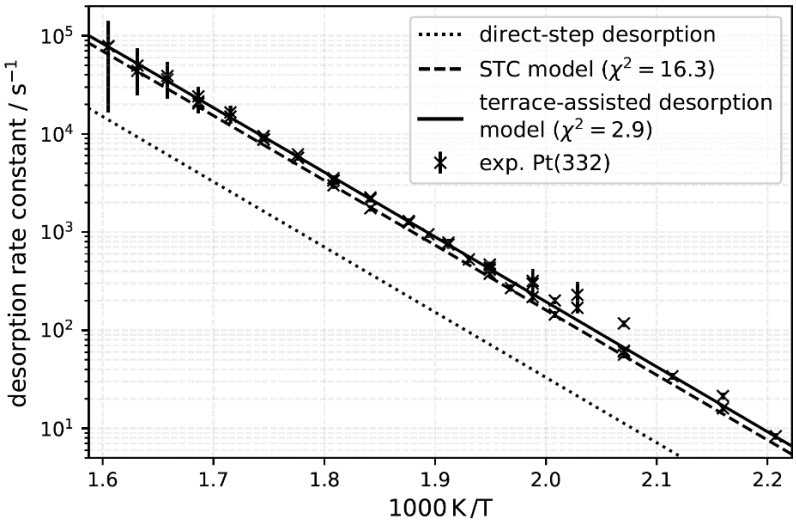

Figure S9: Comparison of experimental NH_3 desorption rate constants obtained with Pt (332) (black crosses) and three models for desorption from stepped surfaces. χ^2 in the legend is the reduced chi-square value.

S9. Coverage dependent desorption rates and adsorption isotherms

While the elementary reaction rate constants reported in this work were obtained for the low coverage limit, they can be used as a starting point to extend our understanding of the kinetics of NH_3 desorption from Pt. Here we explain how we have included the coverage dependence of the desorption rate constant from terraces and steps, based on the arguments elaborated in Section. 8.4.1 of the SI.

The coverage influences both the prefactor and the binding energy of the desorption rate constant:

$$k(T,\theta) = A(T,\theta)\exp\left(-\frac{E_0(\theta)}{k_B T}\right). \tag{S41}$$

From DFT calculations we find that NH_3 binding energy decreases linearly from $\theta = 0.06$ to 0.25 ML with a slope of $\alpha = -1.61$ eV/ML. We use the scaling of binding energy with coverage from DFT calculations, while using the experimentally derived zero-coverage binding energy ($E_{0,\mathrm{d}}^{\mathrm{T}} = 1.13 \pm 0.02$ eV). The resulting coverage dependent NH_3 binding energy at terraces is then the following

$$E_0(\theta)\ /\ \mathrm{eV} = 1.13 - 1.61 \times \left(\frac{\theta}{\mathrm{ML}}\right). \tag{S42}$$

We emphasize that the NH_3 saturation coverage of 0.25 ML is defined with respect to the Pt(111) facet.

We include the coverage dependence of the prefactor, $P_\theta(T)$, using the calculated harmonic frequencies of the adsorbate at 0.06 and 0.25 ML. We assume that the logarithm of the prefactor, which reflects the entropy difference between the initial state and the transition state, scales linearly with coverage and is described by:

$$\log_{10}\big(A(T,\theta)\big) = (1-4\theta)\log_{10}\big(P_{0.06}(T)\big) + 4\theta\log_{10}\big(P_{0.25}(T)\big). \tag{S43}$$

We note in passing that the prefactor calculated with frequencies at 0.06 ML is assumed to represent the prefactor in the zero-coverage limit. This introduces negligible changes in the results because the prefactor has only weak sensitivity to the assumptions of its scaling and the dominant contribution to the desorption rate comes from coverage dependence of NH_3's binding energy.

Using the coverage dependent desorption rate constant we simulate TPD spectra from previous work with the same experimental conditions, results of this simulation are shown in Fig. S10. We find overall good agreement with TPD spectra of the monolayer peak obtained from earlier studies.

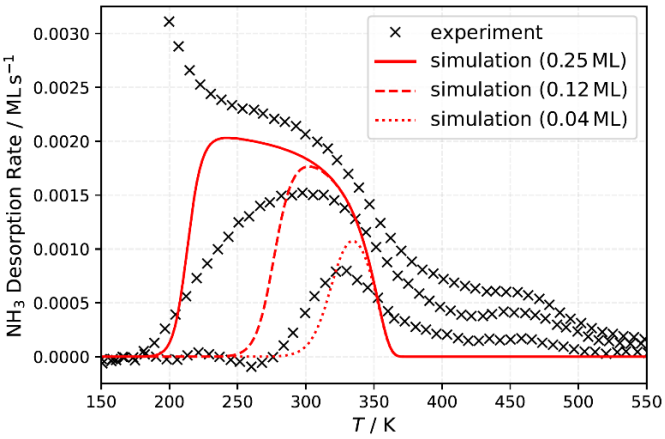

Figure S10: Previously measured NH_3 TPDs from Pt(111) from Ref. [16] (black crosses). Ref. [16] does not explicitly indicate the initial coverage in each of the three TPD spectra. The low temperature feature below 200 K is due to desorption of the multilayer only seen under conditions of the highest initial ammonia dose. At lower dosing, two TPD spectra are reported that represent desorption of the NH_3 monolayer at different initial coverages. The shoulder seen at 450 K emerges most likely from desorption influenced by steps. The red lines show TPD simulations of NH_3 desorption from Pt(111) based on Eq. S41 at three initial NH_3 coverages (see legend). It is clear that at shape of the TPD is strongly dependent on initial coverage—this reflects the influence of adsorbate-adsorbate interactions. The simulation captures this behavior reasonably well, validating our approach.

The adsorption isotherms are simulated using the diffusion-desorption kinetic model described in Section 8.4.2 of the SI. The stationary adsorption flux (at each spatial element i) is described by the Hertz-Knudsen equation:

$$F_{\mathrm{NH_3}} = \frac{p_{\mathrm{NH_3}}}{\sqrt{2\pi m_{\mathrm{NH_3}} k_{\mathrm{B}} T}}, \tag{S44}$$

instead of the molecular beam dosing function. For the chosen range of p_{NH_3} and T the rate equations are propagated in time until the stationary-state is established, from which the coverages at steps and terraces is derived. For simulation of the KB model[17] we use a surface with only terrace sites (as assumed by the KB model) in which the coverage independent NH_3 desorption rate constant is described by:

$$\frac{k_{\mathrm{d}}^{\mathrm{KB}}}{\mathrm{s}^{-1}} = 10^{9.74} \exp\left(-\frac{0.63\ \mathrm{eV}}{k_{\mathrm{B}}T}\right). \tag{S45}$$

The simulation results are shown in Figure 6 of the main text.

S10. Additional References

1. Borodin, D.; Rahinov, I.; Shirhatti, P. R.; Huang, M.; Kandratsenka, A.; Auerbach, D. J.; Zhong, T.; Guo, H.; Schwarzer, D.; Kitsopoulos, T. N.; Wodtke, A. M., Following the microscopic pathway to adsorption through chemisorption and physisorption wells. *Science* **2020,** *369* (6510), 1461-1465.

2. Guthrie, W. L.; Sokol, J. D.; Somorjai, G. A., The Decomposition of Ammonia on the Flat (111) and Stepped (557) Platinum Crystal-Surfaces. *Surf Sci* **1981,** *109* (2), 390-418.

3. Serri, J. A.; Tully, J. C.; Cardillo, M. J., The influence of steps on the desorption kinetics of NO from Pt(111). *The Journal of Chemical Physics* **1983,** *79* (3), 1530-1540.

4. Crank, J., *The Mathematics of Diffusion*. Clarendon Press: Oxford, 1975; Vol. 2.

5. King, D. A., Surface-Diffusion of Adsorbed Species - a Review. *J Vac Sci Technol* **1980,** *17* (1), 241-247.

6. Borodin, D.; Golibrzuch, K.; Schwarzer, M.; Fingerhut, J.; Skoulatakis, G.; Schwarzer, D.; Seelemann, T.; Kitsopoulos, T.; Wodtke, A. M., Measuring Transient Reaction Rates from Nonstationary Catalysts. *ACS Catal* **2020,** *10* (23), 14056-14066.

7. Novell-Leruth, G.; Valcarcel, A.; Clotet, A.; Ricart, J. M.; Perez-Ramirez, J., DFT characterization of adsorbed NHx species on Pt(100) and Pt(111) surfaces. *J Phys Chem B* **2005,** *109* (38), 18061-18069.

8. Garcia-Hernandez, M.; Lopez, N.; Moreira, I. D.; Paniagua, J. C.; Illas, F., Ab initio cluster model approach to the chemisorption of NH3 on Pt(111). *Surf Sci* **1999,** *430* (1-3), 18-28.

9. Sprowl, L. H.; Campbell, C. T.; Arnadottir, L., Hindered Translator and Hindered Rotor Models for Adsorbates: Partition Functions and Entropies. *J Phys Chem C* **2016,** *120* (18), 9719-9731.

10. Borodin, D.; Rahinov, I.; Fingerhut, J.; Schwarzer, M.; Hörandl, S.; Skoulatakis, G.; Schwarzer, D.; Kitsopoulos, T. N.; Wodtke, A. M., NO Binding Energies to and Diffusion Barrier on Pd Obtained with Velocity-Resolved Kinetics. *J Phys Chem C* **2021,** *125* (21), 11773-11781.

11. Jørgensen, M.; Grönbeck, H., Adsorbate Entropies with Complete Potential Energy Sampling in Microkinetic Modeling. *The Journal of Physical Chemistry C* **2017,** *121* (13), 7199-7207.

12. Bajpai, A.; Mehta, P.; Frey, K.; Lehmer, A. M.; Schneider, W. F., Benchmark First-Principles Calculations of Adsorbate Free Energies. *ACS Catal* **2018,** *8* (3), 1945-1954.

13. Nguyen, H. L.; Gulaczyk, I.; Kreglewski, M.; Kleiner, I., Large amplitude inversion tunneling motion in ammonia, methylamine, hydrazine, and secondary amines: From structure determination to coordination chemistry. *Coordin Chem Rev* **2021,** *436*.

14. Herzberg, G., *Electronic spectra and electronic structure of polyatomic molecules*. Van Nostrand: 1966; p 609.

15. Shimanouchi, T., *Tables of Molecular Vibrational Frequencies*. NSRDS: 1972; p 15.

16. Mieher, W. D.; Ho, W., Thermally Activated Oxidation of NH3 on Pt(111) - Intermediate Species and Reaction-Mechanisms. *Surf Sci* **1995,** *322* (1-3), 151-167.

17. Kraehnert, R.; Baerns, M., Kinetics of ammonia oxidation over Pt foil studied in a micro-structured quartz-reactor. *Chem Eng J* **2008,** *137* (2), 361-375.

Chapter 5

Unifying Discussion and Recommendations

In this chapter my aim is not to recapture what has been written in the previous chapters but to provide a link between the different projects and molecule-surface systems. I seek to point out the improvements on the experimental methods in VRK that have been achieved during this work. I also want to give some recommendations on the details of kinetic analysis of kinetic data and on accurate construction of adsorbate partition functions. In the end I provide a discussion on the influence of atomic steps on the desorption rate constants in different molecule-surface systems, where I will especially highlight the importance of entropic effects. In all cases, it was important for me to also highlight the things that have so far not been sufficiently understood or solved and should serve as a starting point for future research effort.

5.1 Current Status of Velocity Resolved Kinetics

In Sec. 1.2 I highlighted some of the challenges of VRK that we have encountered at the beginning of this work. One of the issues was the restriction to study reversible systems. Only those systems can be studied with a pump-probe technique. Unfortunately, a broad range of problems in heterogeneous catalysis are not fully reversible, as either morphological changes or poisoning of the catalyst may occur.

A fast-recording camera, kindly provided from LaVision GmbH, allowed us to test an experimental scheme where we are no longer bound to the reversibility requirement of the studied system—see Sec. 2.1. We tested this new method by following the transient rate of CO oxidation, while CO beam pulses titrate an oxygen atom saturated Pd(332) surface. Each subsequent CO pulse initiates a different transient rate, because oxygen is removed by reaction, allowing us to investigate the CO oxidation kinetics at different oxygen coverages within a single experiment. The high-repetition-rate version of VRK allows us to measure ion signal from each pulse of a Ti:Saphire laser at 1 kHz and probing the CO_2 formation rate induced by the CO pulse-train in real time. Surprisingly, experimental data from only a few short measurements, were instructive enough to follow CO oxidation kinetics from reaction to diffusion controlled regime. On the basis of these data we characterized the reaction, desorption and diffusion rate constants for CO on Pd(332) in Sec. 2.1. A pleasant side effect of this work was that we understood that titrations, which we routinely did for coverage calibration exclusively, have more delicate information that can be used complementary to the steady-state kinetic traces.

While our simple proof-of-principle experiments were restricted to a time resolution of 1 ms, there is room for improvement. State-of-the-art Yb-fiber lasers can operate at 100 kHz, while providing enough peak power for nonresonant multiphoton ionization. This would provide a detection pulse each 10 µs which is also the time resolution of our molecular beams. The acquisition of ion images, as we have done it for the proof-of-principle experiments, at such high repetition-rates is unpractical due to the high amount of data to be stored. In fact, this is not necessary as only a small fraction of the ion image contains ion counts from a single laser pulse. Modern event cameras[125–127], which store information of individual ion occurrences as a function of time, are much better suited for these kind of experiments. Given that a fast responding phosphor screen is used, an event camera will take away the need to pulse the imaging detector. This is due to the high time resolution of these event cameras. It enables us to track multiple species with different mass-to-charge ratios that arrive at the detector after ionization, simultaneously. The combination of a Yb-fiber laser with an event camera, like in Refs. [125–127], has the potential to replace the pump-probe method in VRK studies. It provides the multiplex advantage required for transient kinetics studies with various products at nonstationary catalysts.

Conducting experiments with high-repetition rate detection has the general advantage that the duty cycle of the measurement is increased. This allows low signals and slow reaction rates to be measured more efficiently—see Sec. 2.1. Especially in the context of molecule-surface interactions this is an important advantage because thermal desorption rates can be measured over a broad temperature range with reasonable effort. This provides delicate experimental data to test the applicability of the adsorbate entropy models over a broad temperature range, which also gives rise to more accurate binding energies.

Another issue that we faced at the start of this work, was the absence of a reliable method to determine the absolute reactant flux of a molecular beam. In fact, this is a problem of a broad range of previous kinetic methods in surface science and made accurate studies of second-order reactions very difficult—see for example Refs. [49, 56]. The application of ion imaging allows, not only the characterization of the molecular beam's time profiles but also its spatial distribution of molecular densities. The ion signal was calibrated using a static background gas with a known density. The molecule velocities were derived from the position on the ion image directly. This allows to determine the absolute reactant flux—see Sec. 3.1. This method enabled us to determine the elementary rate constants for the recombination of hydrogen atoms at Pt(111) and Pt(332)—see Sec. 3.1.

Our recent work has shown that a combination of nonequillibrium desorption dynamics with thermal reaction kinetics can be also efficiently used to obtain intermediate adsorption enthalpies. This information was until recently only available to Single Crystal Adsorption Calorimetry experiments. We have demonstrated this method on the example of bidentate formate at Pt, which is a key intermediate in the chemical fixation of CO_2[62].

There are some recent attempts to use VRK for the study surface reaction rates of chiral molecules. It is known that chiral molecules can be distinguished by their photoelectron angular distribution when ionized with a circularly polarized laser (photo electron circular dichroism). Recent work showed that chiral molecules, that were preadsorbed to the surface in subsequent layers could be recognized when they were desorbed from the surface[128]. Certainly, there is more potential in this field to be explored.

Unfortunately, the lack of kinetic information for surface reaction intermediates still persists. In our recent paper we showed that lack of this information, in the seemingly simple H_2 oxidation reaction at Pt(111), precludes the understanding of the underlying kinetic mechanism[57]. Certainly, solving this issue is a matter of effort and time. Despite this difficult task, there is no doubt that VRK has a bright future for the study of surface reaction kinetics.

5.2 Detailed Analysis Does Matter

While it might appear surprising to dedicate an obvious statement an individual chapter, it has to be clear that the understanding of kinetic problems requires a detailed analysis. To a broad range of kinetics problems it is illusory to believe finding solutions only in the lab. Below are three examples from this work to give this statement substance.

The experimental data obtained from high-repetition-rate VRK (see Sec. 2.1) was initially analyzed with a microkinetic mechanism, similar as reported in Ref. [66]. However, it turned out that the data could not be explained with a complicated microkinetic mechanism, but with the nonuniform spatial distribution of CO density, provided from the molecular beam—essentially an experimental artifact. While similar effects were discussed in earlier studies, they were regarded to be negligible[44]. However, only an analysis that consideres the spatial distribution of the projected beam and macroscopic diffusion of the reactants on the surface, is capable to explain the observations with a simple microkinetic mechanism. In this way it was even possible to identify reaction and diffusion limited regimes in the experimental data. Unfortunately, kinetic mechanisms are often derived without consideration of the actual experimental details, like the spatial distribution of molecules at the surface[37, 44, 48]. In such cases, wrong conclusions about the underlying chemistry may be drawn based on an experimental artifact. A simple conclusion can be drawn from this example. Only when all details of the actual experiment are taken into account in the analysis, one can be sure to arrive at the correct reaction mechanism. Only then the interesting details of surface reactions can be discovered.

Another example where a detailed analysis has led to a better understanding of the molecule-surface interaction is the NO/Pd system—see Sec. 4.1. The desorption rate constants of NO from Pd(111) and Pd(332) have almost the same magnitude in the studied temperature range. A naive conclusion from this study could be that steps do not alter the NO binding energy at Pd. However, a more detailed inspection of the underlying temperature dependence shows small but noticeable difference in the Arrhenius rate parameters. We analyzed these data using a simple in-plane model potential for NO interaction with Pd surface, whereby we considered that NO has a different binding energy at the step site of Pd(332) than on (111) terraces. The model potential provided a partition function which was used to calculate the TST rate constant for desorption. The fitted in-plane model potential predicts an energetic preference for NO at steps. At the same time, this preference leads to a reduction of NO's density of states and thus the prefactor of the desorption rate constant increases. The energetic stabilization and the adsorbate entropy reduction compensates, leading to a similar desorption rate constants but different temperature dependence. Without our initial awareness, our work has resolved a small dispute between theory and experiment on NO's energetic preference for Pd steps. Earlier experimental work (erroneously) concluded that NO is not stabilized at steps of Pd single crystals[129]. Unfortunately, they have not assigned

their IR spectra correctly, based on which they draw their conclusions[130]. Later theoretical work indicated that NO is energetically stabilized at steps by 60 meV[131, 132], which is good agreement with our DFT-independent determination of 60^{+15}_{-30} meV.

Especially when more complicated kinetic mechanisms are developed, it is important to be able to use rate constants from complementary experiments. It is essential that such parameters are reliable and do not suffer from inaccuracies of simplified analysis. One of those example encountered us during this work. We aimed to develop a kinetic mechanism explaining the origin of thermally desorbing CO($v = 1$) molecules when a beam of CO($v = 2$) is scattered from a Au(111) surface. Our hypothesis was that chemisorption and physisorption states are involved in the formation of CO($v = 1$), as it was indicated by theory[133, 134]. Previous analysis of the data, reported in Ref. [135], has shown unambiguously that the CO($v = 1$) channel has translational and rotational distributions characteristic for molecules thermally equilibrated with the Au(111) surface. This observation means that statistical mechanics and TST can be used to model the underlying rate constants. Using a neural-network potential developed for CO/Au(111)[133] we modeled thermal rate constants to disentangle the competition between the chemisorption and physisortption states. Modeling of the underlying rate constants allowed us to restrict the number of unknown parameters substantially. Nevertheless, for a long time it seemed as if we would not be able to explain the formation of CO($v = 1$) within the Physisorption And Chemisorption (PAC) model, as it was unable to predict the experimental observations. It turned out that the disagreement was not due to a wrong model but due to a simplified analysis of previous TPD data[136] on which we relied. The rate constants derived from this analysis were obtained at low surface temperature, but the corresponding rate parameter were too inaccurate for extrapolation to high temperatures at which the scattering experiments were conducted. With the help of the CO/Au(111) PES we determined the prefactors for desoprtion, which helped us to reanalyze the TPD spectra and to determine an accurate binding energy of physisorbed CO. With this information, we have successfully reproduced the scattering experiments—see Sec. 4.2. Interestingly, rate constants from earlier analysis and our more reliable analysis deviate by 2 to 4 orders of magnitude in the temperature range of our scattering experiments. It is also interesting to highlight that the more accurate analysis provides a binding energy (0.12 eV, previously 0.18 eV) much closer to predictions by DFT calculations with the BEEF-vdW functional (0.10 eV)[133, 134].

These three examples show that small details in the analysis can be important for the conclusions drawn from kinetic experiments.

5.3 Construction of Adsorbate Partition Functions

In this work, I had the opportunity to test the performance of different adsorbate entropy models against elementary rates of thermal molecular and recombinative desorption. Below, I want to discuss some general considerations for the construction of accurate partition functions.

The CPES approach—see Sec. 1.3.3—is considered as one of the most accurate methods to determine the translational contribution to adsorbate entropy. Unfortunately, as it is conventionally used[92], it is based on a classical partition function. The CPES approach does not provide accurate results at low temperatures, because in this model the in-plane zero-point-energy contribution to the entropy is not considered. While for most adsorbates this contribution is rather low, typically 100 cm^{-1}

and lower, for hydrogen atoms on metals this is on the order of $\sim 600\,\mathrm{cm}^{-1}$ with an equivalent temperature of 700 K. We have solved this problem, assuming a static Pt surface, solving the in-plane Schrödinger equation and counting the eigenstates of H*. This is a similar approach as employed by a recent paper—see Ref. [110]. While this method should always be preferred, a very simple correction scheme for classical partition functions can be applied which improves the accuracy substantially.

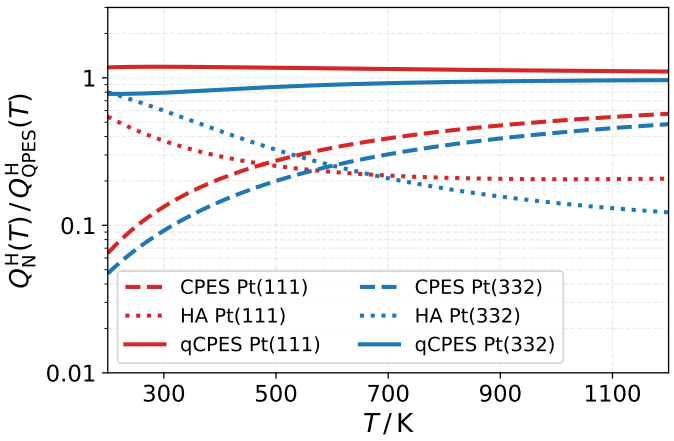

Figure 5.1: Three simplified entropy models—Harmonic Approximation (HA), Complete Potential Energy Sampling (CPES) and quantum limit CPES (qCPES)—are compared to the in-plane Quantum Potential Energy Sampling (QPES) partition function for H at Pt(111) and Pt(332). The qCPES model is closest to the QPES approach because it corrects the wrong low temperature limit of CPES.

The correction scheme was used first by Pitzer and Gwinn[114] for the construction of the hindered rotor model to describe the heat capacity of Ethane's internal rotation. This is also used for the HT model for adsorbate entropy[113]. The idea behind this correction is simple and general. At low temperatures the adsorbate will be restricted to the global minimum of an arbitrary potential. Any PES can be represented by a harmonic potential in its minimum. When a classical partition function approaches 0 K it converges to the numerical value of the classical Harmonic Oscillator (HO) partition function inside this minimum. This convergence can be used to correct the classical partition shown, on the example of a 2D problem, below:

$$Q_{xy}^{\mathrm{qCPES}} = \frac{2\pi m k_{\mathrm{B}} T}{h^2} \int\int \exp\left(-\frac{V(x,y)}{k_{\mathrm{B}} T}\right) \mathrm{d}x\mathrm{d}y \left(\frac{Q_x^{\mathrm{qHO}}}{Q_x^{\mathrm{cHO}}}\right) \left(\frac{Q_y^{\mathrm{qHO}}}{Q_y^{\mathrm{cHO}}}\right), \tag{5.1}$$

where Q^{cHO} and Q^{qHO} are the classical and the quantum HO partition functions, respectively. Here, $V(x,y)$ is the in-plane interaction potential and the configuration integral is obtained for the periodic unit of the surface. At low temperatures Eq. 5.1, which I refer to as quantum limit CPES (qCPES) in the following, will converge to the product of quantum HO partition functions. At high temperature the correction terms in parenthesis cancel each other, since the quantum HO expression converges to the classical HO partition function. This qCPES method is simple to implement as hindered-translator frequencies can be easily calculated from the PES at the most stable binding site. In Fig. 5.1 the performance of qCPES is compared to our Quantum Potential Energy Sampling (QPES) approach for H/Pt(111) and Pt(332)—see Sec. 3.1. As can be seen, qCPES reliably reproduces the in-plane QPES partition function within 20 % between 200 and 1200 K for both facets. Likely, the quality of qCPES will depend somewhat on the impact of anharmonicity on the first few quantum states of a given interaction potential. In this temperature range, qCPES is also more reliable than the HA and simple CPES approach. While this correction is general, for some reason, it is still only rarely applied.

Another quantum mechanical correction, which is not crucial for hydrogen atoms

only, is the electronic partition function of adsorbates. In the case of H* at Pt it is not possible to explain the results of kinetic experiments and the H* entropy at nanoparticles without considering the spin state degeneracy. Also for NO desorption on Pd ignoring the electronic partition function results in diffusion barriers of $\sim 0.5\,\mathrm{eV}$, which is in strong disagreement with theoretical predictions of $\sim 0.3\,\mathrm{eV}$. The deviation are due to the fact that NO has an unpaired electron in the $2\pi^*$ orbital which gives rise to an electronic partition function of ≈ 4. When interacting with Pd, a bonding and a nonbonding orbital forms[137], whereby the nonbonding orbital is too high in energy to be populated under experimental conditions, i.e., the temperature is too low. In this case the electronic partition function takes the value of the spin state degeneracy. If we account for this contribution, we obtain a diffusion barrier of $0.29 \pm 0.11\,\mathrm{eV}$, which is in good agreement with DFT calculations. There is no doubt that these are important effects to be considered for all surface reactions!

Almost all adsorbate entropy models rely on the approximation of normal modes. Even when anharmonic corrections are considered they rely on the diagonal anhamonicity[91, 116] and do not consider coupling of different degrees of freedom. Adsorbed molecules may be differently stabilized at different binding sites on the surface. A weaker binding energy at less stable binding sites on the surface can result in softening of vibrational modes which are associated with the molecule-surface interactions. For NH_3 desorption from Pt(111) we have introduced a simple scheme to account for changes in the frequencies of NH_3 vibrations, depending on the in-plane coordinates along the minimum energy pathway—see Sec. 4.3. We showed that in-plane model potentials constructed based harmonic frequencies and diffusion barriers alone are insufficient for the description of the density of states. The shape of the minimum-energy-pathway reflects the anharmonic coupling between various vibrational modes of NH_3 and allows to account the softening of (harmonic) frequencies using a simple formula given below:

$$Q = \frac{2\pi m k_\mathrm{B} T}{h^2} \int\int \exp\left(-\frac{V(x,y)}{k_\mathrm{B} T}\right) \left(\prod_i Q_i^{\mathrm{qHO}}(x,y)\right) \mathrm{d}x\mathrm{d}y, \tag{5.2}$$

where $V(x,y)$ is the potential energy of the relaxed configuration at a given in-plane coordinates. It is assumed that the vibrational frequencies of NH_3 are coupled to the in-plane coordinates while they are not coupled between each other. Frequencies that depend on in-plane coordinates, enter the xy-dependent quantum HO partition functions $Q_i^{\mathrm{qHO}}(x,y)$ and this way mimic the effect of mode coupling. This method has successfully explained the interactions probed by thermal desorption rates of NH_3 from Pt(111). Clearly, theoretical work is desired to test the accuracy of this approximation. Possibly, a partition function derived from a full-dimensional neuronal-network potential can be used to test the applicability of Eq. 5.2 to a wider extent.

So far, due to the lack of comparison to experiment, it is not clear how much thermal motion of the surface influences the partition functions of adsorbates. In the case of H* recombination on Pt it was enough to consider the partition functions at a static surface, but it cannot be excluded for other systems. Effects of slab elongation on sticking probabilities of H_2/Cu[138] and CH_4/Ni and Pt[139] and H diffusion into Pd bulk[140, 141] are known. Certainly, it will be important to consider the influence of thermal motion of the catalyst on the recrossing corrections for exact thermal rates. Enhanced sampling methods for molecular dynamics in heterogeneous catalysis are used to account for thermal fluctuations[142, 143] and approaches based on path integral methods are already used to obtain rate constants for simple surface processes[144, 145],

which also accounts for quantum effects. Unfortunately, such calculations are very expensive. More efficient approaches for the determination of accurate partition functions are desired.

5.4 Role of Atomic Steps in Thermal Desorption

It is well known that reaction rates are enhanced by atomic steps of metal catalysts[66, 96]. In addition, atomic steps tend to bind reactants more strongly and thus influence their rate of desorption. While the energetic stabilization of reactants and transition-states for reactions is one step-related effect, the decrease of the adsorbate's entropy on the catalyst is another. For thermal desorption rates, an energetic preference for steps will decrease the desorption rate while a decrease of entropy has the opposite effect. The importance of both effects was realized previously, where steps were found to decrease[60, 146] and increase[147] the desorption rate. In this work I have presented three systems for which we have obtained desorption rate constants—H recombination at Pt, NH_3 desorption from Pt and NO desorption from Pd. We used a detailed analysis by providing accurate kinetic models on the basis of transition state theory. For all three systems, we used not only the (111) surface, but also the (332) surface to investigate the influence of steps both experimentally and theoretically. I will highlight the most interesting observations made during the analysis of these systems below. For a detailed discussion—see Sec. 3.1, 4.3 and 4.1.

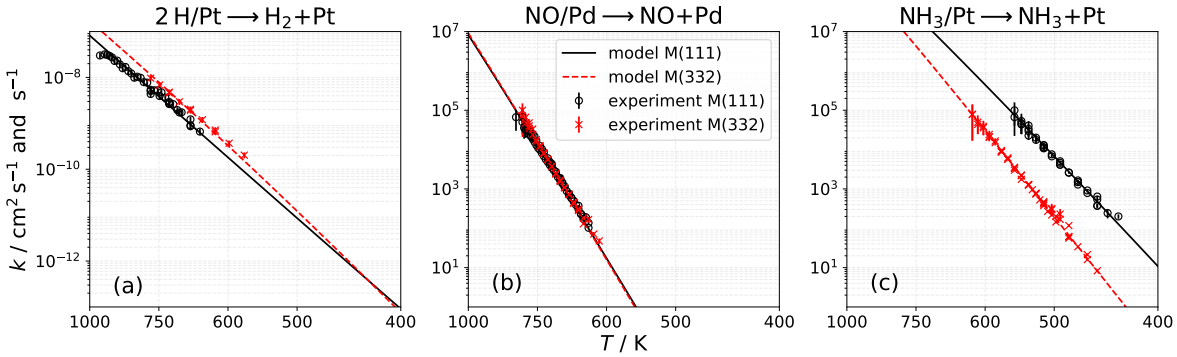

Figure 5.2: Comparison of thermal desorption rate constants for: **(a)** recombinative desorption of H at Pt(111) and Pt(332), **(b)** molecular desorption of NO from Pd(111) and Pd(332) and **(c)** molecular desorption of NH_3 from Pt(111) and Pt(332). The rate constants in (a) have units of $cm^2\,s^{-1}$, while in (b) and (c) these are s^{-1}. In all three cases atomic steps, present on M(332), decrease the adsorbate entropy and increase the binding energy of the molecule, but the degree of entropic influence is always different. See text.

For H* recombination on Pt we obtained a recombination rate constant for Pt(332) that was a factor of ~ 2 larger than on Pt(111), despite energetic stabilization of H* at steps of Pt(332) by 0.09 eV (0.18 eV per molecule)—see Fig. 5.2. The higher rate constant at the stepped surfaces is due to a substantially reduced density of states for H* on Pt(332) compared to Pt(111). While H* has a high number of delocalized states on Pt(111), the energetic preference for steps localizes H* to the step. As a consequence the adsorption entropy of H* is reduced. Since H* recombination is a second-order process, the entropic contribution is twice as important as for molecular desorption and leads to a higher rate constant despite a higher binding energy of H*. Based on our experimentally validated TST model, the rate constants will be equal at 430 K and at lower temperature the recombination rate will be higher on Pt(111).

It is expected that due to the entropic contribution, associated with the prefactor of the rate constant, is most important at high temperatures, while the binding energy dominates the overall rate at low temperatures.

While for molecular desorption the entropic contribution is expected to be less important than in recombinative desorption, it leads for NO desorption from Pd to a peculiar situation. In this case, the energetic preference of NO for steps is only $\sim 60\,\mathrm{meV}$. However, this stabilization increases the curvature of the interaction potential at the energy minimum which leads to a lower NO density of states at the step. As a consequence, in the temperature range of our experiments, the change in the adsorbate entropy and adsorption energy, which arise due to the different surface facets, compensate each other. Hence, only a minor difference in the Arrhenius parameters can be observed—see Sec. 4.1. A similar compensation effect can be expected for hydrogen atom recombination at Pt in the temperature range between 400 and 450 K—see Fig. 5.2(a) and (b).

Very often, the desorption rate is substantially reduced by the presence of steps. This is also the case for NH_3 desorption from Pt. The high energetic prefference of NH_3 for steps, $0.23 \pm 0.03\,\mathrm{eV}$, dominates over the weak entropic contributions. In fact, the local entropic contributions—specific to individual binding sites—are less pronounced for this system due to the high diffusion barrier of $\sim 0.7\,\mathrm{eV}$ at terraces. Such a high energy barrier leads to a strong localization of NH_3 at its respective binding site. Additional stabilization at steps does not substantially alter the density of states of NH_3 at steps. The minor entropic contribution that is present in NH_3 desorption from Pt(332) is due to the configurational entropy only—see Sec. 4.3. The key energetic parameters of the three molecule-surface systems from this section are summarized in Table 5.1.

Table 5.1: Basic energetic parameters for the systems from Fig. 5.2 studied in this work (see Sections 3.1, 4.1, 4.3). Here E_0^{T} is the (111)-terrace binding energy, E_0^{S} is the (111)-type step binding energy and D_0^{T} is the (111)-terrace hopping barrier. The uncertainties enclosure a 95 % confidence interval.

	H_2/Pt	NO/Pd	NH_3/Pt
E_0^{T} / eV	0.75 ± 0.03	1.766 ± 0.024	1.13 ± 0.02
E_0^{S} / eV	0.93 ± 0.03	$1.826^{+0.028}_{-0.038}$	1.36 ± 0.04
D_0^{T} / eV	-	0.29 ± 0.11	0.71 ± 0.04

These three molecule-surface systems show that despite an increased binding energy at steps, entropic effects may still dictate the rate of thermal desorption and likely also for reactions. The ability to predict rates of catalytic reactions, requires accurate site-specific description of the underlying molecule-surface interactions.

Chapter 6

Summary and Conclusions

Being able to predict elementary rate constants for reactions at surfaces is essential to understand heterogeneous catalysis. So far, state-of-the-art models which are used to predict thermal rates of surface processes, were rarely tested against experiments. The reason for the few reliable tests are due to the lack of accurate experimental data on thermal rate constants for surface processes. Usually, a comparison between experiment and theory can only be made when complex multi-step kinetic mechanisms are simulated. Such comparisons have the obvious danger of error-compensation and cannot be seen as critical tests of the underlying *ab initio* theory to predict elementary thermal reaction rates.

My aim of this work was to critically test state-of-the-art methods for predicting rates of thermal surface processes through comparison with accurate kinetics experiments. I have used the surface science approach[14]—well-defined single crystal surfaces and ultrahigh vacuum (UHV) conditions—to achieve this aim. I made use of our newly developed velocity resolved kinetics (VRK) method[65, 66] that allows simultaneous measurement of thermal desorption kinetics and dynamics. Accurate determination of elementary rate constants made it necessary to improve established experimental procedures and to develop proper data analysis methods to account for the complex nature of molecule-surface interactions.

During this research work, I restricted myself to the study of thermal desorption processes like molecular and recombinative desorption from atomically-flat and stepped single crystal surfaces of Pt, Pd and Au. The elementary desorption rate constants were of particular interest as they can be used as a sensitive probe for the adsorbate partition function—a quantity which is strongly associated with the molecule-surface interaction energies (Sec. 1.3.3 and 1.4). In order to probe the molecule-surface interactions, I analyzed the experimentally derived rate constants in the framework of exact thermal rates—transition state theory (TST) with recrossing corrections (see Sec. 1.3.2 and 1.4). In the analysis of thermal rate constants I exploited the flexibility of TST and defined the dividing plane far away from the surface where the transition state corresponds to the molecule in the gas phase (reduced by one translational degree of freedom). This far-transition-state approach has two advantages. Firstly, it allows one to accurately characterize the transition state partition functions by making use of the molecule's gas phase parameters. Secondly, the recrossing correction is equal to the molecule's thermal sticking coefficient[121, 122]. The sticking coefficients can be either obtained from complementary experiments or, using the unique advantage of VRK, from the desorption dynamics, based on the principle of detailed balance[148]. When the transition state contributions are properly taken into account, the remaining un-

known parameters for the description of the desorption rate constants are the adsorbate partition functions and the molecules binding energy to the surface. The contribution of the adsorbate entropy and the binding energy can be disentangled based on the temperature dependence of the desorption rate constant. While an accurate binding energy is a highly desired benchmark for electronic structure theory, an accurately determined adsorbate entropy is a sensitive probe for the features of the molecule-surface energy landscape.

I decided to explore multiple adsorbate-surface systems with different types of adsorbates, like atoms, diatomic and polyatomic molecules. To me, it was also important to investigate the influence of defects on the flat M(111) surface. Since steps are relevant for the kinetics of surface processes, I used the (332) facet of the respective metals, because they have a much larger step-density. This helped to disentangle the active-site specific molecule-surface interactions. The overall goal was to make general conclusions about the quality of adsorbate entropy models when these models are applied for a high variety of molecules and surfaces. This way I could exclude that the conclusions will be specific to individual surfaces or species. Below I point out the main conclusions obtained from different case studies, which I presented in this work.

The far-transition-state approach served as a critical tool to test and quantify the inaccuracy of different adsorbate entropy models. In addition, by seeking agreement between experiment and theory, improvements for established models could be suggested. In Sec. 3.1, we investigated the recombination of hydrogen atoms on Pt(111) and Pt(332). A molecular beam of H_2 and D_2 dosed the surface and the rates of recombination for HD, H_2, D_2 were measured. For second-order processes, it is necessary to know the initial concentration of reactants to disentangle their contribution to the observed recombination rate and to determine the second-order rate constant[44, 57]. Therefore, we established an absolute calibration procedure for the molecular beam flux. With this, the derived experimental rate constants could be compared to a model of exact thermal rates. The model was parametrized based on experimentally obtained sticking probabilities and binding energies[19, 20, 149–151]. This way we surmounted uncertainties that are associated with electronic structure theory used for the calculation of transition states and desorption barriers. To describe the entropy of hydrogen atoms we performed DFT calculations to obtain the in-plane interaction potential and harmonic frequencies of H at a static Pt surface. However, the standard entropy models—Complete Potential Energy Sampling (CPES)[92] and Harmonic Approximation (HA)[8]—were unable to reproduce the correct partition function for hydrogen atoms and lead to rate constants that were inconsistent with the experiment. Only when quantum effects were accurately treated we achieved agreement with the experiment without the need to fit any rate parameters. Two effects were essential: 1) treating the in-plane partition function quantum mechanically, i.e. solving the in-plane nuclear Schrödinger equation and counting the eigenstates, and 2) including the degeneracy of the spin states into the electronic partition function of atomic hydrogen. A complementary analysis, that I presented in Sec. 5.3, shows that the numeric value of the quantum in-plane partition function can be well reproduced with a simple correction scheme[113, 114] for the CPES method. The deviation over a broad temperature range is only 20 %. We observe that the recombination rate constant at Pt(332) is higher than on Pt(111) despite the fact that atomic hydrogen has an energetic preference for steps-over-terraces (0.09 eV). We can explain this effect by the substantially reduced entropy of hydrogen atoms at Pt(332) which overcompensates the effect of the higher binding energy at steps. We also used the quantum mechanical partition

function to model the adsorption entropy of atomic hydrogen at Pt(111) and (332), which turned out to be in agreement with earlier adsorption entropy measurements on Pt nano-particles[124]. The comparison of Pt(111) with Pt(332) explains why the hydrogen adsorbate entropy decreases with decreasing size of the nano-particles.

The very good agreement between experiment and the exact thermal rate model in H recombination at Pt was inspiring. Hydrogen interaction with Pt is an extensively studied system where accurate binding energies and sticking probabilities are well known. These findings initiated an idea: If it is possible to incorporate experimentally known parameters of molecule-surface interactions in a model and get excellent agreement with elementary thermal rate constants, why should it not be possible to reverse this procedure? This means to derive features of molecule-surface interactions based on the comparison of a detailed rate model with the experimental rate constants. This was the central essence of the NO/Pd desorption project from Sec. 4.1. While we used DFT calculations as basis for the analysis of hydrogen recombination at platinum, we decided to avoid electronic structure calculations for the NO/Pd interaction. This is due to inaccuracies of GGA exchange-correlation functionals for the description of $2\pi^* - d$ interactions[117, 137]. This results in overbinding of CO molecules at highly coordinated binding sites of a metal surface which in turn results in the wrong description of relative energies[117]. Since these effects are not well tested for NO, we decided to use an analysis based on a simple model potential that is parametrized with a diffusion barrier. By using this approach the partition functions, which dictate the prefactor of the rate constant, depend on the diffusion barrier. This dependence can be used to fit the NO binding energy and the diffusion barrier from the experimental desorption rate constant data from Pd(111). In addition, following the same strategy for Pd(332) data, we showed that NO has a weak step-over-terraces energetic preference of $\sim 60\,\mathrm{meV}$. This also clarified a minor dispute between theory and experiment regarding this question[129–132].

Accurately modeled thermal desorption rate constants may also serve as a reliable input for development and parametrization of kinetic models. In the case of CO interaction with Au(111), we showed that if thermal desorption rates are correctly modeled, they can be used to obtain further information on the kinetic mechanism—see Sec. 4.2. Earlier experiments showed that CO($v = 1$) molecules thermally desorb from an Au(111) surface after dosing with a molecular beam of CO($v = 2$)[135]. The temperature dependence of the desorption yield of CO($v = 1$) and CO($v = 2$) were instructive enough for the development and parametrization of a kinetic mechanism. In this mechanism, the surface interaction of CO through the physisorption and chemisorption states is taken into account and can explain the desorption pathways of vibrationally excited CO molecules. We were able to determine the energy parameters and vibrational relaxation times relevant for CO's interaction with Au(111). In addition, using the parametrized kinetic mechanism and the principle of detailed balance we could make quantitative conclusions about the microscopic pathways of CO adsorption at Au(111). This work shows a broad applicability of thermal desorption rates to the study of molecule-surface interactions and also demonstrates that the approaches can be manifold.

It is a general question to which degree surface science experiments can contribute to the understanding of industrial catalysis[8]. By studying the desorption rate of NH_3 from Pt surfaces we could identify certain problems and possible limitations of currently applied microkinetic models for the description of industrial ammonia oxidation—see Sec. 4.3. In our desorption studies we found that the desorption rate of NH_3 from

Pt(111) was not following first-order kinetics. Instead, we observed a bimodal decay which could be assigned to interactions at terraces and steps. Based on this observation, and complementary experiments on Pt(332), we constructed and globally fitted a desorption-diffusion kinetic model[146]. From this model we extract the underlying rate parameters. To our surprise the diffusion of NH_3 on (111)-terraces is very slow due to a diffusion barrier that is 65 % of NH_3's binding energy, which is also consistent with our DFT calculations. This contradicts the current view that diffusion barriers are always much smaller than the corresponding binding energies[86, 87]. Based on our derived rate parameters we show that at temperatures typical for the Ostwald process, NH_3 desorption and site-to-site hopping are on a similar timescale. As a consequence, NH_3 molecules, which adsorb primarily at terraces, will not manage to diffuse to steps where they tend to be decomposed by oxygen atoms[96]. Essentially, this means that NH_3 oxidation at Pt is likely to be a diffusion limited reaction under industrially relevant conditions. This is a major problem for kinetic mechanisms based on mean field rate equations, because they are unable to account for diffusion. With the help of our accurate thermal desorption rates, we provided a possible explanation why an established kinetic mechanism tends to overestimate the degree of ammonia slip under Ostwald process conditions[152]: The desorption rate is assumed to be too low at industrially relevant temperatures and overestimates the NH_3 coverages. This leads to a decrease of NO selectivity, because N_2 formation becomes enhanced due to a higher coverage of nitrogen at the catalyst. Consequently, ammonia becomes deactivated. Besides the interesting insights into the ammonia chemistry at industrial conditions, we also identified weaknesses of established adsorbate entropy models for the description of desorption and diffusion rates. The description of adsorbate partition functions almost exclusively relies on the assumption of decoupled degrees of freedom[92, 112, 113]. These models are unable to reproduce the experimental desorption prefactors. Our DFT calculations indicate that NH_3's vibrational frequencies are strongly modified depending on its in-plane coordinates, making decoupled degrees of freedom a bad assumption. We derive a simple correction scheme which includes coupling of different degrees of freedom. This approach accurately reproduces the observed desorption prefactors and may serve as a systematic correction in future rate constant modeling studies.

The molecule-surface systems to which I have restricted my work were nonreactive and could be simply studied with pump-probe experimental methods. However, real catalysts can be nonstationary and may change their morphology or phase, while in use[153, 154]. Here, I have presented a proof-of-principle velocity resolved kinetics experiment, where high-repetition-rate lasers and cameras were combined to study catalytic systems that were dynamically changing while studied—see Sec. 2.1. This approach, if extended appropriately, may replace the standard pump-probe schemes currently employed in velocity resolved kinetics experiments. Due to the high duty cycle of such measurements, it can be used as a more accurate tool for the study of thermal desorption processes with much higher precision and over much broader temperature range.

In this work I showed how the far-transition-state concept can be used to study the basic energy parameters of molecule-surface interactions from the study of thermal desorption rates (Sec. 1.3.2 and 1.4). These include binding energies at terraces, at steps and diffusion barriers. With the experiments on hydrogen atom recombination at platinum, I showed how through laser-based calibration of molecular beams, second-order rate constants can be accurately measured (Sec. 3.1). I also showed how entropic effects, that are associated with steps can dominate the overall rate of thermal

desorption (Sec. 5.4). This is likely to be important for reactions, as well. Based on the thermal desorption studies on four molecule-surface systems I identified normal mode coupling and quantum corrections as crucially important for the description of adsorbate entropies (Sec. 4.3, 3.1 and 5.3). Quantum corrections associated with zero-point energy do not require explicit state counting, but can be included in classical partition functions using the Pitzer-Gwinn correction (Sec. 5.3). I have also shown that the electronic partition functions have to be considered for an accurate description of adsorbate entropy (Sec. 3.1 and 4.1). However, this contribution is usually ignored—which violates basic symmetry rules in quantum mechanics. Furthermore, I demonstrated that some aspects of industrial catalysis and adsorbate thermodynamics on real catalytic materials can be explained with models which are developed based on observations made in surface science experiments (Sec. 4.3 and 3.1). I showed that mean field kinetic models are not applicable to certain aspects of ammonia chemistry on Pt (Sec. 4.3). This might be also true for other ammonia metal surface systems.

I could not find a more appropriate way to conclude this work than by a prospective statement by Wilhelm Ostwald that was made already in 1909[155]:
"It will hence be abundantly clear again that a special problem of chemical kinetics is involved in the special case of these catalyses and that until a way has been found whereby a rate of chemical reaction can generally be calculated in advance [...], the catalysis problem cannot satisfactorily be answered."
To understand heterogeneous catalysis we have to be able to quantify the rates of chemical reactions at surfaces accurately. I hope, this work is a step forward to making chemical reaction kinetics at surfaces a more exact science.

References

[1] D. Borodin, K. Golibrzuch, M. Schwarzer, J. Fingerhut, G. Skoulatakis, D. Schwarzer, T. Seelemann, T. Kitsopoulos, A. M. Wodtke, "Measuring Transient Reaction Rates from Nonstationary Catalysts", *ACS Catalysis* **2020**, *10*, 14056–14066, DOI 10.1021/acscatal.0c03773.

[2] D. Borodin, N. Hertl, G. B. Park, J. Fingerhut, M. Schwarzer, Y. Wang, F. Nitz, G. Skoulatakis, A. Kandratsenka, D. J. Auerbach, D. Schwarzer, H. Guo, T. N. Kitsopoulos, A. M. Wodtke, "Quantum influence on H atom recombination on Pt", **2021**, (submitted).

[3] D. Borodin, I. Rahinov, J. Fingerhut, M. Schwarzer, S. Horandl, G. Skoulatakis, D. Schwarzer, T. N. Kitsopoulos, A. M. Wodtke, "NO Binding Energies to and Diffusion Barrier on Pd Obtained with Velocity-Resolved Kinetics", *Journal of Physical Chemistry C* **2021**, *125*, 11773–11781, DOI 10.1021/acs.jpcc.1c02965.

[4] D. Borodin, I. Rahinov, P. R. Shirhatti, M. Huang, A. Kandratsenka, D. J. Auerbach, T. L. Zhong, H. Guo, D. Schwarzer, T. N. Kitsopoulos, A. M. Wodtke, "Following the microscopic pathway to adsorption through chemisorption and physisorption wells", *Science* **2020**, *369*, 1461–1465, DOI 10.1126/science.abc9581.

[5] D. Borodin, I. Rahinov, O. Galparsoro, J. Fingerhut, M. Schwarzer, K. Golibrzuch, G. Skoulatakis, D. J. Auerbach, A. Kandratsenka, D. Schwarzer, T. N. Kitsopoulos, A. M. Wodtke, "Kinetics of NH3 Desorption and Diffusion on Pt: Implications for the Ostwald Process", *Journal of the American Chemical Society* **2021**, *143*, 18305–18316, DOI 10.1021/jacs.1c09269.

[6] G. Ertl, *Reactions at Solid Surfaces*, John Wiley and Sons, **2009**.

[7] J. Libuda, H.-J. Freund, "Molecular beam experiments on model catalysts", *Surface Science Reports* **2005**, *57*, 157–298, DOI https://doi.org/10.1016/j.surfrep.2005.03.002.

[8] A. Nilsson, L. G. M. Pettersson, J. K. Norskov, *Chemical Bonding at Surfaces and Interfaces*, Elsevier, **2008**.

[9] I. Langmuir, "THE ADSORPTION OF GASES ON PLANE SURFACES OF GLASS, MICA AND PLATINUM.", *Journal of the American Chemical Society* **1918**, *40*, 1361–1403, DOI 10.1021/ja02242a004.

[10] D. J. Auerbach, J. C. Tully, A. M. Wodtke, "Chemical dynamics from the gas-phase to surfaces", *Natural Sciences* **2021**, *1*, e10005, DOI https://doi.org/10.1002/ntls.10005.

[11] G. B. Park, T. N. Kitsopoulos, D. Borodin, K. Golibrzuch, J. Neugebohren, D. J. Auerbach, C. T. Campbell, A. M. Wodtke, "The kinetics of elementary thermal reactions in heterogeneous catalysis", *Nature Reviews Chemistry* **2019**, *3*, 723–732, DOI 10.1038/s41570-019-0138-7.

[12] K. Reuter, M. Scheffler, "First-principles kinetic Monte Carlo simulations for heterogeneous catalysis: Application to the CO oxidation at RuO_2(110)", *Phys. Rev. B* **2006**, *73*, 045433, DOI 10.1103/PhysRevB.73.045433.

[13] J. Wang, C. Y. Fan, K. Jacobi, G. Ertl, "The Kinetics of CO Oxidation on RuO2(110): Bridging the Pressure Gap", *The Journal of Physical Chemistry B* **2002**, *106*, 3422–3427, DOI 10.1021/jp014109k.

[14] I. Langmuir, "Part II.—"Heterogeneous reactions". Chemical reactions on surfaces", *Trans. Faraday Soc.* **1922**, *17*, 607–620, DOI 10.1039/TF9221700607.

[15] P. Sabatier, *Catalysis in Organic Chemistry*, D. Van Nostrand Company, New York, **1922**.

[16] A. J. Medford, A. Vojvodic, J. S. Hummelshoj, J. Voss, F. Abild-Pedersen, F. Studt, T. Bligaard, A. Nilsson, J. K. Norskov, "From the Sabatier principle to a predictive theory of transition-metal heterogeneous catalysis", *Journal of Catalysis* **2015**, *328*, 36–42, DOI 10.1016/j.jcat.2014.12.033.

[17] K. Christmann, O. Schober, G. Ertl, "Adsorption of CO on a Ni(111) surface", *The Journal of Chemical Physics* **1974**, *60*, 4719–4724, DOI 10.1063/1.1680972.

[18] H. Conrad, G. Ertl, E. Latta, "Adsorption of hydrogen on palladium single crystal surfaces", *Surface Science* **1974**, *41*, 435–446, DOI https://doi.org/10.1016/0039-6028(74)90060-0.

[19] B. Poelsema, K. Lenz, G. Comsa, "The dissociative adsorption of hydrogen on defect-'free' Pt(111)", *J Phys Condens Matter* **2010**, *22*, 304006, DOI 10.1088/0953-8984/22/30/304006.

[20] B. J. J. Koeleman, S. T. de Zwart, A. L. Boers, B. Poelsema, L. K. Verhey, "Adsorption study of hydrogen on a stepped Pt (997) surface using low energy recoil scattering", *Nuclear Instruments and Methods in Physics Research* **1983**, *218*, 225–229, DOI 10.1016/0167-5087(83)90983-3.

[21] J. T. Yates, T. M. Duncan, S. D. Worley, R. W. Vaughan, "Infrared spectra of chemisorbed CO on Rh", *The Journal of Chemical Physics* **1979**, *70*, 1219–1224, DOI 10.1063/1.437603.

[22] K. Cao, G. Füchsel, A. W. Kleyn, L. B. F. Juurlink, "Hydrogen adsorption and desorption from Cu(111) and Cu(211)", *Phys. Chem. Chem. Phys.* **2018**, *20*, 22477–22488, DOI 10.1039/C8CP03386B.

[23] Q. Shuai, S. Kaufmann, D. J. Auerbach, D. Schwarzer, A. M. Wodtke, "Evidence for Electron–Hole Pair Excitation in the Associative Desorption of H2 and D2 from Au(111)", *The Journal of Physical Chemistry Letters* **2017**, *8*, 1657–1663, DOI 10.1021/acs.jpclett.7b00265.

[24] P. Redhead, "Thermal desorption of gases", *Vacuum* **1962**, *12*, 203–211, DOI https://doi.org/10.1016/0042-207X(62)90978-8.

[25] J. B. Miller, H. R. Siddiqui, S. M. Gates, J. N. Russell, J. T. Yates, J. C. Tully, M. J. Cardillo, "Extraction of kinetic parameters in temperature programmed desorption: A comparison of methods", *The Journal of Chemical Physics* **1987**, *87*, 6725–6732, DOI 10.1063/1.453409.

[26] D. A. King, "Thermal desorption from metal surfaces: A review", *Surface Science* **1975**, *47*, 384–402, DOI https://doi.org/10.1016/0039-6028(75)90302-7.

[27] C. Borroni-Bird, N. Al-Sarraf, S. Andersoon, D. King, "Single crystal adsorption microcalorimetry", *Chemical Physics Letters* **1991**, *183*, 516–520, DOI https://doi.org/10.1016/0009-2614(91)80168-W.

[28] C. T. Campbell, "Energies of Adsorbed Catalytic Intermediates on Transition Metal Surfaces: Calorimetric Measurements and Benchmarks for Theory", *Accounts of Chemical Research* **2019**, *52*, 984–993, DOI 10.1021/acs.accounts.8b00579.

[29] W. Lew, O. Lytken, J. A. Farmer, M. C. Crowe, C. T. Campbell, "Improved pyroelectric detectors for single crystal adsorption calorimetry from 100 to 350 K", *Rev Sci Instrum* **2010**, *81*, 024102, DOI 10.1063/1.3290632.

[30] T. L. Silbaugh, E. M. Karp, C. T. Campbell, "Energetics of formic acid conversion to adsorbed formates on Pt(111) by transient calorimetry", *J Am Chem Soc* **2014**, *136*, 3964–71, DOI 10.1021/ja412878u.

[31] A.-K. Henß, S. Sakong, P. K. Messer, J. Wiechers, R. Schuster, D. C. Lamb, A. Groß, J. Wintterlin, "Density fluctuations as door-opener for diffusion on crowded surfaces", *Science* **2019**, *363*, 715–718, DOI 10.1126/science.aav4143.

[32] T. Mitsui, M. K. Rose, E. Fomin, D. F. Ogletree, M. Salmeron, "Diffusion and Pair Interactions of CO Molecules on Pd(111)", *Phys. Rev. Lett.* **2005**, *94*, 036101, DOI 10.1103/PhysRevLett.94.036101.

[33] J. E. Reutt-Robey, D. J. Doren, Y. J. Chabal, S. B. Christman, "CO diffusion on Pt(111) with time-resolved infrared-pulsed molecular beam methods: Critical tests and analysis", *The Journal of Chemical Physics* **1990**, *93*, 9113–9129, DOI 10.1063/1.459202.

[34] K. Mudiyanselage, M. Trenary, R. J. Meyer, "Kinetics of NH Formation and Dissociation on Pt(111)", *The Journal of Physical Chemistry C* **2007**, *111*, 7127–7136, DOI 10.1021/jp068907s.

[35] J. Libuda, I. Meusel, J. Hartmann, H.-J. Freund, "A molecular beam/surface spectroscopy apparatus for the study of reactions on complex model catalysts", *Review of Scientific Instruments* **2000**, *71*, 4395–4408, DOI 10.1063/1.1318919.

[36] R. I. Masel, *Principles of Adsorption and Reaction on Solid Surfaces*, Wiley, New York, **1996**.

[37] M. P. D'Evelyn, R. J. Madix, "Reactive scattering from solid surfaces", *Surface Science Reports* **1983**, *3*, 413–495, DOI https://doi.org/10.1016/0167-5729(83)90002-X.

[38] R. Opila, R. Gomer, "Thermal desorption of Xe from the W(110) plane", *Surface Science* **1981**, *112*, 1–22, DOI https://doi.org/10.1016/0039-6028(81)90330-7.

[39] M. Eigen, "Methods for investigation of ionic reactions in aqueous solutions with half-times as short as 10^{-9} sec. Application to neutralization and hydrolysis reactions", *Discuss. Faraday Soc.* **1954**, *17*, 194–205, DOI 10.1039/DF9541700194.

[40] E. Gaviola, "Ein Fluorometer - Apparat zur Messung von Fluoreszenzabklingungszeiten", *Zeitschrift für Physik* **1927**, *42*, 853–861, DOI https://doi.org/10.1007/BF01776683.

[41] G. B. Park, B. C. Kruger, D. Borodin, T. N. Kitsopoulos, A. M. Wodtke, "Fundamental mechanisms for molecular energy conversion and chemical reactions at surfaces", *Reports on Progress in Physics* **2019**, *82*, DOI ARTN09640110.1088/1361-6633/ab320e.

[42] D. F. Padowitz, S. J. Sibener, "Multiple source modulated molecular beam reactive scattering applied to hydrogen recombination and oxidation on the Rh(111) surface", *Journal of Vacuum Science & Technology A* **1991**, *9*, 2289–2301, DOI 10.1116/1.577311.

[43] T. Engel, G. Ertl, "A molecular beam investigation of the catalytic oxidation of CO on Pd (111)", *The Journal of Chemical Physics* **1978**, *69*, 1267–1281, DOI 10.1063/1.436666.

[44] D. R. Olander, "Heterogeneous chemical kinetics by modulated molecular beam mass spectrometry", *Journal of Colloid and Interface Science* **1977**, *58*, 169–183, DOI 10.1016/0021-9797(77)90379-4.

[45] R. H. Jones, D. R. Olander, W. J. Siekhaus, J. A. Schwarz, "Investigation of Gas–Solid Reactions by Modulated Molecular Beam Mass Spectrometry", *Journal of Vacuum Science and Technology* **1972**, *9*, 1429–1441, DOI 10.1116/1.1317055.

[46] H. H. Sawin, R. P. Merrill, "Fourier analysis of linear surface kinetics in reactive molecular beam scattering", *Journal of Vacuum Science and Technology* **1981**, *19*, 40–46, DOI 10.1116/1.571014.

[47] J. A. Schwarz, R. J. Madix, "Modulated beam relaxation spectrometry", *Surface Science* **1974**, *46*, 317–341, DOI 10.1016/0039-6028(74)90260-x.

[48] C. T. Campbell, G. Ertl, H. Kuipers, J. Segner, "A molecular beam study of the catalytic oxidation of CO on a Pt(111) surface", *The Journal of Chemical Physics* **1980**, *73*, 5862–5873, DOI 10.1063/1.440029.

[49] M. Salmeróna, R. J. Gale, G. A. Somorjai, "A modulated molecular beam study of the mechanism of the H2–D2 exchange reaction on Pt(111) and Pt(332) crystal surfaces", *The Journal of Chemical Physics* **1979**, *70*, 2807–2818, DOI 10.1063/1.437787.

[50] W. L. Guthrie, J. D. Sokol, G. A. Somorjai, "The Decomposition of Ammonia on the Flat (111) and Stepped (557) Platinum Crystal-Surfaces", *Surface Science* **1981**, *109*, 390–418, DOI Doi10.1016/0039-6028(81)90496-9.

[51] G. E. Gdowski, J. A. Fair, R. J. Madix, "Reactive scattering of small molecules from platinum crystal surfaces: D2CO, CH3OH, HCOOH, and the nonanomalous kinetics of hydrogen atom recombination", *Surface Science* **1983**, *127*, 541–554, DOI 10.1016/0039-6028(83)90046-8.

[52] P. L. Houston, *Chemical Kinetics and Reaction Dynamics*, Dover Publications, Mineola, **2001**.

[53] D. R. Olander, A. Z. Ullman, "Analysis of nonlinear reactions in modulated molecular beam surface experiments", *International Journal of Chemical Kinetics* **1976**, *8*, 625–637.

[54] L. S. Brown, S. J. Sibener, "A molecular beam scattering investigation of the oxidation of CO on Rh(111). I. Kinetics and mechanism", *The Journal of Chemical Physics* **1988**, *89*, 1163–1169, DOI 10.1063/1.455224.

[55] L. S. Brown, S. J. Sibener, "A molecular beam scattering investigation of the oxidation of CO on Rh(111). II. Angular and velocity distributions of the CO2 product", *The Journal of Chemical Physics* **1989**, *90*, 2807–2815, DOI 10.1063/1.455930.

[56] K. A. Peterlinz, T. J. Curtiss, S. J. Sibener, "Coverage dependent desorption kinetics of CO from Rh(111) using time-resolved specular helium scattering", *The Journal of Chemical Physics* **1991**, *95*, 6972–6985, DOI 10.1063/1.461508.

[57] D. Borodin, M. Schwarzer, H. W. Hahn, J. Fingerhut, Y. Q. Wang, D. J. Auerbach, H. Guo, J. Schroeder, T. N. Kitsopoulos, A. M. Wodtke, "The puzzle of rapid hydrogen oxidation on Pt(111)", *Molecular Physics* **2021**, DOI 10.1080/00268976.2021.1966533.

[58] E. M. Karp, C. T. Campbell, F. Studt, F. Abild-Pedersen, J. K. Norskov, "Energetics of Oxygen Adatoms, Hydroxyl Species and Water Dissociation on Pt(111)", *Journal of Physical Chemistry C* **2012**, *116*, 25772–25776, DOI 10.1021/jp3066794.

[59] W. Lew, M. C. Crowe, E. Karp, O. Lytken, J. A. Farmer, L. Árnadóttir, C. Schoenbaum, C. T. Campbell, "The Energy of Adsorbed Hydroxyl on Pt(111) by Microcalorimetry", *The Journal of Physical Chemistry C* **2011**, *115*, 11586–11594, DOI 10.1021/jp201632t.

[60] K. Golibrzuch, P. R. Shirhatti, J. Geweke, J. Werdecker, A. Kandratsenka, D. J. Auerbach, A. M. Wodtke, C. Bartels, "CO Desorption from a Catalytic Surface: Elucidation of the Role of Steps by Velocity-Selected Residence Time Measurements", *Journal of the American Chemical Society* **2015**, *137*, 1465–1475, DOI 10.1021/ja509530k.

[61] F. Zaera, "A step in the right direction", *Nature Chemistry* **2015**, *7*, 279–280, DOI https://doi.org/10.1038/nchem.2217.

[62] J. Fingerhut, D. Borodin, M. Schwarzer, G. Skoulatakis, D. J. Auerbach, A. M. Wodtke, T. N. Kitsopoulos, "The Barrier for CO2 Functionalization to Formate on Hydrogenated Pt", *J Phys Chem A* **2021**, DOI 10.1021/acs.jpca.1c04833.

[63] A. T. J. B. Eppink, D. H. Parker, "Velocity map imaging of ions and electrons using electrostatic lenses: Application in photoelectron and photofragment ion imaging of molecular oxygen", *Review of Scientific Instruments* **1997**, *68*, 3477–3484, DOI 10.1063/1.1148310.

[64] D. W. Chandler, P. L. Houston, "Two-dimensional imaging of state-selected photodissociation products detected by multiphoton ionization", *The Journal of Chemical Physics* **1987**, *87*, 1445–1447, DOI 10.1063/1.453276.

[65] D. J. Harding, J. Neugebohren, H. Hahn, D. J. Auerbach, T. N. Kitsopoulos, A. M. Wodtke, "Ion and velocity map imaging for surface dynamics and kinetics", *Journal of Chemical Physics* **2017**, *147*, DOI 10.1063/1.4983307.

[66] J. Neugebohren, D. Borodin, H. W. Hahn, J. Altschaeffel, A. Kandratsenka, D. J. Auerbach, C. T. Campbell, D. Schwarzer, D. J. Harding, A. M. Wodtke, T. N. Kitsopoulos, "Velocity-resolved kinetics of site-specific carbon monoxide oxidation on platinum surfaces", *Nature* **2018**, *558*, 280–283, DOI 10.1038/s41586-018-0188-x.

[67] J. Neugebohren, Thesis, **2018**.

[68] T. H. Madey, J. J. Czyzewski, J. T. Yates, "Ion angular distributions in electron stimulated desorption: Adsorption of O2 and H2 on W(100)", *Surface Science* **1975**, *49*, 465–496, DOI https://doi.org/10.1016/0039-6028(75)90365-9.

[69] C. H. Hoffman, D. J. Nesbitt, "Quantum State Resolved 3D Velocity Map Imaging of Surface-Scattered Molecules: Incident Energy Effects in HCl + Self-Assembled Monolayer Collisions", *The Journal of Physical Chemistry C* **2016**, *120*, 16687–16698, DOI 10.1021/acs.jpcc.6b03973.

[70] K. Tonokura, T. Suzuki, "Slicing photofragment spatial distribution by laser sheet ionization", *Chemical Physics Letters* **1994**, *224*, 1–6, DOI https://doi.org/10.1016/0009-2614(94)00533-8.

[71] S. L. Bernasek, G. A. Somorjai, "Molecular beam study of the mechanism of catalyzed hydrogen–deuterium exchange on platinum single crystal surfaces", *The Journal of Chemical Physics* **1975**, *62*, 3149–3161, DOI 10.1063/1.430862.

[72] I. E. Wachs, R. J. Madix, "On the H2-D2 exchange on stepped platinum surfaces", *Surface Science* **1976**, *58*, 590–596, DOI https://doi.org/10.1016/0039-6028(76)90494-5.

[73] H. Chadwick, H. Guo, A. Gutiérrez-González, J. P. Menzel, B. Jackson, R. D. Beck, "Methane dissociation on the steps and terraces of Pt(211) resolved by quantum state and impact site", *The Journal of Chemical Physics* **2018**, *148*, 014701, DOI 10.1063/1.5008567.

[74] M. R. Tate, D. Gosalvez-Blanco, D. P. Pullman, A. A. Tsekouras, Y. L. Li, J. J. Yang, K. B. Laughlin, S. C. Eckman, M. F. Bertino, S. T. Ceyer, "Fluorine atom abstraction by Si(100). I. Experimental", *The Journal of Chemical Physics* **1999**, *111*, 3679–3695, DOI 10.1063/1.479677.

[75] T. Matsushima, "Angle-resolved measurements of product desorption and reaction dynamics on individual sites", *Surface Science Reports* **2003**, *52*, 1–62, DOI https://doi.org/10.1016/j.surfrep.2003.09.002.

[76] M. Andersen, C. Panosetti, K. Reuter, "A Practical Guide to Surface Kinetic Monte Carlo Simulations", *Frontiers in Chemistry* **2019**, *7*, 202, DOI 10.3389/fchem.2019.00202.

[77] K. Reuter in *Modeling and Simulation of Heterogeneous Catalytic Reactions*, John Wiley and Sons, **2011**, Chapter 3, pp. 71–111, DOI https://doi.org/10.1002/9783527639878.ch3.

[78] J. K. Norskov, T. Bligaard, J. Rossmeisl, C. H. Christensen, "Towards the computational design of solid catalysts", *Nature Chemistry* **2009**, *1*, 37–46, DOI 10.1038/nchem.121.

[79] K. Honkala, A. Hellman, I. N. Remediakis, A. Logadottir, A. Carlsson, S. Dahl, C. H. Christensen, J. K. Nørskov, "Ammonia Synthesis from First-Principles Calculations", *Science* **2005**, *307*, 555–558, DOI 10.1126/science.1106435.

[80] A. Logadottir, T. Rod, J. Nørskov, B. Hammer, S. Dahl, C. Jacobsen, "The Brønsted–Evans–Polanyi Relation and the Volcano Plot for Ammonia Synthesis over Transition Metal Catalysts", *Journal of Catalysis* **2001**, *197*, 229–231, DOI https://doi.org/10.1006/jcat.2000.3087.

[81] M. G. Evans, M. Polanyi, "Inertia and driving force of chemical reactions", *Trans. Faraday Soc.* **1938**, *34*, 11–24, DOI 10.1039/TF9383400011.

[82] C. Campbell, "Future Directions and Industrial Perspectives Micro- and macrokinetics: Their relationship in heterogeneous catalysis", *Top Catal* **1994**, *1*, 353–366, DOI https://doi.org/10.1007/BF01492288.

[83] C. T. Campbell, "The Degree of Rate Control: A Powerful Tool for Catalysis Research", *ACS Catalysis* **2017**, *7*, 2770–2779, DOI 10.1021/acscatal.7b00115.

[84] C. F. Goldsmith, R. H. West, "Automatic Generation of Microkinetic Mechanisms for Heterogeneous Catalysis", *The Journal of Physical Chemistry C* **2017**, *121*, 9970–9981, DOI 10.1021/acs.jpcc.7b02133.

[85] M. Liu, A. Grinberg Dana, M. S. Johnson, M. J. Goldman, A. Jocher, A. M. Payne, C. A. Grambow, K. Han, N. W. Yee, E. J. Mazeau, K. Blondal, R. H. West, C. F. Goldsmith, W. H. Green, "Reaction Mechanism Generator v3.0: Advances in Automatic Mechanism Generation", *Journal of Chemical Information and Modeling* **2021**, *61*, 2686–2696, DOI 10.1021/acs.jcim.0c01480.

[86] A. U. Nilekar, J. Greeley, M. Mavrikakis, "A simple rule of thumb for diffusion on transition-metal surfaces", *Angewandte Chemie-International Edition* **2006**, *45*, 7046–7049, DOI 10.1002/anie.200602223.

[87] G. W. Peng, M. Mavrikakis, "Adsorbate Diffusion on Transition Metal Nanoparticles", *Nano Letters* **2015**, *15*, 629–634, DOI 10.1021/nl504119j.

[88] S. Günther, T. Menteş, M. Niño, A. Locatelli, B. S., J. Wintterlin, "Desorption kinetics from a surface derived from direct imaging of the adsorbate layer", *Nature Communications* **2014**, *5*, 3853, DOI https://doi.org/10.1038/ncomms4853.

[89] J. Wintterlin, S. Völkening, T. V. W. Janssens, T. Zambelli, G. Ertl, "Atomic and Macroscopic Reaction Rates of a Surface-Catalyzed Reaction", *Science* **1997**, *278*, 1931–1934, DOI 10.1126/science.278.5345.1931.

[90] H. Tian, S. Rangarajan, "Machine-Learned Corrections to Mean-Field Microkinetic Models at the Fast Diffusion Limit", *The Journal of Physical Chemistry C* **2021**, *125*, 20275–20285, DOI 10.1021/acs.jpcc.1c04495.

[91] G. Piccini, J. Sauer, "Effect of Anharmonicity on Adsorption Thermodynamics", *Journal of Chemical Theory and Computation* **2014**, *10*, 2479–2487, DOI 10.1021/ct500291x.

[92] M. Jørgensen, H. Grönbeck, "Adsorbate Entropies with Complete Potential Energy Sampling in Microkinetic Modeling", *The Journal of Physical Chemistry C* **2017**, *121*, 7199–7207, DOI 10.1021/acs.jpcc.6b11487.

[93] M. Stamatakis, Y. Chen, D. G. Vlachos, "First-Principles-Based Kinetic Monte Carlo Simulation of the Structure Sensitivity of the Water–Gas Shift Reaction on Platinum Surfaces", *The Journal of Physical Chemistry C* **2011**, *115*, 24750–24762, DOI 10.1021/jp2071869.

[94] S. Bhandari, S. Rangarajan, C. T. Maravelias, J. A. Dumesic, M. Mavrikakis, "Reaction Mechanism of Vapor-Phase Formic Acid Decomposition over Platinum Catalysts: DFT, Reaction Kinetics Experiments, and Microkinetic Modeling", *ACS Catalysis* **2020**, *10*, 4112–4126, DOI 10.1021/acscatal.9b05424.

[95] A. Trinchero, A. Hellman, H. Grönbeck, "Methane oxidation over Pd and Pt studied by DFT and kinetic modeling", *Surface Science* **2013**, *616*, 206–213, DOI https://doi.org/10.1016/j.susc.2013.06.014.

[96] H. Ma, W. F. Schneider, "Structure- and Temperature-Dependence of Pt-Catalyzed Ammonia Oxidation Rates and Selectivities", *ACS Catalysis* **2019**, *9*, 2407–2414, DOI 10.1021/acscatal.8b04251.

[97] J. P. Clay, J. P. Greeley, F. H. Ribeiro, W. Nicholas Delgass, W. F. Schneider, "DFT comparison of intrinsic WGS kinetics over Pd and Pt", *Journal of Catalysis* **2014**, *320*, 106–117, DOI https://doi.org/10.1016/j.jcat.2014.09.026.

[98] M. Jørgensen, H. Grönbeck, "Perspectives on Computational Catalysis for Metal Nanoparticles", *ACS Catalysis* **2019**, *9*, 8872–8881, DOI 10.1021/acscatal.9b02228.

[99] J. Sutton, W. Guo, M. Katsoulakis, D. G. Vlachos, "Effects of correlated parameters and uncertainty in electronic-structure-based chemical kinetic modelling", *Nature Chemistry* **2016**, *8*, 331–337, DOI https://doi.org/10.1038/nchem.2454.

[100] H. Eyring, "The Activated Complex in Chemical Reactions", *The Journal of Chemical Physics* **1935**, *3*, 107–115, DOI 10.1063/1.1749604.

[101] D. G. Truhlar, B. C. Garrett, S. J. Klippenstein, "Current Status of Transition-State Theory", *The Journal of Physical Chemistry* **1996**, *100*, 12771–12800, DOI 10.1021/jp953748q.

[102] J. I. Steinfeld, J. S. Francisco, W. L. Hase, *Chemical Kinetics and Dynamics*, Prentice Hall, New Jersey, **1989**.

[103] K. A. Holbrook, M. J. Pilling, S. H. Robertson, *Unimolecular Reactions*, 2nd, John Wiley and Sons, New York, **1996**.

[104] J. L. Bao, D. G. Truhlar, "Variational transition state theory: theoretical framework and recent developments", *Chem. Soc. Rev.* **2017**, *46*, 7548–7596, DOI 10.1039/C7CS00602K.

[105] E. Nour Ghassemi, M. Wijzenbroek, M. F. Somers, G.-J. Kroes, "Chemically accurate simulation of dissociative chemisorption of D2 on Pt(1 1 1)", *Chemical Physics Letters* **2017**, *683*, 329–335, DOI 10.1016/j.cplett.2016.12.059.

[106] O. Galparsoro, S. Kaufmann, D. J. Auerbach, A. Kandratsenka, A. M. Wodtke, "First principles rates for surface chemistry employing exact transition state theory: application to recombinative desorption of hydrogen from Cu(111)", *Phys. Chem. Chem. Phys.* **2020**, *22*, 17532–17539, DOI 10.1039/D0CP02858D.

[107] H. Kramers, "Brownian motion in a field of force and the diffusion model of chemical reactions", *Physica* **1940**, *7*, 284–304, DOI https://doi.org/10.1016/S0031-8914(40)90098-2.

[108] P. Hänggi, P. Talkner, M. Borkovec, "Reaction-rate theory: fifty years after Kramers", *Rev. Mod. Phys.* **1990**, *62*, 251–341, DOI 10.1103/RevModPhys.62.251.

[109] J. Wellendorff, T. L. Silbaugh, D. Garcia-Pintos, J. K. Nørskov, T. Bligaard, F. Studt, C. T. Campbell, "A benchmark database for adsorption bond energies to transition metal surfaces and comparison to selected DFT functionals", *Surface Science* **2015**, *640*, 36–44, DOI https://doi.org/10.1016/j.susc.2015.03.023.

[110] K. Blöndal, K. Sargsyan, D. H. Bross, B. Ruscic, C. F. Goldsmith, "Adsorbate Partition Functions via Phase Space Integration: Quantifying the Effect of Translational Anharmonicity on Thermodynamic Properties", *The Journal of Physical Chemistry C* **2021**, *125*, 20249–20260, DOI 10.1021/acs.jpcc.1c04009.

[111] A. Bajpai, P. Mehta, K. Frey, A. M. Lehmer, W. F. Schneider, "Benchmark First-Principles Calculations of Adsorbate Free Energies", *ACS Catalysis* **2018**, *8*, 1945–1954, DOI 10.1021/acscatal.7b03438.

[112] C. Waitt, A. R. Miles, W. F. Schneider, "Adsorbate Free Energies from DFT-Derived Translational Energy Landscapes", *The Journal of Physical Chemistry C* **2021**, *125*, 20331–20342, DOI 10.1021/acs.jpcc.1c05917.

[113] L. H. Sprowl, C. T. Campbell, L. Arnadottir, "Hindered Translator and Hindered Rotor Models for Adsorbates: Partition Functions and Entropies", *Journal of Physical Chemistry C* **2016**, *120*, 9719–9731, DOI 10.1021/acs.jpcc.5b11616.

[114] K. S. Pitzer, W. D. Gwinn, "Energy Levels and Thermodynamic Functions for Molecules with Internal Rotation I. Rigid Frame with Attached Tops", *The Journal of Chemical Physics* **1942**, *10*, 428–440, DOI 10.1063/1.1723744.

[115] R. B. McClurg, R. C. Flagan, W. A. Goddard III, "The hindered rotor density-of-states interpolation function", *The Journal of Chemical Physics* **1997**, *106*, 6675–6680, DOI 10.1063/1.473664.

[116] J. Amsler, P. N. Plessow, F. Studt, T. Bučko, "Anharmonic Correction to Adsorption Free Energy from DFT-Based MD Using Thermodynamic Integration", *Journal of Chemical Theory and Computation* **2021**, *17*, 1155–1169, DOI 10.1021/acs.jctc.0c01022.

[117] P. J. Feibelman, B. Hammer, J. K. Norskov, F. Wagner, M. Scheffler, R. Stumpf, R. Watwe, J. Dumesic, "The CO/Pt(111) puzzle", *Journal of Physical Chemistry B* **2001**, *105*, 4018–4025, DOI 10.1021/jp002302t.

[118] C. Campbell, G. Ertl, H. Kuipers, J. Segner, "A molecular beam study of the adsorption and desorption of oxygen from a Pt(111) surface", *Surface Science* **1981**, *107*, 220–236, DOI https://doi.org/10.1016/0039-6028(81)90622-1.

[119] G.-J. Kroes, "Computational approaches to dissociative chemisorption on metals: towards chemical accuracy", *Phys. Chem. Chem. Phys.* **2021**, *23*, 8962–9048, DOI 10.1039/D1CP00044F.

[120] F. Studt, "Grand Challenges in Computational Catalysis", *Frontiers in Catalysis* **2021**, *1*, 2, DOI 10.3389/fctls.2021.658965.

[121] J. C. Tully, "Computer simulation of the dynamics of chemical processes", *Computers & Chemistry* **1981**, *5*, 159–165, DOI https://doi.org/10.1016/0097-8485(81)80103-9.

[122] J. C. Tully, "The Dynamics of Adsorption and Desorption", *Surface Science* **1994**, *299*, 667–677, DOI Doi10.1016/0039-6028(94)90688-2.

[123] I. G. Pitt, R. G. Gilbert, K. R. Ryan, "Application of Transition-State Theory to Gas-Surface Reactions: Barrierless Adsorption on Clean Surfaces", *The Journal of Physical Chemistry* **1994**, *98*, 13001–13010, DOI 10.1021/j100100a031.

[124] M. García-Diéguez, D. D. Hibbitts, E. Iglesia, "Hydrogen Chemisorption Isotherms on Platinum Particles at Catalytic Temperatures: Langmuir and Two-Dimensional Gas Models Revisited", *The Journal of Physical Chemistry C* **2019**, *123*, 8447–8462, DOI 10.1021/acs.jpcc.8b10877.

[125] T. Poikela, J. Plosila, T. Westerlund, M. Campbell, M. D. Gaspari, X. Llopart, V. Gromov, R. Kluit, M. van Beuzekom, F. Zappon, V. Zivkovic, C. Brezina, K. Desch, Y. Fu, A. Kruth, "Timepix3: a 65K channel hybrid pixel readout chip with simultaneous ToA/ToT and sparse readout", **2014**, *9*, C05013–C05013, DOI 10.1088/1748-0221/9/05/c05013.

[126] A. Zhao, M. van Beuzekom, B. Bouwens, D. Byelov, I. Chakaberia, C. Cheng, E. Maddox, A. Nomerotski, P. Svihra, J. Visser, V. Vrba, T. Weinacht, "Coincidence velocity map imaging using Tpx3Cam, a time stamping optical camera with 1.5 ns timing resolution", *Review of Scientific Instruments* **2017**, *88*, 113104, DOI 10.1063/1.4996888.

[127] D. A. Debrah, G. A. Stewart, G. Basnayake, A. Nomerotski, P. Svihra, S. K. Lee, W. Li, "Developing a camera-based 3D momentum imaging system capable of 1 Mhits/s", *Review of Scientific Instruments* **2020**, *91*, 023316, DOI 10.1063/1.5138731.

[128] G. Westphal, J. Wega, R. E. A. Dissanayake, T. Schäfer, "Chirality detection of surface desorption products using photoelectron circular dichroism", *The Journal of Chemical Physics* **2020**, *153*, 054707, DOI 10.1063/5.0014917.

[129] R. Ramsier, Q. Gao, H. Waltenburg, K.-W. Lee, O. Nooij, L. Lefferts, J. Yates, "NO adsorption and thermal behavior on Pd surfaces. A detailed comparative study", *Surface Science* **1994**, *320*, 209–237, DOI https://doi.org/10.1016/0039-6028(94)90310-7.

[130] D. Loffreda, D. Simon, P. Sautet, "Vibrational frequency and chemisorption site: a DFT-periodic study of NO on Pd (111) and Rh (111) surfaces", *Chemical Physics Letters* **1998**, *291*, 15–23, DOI https://doi.org/10.1016/S0009-2614(98)00569-7.

[131] B. Hammer, J. K. Norskov, "Adsorbate reorganization at steps: NO on Pd(211)", *Physical Review Letters* **1997**, *79*, 4441–4444, DOI DOI10.1103/PhysRevLett.79.4441.

[132] B. Hammer, "The NO+CO Reaction Catalyzed by Flat, Stepped, and Edged Pd Surfaces", *Journal of Catalysis* **2001**, *199*, 171–176, DOI https://doi.org/10.1006/jcat.2000.3147.

[133] M. Huang, X. Zhou, Y. Zhang, L. Zhou, M. Alducin, B. Jiang, H. Guo, "Adiabatic and nonadiabatic energy dissipation during scattering of vibrationally excited CO from Au(111)", *Phys. Rev. B* **2019**, *100*, 201407, DOI 10.1103/PhysRevB.100.201407.

[134] I. Lončarić, M. Alducin, J. I. Juaristi, D. Novko, "CO Stretch Vibration Lives Long on Au(111)", *The Journal of Physical Chemistry Letters* **2019**, *10*, 1043–1047, DOI 10.1021/acs.jpclett.9b00069.

[135] P. R. Shirhatti, I. Rahinov, K. Golibrzuch, J. Werdecker, J. Geweke, J. Altschäffel, S. Kumar, D. J. Auerbach, C. Bartels, A. M. Wodtke, "Observation of the adsorption and desorption of vibrationally excited molecules on a metal surface", *Nature Chemistry* **2018**, *10*, 592–598, DOI 10.1038/s41557-018-0003-1.

[136] D. P. Engelhart, R. J. Wagner, A. Meling, A. M. Wodtke, T. Schäfer, "Temperature programmed desorption of weakly bound adsorbates on Au(111)", *Surface Science* **2016**, *650*, The surface science of heterogeneous catalysis: In honor of Robert J. Madix, 11–16, DOI https://doi.org/10.1016/j.susc.2015.06.010.

[137] X. Huang, S. E. Mason, "DFT-GGA errors in NO chemisorption energies on (111) transition metal surfaces", *Surface Science* **2014**, *621*, 23–30, DOI https://doi.org/10.1016/j.susc.2013.09.024.

[138] M. J. Murphy, A. Hodgson, "Adsorption and desorption dynamics of H-2 and D-2 on Cu(111): The role of surface temperature and evidence for corrugation of the dissociation barrier", *Journal of Chemical Physics* **1998**, *108*, 4199–4211, DOI Doi10.1063/1.475818.

[139] S. Nave, A. K. Tiwari, B. Jackson, "Dissociative Chemisorption of Methane on Ni and Pt Surfaces: Mode-Specific Chemistry and the Effects of Lattice Motion", *The Journal of Physical Chemistry A* **2014**, *118*, 9615–9631, DOI 10.1021/jp5063644.

[140] T. Maeda, S. Naito, M. Yamamoto, M. Mabuchi, T. Hashino, "High-temperature diffusion of hydrogen and deuterium in palladium", *J. Chem. Soc. Faraday Trans.* **1994**, *90*, 899–903, DOI 10.1039/FT9949000899.

[141] H. Kimizuka, S. Ogata, M. Shiga, "Mechanism of fast lattice diffusion of hydrogen in palladium: Interplay of quantum fluctuations and lattice strain", *Phys. Rev. B* **2018**, *97*, 014102, DOI 10.1103/PhysRevB.97.014102.

[142] G. Collinge, S. F. Yuk, M.-T. Nguyen, M.-S. Lee, V.-A. Glezakou, R. Rousseau, "Effect of Collective Dynamics and Anharmonicity on Entropy in Heterogenous Catalysis: Building the Case for Advanced Molecular Simulations", *ACS Catalysis* **2020**, *10*, 9236–9260, DOI 10.1021/acscatal.0c01501.

[143] G. Piccini, M.-S. Lee, S. F. Yuk, D. Zhang, G. Collinge, L. Kollias, M.-T. Nguyen, V.-A. Glezakou, R. Rousseau, "Ab initio molecular dynamics with enhanced sampling in heterogeneous catalysis", *Catal. Sci. Technol.* **2021**, DOI 10.1039/D1CY01329G.

[144] Y. V. Suleimanov, "Surface Diffusion of Hydrogen on Ni(100) from Ring Polymer Molecular Dynamics", *The Journal of Physical Chemistry C* **2012**, *116*, 11141–11153, DOI 10.1021/jp302453z.

[145] Y. V. Suleimanov, F. J. Aoiz, H. Guo, "Chemical Reaction Rate Coefficients from Ring Polymer Molecular Dynamics: Theory and Practical Applications", *The Journal of Physical Chemistry A* **2016**, *120*, 8488–8502, DOI 10.1021/acs.jpca.6b07140.

[146] J. A. Serri, J. C. Tully, M. J. Cardillo, "The influence of steps on the desorption kinetics of NO from Pt(111)", *The Journal of Chemical Physics* **1983**, *79*, 1530–1540, DOI 10.1063/1.445946.

[147] D. E. Starr, C. T. Campbell, "Large Entropy Difference between Terrace and Step Sites on Surfaces", *Journal of the American Chemical Society* **2008**, *130*, 7321–7327, DOI 10.1021/ja077540h.

[148] C. T. Rettner, E. K. Schweizer, C. B. Mullins, "Desorption and Trapping of Argon at a 2H-W(100) Surface and a Test of the Applicability of Detailed Balance to a Nonequilibrium System", *Journal of Chemical Physics* **1989**, *90*, 3800–3813, DOI Doi10.1063/1.455838.

[149] R. van Lent, S. V. Auras, K. Cao, A. J. Walsh, M. A. Gleeson, L. B. F. Juurlink, "Site-specific reactivity of molecules with surface defects-the case of H2 dissociation on Pt", *Science* **2019**, *363*, 155–157, DOI 10.1126/science.aau6716.

[150] I. M. N. Groot, A. W. Kleyn, L. B. F. Juurlink, "Separating Catalytic Activity at Edges and Terraces on Platinum: Hydrogen Dissociation", *Journal of Physical Chemistry C* **2013**, *117*, 9266–9274, DOI 10.1021/jp401355c.

[151] A. C. Luntz, J. K. Brown, M. D. Williams, "Molecular beam studies of H2 and D2 dissociative chemisorption on Pt(111)", *The Journal of Chemical Physics* **1990**, *93*, 5240–5246, DOI 10.1063/1.459669.

[152] R. Kraehnert, M. Baerns, "Kinetics of ammonia oxidation over Pt foil studied in a micro-structured quartz-reactor", *Chemical Engineering Journal* **2008**, *137*, 361–375, DOI 10.1016/j.cej.2007.05.005.

[153] K. Reuter, M. Scheffler, "Composition, structure, and stability of RuO_2(110) as a function of oxygen pressure", *Phys. Rev. B* **2001**, *65*, 035406, DOI 10.1103/PhysRevB.65.035406.

[154] R. Imbihl, A. Scheibe, Y. F. Zeng, S. Gunther, R. Kraehnert, V. A. Kondratenko, M. Baerns, W. K. Offermans, A. P. J. Jansen, R. A. van Santen, "Catalytic ammonia oxidation on platinum: mechanism and catalyst restructuring at high and low pressure", *Physical Chemistry Chemical Physics* **2007**, *9*, 3522–3540, DOI 10.1039/b700866j.

[155] W. Ostwald, *Nobel Lectures In Chemistry (1901-1921)*, World Scientific Publishing Co Pte Ltd, **1999**.